

**STUDY OF THE EFFECT OF HOT ROLLING PROCESSING PARAMETERS ON THE  
VARIABILITY OF HSLA STEELS**

by

Jose Enrique Garcia Gonzalez

B.S in Materials Engineering, Instituto Tecnológico de Saltillo, Mexico, 1999

Submitted to the Graduate Faculty of  
the School of Engineering in partial fulfillment  
of the requirements for the degree of  
Master of Science in Materials Science and Engineering

University of Pittsburgh

2002

**UNIVERSITY OF PITTSBURGH**

**SCHOOL OF ENGINEERING**

This thesis was presented

by

Jose Enrique Garcia Gonzalez

It was defended on

November 22, 2002

and approved by

Dr. C. I. Garcia, Research Professor, Materials Science and Engineering

Dr. I. Nettleship, Associate Professor, Materials Science and Engineering

Thesis Advisor: Dr. A. J. DeArdo, William Kepler Whiteford Professor, Department of Materials  
Science and Engineering

## **ABSTRACT**

### **STUDY OF THE EFFECT OF HOT ROLLING PROCESSING PARAMETERS ON THE VARIABILITY OF HSLA STEELS**

Jose Enrique Garcia Gonzalez, M.Sc.

University of Pittsburgh, 2002

The effect of different hot mill processing parameters and their influence on the variability of mechanical properties of HSLA steels has been studied. This work presents an analysis of the relative contribution of the different hot mill processing parameters to the variability of HSLA steels. The experimental design includes variation of Reheating, Roughing, Finishing, and Coiling temperatures, as well as Cooling Rate through the  $\gamma \rightarrow \alpha$ , and from coiling to room temperature. The variation in finishing and coiling temperature results in an average variation of 12% in mechanical properties. The variation of the cooling rate, through the  $\gamma \rightarrow \alpha$ , and from coiling to room temperature has the largest impact on the variability of microstructure and properties. A correlation between the various microstructural features, dislocation densities and precipitation behavior, with mechanical properties is presented.

## **ACKNOWLEDGMENTS**

I would like to express my appreciation and gratitude to my advisors Dr. A.J DeArdo, Dr. C.I. Garcia, and P. Wray for their guidance and encouragement throughout the course of this project.

I would also like to thank Dr. M. Hua for his help with the TEM and APFIM. I want to thank all BAMPRI and graduate students for their friendship, support, and stimulating discussions during my years here at the University of Pittsburgh. I would like to thank J. Wu with whom I shared this project.

Special thanks to Dr. K. Goldman for all his advises and patient proof-reading, as well as for making corrections to my drafts.

Gratitude is expressed to Rouge, USX, Hylsa, Reference Metals and AISI for funding this study. I want to thank Rouge Steel for supplying the steel and USX for their help with the hot rolling.

I would also like to thank my parents, relatives and my friends in Mexico, for their constant support and encouragement.

Finally, I would like to thank my wife, Nadia, for her constant praying and love, without whom this could not have been achieved. I dedicate this work to her.

## TABLE OF CONTENTS

ABSTRACT.....	iii
ACKNOWLEDGMENTS .....	iv
TABLE OF CONTENTS .....	v
LIST OF TABLES .....	ix
LIST OF FIGURES .....	xi
1.0 INTRODUCTION.....	1
2.0 BACKGROUND.....	3
2.1 Commercial Thermomechanical Processing of HSLA Steels .....	5
2.2 Metallurgy of HSLA Steels/Effect of Hot Rolling Processing Conditions on HSLA Steels.....	7
2.2.1 Reheating Temperature .....	7
2.2.2 Roughing Temperature .....	13
2.2.3 Finishing Temperature .....	14
2.2.4 Effect of Coiling Temperature / Transformation Temperature.....	21
2.3 Evolution of Microstructure during Hot Rolling .....	25
2.3.1 Grain Size.....	25
2.3.2 Types of Ferrite Formed During Hot Rolling .....	27
2.3.3 Precipitation.....	29
2.3.3.1 Precipitation in Austenite.....	31
2.3.3.2 Precipitation in Ferrite .....	34
2.3.4 Texture Evolution During Hot Rolling .....	37

2.4	Strengthening Mechanisms .....	40
2.4.1	Grain Size Strengthening / The Hall-Petch Equation .....	40
2.4.2	Solid Solution Strengthening .....	45
2.4.3	Dislocation Strengthening.....	46
2.4.4	Precipitation Strengthening.....	47
2.4.5	Subgrain Strengthening.....	51
2.4.6	Texture Strengthening.....	52
3.0	STATEMENT OF OBJECTIVES .....	53
4.0	EXPERIMENTAL PROCEDURE.....	54
4.1	Materials / Alloy Design.....	54
4.2	Material Processing / Hot Rolling Study .....	54
4.3	Cooling Rate Experiment.....	58
4.4	Experimental Techniques / Microstructural Analysis.....	61
4.4.1	Optical Microscopy.....	61
4.4.2	Scanning Electron Microscopy and EBSD .....	62
4.4.3	Transmission Electron Microscopy ( TEM ) .....	62
4.4.4	Atom Probe Field Ion Microscopy ( APFIM ).....	63
4.5	Tensile Tests .....	64
4.6	Microhardness Measurements.....	65
5.0	RESULTS .....	66
5.1	Variability of Tensile Properties with Processing Condition .....	67
5.1.1	LYP .....	67
5.1.2	UTS .....	72
5.1.3	YPE.....	77
5.1.4	Work Hardening.....	80

5.1.5	Total Elongation.....	84
5.1.6	R-values .....	88
5.1.7	Hardness Values.....	91
5.2	Effect of Hot Rolling Parameters on the Microstructure .....	93
5.2.1	Effect of the Variation of the Processing Parameters on the Type of Phases ...	93
5.2.2	Effect of Processing Parameters on the Grain Size.....	100
5.2.3	Grain Boundary Misorientation. ....	104
5.2.4	Dislocation Density. ....	108
5.2.5	Precipitation.....	111
5.3	Cooling Rate Experiment.....	114
5.3.1	Effect of Variation of Cooling Rate on Hardness .....	114
5.3.2	Effect of Cooling Rate on Microstructure.....	118
5.3.2.1	Grain Size.....	120
5.3.2.2	Precipitation . ....	121
6.0	DISCUSSION.....	123
6.1	Microstructure Analysis.....	123
6.1.1	Types of Ferrite .....	123
6.1.2	LAGB's .....	125
6.1.3	Dislocation Density.....	127
6.1.4	Precipitation.....	129
6.2	Tensile Properties.....	130
6.3	Individual and Combined Effect of the Processing Parameters on the Tensile Properties and Microstructural Variability .....	132
6.3.1	Effect of the Reheating Temperature .....	132
6.3.2	Effect of Roughing Temperature .....	134
6.3.3	Effect of Finishing Temperature .....	135

6.3.4	Effect of Coiling Temperature .....	141
6.4	Comparison of Laboratory Hot Rolling Experiment and Commercial Hot Band ..	143
6.5	Modeling the Effect of Microstructure Variability.....	144
6.5.1	Application of the Models.....	147
6.6	Combined Effect of Cooling Rate and Coiling Temperature on the Variability of Microstructure and Mechanical Properties .....	152
6.6.1	Types of Transformation Product. ....	161
6.6.2	Precipitation and Cluster Formation. ....	163
7.0	CONCLUSIONS.....	166
APPENDICES .....		168
APPENDIX A	Processing Conditions and Mechanical Properties of the Individual Hot Bands.....	169
APPENDIX B	Micrographs of the Various Hot Bands Obtained After the Laboratory Hot Rolling Trials .....	173
APPENDIX C	Micrographs from Cooling Rate Experiment with Rouge Steel .....	184
BIBLIOGRAPHY.....		192

## LIST OF TABLES

Table 1 Possible variation of the microstructure with processing variability.....	4
Table 2 Molar volumes of microalloy carbides and nitrides, based on room temperature lattice parameters. After Gladman. ....	30
Table 3 Chemistry of 70 ksi HR HSLA material, wt.pct .....	55
Table 4 Design of the hot rolling experiment .....	56
Table 5 Hot rolling deformation schedule .....	56
Table 6 Processing variables for the cooling experiment .....	61
Table 7 Overall variability of LYP and TS .....	66
Table 8 Variability of the LYP with various processing conditions.....	67
Table 9 Variability of the UTS with various processing conditions.....	72
Table 10 Variability of the YPE with various processing conditions.....	77
Table 11 Variability of the work hardening with various processing conditions .....	81
Table 12 Variability of the total elongation with various processing conditions .....	85
Table 13 Variability of the R-bar and $\Delta R$ values with various processing conditions .....	89
Table 14 R-bar and $\Delta R$ values for different processing conditions .....	90
Table 15 Through-thickness hardness profile for hot-band samples .....	91
Table 16 Occurrence and volume fractions of constituent phases.....	95
Table 17 Variability of the polygonal ferrite with various processing conditions .....	99
Table 18 Grain size variation with processing conditions .....	100
Table 19 Variability of the grain size .....	101
Table 20 Grain boundary misorientation.....	105

Table 21 Dislocation densities for various individual processing conditions .....	108
Table 22 Average dislocation densities for the different processing parameters .....	109
Table 23 Hardness values for the different cooling rates from the finishing to coiling temperature, and coiling to room temperature at different coiling temperatures.....	114
Table 24 Microstructural components in Rouge steel .....	119
Table 25 TEM particle analysis for different coiling temperatures, with a 5 C/s cooling rate from FT to CT, and 0.01 C/s from CT to RT .....	122
Table 26 Relation between dislocation density and observed subgrain structure .....	127
Table 27 Calculated contributions of constituents to the lower yield stress .....	149
Table 28 Comparison of the precipitation strengthening as a function of finishing temperature, obtained as the difference between the calculated LYP without the precipitation strengthening contribution and the measured LYP .....	151
Table 29 Summary of the literature review of the effect of coiling temperature on the yield strength of HSLA steels .....	157
Table A Processing conditions of the laboratory hot rolled HSLA steel.....	169
Table B LYP and TS values for the different processing conditions, in the rolling direction..	170
Table C LYP and TS values for the different processing conditions, in the transverse direction .....	171
Table D LYP and TS values for the different processing conditions, in the diagonal direction	172

## LIST OF FIGURES

Figure 1 Coil-to-coil yield strength of 340 MPa grade HSLA steels .....	2
Figure 2 Tensile strength distribution along the coil length for two commercially hot rolled Nb-HSLA strip steels .....	2
Figure 3 Thermomechanical rolling of hot strip and plate .....	6
Figure 4 Schematic representation of austenite microstructure when deformed above or below the recrystallization stop temperature of austenite, with corresponding description of Sv. Note that the superscripts GB,DB,TB, and NPD denote the contribution to the total Sv from grain boundaries, deformation twins, twin boundaries and near planar defects.7	7
Figure 5 Austenite grain growth characteristics in steels containing various microalloy additions .....	8
Figure 6 Effect of fine Nb(CN) precipitates on the austenite grain coarsening temperature (Tgc).....	10
Figure 7 Schematic illustration of different austenite microstructures resulting from various deformation conditions .....	15
Figure 8 Effect of microalloying solute elements on the recrystallization stop temperature in a 0.07 C, 1.40 Mn, 0.25 Si steel.....	17
Figure 9 Different ranges of interpass time and its effect on the non-recrystallization temperature (Tnr).....	18
Figure 10 Effect of the transformation temperature on the strengthening mechanisms in an HSLA steel.....	21
Figure 11 Effect of cooling rate on the intensity of precipitation strengthening .....	22
Figure 12 Effect of coiling temperature and total nitrogen content on the yield strength of ¼” thick coil finished at 900 C and cooled at 17 C/sec. Fe-0.13C -1.40Mn -0.5Si - 0.12V.....	23
Figure 13 Effect of water-end temperature and total nitrogen content on the yield strength of ¼” thick coil finished at 900 C and cooled at 17 C/sec. Fe-0.13C -1.40Mn -0.5Si - 0.12V.....	23

Figure 14	Precipitation hardening in Nb-containing HSLA steels. Solid line indicates the predicted precipitation strengthening.....	24
Figure 15	Prediction of normalized precipitation strength as a function of coiling temperature when a 30C/h cooling is assumed to characterize coiling .....	25
Figure 16	Effect of the cooling rate on the final ferrite grain size transformed from deformed and recrystallized austenite .....	26
Figure 17	Optical micrographs of various microstructures appearing in controlled rolled and cooled HSLA steels. Fe - 0.03%C – 1.7%Mn and microalloying elements, except (d). (a) Quasipolygonal + bainitic ferrite; (b) Bainitic and quasipolygonal ferrite, both (a) and (b) transformed from recrystallized austenite. (c) quasipolygonal + bainitic ferrite, transformed from unrecrystallized austenite; (d) fine polygonal ferrite + pearlite; (e) acicular and quasipolygonal ferrite; (f) quasipolygonal + bainitic + acicular ferrite, both (e) and (f) with C-enriched minor phases.....	28
Figure 18	Effect of microalloy precipitates on microstructure of steel .....	29
Figure 19	Comparison of the solubility products of the microalloy carbides and nitrides, showing the greater stabilities of the nitrides relative to those of the carbides, and solubility products in ferrite lower than those in austenite. ....	30
Figure 20	Typical precipitation curves for niobium carbonitrides in austenite following a 50% reduction in thickness by hot rolling.....	31
Figure 21	Particle size distributions for a high N Nb-steel deformed at (a) 900°C, (b) 1000°C..	33
Figure 22	(a) Comparison of the start of recrystallization, $R_s$ , and the finish of recrystallization, $R_f$ , of a plain carbon steel (C) and a niobium steel (Nb). (b)The suggested effect of dissolved niobium is indicated by the curves $R_s(S)$ and $R_f(S)$ . (c) The additional effect of strain induced precipitation is coincident with high rates of precipitation indicated by the precipitation start, $P_s$ , and finish, $P_f$ , curves. After Jonas and Weiss. ....	34
Figure 23	(a) Structure of the metastable compound $Fe_{16}N_2(\alpha')$ , crosses indicate N atoms; (b) structure of the TiC, VC, NbC and carbonitride as $Ti(C,N)$ .....	35
Figure 24	Precipitation strengthening due to Nb carbonitride. The 0.02%Nb steel was rolled and then cooled rapidly to avoid precipitation. Sub-critical heat treatments, expressed by the Larsen-Miller parameter, allow precipitation, giving rise to a precipitation hardening curve.....	36
Figure 25	Inverse pole figure of hot rolled sheet. Finishing temperature: 885 C – 900 C; coiling temperature: 550 C.....	38
Figure 26	Inverse pole figure of hot rolled sheet. Finishing temperature: 830 C; coiling temperature: 620 C.....	38

Figure 27 Inverse pole figure of hot rolled sheet. Finishing temperature: 805 C; coiling temperature: 550 C.....	39
Figure 28 Change in texture with depth from the surface: (a) rolled at low temperature; (b) rolled at higher temperature .....	40
Figure 29 Yield strength dependence on grain size. Hall-Petch relationship. ....	41
Figure 30 Ky recovery after aging at 90 C, in a Fe-0.003C-0.003N steel , water-quenched from 700 C.....	43
Figure 31 The effect of the different strengthening contributions to the observed yield strength, for different manganese content.....	44
Figure 32 Solid solution strengthening effects in high strength low alloy steels. ....	45
Figure 33 Effect of transformation temperature on the dislocation density in a Fe-0.08C-0.21Ti steel.....	47
Figure 34 Orowan Mechanism. A dislocation meets hard undeformable second phase particles and loop between them. At higher stresses dislocations are released by Orowan looping or cross slip. ....	48
Figure 35 Dislocations may continue through the second phase particles (particle cutting). The second phase particle becomes deformed and the interfacial area of the particle/matrix is increased.....	49
Figure 36 Schematic representation of precipitation strengthening by particles of increased hardness according to the combined Orowan and shear mechanisms .....	49
Figure 37 The dependence of precipitation strengthening on precipitate size and volume fraction according to the Ashby-Orowan mechanism, compared with experimental observations for given microalloy conditions. ....	51
Figure 38 Variation in the relative yield strength for different texture components .....	52
Figure 39 Representation of the hot rolling experiment variables.....	57
Figure 40 Schematic representation of the cooling rate experiment.....	59
Figure 41 Shape of the modified Rastegaev's compression specimen design.....	60
Figure 42 Dimensions of the tensile specimens obtained for the mechanical testing .....	64
Figure 43 Effect of coiling temperature on LYP, for various processing conditions .....	68
Figure 44 Effect of finishing temperature on LYP, for various processing conditions .....	69
Figure 45 Effect of reheating temperature on LYP, for various processing conditions .....	70

Figure 46 Effect of roughing temperature on LYP, for various processing conditions.....	71
Figure 47 Effect of coiling temperature on UTS, for various processing conditions .....	73
Figure 48 Effect of reheating temperature on UTS, for various processing conditions .....	74
Figure 49 Effect of finishing temperature on UTS, for various processing conditions .....	75
Figure 50 Effect of roughing temperature on UTS, for various processing conditions.....	76
Figure 51 Effect of finishing temperature on YPE, for various processing conditions.....	78
Figure 52 Effect of roughing temperature on YPE, for various processing conditions.....	78
Figure 53 Effect of coiling temperature on YPE, for various processing conditions .....	79
Figure 54 Effect of reheating temperature on YPE, for various processing conditions .....	80
Figure 55 Effect of reheating temperature on the ‘n’ value, for various processing conditions ...	82
Figure 56 Effect of roughing temperature on the ‘n’ value, for various processing conditions ...	82
Figure 57 Effect of finishing temperature on the ‘n’ value, for various processing conditions ...	83
Figure 58 Effect of coiling temperature on the ‘n’ value, for various processing conditions .....	84
Figure 59 Effect of reheating temperature on %elongation, for various processing conditions...	86
Figure 60 Effect of coiling temperature on %elongation, for various processing conditions .....	86
Figure 61 Effect of finishing temperature on %elongation, for various processing conditions ...	87
Figure 62 Effect of roughing temperature on %elongation, for various processing conditions ...	88
Figure 63 Variation of hardness (through thickness) with processing conditions, indicating the higher hardness values for the high coiling temperature conditions .....	92
Figure 64 Effect of finishing and coiling temperature on the occurrence of different constituents, for the four combinations of reheating and roughing temperatures.....	94
Figure 65 Variation of the volume fraction of polygonal ferrite, for different coiling conditions .....	96
Figure 66 Variation of the volume fraction of polygonal ferrite, for different finishing conditions .....	96
Figure 67 Variation of the volume fraction of polygonal ferrite, for different roughing conditions .....	98

Figure 68 Variation of the volume fraction of polygonal ferrite, for different reheating conditions .....	98
Figure 69 Variation of the grain size for different reheating temperatures .....	102
Figure 70 Variation of the grain size for different roughing temperatures .....	103
Figure 71 Variation of the grain size for different finishing temperatures .....	103
Figure 72 Variation of the grain size for different coiling temperatures .....	104
Figure 73 Frequency distribution of the grain boundary misorientation for four extreme conditions of finishing and coiling temperatures .....	106
Figure 74 Average LAGB area fractions below 15 degrees misorientation, for the different processing conditions .....	107
Figure 75 Effect of coiling temperature on dislocation density, for various processing conditions .....	110
Figure 76 Effect of finishing temperature on dislocation density, for various processing conditions .....	110
Figure 77 Presence of Nb,V(C,N) clusters in the samples coiled at 650 C (a) 1132 processing condition and (b) 2132 processing condition.....	112
Figure 78 Character Plot from a small cluster, APFIM analysis .....	113
Figure 79 Composition and atomic percent of elements found in two clusters .....	113
Figure 80 The effect of coiling temperature and cooling rate from the coiling temperature to room temperature (CT to RT), for a fixed cooling rate from the finishing pass to coiling temperature (FT to CT) of 5 C/sec.....	115
Figure 81 The effect of coiling temperature and cooling rate from the coiling temperature to room temperature (CT to RT), for a fixed cooling rate from the finishing pass to coiling temperature (FT to CT) of 10 C/sec.....	116
Figure 82 The effect of increasing the cooling rate through the transformation temperature is shown as a comparison of the hardness values obtained at both 5 C/sec and 10 C/sec, for different coiling temperatures and varying cooling rates from the coiling to room temperature.....	118
Figure 83 CCT diagram constructed from the different microstructures observed at the various cooling conditions .....	119
Figure 84 Variation in grain size for different coiling temperature and cooling conditions .....	120

Figure 85 Particle size distribution for the 600 C and 700 C coiling temperatures, at a 0.01 C/sec cooling rate from CT to RT, and 5 C/sec from FT to CT.....	121
Figure 86 Typical phases in the hot band of the 70 ksi Rouge steel.....	123
Figure 87 Microstructure evolution based on finishing and coiling temperatures .....	124
Figure 88 Orientation map obtained by EBSD and the effect of coiling temperature on low angle grain boundary distribution. ....	125
Figure 89 Effect of processing conditions on dislocation strengthening .....	128
Figure 90 Range of dislocation densities as a function of coiling temperature .....	128
Figure 91 Effect of the processing conditions on the formation of small Nb,V(C,N) clusters ..	129
Figure 92 Analysis of the variability of the different hot mill processing parameters .....	130
Figure 93 Effect of processing variation on the average LYP variability .....	131
Figure 94 Variation of LYP with two different levels of reheating temperatures .....	133
Figure 95 Variation of LYP for different roughing temperature conditions .....	134
Figure 96 Variation of LYP for different finishing temperature conditions.....	136
Figure 97 Temperature profile during the finishing stage .....	138
Figure 98 Schematic illustration for estimation of strain retained prior to transformation .....	140
Figure 99 Variation of LYP for different coiling temperature conditions .....	141
Figure 100 Nb migration as a function of coiling temperature and time .....	143
Figure 101 Comparison of LYP and TS values of laboratory and commercial thermomechanically rolled 70 ksi HSLA steel. Finishing temperature: 900 C, coiling temperature: 650 C.....	144
Figure 102 Dependence of the precipitate strengthening contribution to the yield strength, at different volume fractions, for a mean particle diameter of 2 nm. ....	147
Figure 103 Calculated contributions to the lower yield stress, with processing conditions corresponding to the processing conditions 1211 through 2212. ....	150
Figure 104 Effect of finishing temperature on precipitation strengthening, for samples coiled at 650 C.....	151
Figure 105 Cooling of the head and tail of a coil, at the edge and middle (centerline) positions .....	153

Figure 106	The two cooling curves that envelope the possible thermal paths in a coil for which the Coiling Temperature is 700 C. The locations of the thermal paths are on the centerlines of the outer wrap and the middle wrap of the coil. ....	153
Figure 107	Nb migration distance for outer and middle wraps within a coil .....	154
Figure 108	Shift in the type of ferrite from polygonal and non-polygonal to acicular ferrite cooling at (a) 5C/sec from finishing to coiling temperature and (b) 10 C/sec from finishing to coiling temperature. Coiling temperature: 600 C, cooling rate from coiling to room temperature: 0.01 C/sec .....	155
Figure 109	Hardness after cooling from the coiling temperature at 0.01 C/s. The two curves for each steel are for different cooling rates from the finishing to the coiling temperature.....	156
Figure 110	Effect of stop cooling temperatures on the yield strength and precipitation strengthening for various HSLA steels .....	159
Figure 111	Calculated CCPT diagram of a 0.09% C - 1.46% Mn - 0.028 Nb steel.....	160
Figure 112	The variation of hardness of samples of Rouge Steel with different microstructural mixtures. The mixtures progress from polygonal ferrite to fully bainitic mixtures. P= Polygonal ferrite, NP=non polygonal ferrite, A=acicular ferrite, LB=lower bainite, UB=upper bainite .....	162
Figure 113	TEM dark field micrographs, (a) and (b). Precipitates formed during coiling, in the ferrite matrix, as observed in the diffraction patterns that show the Baker-Nutting relationship between precipitates and ferrite matrix. Processing conditions: cooling rate FT to CT 5C/sec, cooling rate CT to RT 0.01 C/sec, coiling temperature 600 C.....	163
Figure 114	TEM dark field micrographs of precipitates formed during austenite to ferrite transformation as illustrated by the interphase precipitation, and during coiling in the ferrite matrix, as observed in the diffraction patterns showing the Baker-Nutting relationship between precipitates and ferrite matrix. Processing conditions: cooling rate FT to CT 5C/sec, cooling rate CT to RT 0.01 C/sec, coiling temperature 700 C.....	164
Figure 115	Sequence of APFIM pictures of ultra-fine Nb,V(C,N) particles, taken at every five atomic layer evaporation, with CT = 600 °C. The fine particles are seen to form and disappear around the large probe hole at left-of-center.....	165

## 1.0 INTRODUCTION

The automotive industry is constantly striving to produce vehicles that are lighter, safer and more enduring. One of the tools available to meet these formidable challenges is the use of higher strength steels as a replacement for lower strength steels. These high strength strip and sheet steels have become ever more widely used in automobiles since the 1970's<sup>(1)</sup>. With the passage of time and with the need for higher strength, these HSLA steels have changed character from 350 MPa microalloyed ferrite-pearlite steels to the current 700 MPa multiphase steels. Unfortunately, as the strength level increases, so does the variability in properties such as yield strength and springback<sup>(2)</sup>. It is this variability that has limited the acceptance in use of higher strength HSLA steels in the automotive industry. The literature shows examples of the property variability encountered by HSLA steels, as shown in Figures 1 and 2<sup>(3,4)</sup>. These variations can approach 25% in the YS for 350 grade HSLA steel in heat to heat comparisons, Figure 1. Therefore, if the variation in yield strength can be understood and reduced, not only will higher strength levels be fully utilized, but rejection rates and costs will be lowered.

The obvious question then becomes: what is the source of the property variation for a given grade of HSLA strip steel, even with rather tight limits on composition? The answer lies in the hot strip mill. To discover where the variation in microstructure and properties originates, this research project was conducted to determine how variations in the stages of a hot strip mill, e.g., temperatures of reheating, rough rolling, finish rolling and coiling, may contribute to the final variation in microstructure and properties. In these experiments, steels are subjected to predetermined levels of the four control temperatures described above. The influence of these changes in temperatures on changes in microstructure and properties was determined. Therefore,

the goal of this research is to define the temperature variation(s) most strongly associated with variations in microstructure and properties.

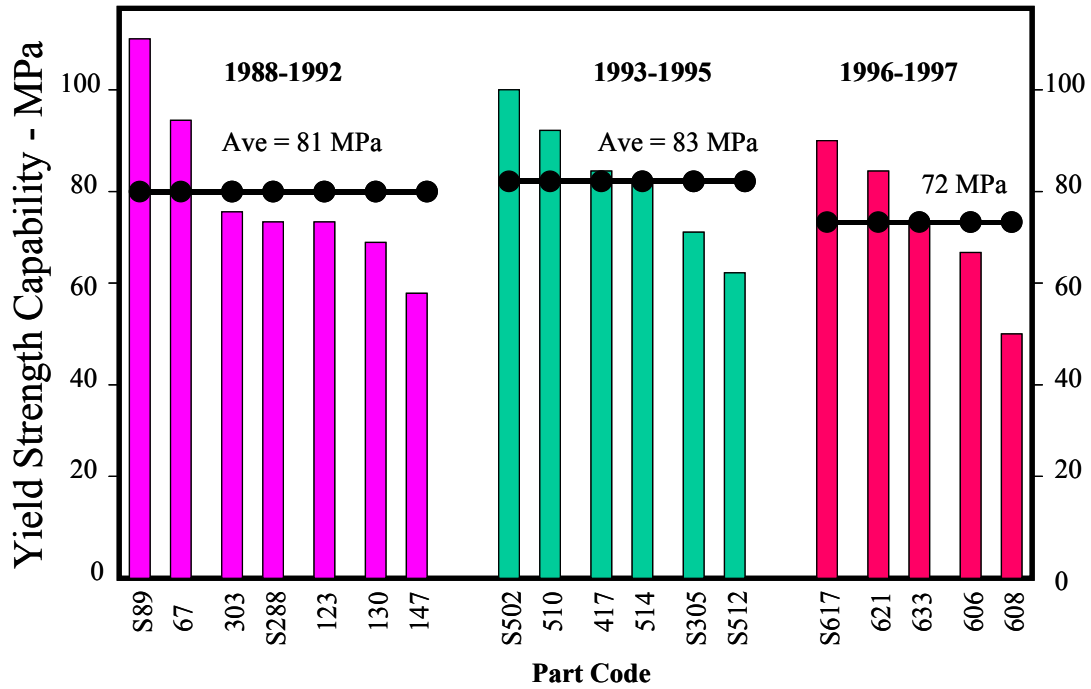


Figure 1 Coil-to-coil yield strength of 340 MPa grade HSLA steels

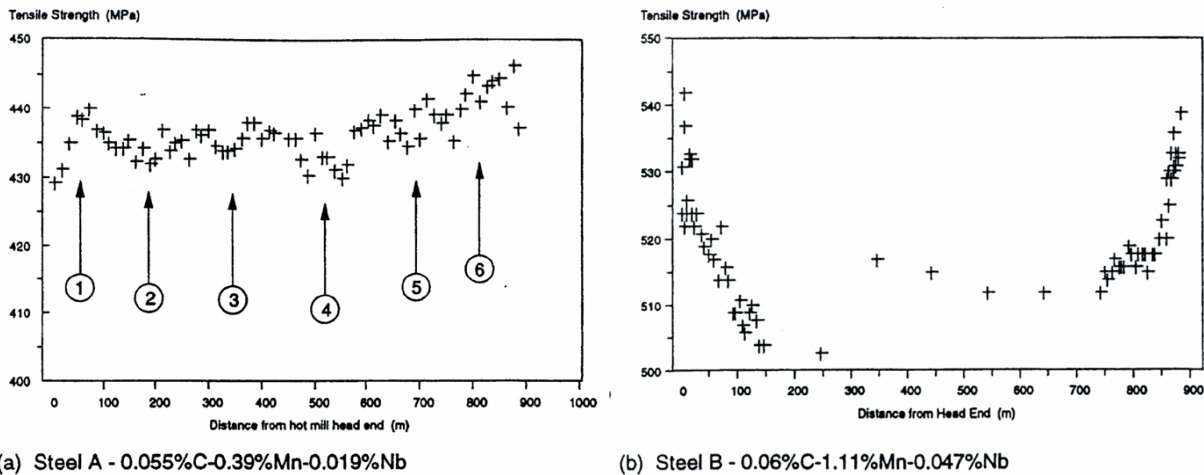


Figure 2 Tensile strength distribution along the coil length for two commercially hot rolled Nb-HSLA strip steels

## 2.0 BACKGROUND

The thermomechanical treatment of microalloyed steels is recognized as an alternative to traditional plain carbon steels. Microalloyed steels contain small amounts of microalloying elements such as Nb, Ti and V, and are used for their ability to increase the strength and toughness of the steel. The effects of these microalloying elements in HSLA steels are generally understood<sup>(5-7,12,26)</sup>. They impede motion of crystalline defects, and can be present as precipitates or solutes. With the proper thermomechanical rolling, it is possible to control the austenite microstructure, and through controlled cooling, a final microstructure is achieved. Precipitation, during or after deformation, leads to an additional strengthening. The microalloys control the microstructure of high strength low alloy (HSLA) steels by several mechanisms, which vary with the alloy, but their function is monitored by the properties required in the final product.

The extent in the control of the hot rolling parameters and controlled cooling in the thermomechanical processing of the steel, will allow an optimization of the mechanical characteristics. It is now recognized that the variability of the mechanical properties of HSLA steels increases as the design for higher yield strength increases. The thermomechanical processing of steels allows the use of sophisticated automatic process control for targeted setting and monitoring of rolling temperatures, deformation degrees, and cooling rates after hot rolling, so that defined and reproducible materials conditions can be set to be obtained after cooling of the rolled product in the coil. Thus, microstructural engineering has the goal of quantitatively linking the operational parameters of a hot strip mill with the properties of the hot band.

The processing in a hot-strip mill can be subdivided into three principal stages:

- 1.- Reheating
- 2.- Rolling ( in both roughing and finishing mill ) and
- 3.- Cooling ( water cooling in the run-out table and coiling )

Different processing stages have a strong effect on the microstructure development, which has a direct relationship with the final mechanical properties. The metallurgical phenomena, which occur during these processing stages, are shown in Table 1.

Table 1 Possible variation of the microstructure with processing variability

<u>Variable Processing Step</u>	<u>Microstructural Variability</u>
Reheating Temperature	<ul style="list-style-type: none"> <li>• Dissolution of precipitates.</li> <li>• Austenite grain coarsening.</li> </ul>
Roughing Temperature	<ul style="list-style-type: none"> <li>• Recrystallization.</li> <li>• Grain growth.</li> <li>• Texture development.</li> </ul>
Finishing Temperature	<ul style="list-style-type: none"> <li>• Precipitation.</li> <li>• Degree of recrystallization.</li> <li>• Ferrite transformation.</li> </ul>
Coiling Temperature	<ul style="list-style-type: none"> <li>• Ferrite grain coarsening.</li> <li>• Precipitation.</li> <li>• Ferrite transformation products</li> </ul>

The final mechanical properties of the hot band will depend on the different strengthening mechanisms that result from TMP. The microstructural features in the steel can be related to the yield strength by the use of the Hall-Petch relationship, and by additional parameters that are added to this relationship, which account for additional strengthening mechanisms. These relationships form the basis for the prediction of strength from microstructural analysis, and will be reviewed later.

## **2.1 Commercial Thermomechanical Processing of HSLA Steels**

The thermomechanical process of controlled rolling makes use of an optimized rolling schedule in which the finishing passes are applied at temperatures close to 900 C, with the purpose to obtain a substantial refinement of the austenitic grain size, or an increase in Sv. This will result in a fine ferrite grain size. The process for the thermomechanical rolling of hot strip and plate is shown in Figure 3<sup>(7)</sup>.

From a physical metallurgy point of view, two types of steel behavior can be distinguished<sup>(8)</sup>, and are represented in Figure 4. One is when recrystallization of the austenite occurs between rolling passes. In this case, fine austenite grain size is obtained by recrystallization after each pass. In the second case, recrystallization does not occur between passes in the final stage of rolling. At lower temperature ranges, recrystallization is first partial and then completely inhibited. The austenite grains are sufficiently fine at the point where recrystallization ceases to occur, and sufficient reduction in thickness is effected beyond this stage, so that the final austenite grains will be thin and highly elongated, called “pancaked structure” provides a high austenite grain boundary area/unit volume. This produces a high density of nucleation sites for ferrite grains giving a very fine structure. If the austenite grain size

is too coarse prior to the passes at temperatures below the recrystallization range, or if the amount of deformation introduced in this latter range is insufficient, mixed structures such as acicular and bainitic ferrite can be obtained.

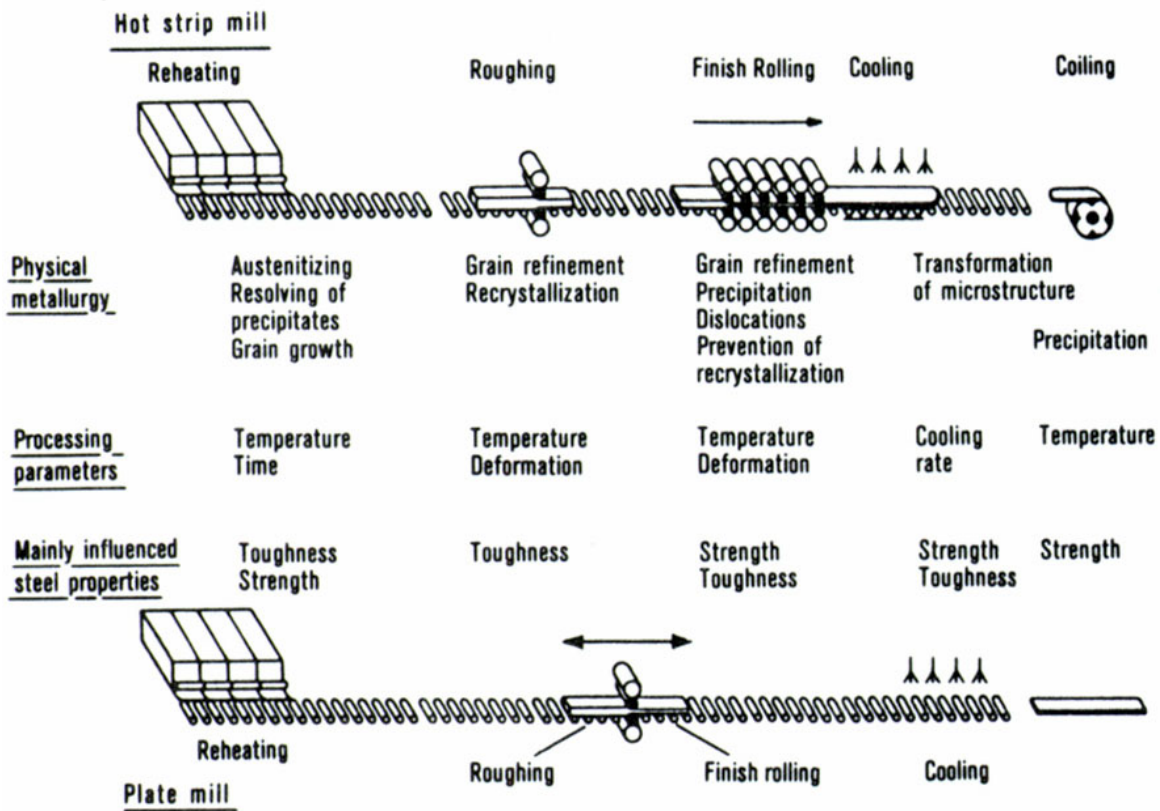


Figure 3 Thermomechanical rolling of hot strip and plate

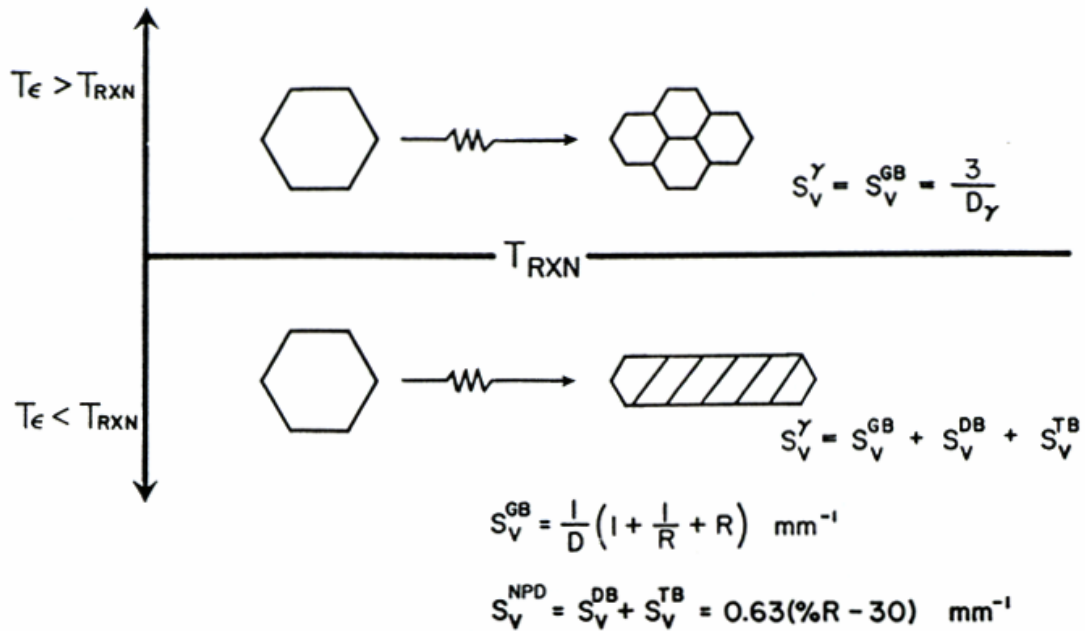


Figure 4 Schematic representation of austenite microstructure when deformed above or below the recrystallization stop temperature of austenite, with corresponding description of  $S_v$ . Note that the superscripts GB, DB, TB, and NPD denote the contribution to the total  $S_v$  from grain boundaries, deformation twins, twin boundaries and near planar defects.

## 2.2 Metallurgy of HSLA Steels/Effect of Hot Rolling Processing Conditions on HSLA steels

### 2.2.1 Reheating Temperature

The main objective of the slab reheating stage, is to achieve a uniform slab temperature, to form a correct and uniform starting austenite grain size, and to ensure that all the microalloying elements (Ti, Nb and V), are in complete solid solution. The choice of the reheating temperature for a given microalloyed steel determines both the initial grain size and the initial microalloying element solute content of the austenite. Figure 5 shows the characteristics of the grain coarsening behavior of austenite during reheating for various microalloy additions<sup>(9)</sup>.

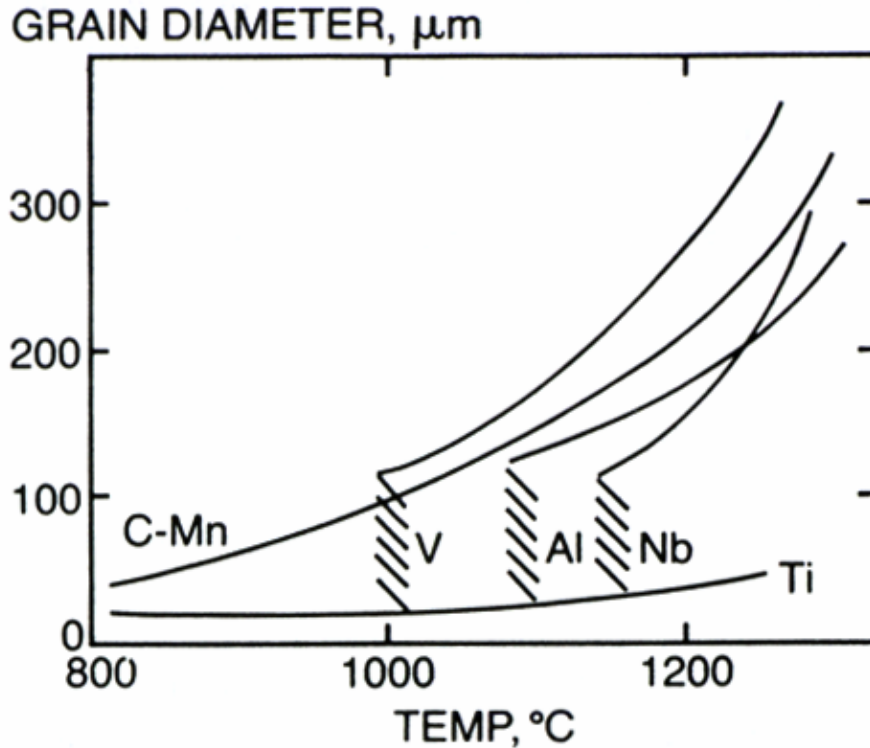


Figure 5 Austenite grain growth characteristics in steels containing various microalloy additions

The left side of the hatched region of the curves represents the suppression of primary recrystallization, and at the hatched region, the grain coarsening temperature ( $T_{gc}$ ) for each steel occurs. At the  $T_{gc}$ , a region of mixed primary and secondary grains coexists. At higher temperatures, secondary recrystallization occurs. The grain coarsening temperature is controlled by the stability and solubility of the precipitates, which are pinning the austenite grains. The stability of these precipitates is controlled by their composition. For most commercial grades of steel, complete solution of VC is expected at 920 C, and VN at higher temperatures, whereas Nb(CN), AlN and TiC require temperatures in the range 1150-1300 C<sup>(10)</sup>. Precipitates in Nb-V steels containing high N content are more stable and are responsible for the fine austenite grains

which are observed after reheating to temperatures as high as 1200 C<sup>(11)</sup>. TiN is the most stable compound and little dissolution is expected to take place at normal reheating temperatures.

Solubility products play a vital role in understanding the physical metallurgy of microalloyed steel, specially those aspects which are concerned with precipitation-related phenomena. Solubility products can be influenced by the presence of elements that do not directly participate in the precipitation reaction. This effect occurs through the influence of third and higher order elements in solution on the interaction coefficients, hence activities, for Nb and C in austenite. Third elemental solutes that raise the activity of Nb or C, through a positive interaction coefficient, decrease their solubility while those that decrease the activity through negative coefficients increase it. Solubility products relations have been published and can be found elsewhere <sup>(12,35,39)</sup>.

Pohts et al.<sup>(13)</sup> investigated the dissolution behavior of complex precipitates during reheating at 1150 C. They found a large number of precipitates containing Nb and Ti. The observed range in sizes was 70-150 nm. Elemental mapping of these precipitates showed the inner particles to be Ti and N rich. NbC was situated in the outside layer, suggesting that NbC nucleated on preexisting Ti-rich particles. At 1200 C, they found fewer particles, all of them with smaller amounts of Nb, and the size ranging from 40-100 nm. This suggests that at this reheating temperature, more Nb has been put into solution in the austenite. At 1250 C, they found far fewer particles, with a smaller size range and small traces of Nb.

The austenite grain coarsening behavior for various Nb and V steels have been further investigated extensively <sup>(14,15,83)</sup>. It has been shown that Nb steels have higher grain coarsening temperatures than V steels. A maximum grain coarsening temperature occurs at the stoichiometric ratio in Nb steels, whereas for V steels this is less marked . In Nb steels, this is

due to the fact that the estimated volume fraction of fine Nb(CN) precipitates is a maximum at this ratio<sup>(15)</sup>. Increasing the Nb content refines the austenite grain size at all temperatures up to 1200 C, presumably due to undissolved Nb(CN). The effect of fine precipitates in controlling the Tgc is confirmed by the relationship shown in Figure 6<sup>(16)</sup>, where the Tgc increases with increasing amount of fine Nb(CN) precipitates.

However, there is a limiting austenite grain size below which even the highest Nb contents cannot produce further refinement. This limiting grain size increases with increasing temperature because of both solution of the Nb(CN) and particle coarsening. For a constant particle volume fraction, increasing particle size with increasing temperature results in a coarser austenite grain size.

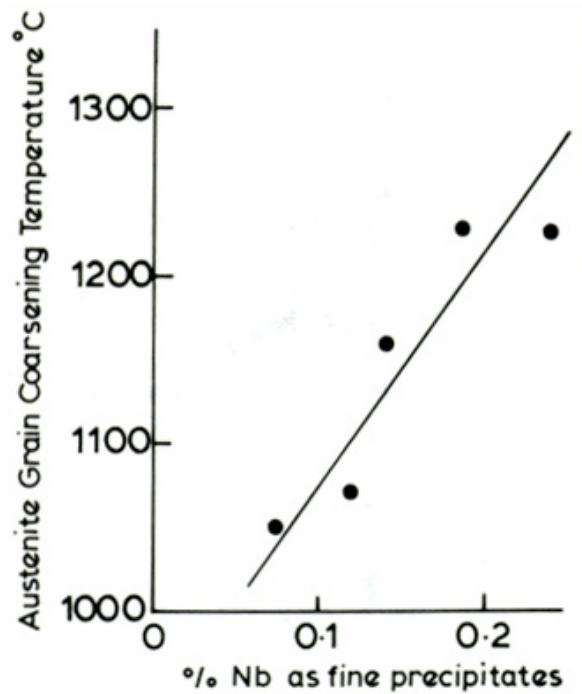


Figure 6 Effect of fine Nb(CN) precipitates on the austenite grain coarsening temperature (Tgc )

The principles of the inhibition of grain growth by small particles are very well understood. The model developed by Zener<sup>(17)</sup> produces a simple relationship between the grain radius, the particle volume fraction, and the particle radius. Basically, it is based on the fact that any particle will interact with a grain boundary because of the elimination of that part of the grain boundary that is occupied by the particle. Then, if the particle and boundary are to be separated, it would involve the creation of the grain boundary area destroyed by the particle. This unpinning process requires a supply of energy, additional to that supplied by the thermal activation, so this is supplied from the energy release accompanying the grain growth process.

The pinning force per particle was taken from the bubble theory as ' $\pi r \gamma$ ' where ' $r$ ' is the spherical pinning particle radius, and  $\gamma$  is the grain boundary energy. The supply of energy was calculated on the basis of an isolated shrinking spherical grain of surface  $4\pi R^2$ , where ' $R$ ' is the grain radius. This gives the rate of supply of energy with respect to the shrinking grain (per unit area of grain boundary):

$$\frac{8\pi R \gamma}{4\pi R^2} \quad (1)$$

or

$$\frac{2\gamma}{R} \quad (1a)$$

Considering  $2rN_v$  particles per unit area of grain boundary, this can be expressed in terms of particle size and volume fraction (  $N_v$  is the number of particles per unit volume and random distributed ):

$$f = N_v \cdot \frac{4\pi r^3}{3} \quad (2)$$

and the pinning force per unit area of grain boundary is

$$2r \cdot 3f \cdot \pi r \gamma / 4\pi r^3 = 3f \cdot \gamma / 2r \quad (3)$$

Equating driving and pinning forces:

$$2\gamma/R = 3f \cdot \gamma / 2r \quad (4)$$

or

$$R = 4r / 3f \quad (4a)$$

which is the Zener equation.

Gladman<sup>(18)</sup> has reviewed this model, and he has considered a model of a growing tetrakaidecahedral grain of radius  $R$  in a matrix of tetrakaidecahedral grains of radius  $R_0$ , which gives a better understanding of grain growth<sup>(19)</sup>. Gladman assumed the rigid motion of grain boundaries through a regular array of spherical particles. It was shown that the pinning force for each particle, 'F', and the particle radius, 'r', were related by:

$$F = 4r\sigma \quad (5)$$

where  $\sigma$  is the interfacial energy per unit area of boundary. Subsequently, an expression for the critical particle size,  $r_c$ , was derived, below which grain boundaries are pinned:

$$r_c = \frac{6R_0 f_v}{\pi} \times \left( \frac{3}{2} - \frac{2}{Z} \right)^{-1} \quad (6)$$

which is known as the Gladman Equation<sup>(20)</sup>, and the relationship is obtained by equating the rates of the grain boundary energy increase during grain growth and the particle pinning force.  $R_0$  is the mean radius of the matrix grain and  $f_v$  is the volume fraction of second phase particles.  $Z$  represents the ratio of the radii of growing and matrix grains. Hillert<sup>(21)</sup> has deduced that  $Z$  can

have values ranging between  $2^{1/2}$  to 2 throughout the grain growth process. For a value of  $Z=2$ , equation 6 reduces to:

$$r_c \cong 4R_0 f_v \quad (7)$$

### 2.2.2 Roughing Temperature

The metallurgical objective of the roughing rolling phase is to achieve the finest possible recrystallized austenite grain size before the finishing stage, and it is completed at temperatures above 1000 C. During the roughing stage, most of the plastic deformation takes place, and austenite grain refinement through recrystallization is achieved. In industrial plate rolling practice, the interpass time during which a plate may experience static structural change is approximately 20-30 secs. In tandem rolling, the interpass time is less than 5 seconds. During this period of interpass time, both recrystallization and precipitation may take place, competing with each other. Kwon<sup>(22)</sup> showed that recrystallization in Nb-steels precedes precipitation at 1000 C, resulting in a partially recrystallized grain structure during the interpass time. This partial recrystallization regime should be avoided in the rough rolling stage of hot deformation to benefit the grain uniformity and mechanical properties of the final products. Therefore, the roughing passes must be completed at a temperature higher than 1000 C.

An important feature of the resulting austenite microstructure is the grain size. As long as recrystallization is complete, repeated grain refinement can be obtained from stand to stand, with the recrystallized grain size given by<sup>(23)</sup>:

$$d_{rex} = Ad_0^{1/3} \varepsilon^{-p} \exp(-Q_{gx} / RT) \quad \text{for } d_{rex} < d_0 \quad (8)$$

where ' $d_0$ ' is the initial grain size, ' $\epsilon$ ' is the applied strain, ' $R$ ' is the gas constant, ' $Q_{gx}$ ' is an activation energy parameter and ' $A$ ' and ' $p$ ' are material dependent parameters.

The statically recrystallized grain size decreases with increasing strain, decreasing initial austenite grain size, and decreasing temperature. The more extensive grain refinement obtained at lower temperatures can be attributed to the reduced recovery and the associated increased dislocation density, which enhances the driving force for nucleation of recrystallized grains. Larger deformation (strain) generates a higher dislocation density and introduces smaller subgrains, thus increasing the density of nucleation sites for static recrystallization, which results in finer new grains. The effect of initial austenite grain size can be rationalized, assuming that the predominant nucleation occurs at grain boundaries and that the nucleation rate per boundary area is independent of grain size. These assumptions suggest a grain size exponent of  $1/3$ . Consequently, larger initial grains are better refiners than smaller grains. A grain refinement limit is obtained when  $d_{rex} = d_0$ . This usually falls in the range from 20 to 40  $\mu\text{m}$ . Austenite grain size at the exit of the roughing mill is primarily given by the recrystallized grain size and is little affected by grain growth at the low roughing temperatures, prior to the finishing stand <sup>(23)</sup>.

### **2.2.3 Finishing Temperature**

The range in behavior of austenite during hot deformation at different finishing temperatures can be observed in Figure 7<sup>(24)</sup>. This figure shows the influence of both deformation temperature and amount of strain on the microstructure of statically recrystallized austenite. As deformation temperature is decreased, such that the progress of recrystallization becomes increasingly difficult, a partially recrystallized microstructure is observed. This microstructure is often referred as duplex because of a non-uniform grain size. When reductions are applied at

temperatures below the no-recrystallization temperature ( $T_{nr}$ ), the austenite grains are elongated in the rolling direction, and twins and deformation bands form in the unrecrystallized grains. As the temperature decreases, recrystallization becomes more difficult and reaches a stage where it ceases. Cuddy<sup>(24)</sup> has defined the “recrystallization stop temperature” as the temperature at which recrystallization is incomplete after 15 seconds, after a particular sequence. A completely unrecrystallized microstructure is present when deformation occurs below the recrystallization-stop-temperature of austenite.

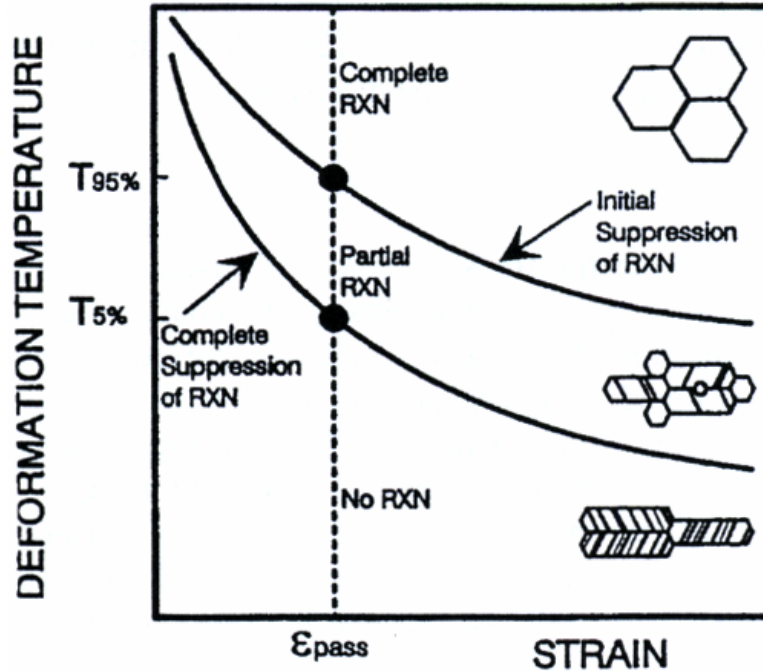


Figure 7 Schematic illustration of different austenite microstructures resulting from various deformation conditions

Since unrecrystallized austenite grains containing deformation bands promotes the austenite-to-ferrite transformation, fine ferrite grains in steel can be obtained due to an accelerated transformation given by this controlled-rolling process, which, without being control rolled, would transform to a bainitic structure, resulting in poor toughness. Therefore, it is very

important to produce the as-deformed austenite state, which is realized by the suppression and/or retardation of recrystallization after deformation<sup>(25)</sup>.

The density of near planar crystalline defects (i.e. grain boundaries, deformation bands, twin boundaries, etc), labeled as  $S_v$ , increases with increasing deformation in the non-recrystallized region. These defects act as nucleation sites for proeutectoid ferrite during subsequent cooling, and there is a strong relationship between the final ferrite grain size and  $S_v$ . The achievement of high levels of  $S_v$  depends on the ability to control the restoration processes that can occur during the thermomechanical processing<sup>(26)</sup>.

The effect of alloying elements on the restoration process during or after the hot deformation is very important. Microadditions of Nb and Ti cause a remarkable retardation effect on recrystallization due to the suppression of crystalline defects. The suppression of grain boundary migration due to microalloying is caused by either a solute dragging effect due to segregation of alloying elements to the boundaries, or by a pinning effect due to precipitates of carbonitrides of alloying elements, such as Nb, and Ti, at the grain boundaries<sup>(27)</sup>.

The retardation effects of the various elements are dependent on their relative solubilities in austenite, the least soluble having the largest driving force for precipitation at a given temperature and, with the proper particle size, creating a greater effect in raising the recrystallization temperature than the more soluble elements<sup>(28)</sup>. The effect of the microalloying elements on recrystallization is shown in Figure 8, and illustrates the strong effect of Nb, which forms fine precipitates in the finishing temperature range and, therefore, has the largest effect on suppressing recrystallization.

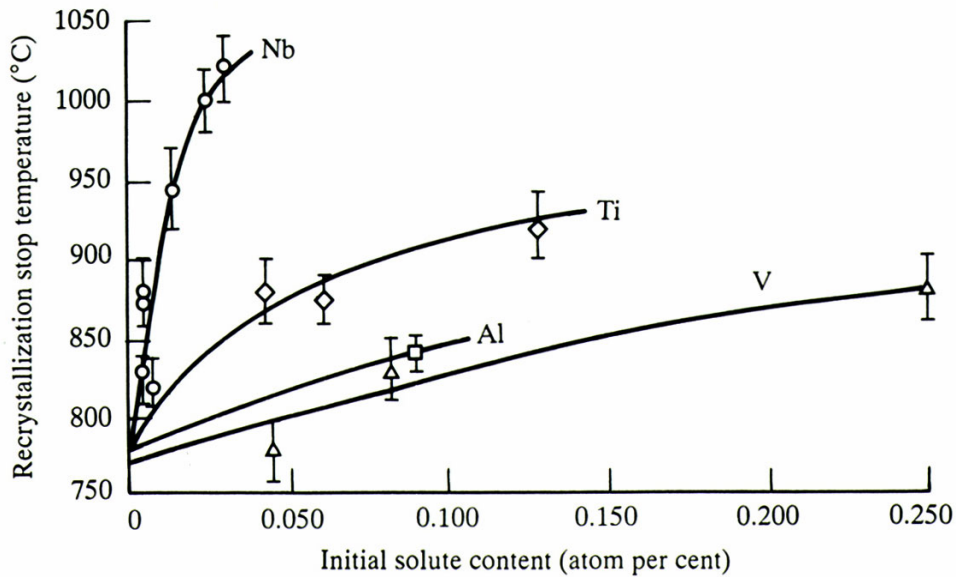


Figure 8 Effect of microalloying solute elements on the recrystallization stop temperature in a 0.07 C, 1.40 Mn, 0.25 Si steel

Bai and Sue<sup>(29)</sup> showed in experiments carried on a torsion machine, that two different curves of non-recrystallization temperature ( $T_{nr}$ ) vs time exist, Figure 9. In the first one, there is no precipitation (dash-line). The interpass times are short, and static precipitation is unable to take place and only solute atoms control the rate of recrystallization, the extent of which decreases as times are increased. In the other curve, precipitation occurs. This is characterized by long interpass times, and precipitation retards recrystallization and  $T_{nr}$  shifts from the dash-line to the solid curve in the stage II. In the last stage, the retardation of recrystallization due to precipitation is weakened because precipitates coarsen and, hence,  $T_{nr}$  decreases. It must be pointed out, however, that interpass times under industrial conditions varies from 0.1 to 30 seconds.

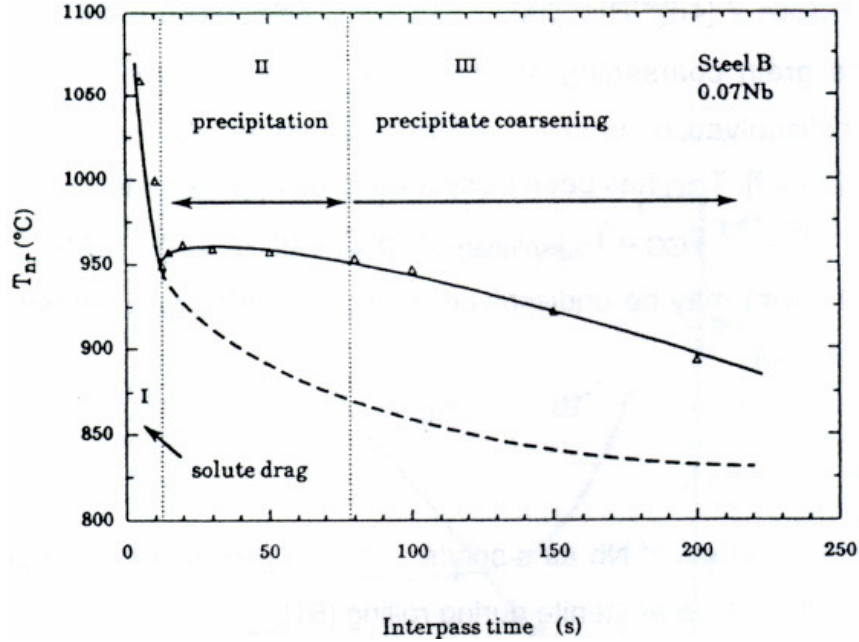


Figure 9 Different ranges of interpass time and its effect on the non-recrystallization temperature ( $T_{nr}$ )

In other words, solute Nb atoms can retard recovery and recrystallization until the occurrence of strain-induced precipitation due to a solute drag effect, while strain-induced precipitation retards the onset and progress of recrystallization.

The driving force for recovery and recrystallization has been shown to be equal to the difference in dislocation density that is present between strained and strain-free local volumes. This driving force has been estimated and is expressed by the following equation:

$$\Delta\sigma = 0.2\mu b (\Delta\rho)^{1/2} \quad (9)$$

where  $\Delta\sigma$  is the increment in flow stress due to work hardening,  $\mu$  is the shear modulus,  $b$  is the Burgers vector, and  $\Delta\rho$  is the excess dislocation density<sup>(26, 30)</sup>.

The two major retarding forces that resist the progress of these restoration processes are solute drag and particle pinning. The effectiveness of solute drag has been shown to be related to differences in size and valence between the solute and solvent atoms. Hence, the level of solute

drag depends on the nature of the solute and its concentration in solid solution. Particle pinning treats the retarding effects of second phase particles on a migrating grain boundary. Recalling equation 5, this can be expanded to account for the total pinning force,  $F_{PIN}$ , that a number of particles per unit area,  $N_s$ , exert on a migrating boundary. This total pinning force is expressed as:

$$F_{PIN} = 4r\sigma N_s \quad (10)$$

There are three different models postulated to explain how microalloy precipitates suppress austenite recrystallization, and all are based on the general equation 9. Their differences arise from the method by which  $N_s$  is calculated.

Model 1. Rigid Boundary Model<sup>(19)</sup>. It assumes the motion of a rigid grain boundary which is capable of interacting with those particles lying within  $\pm r$  of the boundary plane. Under this set of conditions,  $N_s$  is defined as:

$$N_s = 2rN_v \quad (11)$$

where  $N_v$  is the number of particles per unit volume. Assuming spherical particles having radius 'r' and volume fraction 'f<sub>v</sub>',  $N_v$  is defined by:

$$N_v = 3f_v/4\pi r^3 \quad (12)$$

and combining these two equations, yields the number of particles per unit area assuming a rigid boundary model,  $N_s^R$ :

$$N_s^R = 3f_v/2\pi r^2 \quad (13)$$

and the pinning force is:

$$F_{PIN}^R = 6\sigma f_v/ \pi r \quad (14)$$

This rigid boundary model is rather simple and unrealistic since it does not account for any flexibility of the austenite grain boundaries.

Model 2. Flexible Boundary Model. It assumes that an infinitely flexible boundary is capable of interacting with every particle in the three dimensional array until it is fully pinned. This leads to the relationship:

$$N_s = rf_V^{-1/3} N_V \quad (15)$$

which yields the number of particles per unit area assuming a flexible boundary model,  $N_s^F$ :

$$N_s^F = 3f_V^{2/3} / 4\pi r^2 \quad (16)$$

The resulting pinning force for this model is:

$$F_{PIN}^F = 3\sigma f_V^{2/3} / \pi r \quad (17)$$

Model 3. Subgrain Boundary Model<sup>(33)</sup>. This is the most realistic model. It considers the effect of a precipitate distribution that could exist on austenite subgrain boundaries prior to the start of recrystallization. Assuming that the average subgrain intercept is ' $l$ ', the surface area per unit volume for such subgrain boundaries would be  $2/l$ , and the number of particles per unit subgrain boundary area would be given by:

$$N_s = lN_V/2 \quad (18)$$

which gives the number of particles per unit area assuming a subgrain boundary model,  $N_s^S$ :

$$N_s^S = 3f_V l / 8\pi r^3 \quad (19)$$

The pinning force is:

$$F_{PIN}^S = 3\sigma f_V l / 2\pi r^2 \quad (20)$$

## 2.2.4 Effect of Coiling Temperature / Transformation Temperature

In general, the lower the transformation temperature, the greater is the strengthening effect, affecting all the strengthening mechanisms<sup>(34)</sup>. The lower the transformation temperature, the finer the grain size of the transformation product, and the greater the dislocation density. Also, as transformation temperature is lowered, the finer is the dispersion of any precipitated phases. The tendency to retain solute in supersaturated solution is also increased, thus giving increased solid solution strengthening, Figure 10<sup>(34)</sup>

The cooling rate also affects the intensity of precipitation-strengthening by altering the transformation temperature<sup>(36)</sup>. Fast cooling rates can prevent precipitation, intermediate cooling rates cause maximum age-hardening, while slow cooling rates give over-aging which produces low strengths. If the precipitation has been suppressed during cooling, it can be induced during aging.

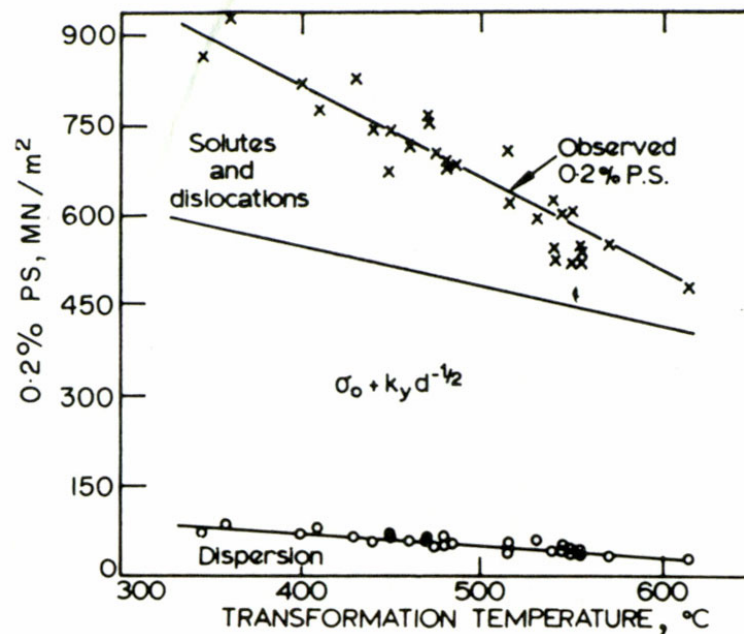


Figure 10 Effect of the transformation temperature on the strengthening mechanisms in an HSLA steel

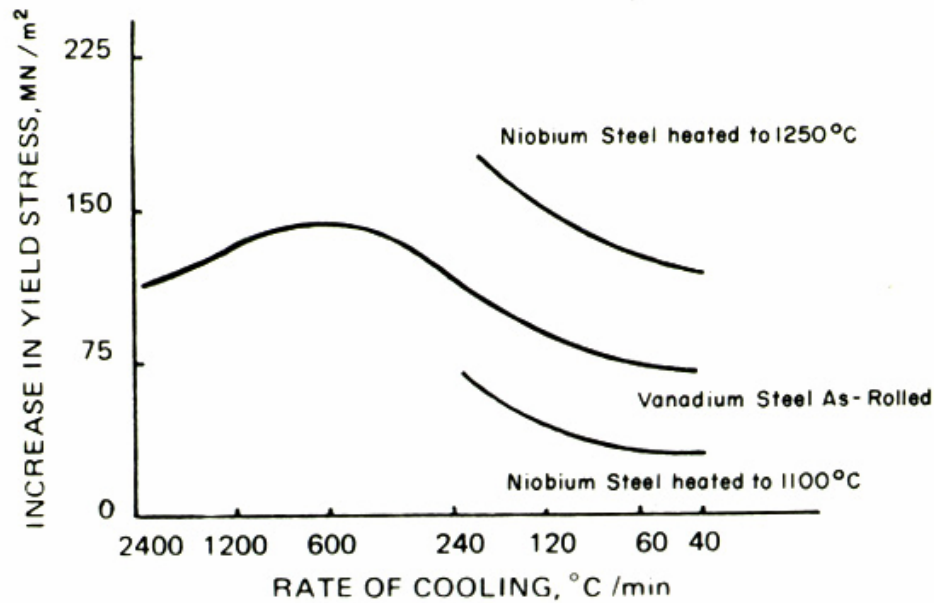


Figure 11 Effect of cooling rate on the intensity of precipitation strengthening

Grozier<sup>(37)</sup> presented the effect of coiling and water-end temperatures on the yield strength of a microalloyed vanadium-nitrogen steel, Figures 12 and 13. These curves show the results of laboratory simulations of hot strip mill practices. It can be seen that there is an optimum coiling and water-end temperature, where the yield strength has a maximum. The strength of the coils decreases at low temperatures due to the absence of precipitation, and at high temperatures, due to overaging of the vanadium nitride precipitates, resulting from the slow cooling rate in coils.

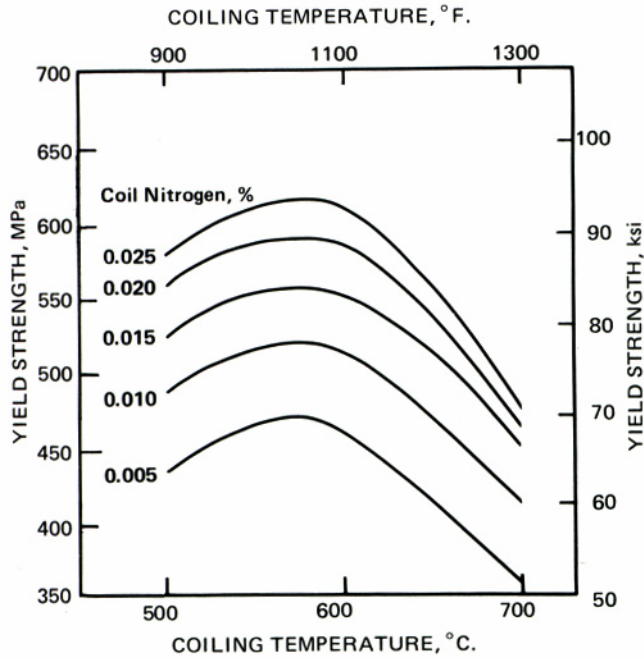


Figure 12 Effect of coiling temperature and total nitrogen content on the yield strength of 1/4" thick coil finished at 900 C and cooled at 17 C/sec. Fe-0.13C -1.40Mn -0.5Si -0.12V

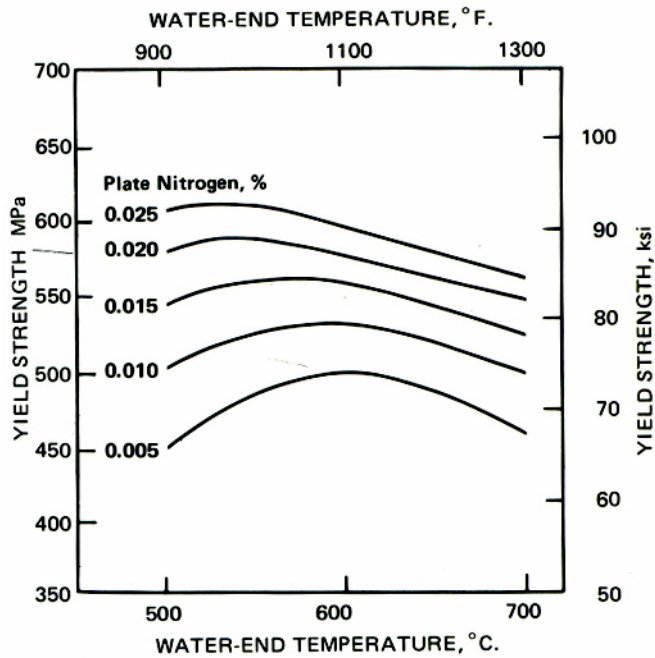


Figure 13 Effect of water-end temperature and total nitrogen content on the yield strength of 1/4" thick coil finished at 900 C and cooled at 17 C/sec. Fe-0.13C -1.40Mn -0.5Si -0.12V

Militzer et al.<sup>(38)</sup> have shown in Figure 14, the change in strength contribution with change in the temperature corrected time parameter, P, which characterizes precipitation,

$$P = \frac{t \exp(-Q/RT)}{T} \quad (21)$$

This is clearly described in Figure 15, where the relation between precipitation strength contribution as a function of coiling temperatures for both V and Nb microalloyed steels, is shown. The results show the ideal coiling temperatures for the Nb and V steels, with the maximum precipitation strength for each steel being observed at 675C for the V steel and 625C for the Nb steel.

Yield strength peak phenomena as a function of coiling temperature has been also found in other investigations<sup>(110-120)</sup>.

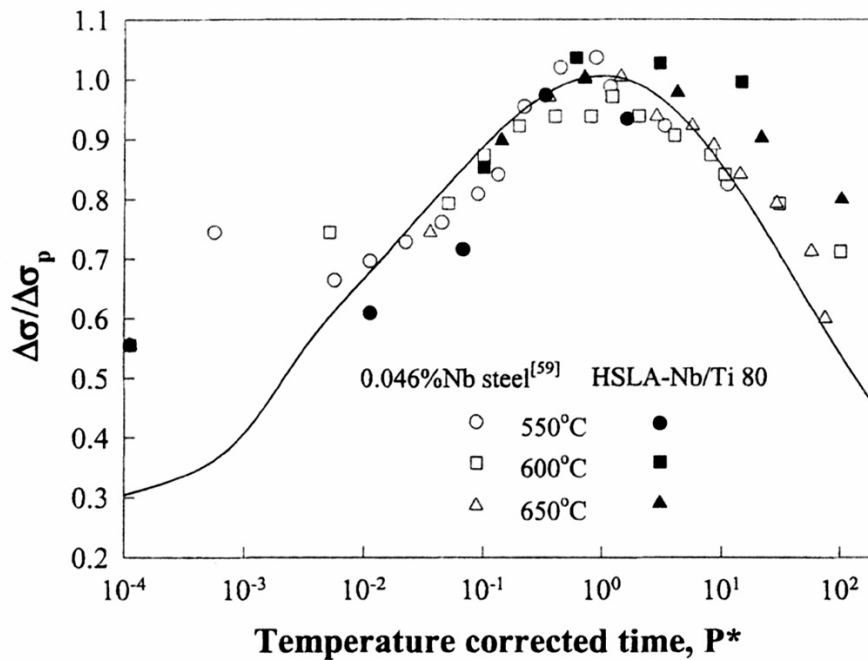


Figure 14 Precipitation hardening in Nb-containing HSLA steels. Solid line indicates the predicted precipitation strengthening

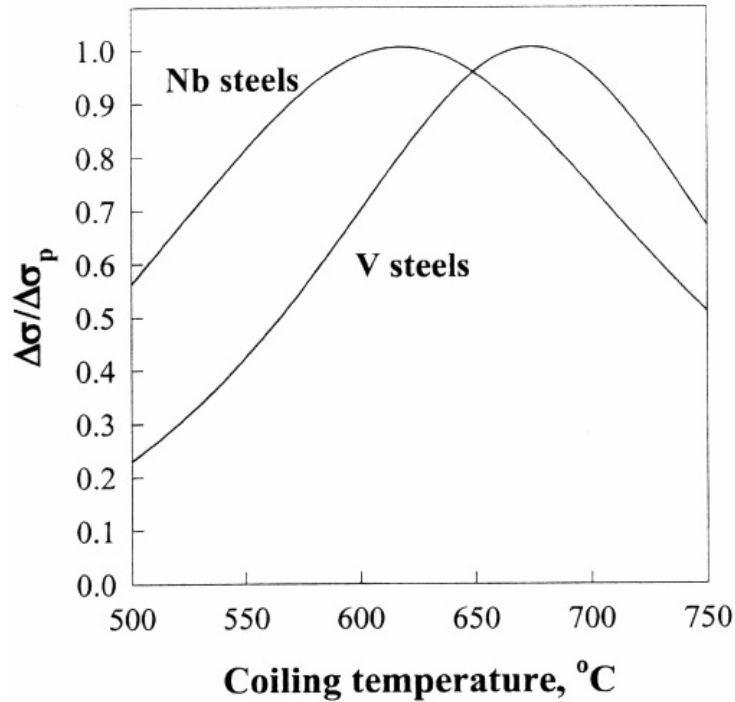


Figure 15 Prediction of normalized precipitation strength as a function of coiling temperature when a 30C/h cooling is assumed to characterize coiling

## 2.3 Evolution of Microstructure during Hot Rolling

### 2.3.1 Grain Size

Fine ferrite grain sizes can be developed from highly deformed unrecrystallized austenite grains that are retained in niobium-treated steels rolled at low temperatures in the austenite range. Alternatively, ferrite grain refinement may result from fine recrystallized austenite grains, where solute niobium or strain-induced precipitates inhibits grain growth following the recrystallization process. This latter process is observed in steels finish rolled at high temperatures ( 950-1050 C )<sup>(40)</sup>.

In clean steels, the most relevant nucleation sites for the austenite to ferrite transformation are the austenite grain boundaries with preference to edges and corners, and to a

certain extent also deformation bands within the grain. If  $S_v$  is substituted by the austenite dimension perpendicular to the rolling plane, the transformation from equiaxed austenite as well as from flattened grains, is well described by ( when air cooling is applied ):

$$d(\alpha) = 0.4 * h(\gamma) \tag{22}$$

where  $d(\alpha)$  is ferrite grain size, and  $h(\gamma)$  is the austenite grain dimension perpendicular to the rolling plane<sup>(41)</sup>. Therefore, a finer ferrite grain results from the deformed austenite. This is also maintained at higher cooling rates, as seen in Figure 16.

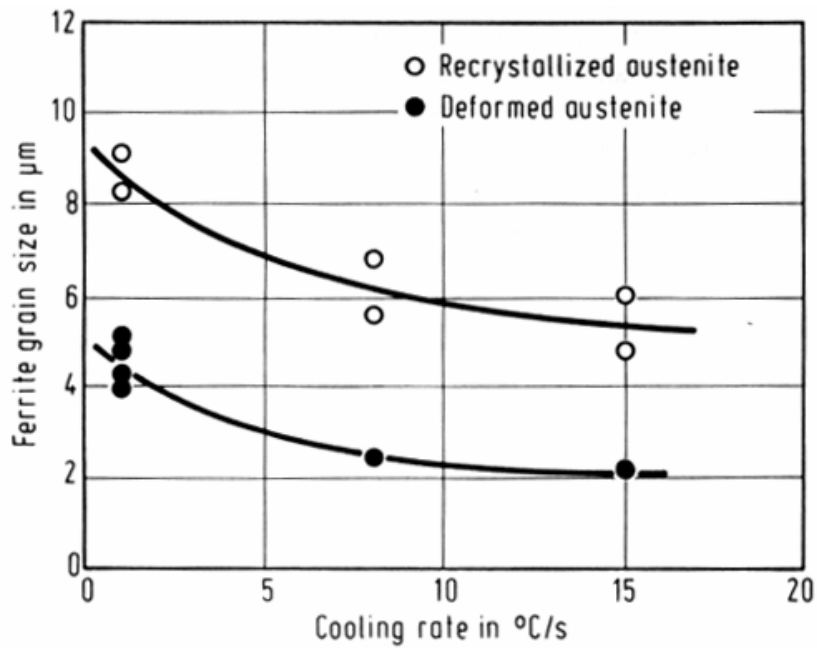


Figure 16 Effect of the cooling rate on the final ferrite grain size transformed from deformed and recrystallized austenite

### 2.3.2 Types of Ferrite Formed During Hot Rolling

Very low carbon HSLA steels have various mixtures of intermediate transformation products such as acicular ferrite, granular bainite, etc., which results in a confusion in terminology and microstructural identifications. These various microstructures form depending on the processing parameters during the thermomechanical processing of the microalloyed steel. The steels with a trend from 0.1% to 0.01% C, show a kind of composite microstructure consisting of  $\alpha$ -matrices and C-enriched secondary phases islands.

During thermomechanical processing, the transforming austenite is, in general, strongly deformed and the austenite microstructure sometimes is not fully recrystallized, so that the resulting microstructure can have different ferrite structures, C-enriched secondary phases, pearlite and precipitates. The different microstructures that can be found will depend on transformation recrystallized and unrecrystallized austenite. Therefore, final finishing temperature and deformation degree, as well as the transformation temperature (coiling temperature), have a direct impact on the final microstructure. Some of the different microstructures that can be found in HSLA steels are shown in Figure 17<sup>(42)</sup>, and these can include:

- Widmanstätten Ferrite
- Polygonal Ferrite
- Quasi Polygonal
- Bainitic Ferrite
- Lath Martensite
- Acicular Ferrite

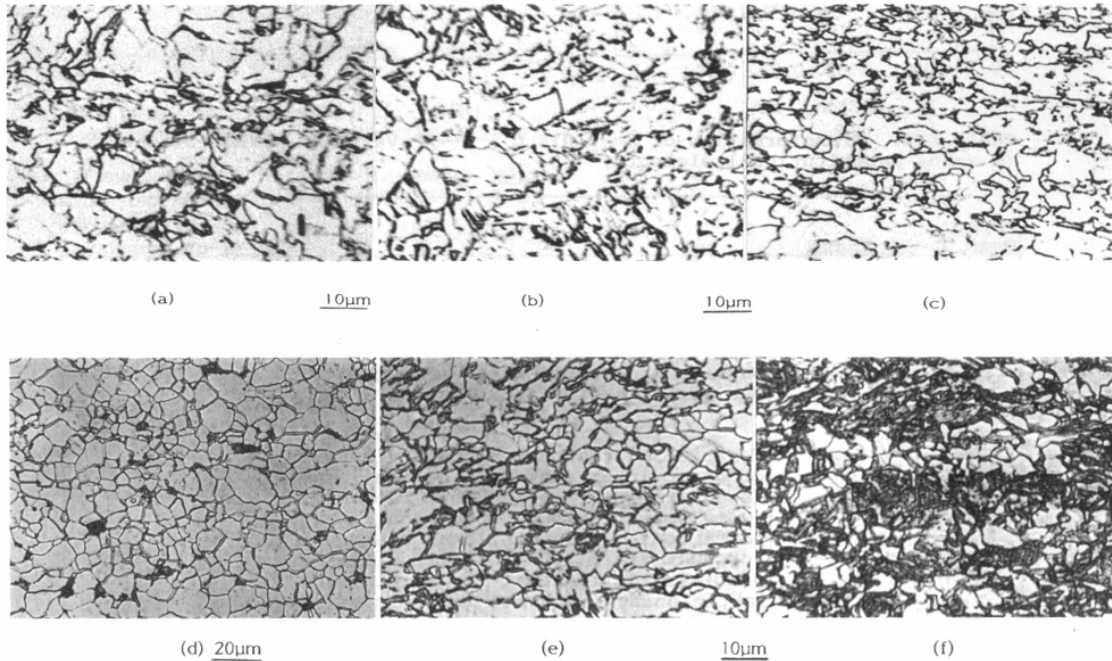


Figure 17 Optical micrographs of various microstructures appearing in controlled rolled and cooled HSLA steels. Fe - 0.03%C – 1.7%Mn and microalloying elements, except (d). (a) Quasipolygonal + bainitic ferrite; (b) Bainitic and quasipolygonal ferrite, both (a) and (b) transformed from recrystallized austenite. (c) quasipolygonal + bainitic ferrite, transformed from unrecrystallized austenite; (d) fine polygonal ferrite + pearlite; (e) acicular and quasipolygonal ferrite; (f) quasipolygonal + bainitic + acicular ferrite, both (e) and (f) with C-enriched minor phases.

Studies on the factors enhancing acicular ferrite formation have reached the conclusion that a reduction in austenite grain boundary surface per unit of volume favors the formation of acicular ferrite, to the detriment of bainite, due to a reduction in the number of bainite nucleation sites. A similar effect is obtained by increasing the number of inclusions present in the steel. A higher acicular ferrite volume fraction can also be achieved if a thin layer of allotriomorphic ferrite forms first at the austenite grain boundaries<sup>(43)</sup>.

### 2.3.3 Precipitation

One of the main roles of the microalloying elements is through their carbonitrides formation, which influences the properties of a steel through various mechanisms, shown in Figure 18<sup>(44)</sup>. The role of the precipitate will depend on the temperature at which it forms in relation to the transformation temperature of the steel and the recrystallization temperature of the austenite. The use of solubility thermodynamical data has been used to understand and explain the physical metallurgy of precipitation in microalloyed steels. Some solubility products for carbides and nitrides in steel are shown in Figure 19<sup>(45)</sup>, and it can be seen that carbide solubilities in ferrite are considerably lower than in austenite. Table 2 shows the molar volumes derived from the atomic masses, crystalline structures and lattice parameters of the various carbides and nitrides that can be present in austenite and/or ferrite<sup>(46)</sup>.

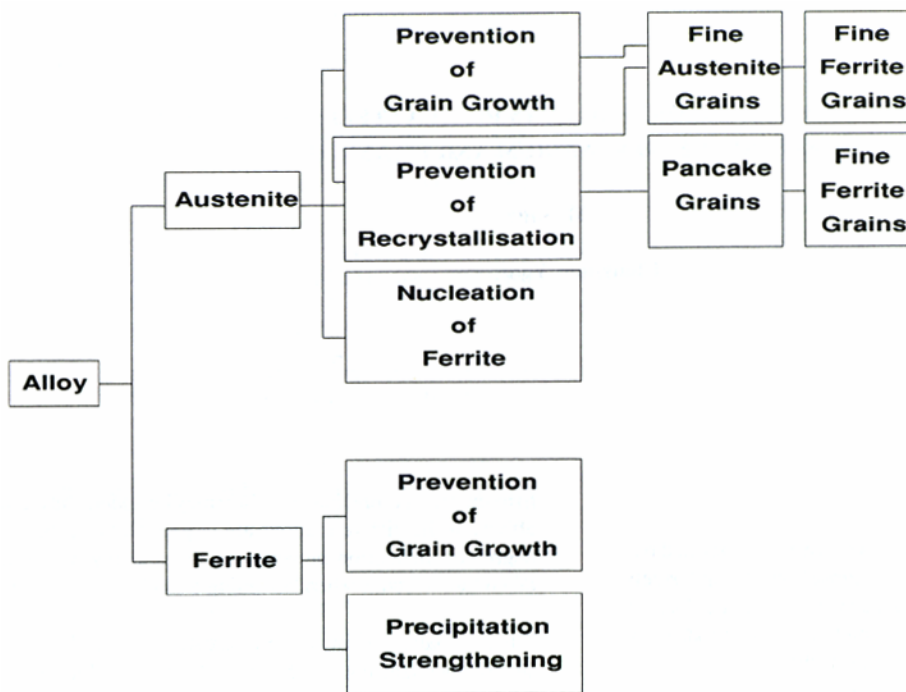


Figure 18 Effect of microalloy precipitates on microstructure of steel

Table 2 Molar volumes of microalloy carbides and nitrides, based on room temperature lattice parameters. After Gladman.

Compound (structure)	Molecular mass	Lattice parameter (nm)	Molecules per unit cell	Density (Mgm <sup>-3</sup> )	Molar volume (cm <sup>3</sup> )
NbC (f.c.c.)	105	0.4462	4	7.84	13.39
NbN (f.c.c.)	107	0.4387	4	8.41	12.72
VC (f.c.c.)	63	0.4154	4	5.83	10.81
VN (f.c.c.)	65	0.4118	4	6.18	10.52
TiC (f.c.c.)	60	0.4313	4	4.89	12.27
TiN (f.c.c.)	62	0.4233	4	5.42	11.44
AlN (c.p.h.)	41	c=0.4965 a=0.311	6	3.27	12.54
γ-Fe (f.c.c.)	56	0.357	4	8.15	6.85
α-Fe (b.c.c.)	56	0.286	2	7.85	7.11

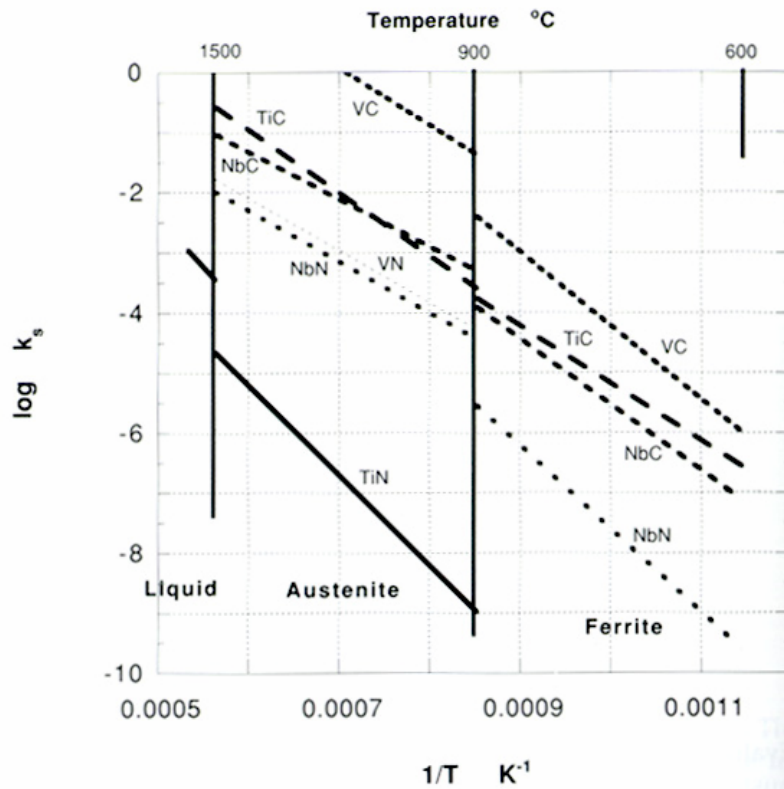


Figure 19 Comparison of the solubility products of the microalloy carbides and nitrides, showing the greater stabilities of the nitrides relative to those of the carbides, and solubility products in ferrite lower than those in austenite.

**2.3.3.1 Precipitation in Austenite.** In the absence of any hot deformation, the precipitation of microalloy carbides and nitrides is extremely slow, and the solute content of austenite can be expected to remain unchanged during cooling from the reheating temperature. However, when hot deformation is applied, the introduction of line defects, such as dislocations and deformation bands, provides numerous sites for the precipitation of carbides and nitrides, provided that the deformation is carried out below the solvus. A typical precipitation curve is shown in Figure 20(47). Hot deformation causes a marked acceleration of the precipitation, and can be substantially completed within a minute at temperatures 900-1000 C. The nose of the curve depends on the level of supersaturation. Little precipitation would be expected with low levels of supersaturation, and no precipitation would ever occur at temperature above the solvus. Strain-induced acceleration of the precipitation process is also dependent on the level of strain.

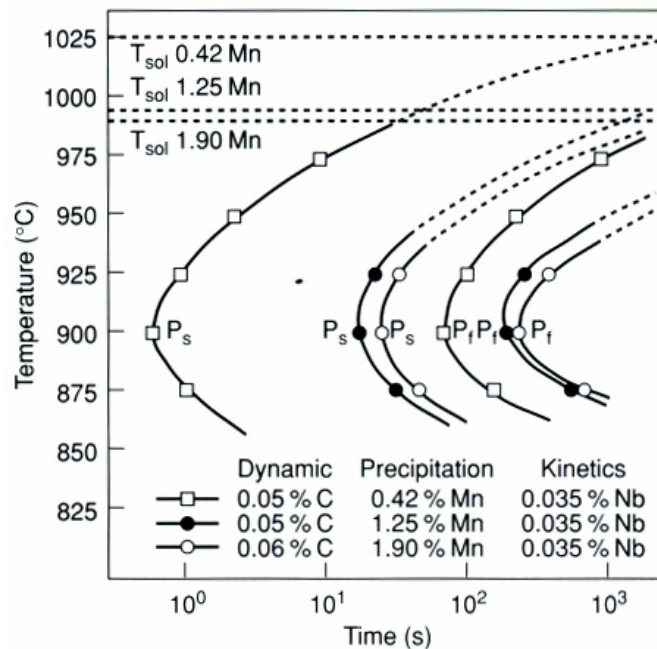


Figure 20 Typical precipitation curves for niobium carbonitrides in austenite following a 50% reduction in thickness by hot rolling

Kwon and DeArdo<sup>(48)</sup> studied the precipitation characteristics of low alloy steels. They studied the precipitation kinetics from compression samples of Nb-steels, deformed 0.3 true strain at 900 C and 1000 C. At 900 C, precipitation started at holding times ranging from 5 to 20 secs and took place before the start of recrystallization. At 1000 C, on the other hand, precipitation kinetics were much faster. The measured particle size distributions at these two deformation temperatures are presented in Figure 21 for various holding times after deformation. At 900 C the average particle size in the initial stages of precipitation was very small, less than 5 nm for the delay time of 10 sec. The average particle size increased significantly as the delay time was increased. On holding to 1000 s, the average particle size was doubled to approximately 10 nm. The particle size distributions at 1000 C show two distinct features when compared to the results obtained at 900 C. First, the average particle size of NbCN formed at 1000 C was much larger during the same holding period, although the precipitation kinetics seemed to be similar. Secondly, a bimodal particle size distribution appeared in the initial stage of the precipitation process; the smaller particles were less than 12 nm, and the larger particles were about 20 nm in diameter. Those finer particles, formed in the early stages of precipitation, seemed to coarsen very rapidly at this temperature.

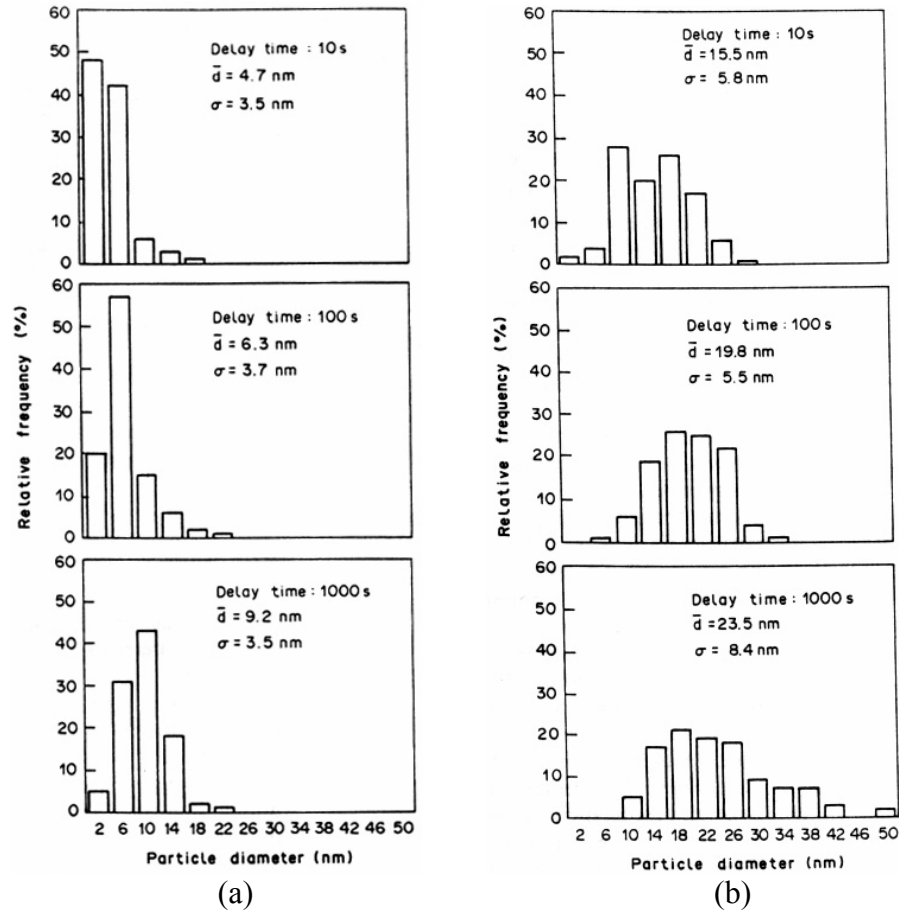


Figure 21 Particle size distributions for a high N Nb-steel deformed at (a) 900°C, (b) 1000°C

Jonas and Weiss<sup>(49)</sup> have presented the effect of precipitation of Nb on recrystallization behavior, Figure 22. When the time for the start of precipitation,  $P_s$ , is longer than the recrystallization start time,  $R_s$ , the recrystallization-precipitation-time curve has the normal dependence on temperature affected by solute drag. When  $P_s$  is less than  $R_s$ , the nucleation and growth of recrystallization is severely impeded.

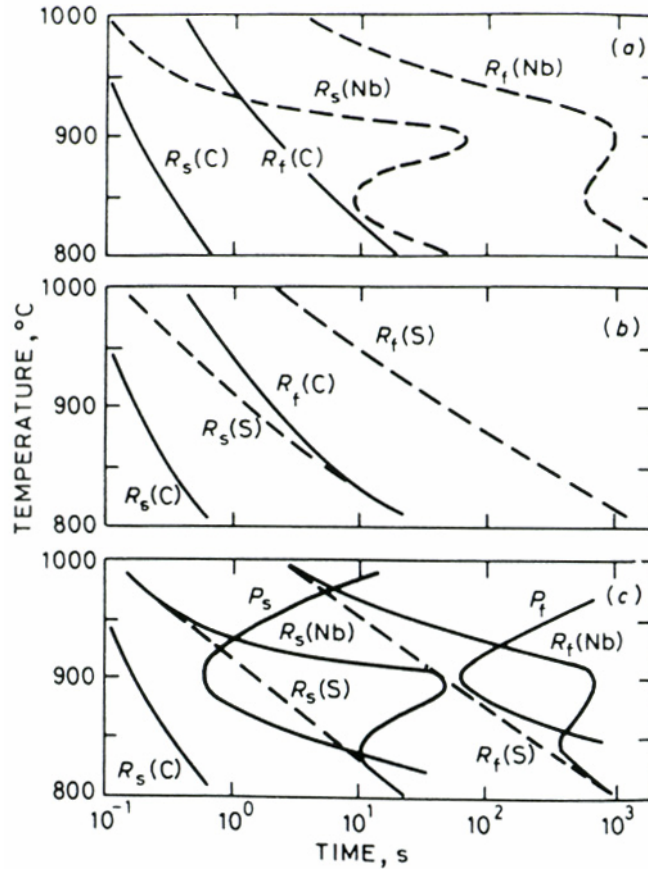


Figure 22 (a) Comparison of the start of recrystallization,  $R_s$ , and the finish of recrystallization,  $R_f$ , of a plain carbon steel (C) and a niobium steel (Nb). (b) The suggested effect of dissolved niobium is indicated by the curves  $R_s(S)$  and  $R_f(S)$ . (c) The additional effect of strain induced precipitation is coincident with high rates of precipitation indicated by the precipitation start,  $P_s$ , and finish,  $P_f$ , curves. After Jonas and Weiss.

### 2.3.3.2 Precipitation in Ferrite.

Metastable carbides that form in ferrite are characterized by greater similarity to  $\alpha$ -iron as compared to the more stable carbides. This allows them to form semicoherent or coherent interfaces with  $\alpha$ -Fe. Figure 23a shows the structure which fulfills the requirements for full coherency if the particles are small. An ordered arrangement of interstitials that only distorts the BCC lattice ( $\alpha'$ ) has been found in Fe-N alloys. This structure forms during aging of Fe-N alloys at low temperature. The iron-free carbides TiC, VC, and NbC have face-centered cubic structures with lattice parameters 20-25% greater than those of the austenite (

Figure 23b ). They can form as ultra fine dispersions, which raise the yield stress of microalloyed steels<sup>(50)</sup>.

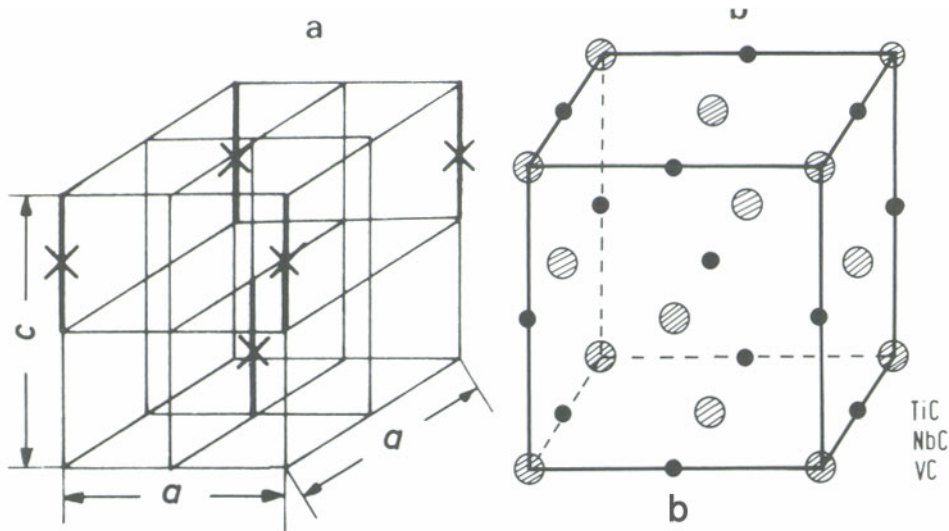


Figure 23 (a) Structure of the metastable compound  $Fe_{16}N_2(\alpha')$ , crosses indicate N atoms; (b) structure of the TiC, VC, NbC and carbonitride as  $Ti(C,N)$

Several steels were developed using TiC precipitation for strengthening. The results were, in general, disappointing because of the difficulties in maintaining consistent properties. Because of its high reactivity, part of the titanium added combined with oxygen, nitrogen and sulfur, and only the remaining “effective” titanium was available for precipitation. Variability of “effective” titanium contributes to inconsistent properties<sup>(31)</sup>. Therefore, Nb and V have been used for precipitation strengthening, because they can precipitate in ferrite either as carbides, carbonitrides or nitrides. The most effective precipitation strengthening is due to precipitation of vanadium carbonitrides<sup>(51)</sup>.

Precipitation processes in ferrite can be expressed in terms of the Larsen-Miller Parameter, ‘P’, that describes the combined effects of time and temperature, defined by:

$$P = T(20 + \log_{10} t) \quad (23)$$

where  $T$  is the aging temperature (K) and  $t$  is the aging time (h). Any particular value of the parameter  $P$ , expresses a metallurgical state of precipitation, which can be attained through the temperature compensated aging time equation. Any combination of aging temperature and time that gives the same parameter value will show the same state of precipitation and, therefore, the same property response, so that the property changes resulting from aging at different temperatures can be expressed in terms of a unique relationship with the tempering parameter, Figure 24<sup>(52)</sup>. Once a relationship is illustrated, then the effects of aging at any time and temperature can be assessed, provided that the Larsen-Miller parameter is within the range over which the property-parameter relationship was established.

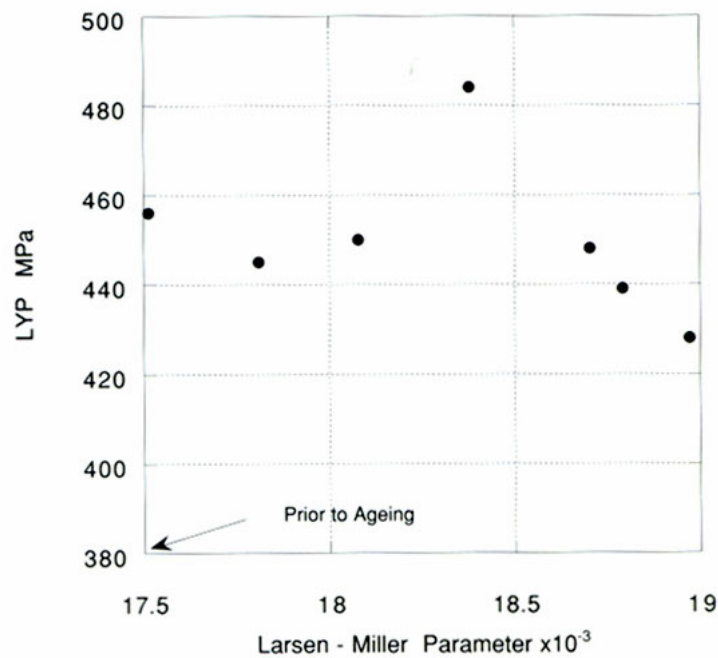


Figure 24 Precipitation strengthening due to Nb carbonitride. The 0.02%Nb steel was rolled and then cooled rapidly to avoid precipitation. Sub-critical heat treatments, expressed by the Larsen-Miller parameter, allow precipitation, giving rise to a precipitation hardening curve.

### 2.3.4 Texture Evolution During Hot Rolling

Takechi and Kato<sup>(53)</sup> showed the influence of rolling temperature on the crystallographic texture, for both surface and central layers of hot-rolled steels. They found that, when the finishing temperature is about 900 C, both layers have nearly random orientation. However, lower finishing temperatures result in texture differences between the surface and center of sheets. At the surface, the ND density of (110) is high while at the center, (100) is high. No effect of coiling temperature on texture was detected. Figure 25 shows the inverse pole figures of hot-rolled sheet which was rolled at 885-900 C, above Ar<sub>3</sub>. It can be seen that a slight amount of cold-rolling texture is retained in the central layer.

Figure 26 shows the inverse pole figure for the coil with a medium finishing temperature of about 830 C. At the surface, the density along (110)-(321)-(211) in ND and the density of (111) in RD are high, which shows that the rotation series about  $\langle 111 \rangle$  in RD exists. At the same time, the high density along (100)-(411)-(211)-(111) in RD and of (110) in ND indicated the existence of a rotation series about  $\langle 110 \rangle$  in ND. Therefore, the orientations of the surface are represented by two series. One is the  $\{hkl\}\langle 111 \rangle$  group, and the other is the  $\{110\}\langle uvw \rangle$  group. For the central layer, the density of ND is the highest at (100) and extends along (611)-(411)-(311)-(211), while the density of RD is high at only (110). Thus in the central layer, there is the rotation series about  $\langle 110 \rangle$  in RD.

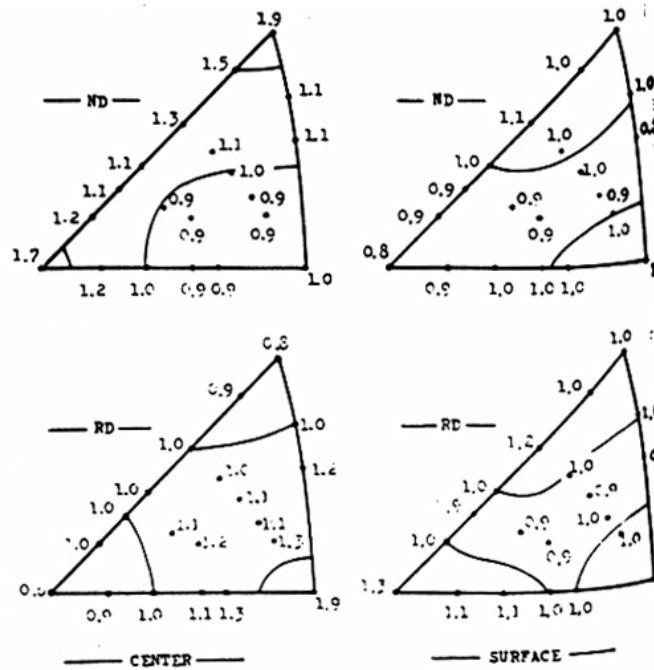


Figure 25 Inverse pole figure of hot rolled sheet. Finishing temperature: 885 C – 900 C; coiling temperature: 550 C

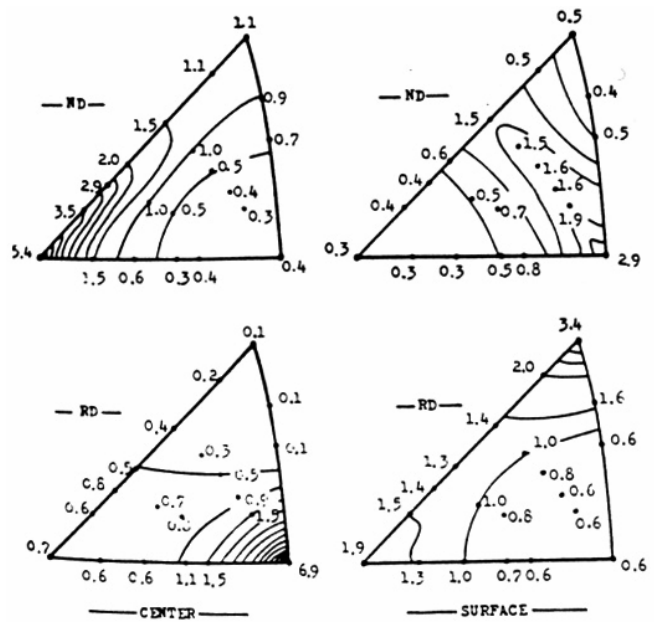


Figure 26 Inverse pole figure of hot rolled sheet. Finishing temperature: 830 C; coiling temperature: 620 C

In Figure 27 the texture of the coil with the lowest finishing temperature is shown. In this case, the surface has a little of the texture of the central layer, but the relatively high density of (111) in RD shows that the  $\{hkl\}\langle 111 \rangle$  group is confined to the surface. For the center, the density of (100) in ND and of (110) in RD are both very high. This fact emphasizes that the preferred orientation of rolling,  $\{100\}\langle 011 \rangle$ , is strongly developed. So, there is a remarkable difference in texture between the surface and central layers of hot rolled steel. Textural changes as a function of depth in the sheet are shown in Figure 28. For the lower finishing temperatures, (110) orientation is developed strongly at a depth of 0.5mm from the surface (one fifth of the thickness), while in the inner layer, the preferred orientation of rolling, (100), develops instead of (110). For the high finishing temperature, the same tendency developed but deviation from random orientation is much smaller.

Also, based on a 111/100 ratio for r-bar, high temperature rolling is much better.

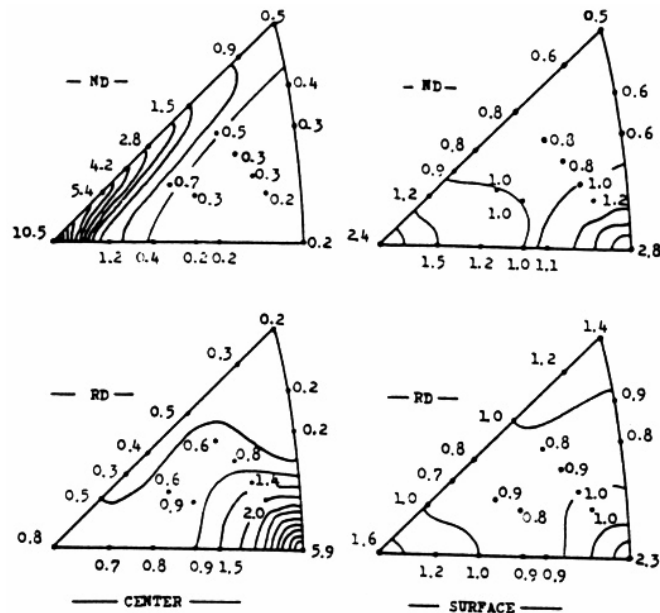


Figure 27 Inverse pole figure of hot rolled sheet. Finishing temperature: 805 C; coiling temperature: 550 C

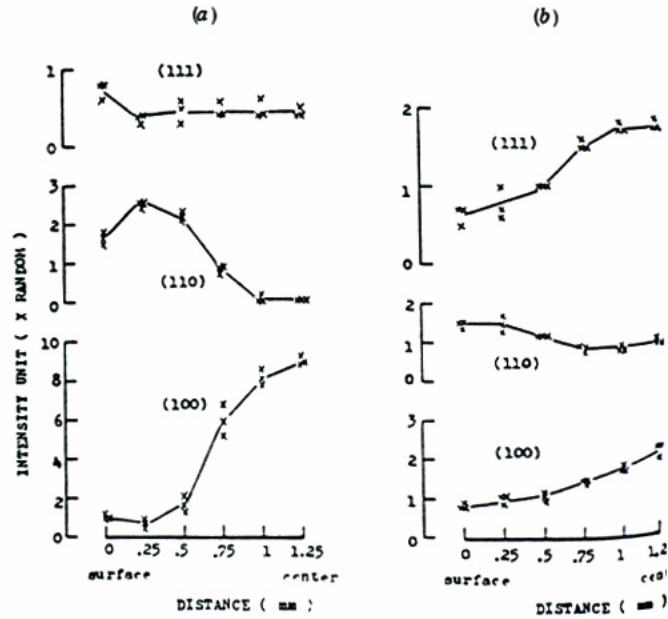


Figure 28 Change in texture with depth from the surface: (a) rolled at low temperature; (b) rolled at higher temperature

## 2.4 Strengthening Mechanisms

### 2.4.1 Grain Size Strengthening / The Hall-Petch Equation

The plastic deformation of polycrystals involves two important aspects: firstly, grain boundaries act as obstacles to dislocation movement and secondly, the individual grains in a polycrystal possess a wide variety of orientations considered to be randomly distributed. Considering these two influences, a dislocation in a grain moving towards the grain boundary, does not usually find a plane matching its Burgers vector in the next grain, nor can be absorbed by the high angle grain boundary without modifying the structure of the latter. Thus, this dislocation and those following it on the same plane pile up at the grain boundary. Finally, the stress concentration at the pile-up is so large, that, at a stress  $\tau_0$ , dislocation sources in the neighboring grain are activated. If  $\lambda$  is the distance of the source from the pile-up, then<sup>(54)</sup>:

$$\tau_0 = \tau_1 + m_{12}\tau_l\sqrt{\lambda/d} \equiv \tau_1 + k_y d^{-1/2} \quad (24)$$

where  $\tau_1$  is the critical shear stress in grain 1 and  $\tau_l$  is the minimum stress for activation in grain 2;  $m_{12}$  transforms the shear stress from the slip system in the first grain to that in the second. This relationship, known as the Hall-Petch<sup>(55,56)</sup> relationship, describes the dependence of yield stress of polycrystals on grain size (Figure 29). The Hall-Petch relationship has been extensively reviewed by Irvine, Gladman, and Pickering.<sup>(57,58)</sup>

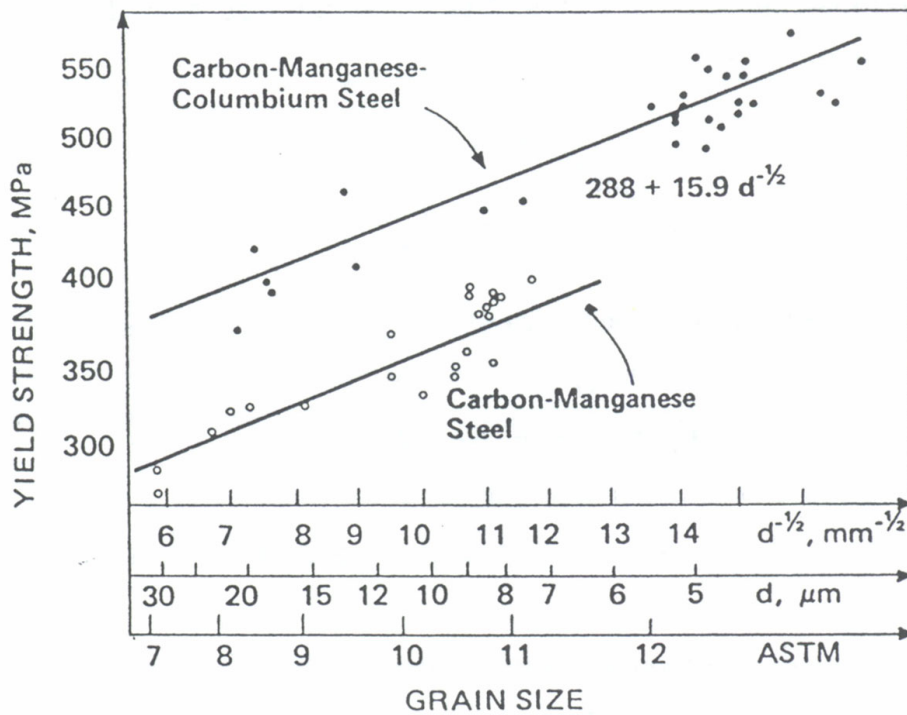


Figure 29 Yield strength dependence on grain size. Hall-Petch relationship.

While the Hall-Petch equation describes the lower yield stress in a discontinuously yielding material, very frequently it is applied to a material that shows continuing yielding<sup>(59)</sup>.

The Hall-Petch relationship is usually described in the form of:

$$\sigma_y = \sigma_i + k_y d^{-1/2} \quad (25)$$

where  $\sigma_y$  = lower yield stress,  $\sigma_i$  = friction stress which opposes dislocation motion,  $k_y$  = a constant related to the difficulty in spreading yielding from grain to grain, often called the dislocation locking term, and  $d$  = a linear function of grain size. The mechanistic model for this equation assumed dislocation sources to operate within a grain to give a dislocation pile-up at the grain boundary, causing a stress to be generated in the next grain which, and, once achieving a critical intensity, operated a new dislocation source within that grain. Thus, yielding propagated from grain to grain. The grain size determined the number of dislocations in the pile-up and, hence, the stress generated. It is easy to see that a coarser grain size will provide more dislocations in the pile-up, greater stress intensification, and propagation of yielding at a lower applied stress. The major criticism of this model is that dislocation pile-ups are not observed in bcc structures, steels in particular, and are infrequent in many fcc structures, unless the stacking fault energy is low. However, a similar relationship holds when considering shear stresses ahead of a slip band. The evidence that shows that the yield stress is related linearly to the reciprocal of the square root of the grain size, simply relates the obstacle imposed by a grain boundary to the propagation of slip, and the movement of dislocations. By decreasing the effective dislocation free path, or slip distance, a fine grain size provides an effective strengthening mechanism.

The effect of the  $K_y$  term has also been investigated<sup>(60)</sup>. Initially, it was thought that  $K_y$  was determined by the unlocking of a dislocation from its atmosphere in the grain ahead of the blocked slip band. Now, it is considered that, for an annealed steel, dislocations are derived from

the grain boundaries that block the slip band. The stress required is influenced by the segregation of interstitials to the boundary<sup>(61)</sup>. Thus,  $K_y$  can be affected by allowing interstitial atoms to segregate to the grain boundaries, either by deoxidation procedures or by heat treatments. Wilson<sup>(61)</sup> has observed a variation in  $K_y$  with different aging times at 90 C in a Fe-0.003C-0.003N, water quenched from 700 C, Figure 30.

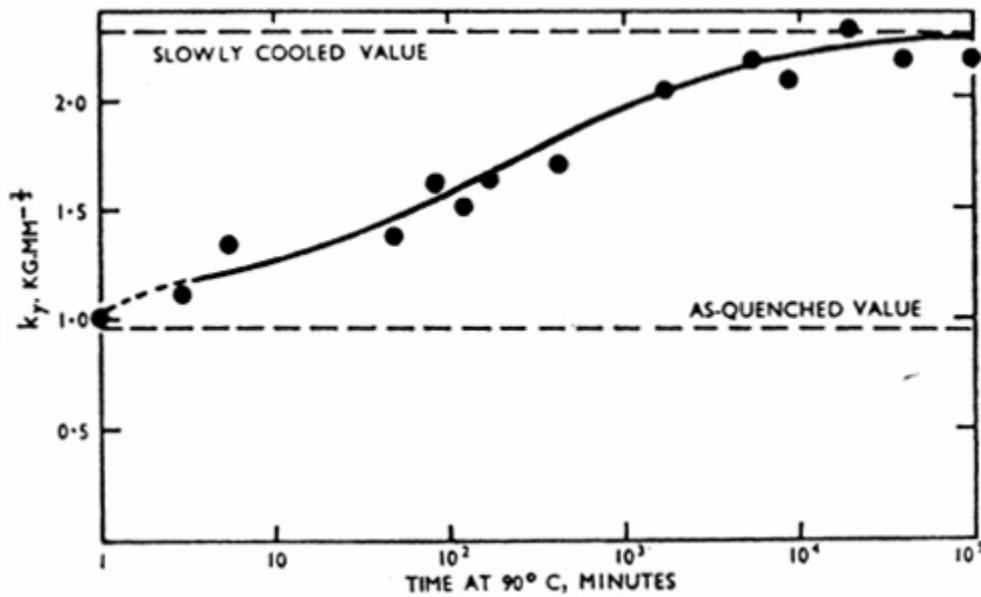


Figure 30  $K_y$  recovery after aging at 90 C, in a Fe-0.003C-0.003N steel , water-quenched from 700 C

While the Hall-Petch relationship can be used to describe the lower yield stress, this is only valid provided that the mean free path for dislocation movement is not severely restricted by other microstructural features. Therefore, various other strengthening mechanisms may be incorporated into the  $\sigma_i$  value, leading to an expanded Hall-Petch relationship:

$$\sigma_y = (\sigma_i + \sigma_{sss} + \sigma_{pptn} + \sigma_{\perp} + \sigma_{sg} + \sigma_t) + k_y d^{-1/2} \quad (25)$$

where  $\sigma_{\text{SSS}}$  is the solid solution strengthening,  $\sigma_{\text{pptn}}$  is precipitation strengthening,  $\sigma_{\perp}$  is dislocation strengthening,  $\sigma_{\text{sg}}$  is subgrain strengthening, and  $\sigma_{\text{t}}$  is texture strengthening. This is represented schematically in Figure 31<sup>(62)</sup>. Different types of summation have also been proposed<sup>(99)</sup>.

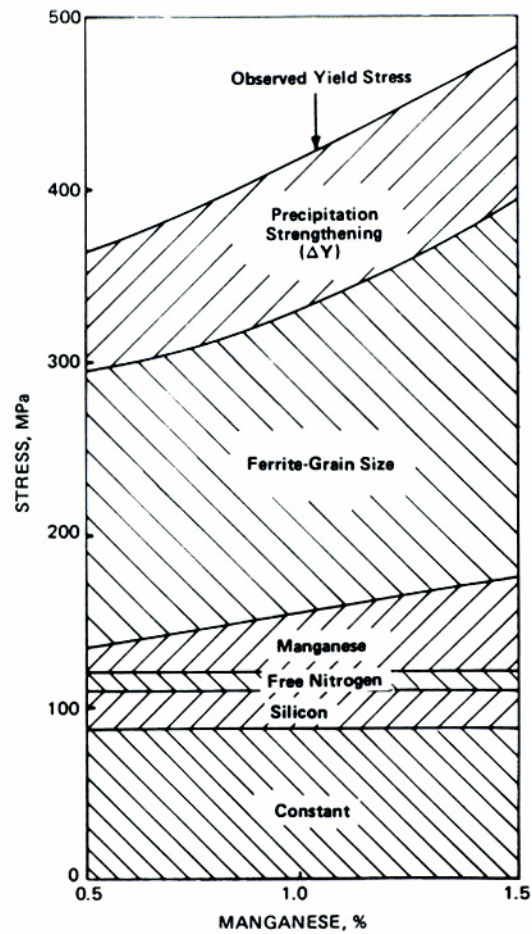


Figure 31 The effect of the different strengthening contributions to the observed yield strength, for different manganese content.

## 2.4.2 Solid Solution Strengthening

Pickering<sup>(63)</sup> studied the effect of solute elements on yield and tensile strength and found that these depend largely on the difference in atomic size between the element and iron. Substitutional and interstitial solutes obey a linear relationship between strength and the square root of their concentration but, over a limited range, this can be simplified to a linear relationship, Figure 32. The effect of substitutional solutes on strength is small, and it would be expensive to use them deliberately. Interstitial solutes are more potent strengtheners, but their solubility is limited, and cannot be used to a great extent.

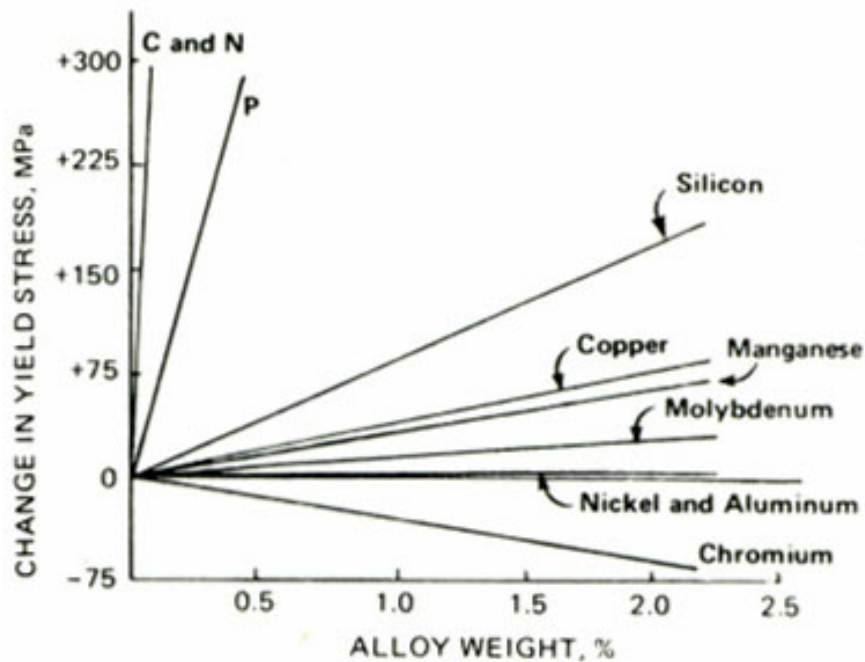


Figure 32 Solid solution strengthening effects in high strength low alloy steels.

### 2.4.3 Dislocation Strengthening

The strengthening that results from the short-range interaction of dislocations with other dislocations is considered by using the notion of dislocation density. Dislocations can provide a “forest” of obstacles impeding the motion of dislocations. Taylor<sup>(64)</sup> has shown that the additional stress required to cut through the forest provides the hardening:

$$\Delta\sigma = \alpha G b \rho^{0.5} \quad (26)$$

where  $b$  is the Burgers vector of a dislocation,  $G$  is the shear modulus, and  $\alpha$  is a numerical factor dependent of the crystal structure. This strengthening mechanism is very important in heavily cold rolled metals, because of their high dislocation densities. In HSLA steels, this mechanism is also used. For example, when Widmanstätten ferrite is formed, the ferrite formation mechanism changes to shear and the dislocation density increases substantially and then dislocations make a significant contribution to strength<sup>(65)</sup>. Figure 33 shows the effect of transformation temperature on dislocation density<sup>(66)</sup>.

Takahashi and Bhadeshia proposed an empirical relation to calculate the dislocation density in ferrite as a function of the temperature, in the range 297 C to 647 C<sup>(67)</sup>

$$\log_{10}(\rho) = 9.28480 + 6880.73/(T+273) - 1780360/(T+273)^2 \quad (28)$$

with  $\rho$  the dislocation density in  $m^{-2}$ ,  $T$  is the reaction temperature in C in the 297 C to 647 C range.

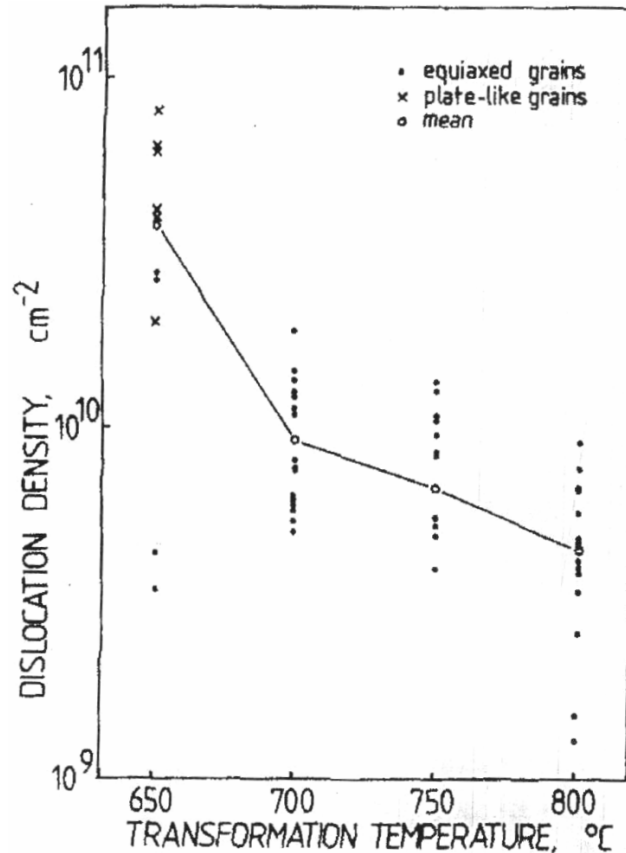


Figure 33 Effect of transformation temperature on the dislocation density in a Fe-0.08C-0.21Ti steel

#### 2.4.4 Precipitation Strengthening

For systems that show precipitation strengthening, there are a number of mechanisms that can contribute to the observed increases in strength. Some of these are:

- a) Coherency Strengthening.- The strengthening is related to the coherency strains that develop in a matrix surrounding a coherent precipitate,
- b) Chemical Hardening.- The strengthening is due to the development of antiphase boundaries (APB's), which form when a dislocation cuts through a particle,
- c) Dispersion Strengthening (Orowan Mechanism)<sup>(68)</sup>.- Arises from the looping of dislocations between hard undeformable particles, Figure 34.

d) Particle Shear Mechanism<sup>(69)</sup>.- A dislocation will continue through a second phase particle. The second phase particle becomes deformed and the interfacial area of the particle/matrix is increased, Figure 35.

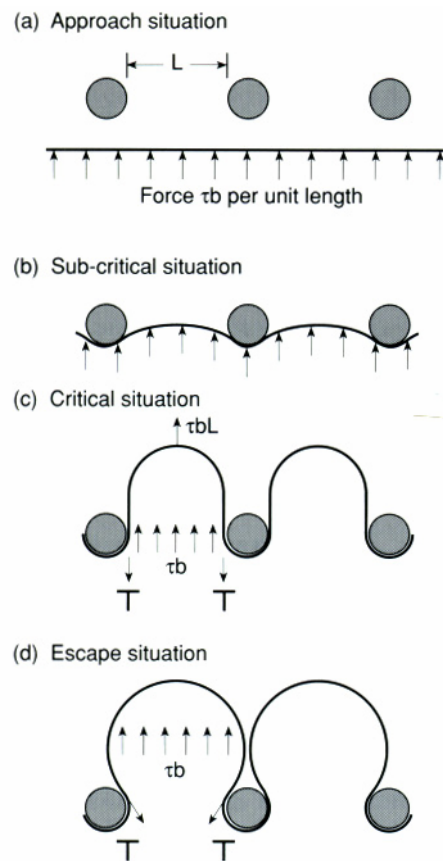


Figure 34 Orowan Mechanism. A dislocation meets hard undeformable second phase particles and loop between them. At higher stresses dislocations are released by Orowan looping or cross slip.

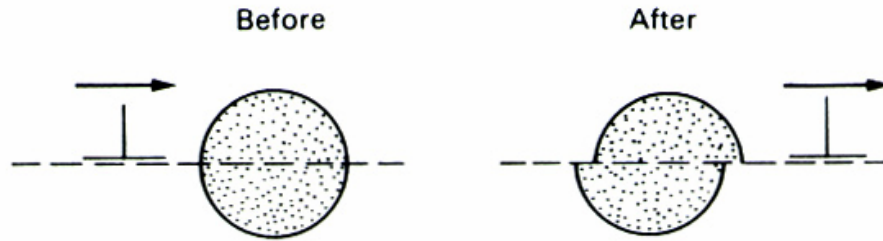


Figure 35 Dislocations may continue through the second phase particles (particle cutting). The second phase particle becomes deformed and the interfacial area of the particle/matrix is increased

There is an important distinction between the mechanisms of particle shearing and particle bypass in their response to particle size. The particle shearing mechanisms generally show a positive dependence with particle size, whereas the looping mechanism shows an inverse dependence on particle size, Figure 36. The strengthening contribution of the hard carbides and nitrides appears to decrease with increasing particle size, and hence, shows remarkably good agreement with theories based on the dislocation bypassing (Orowan Mechanism)<sup>(68)</sup>.

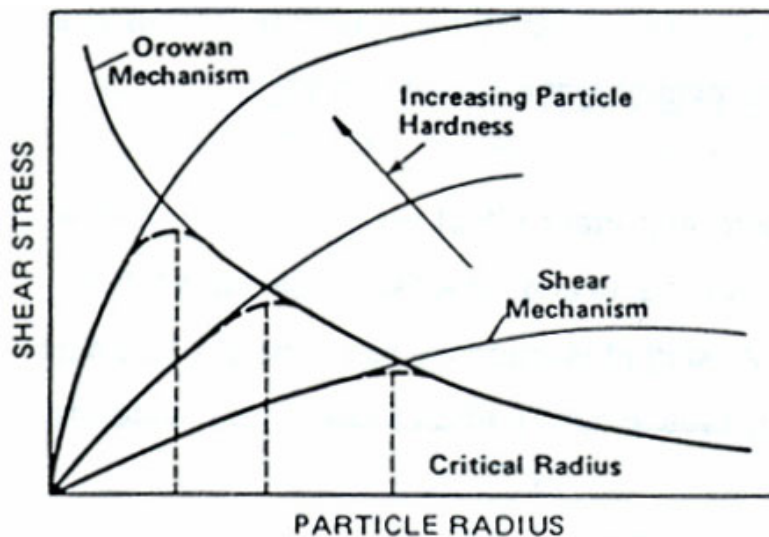


Figure 36 Schematic representation of precipitation strengthening by particles of increased hardness according to the combined Orowan and shear mechanisms

In precipitation strengthened alloys, the stress required to move dislocations appreciable distances in a slip plane is assumed to be higher than the stress needed to generate dislocations from a source. Hence, the yield strength is associated with the stress required for dislocations to sweep out areas in the slip planes, which are large compared with dispersion spacing. The most accepted model that describes precipitation strengthening is that of Orowan-Ashby<sup>(70)</sup>. This model incorporates a realistic, random particle distribution model proposed by Kocks<sup>(71)</sup>. The Orowan-Ashby model can be expressed as:

$$\tau = \frac{1}{1.18} \left( \frac{1.2Gb}{2\pi L} \right) \left[ \ln \left( \frac{x}{2b} \right) \right] \quad (28)$$

where  $\tau$  = resolved shear stress to overcome the effect of the precipitates,  $x$  = the mean planar intercept diameter of a precipitate,  $L$  = the surface to surface precipitate spacing defined as  $\frac{1}{\sqrt{n_s}} - x$  with  $n_s$  being the number of precipitates per unit area of slip plane,  $G$  = the shear modulus which is 80,300 Mpa for ferrite, and  $b$  = the Burgers vector in the slip direction which is 2.5 Å for ferrite.

This equation can be modified to include particle fraction and size, and is written as:

$$\sigma(MPa) = \frac{5.9\sqrt{f}}{x} \ln \left( \frac{x}{2.5 \times 10^{-4}} \right) \quad (29)$$

where  $\sigma$  = precipitation strengthening,  $f$  = volume fraction of precipitates, and  $x$  = precipitate diameter ( $\mu\text{m}$ ).

Therefore, the stress increases as the volume fraction of precipitates increases, and precipitate size decreases. This can be observed in Figure 37, where the strengthening values are the maximum values that can be obtained.

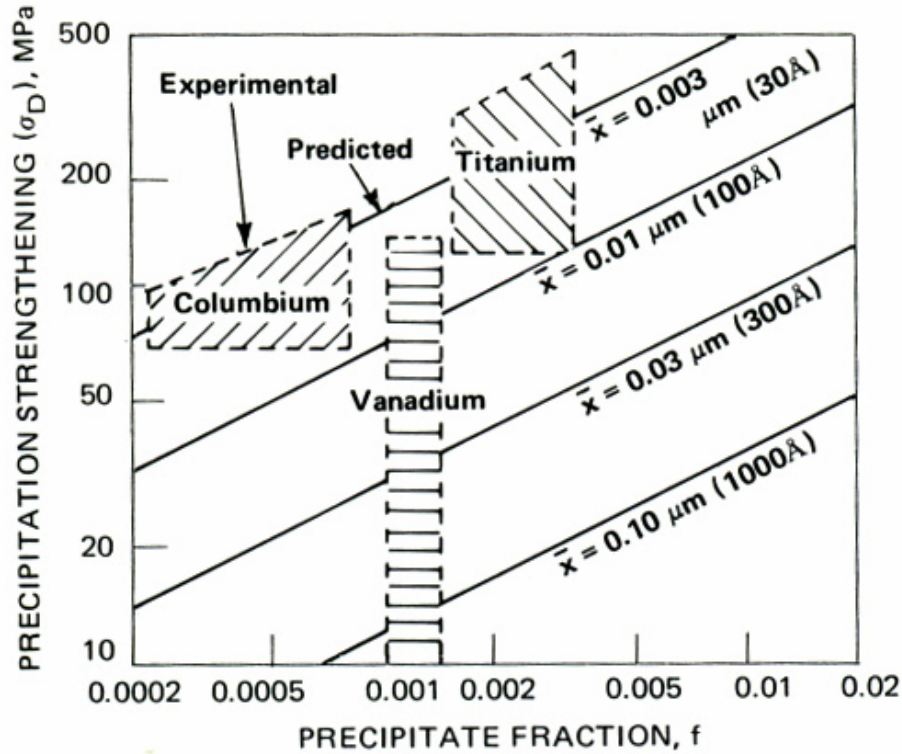


Figure 37 The dependence of precipitation strengthening on precipitate size and volume fraction according to the Ashby-Orowan mechanism, compared with experimental observations for given microalloy conditions.

#### 2.4.5 Subgrain Strengthening

The subgrain strengthening can be expressed as:

$$\sigma_{sg} = k_s l^{1/2} \quad (30)$$

where  $l$  is the subgrain boundary average intercept distance, and  $k_s$  is a constant associated with subgrain boundary strength. The subgrain strengthening has been associated with the misorientation across the subgrain boundary to allow  $k_s$  values to be calculated<sup>(72)</sup>. Adopting the model proposed by Li to calculate  $k_s$  as a function of the subgrain misorientation,  $\theta$ , it leads to:

$$k_s = \frac{1.6G\sqrt{b\theta}}{2\pi(1-\nu)} \quad (31)$$

where  $\nu$  is Poisson's ratio, taken as 0.3 for iron. Putting the appropriate constants for iron in the above equation, this results in:

$$k_s (N/mm^{3/2}) = 2.1\sqrt{\theta} \quad (32)$$

where  $\theta$  is in degrees.

#### 2.4.6 Texture Strengthening

The influence of texture on yield strength has been studied by Kozasu<sup>(73)</sup>. In Figure 38, the  $(111)\langle 112 \rangle$  texture is seen to be considerably larger than the  $(110)\langle 001 \rangle$  and  $(100)\langle 011 \rangle$  textures, when compared in the rolling direction ( $\theta=0$ ), for the same steel.

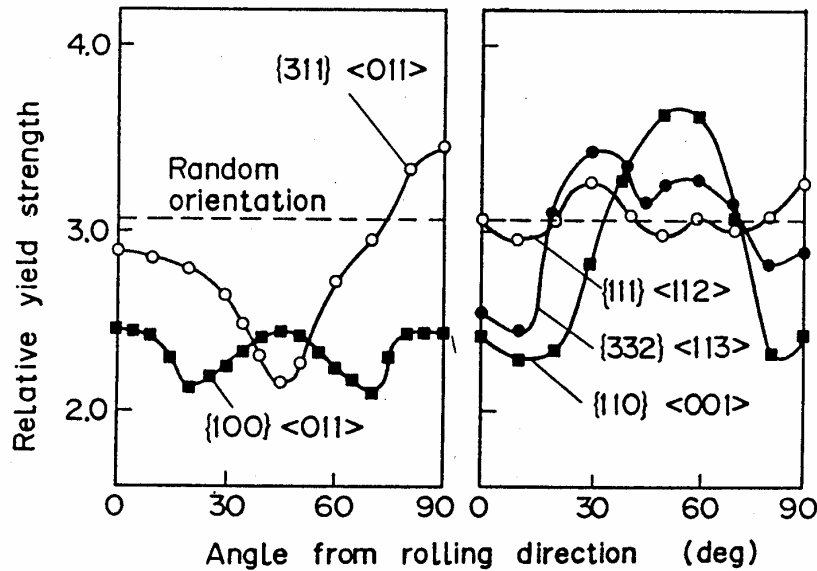


Figure 38 Variation in the relative yield strength for different texture components

In a similar study, Kozasu<sup>(74)</sup> has also shown that the texture of controlled rolled steels seems to improve the yield strength and the fracture appearance transition temperature (FATT) in the transverse direction.

### **3.0 STATEMENT OF OBJECTIVES**

To discover where the variation in microstructure and properties originates, this research project was conducted to determine how variations in the stages of a hot strip mill, e.g., temperatures of reheating, rough rolling, finish rolling and coiling, may contribute to the final variation in microstructure and properties. In these experiments, steels are subjected to predetermined levels of the four control temperatures described before.

Therefore, the objective of the present work is to investigate the influence of these changes in temperatures on changes in microstructure and mechanical properties. Also, the goal of this research is to define the temperature variation(s) most strongly associated with variations in microstructure and properties. In this manner, guidelines for processing, which will minimize property variation, will be established.

## **4.0 EXPERIMENTAL PROCEDURE**

### **4.1 Materials / Alloy Design**

Since the aim of this research is to evaluate the effect of hot rolling processing parameters on the variability of HSLA steel properties, it was determined that only one alloy design would be chosen for the hot rolling experiment.

It is known that the greater the grade (strength), the greater the variability. Because of this, a 70 ksi grade HSLA steel was chosen for use in the hot rolling experiment. Rouge Steel supplied the commercial steel used for the hot rolling experiment. The material consisted of several slab blocks with a 2"x3"x4" dimension, taken from a commercial slab. The same steel was used for the second stage of this investigation, a cooling rate experiment. The slab and heat chemistry analysis of this steel is shown in Table 3. The designation used for this material is Rouge steel.

### **4.2 Material Processing / Hot Rolling Study**

Slabs provided by Rouge steel were employed in the hot rolling trials at the USS Technical Center. The original design of the temperatures to be used is given in Table 4, where temperatures were chosen to vary around a set point. Figure 39 shows a schematic representation of the experimental rolling trials.

Table 3 Chemistry of 70 ksi HR HSLA material, wt.pct

Element	- <u>Slab</u> <u>Analysis</u>	<u>Rouge</u> <u>Heat</u> <u>Analysis</u>	- <u>Difference</u> <u>Heat-Slab</u>
C	0.0780	0.0790	0.0010
Mn	1.3000	1.3500	0.0500
P	0.0110	0.0080	-0.0030
S	0.0032	0.0031	-0.0001
Si	0.0200	0.0180	-0.0020
Cu	0.0230	0.0230	0.0000
Ni	0.0220	0.0260	0.0040
Cr	0.0230	0.0230	0.0000
Mo	0.0050	0.0180	0.0130
V	0.0500	0.0520	0.0020
Ti	< 0.002	0.0020	-
Al	0.0450	0.0400	-0.0050
N	0.0043	0.0049	0.0006
B	< 0.0002	-	-
Nb	0.0380	0.0490	0.0110
Sn	0.0040	0.0040	0.0000

Table 4 Design of the hot rolling experiment

<u>Variables</u>	<u>Experimental Temperature Design</u> Deg. C	<u>Temperature Variables (Levels)</u>	
		Deg. C	Deg. F
Reheating Temperature	1240 ± 40	1200, 1280	2192, 2336
Roughing Temperature	1100 ± 50	1050, 1150	1922, 2102
Finishing Temperature	950 ± 50	900, 950, 1000	1652, 1742, 1832
Coiling Temperature	600 ± 50	550, 650	1022, 1202

The matrix of the experimental plan calls for 24 different processing paths. A rolling schedule with only three passes, each of 50% deformation, as shown in Table 5, was used in the hot rolling experiment.

Table 5 Hot rolling deformation schedule

Pass	Thickness	Reduction pct	True Strain
	2.00	-	-
R1	1.00	50	0.69
R2	0.50	50	0.69
F1	0.25	50	0.69

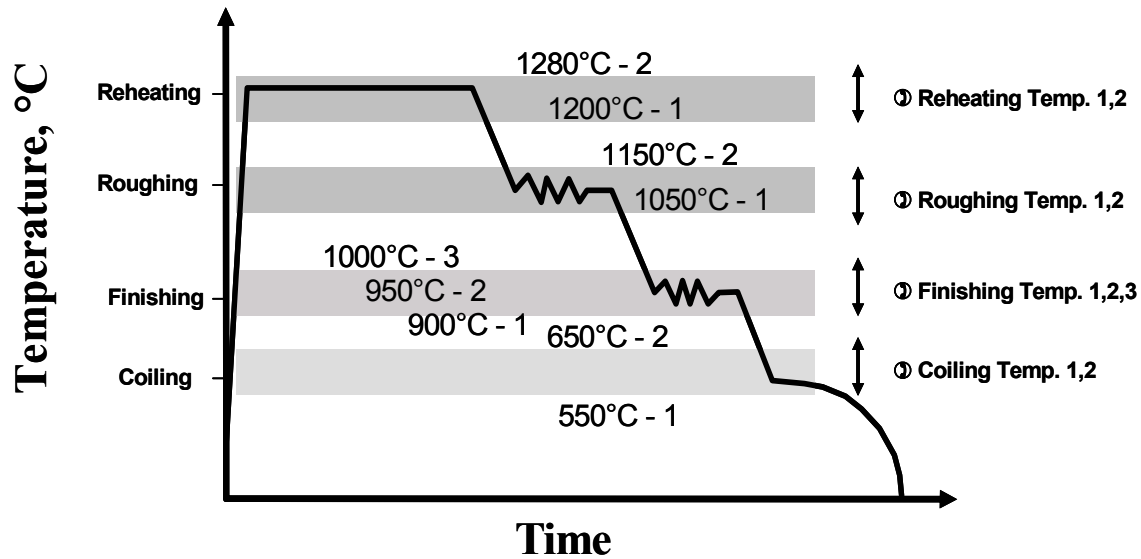


Figure 39 Representation of the hot rolling experiment variables

To ensure that the temperatures selected in the experimental design are suitable for the purpose of examining the effect of processing variability, the Grain Coarsening Temperature (GCT) and the Recrystallization Stop Temperature (RST) of the steel, were determined in the laboratory.

To determine the (GCT), samples of the as-cast slab material were heated for one hour at intervals of 50 C over the range 950 C to 1300 C (1742 F to 2372 F) and water quenched. Tempering of the quenched samples revealed the prior-austenite grain structure. From measurement of the prior-austenite grain sizes it was concluded that in this HSLA steel, grain coarsening occurs over the range of 1050 C to 1100 C (1922 F to 2012 F). Thus, it is concluded that dissolution of the grain boundary migration inhibiting precipitates will be complete at even the lowest reheat temperature of 1200 C. The microstructural variable of importance in the reheating stage will therefore be the austenite grain size.

To determine the RST, samples of the as-cast slab material were heated for one hour at 1250 C, cooled to “finishing” temperatures at 50 C intervals in the range of 900 C to 1100 C, and deformed in compression 30 pct before quenching. The microstructures of the quenched samples indicated that, below 900 C, a fully pancaked structure is obtained. At 950 C, a mixed austenite microstructure of unrecrystallized and recrystallized grains exists, and above 1000 C, a fully recrystallized austenite is observed. With the experimentally determined values of GCT and RST, it was agreed that the temperature levels of the experimental plan would be satisfactory.

### **4.3 Cooling Rate Experiment**

One important variable that is not always considered is the combined effect of cooling rate from the finishing to coiling temperature, and from coiling temperature to room temperature. It becomes clear that before the variability of the lower yield point can be reduced, the cooling rate parameters, and their influence on microstructural features and mechanical properties, need to be properly understood.

The experimental procedure consisted of a common processing path of reheating the as-cast material to 1250 C for one hour, deforming in three passes with equal pass reduction of 50%, at 1200 C, 1150 C, and an aimed temperature at 950 C. The cooling rates used from the finishing to coiling temperatures were 5 C/sec and 10 C/sec, and the coiling temperatures were 700C, 600C, and 550 C. The variables in the experimental design are shown in Table 6 and schematically presented in Figure 40. The resulting matrix consists of eighteen combinations of coiling temperatures and cooling rates.

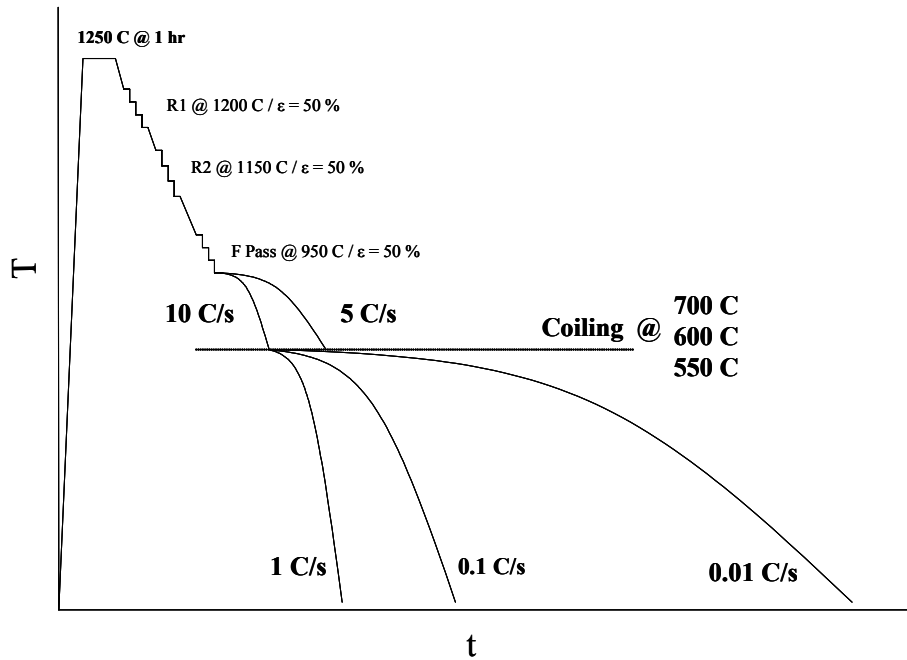


Figure 40 Schematic representation of the cooling rate experiment

The hot compression tests were conducted using an MTS-458 unit modified for deformation under constant true strain rate conditions. A radiation furnace mounted on the upper frame of the MTS was used. Cylindrical specimens with 0.5” x 0.75” dimensions were machined. To monitor the specimen temperature during the deformation sequence and cooling path, a hole of 1/16” in diameter was drilled into the cylinders at mid-height. The depth of this hole was approximately 0.2”. An additional modification was made to the geometry of the cylinders in order to minimize die-specimen friction effects. This is known as the modified Rastegaev’s<sup>(75)</sup> design, which retards friction and barreling effects by retaining the lubricant during deformation. The shape of the compression specimen is shown in Figure 41.

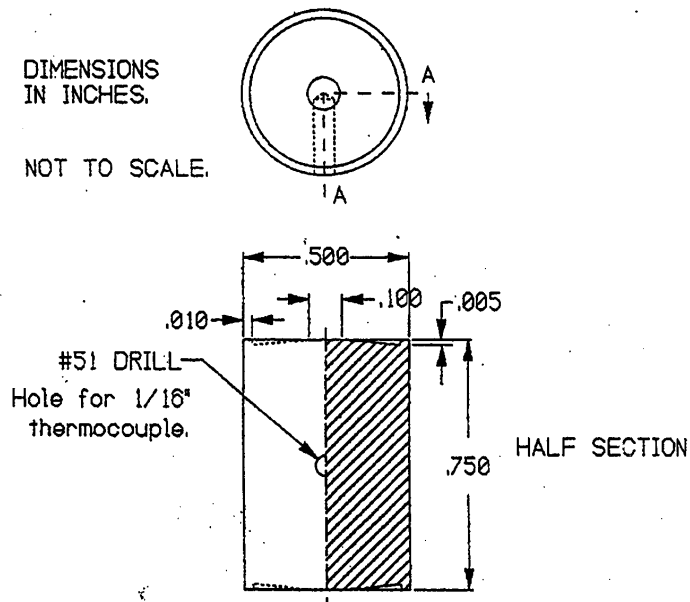


Figure 41 Shape of the modified Rastegaev's compression specimen design

A two-stage reheating cycle was used in the specimens. The first stage consisted of reheating the samples at the reheating temperature for 1 hour, and then quenching into an ice-brine solution, in order to retain the austenite composition. Prior to reheating in the radiation furnace, the as-quenched specimens were nickel plated<sup>(76)</sup> to prevent surface oxidation during reheating, since there is no controlled atmosphere within the radiation furnace. Specimens were then reheated and held at the reheating temperature for 2 minutes. A water-based lubricant, Delta Glaze 29, was used in both the upper and lower surfaces of the cylinders to minimize friction effects.

Table 6 Processing variables for the cooling experiment

Variable	
Cooling rate from finishing to coiling temperature	5, 10 C/sec
Coiling temperature	550, 600, 700 C
Cooling rate from coiling to room temperature	1.0, 0.1, 0.01 C/sec

#### 4.4 Experimental Techniques / Microstructural Analysis

##### 4.4.1 Optical Microscopy

Optical microscopy was used for examination and identification of the different types of ferrite and other microconstituents. The samples, for the case of the hot rolling experiment, were cut perpendicular to the rolling plane, and for the cooling rate experiment, were cut parallel to the deformation axis. All were mounted in bakelite. The specimens were ground using 180, 240, 320, 400 and 600 grit abrasive papers, and polished using 1  $\mu\text{m}$  and 0.05  $\mu\text{m}$  alumina paste. The polished sample was etched using 2% nital for 10-15 seconds.

Measurements of grain size and volume fractions of microconstituents were performed using a computer controlled Bioquant IV system attached to an optical microscope. For each test condition analyzed, approximately 200 grains were measured by manually tracing the grain boundaries. For the determination of volume fraction of microconstituents, manually tracing was also used, using a magnification of 452X.

#### **4.4.2 Scanning Electron Microscopy and EBSD**

Thin foils were prepared as described in Section 4.4.3, and were analyzed for the chemical composition of the precipitates that were in the visible range for the SEM. Samples prepared for optical microscopy were also used for a more comprehensive and detailed identification of microconstituents. Also, Electron Back Scattering Diffraction (EBSD) analysis was used to determine the crystallographic texture and grain boundary misorientation. The samples used for EBSD analysis were cut at a distance of one half from the sample surface, grounded and polished as described in section 4.4.1.

#### **4.4.3 Transmission Electron Microscopy ( TEM )**

TEM examination of materials was conducted using a JEM-200CX electron microscope operated at 200 kV. The analysis included bright field, dark field, and selected area diffraction. The microstructural features that were studied included examination of the ferrite morphology, identification of second phase microconstituents, search for fine precipitates, and measurement of dislocation densities. Thin foils were prepared by cutting the samples parallel to the rolling direction, and in the case of the cooling rate experiment, perpendicular to the deformation axis direction. In both cases, the foils were obtained at half-thickness of the specimens. A low speed saw was used and the thickness obtained was 0.8 mm. No grinding was used. The samples were chemically thinned to a thickness of 80-90  $\mu\text{m}$ . Two separate solutions were used for the chemical thinning. The first solution consisted of 50 ml  $\text{H}_2\text{O}$ , 50 ml  $\text{H}_2\text{O}_2$  ( 30% ), and 7 ml HF. The second solution consisted of 50 ml  $\text{H}_2\text{O}$ , 30 ml  $\text{HNO}_3$ , 15 ml  $\text{HCl}$ , and 10 ml HF. The foils were immersed in the first solution to thin the samples to about 0.1 mm. Then the foil was immersed in the second solution for a few seconds to obtain the final thickness. Finally, 3 mm

discs were punched from the foils, and were subsequently polished with a twin jet polisher, using an electrolytic solution of 95% acetic acid and 5% perchloric acid at 40-50 volts and 50 mA.

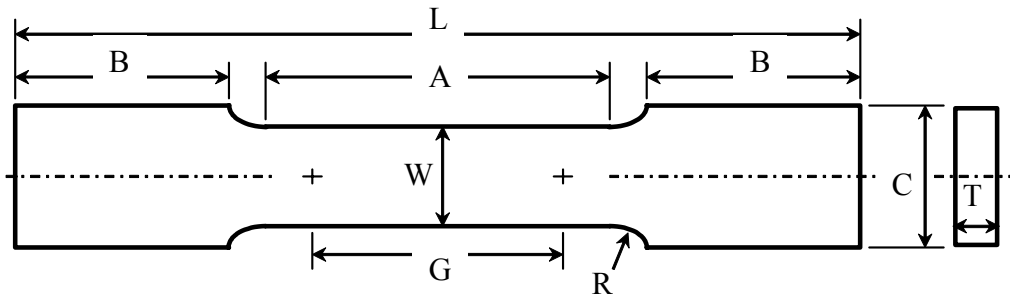
#### **4.4.4 Atom Probe Field Ion Microscopy ( APFIM )**

Atom probe analysis was performed on selected specimens. Using the atom probe, it was determined which processing conditions resulted in fine precipitation of carbonitrides. Also, it was necessary to determine the amount of Nb in the ferrite matrix, to obtain a good approximation of the volume fraction of the particles.

The specimens analyzed were taken at half-thickness of the plates. Using a low speed cutting wheel, 0.4 mm thick sheets were cut. These sheets were then sheared such that 0.4x0.4 mm square wires were obtained. A two stage technique<sup>(77)</sup> was used for the electropolishing of the specimens. The first solution consisted of 25% perchloric acid in acetic acid suspended over carbon tetrachloride. Polishing conditions were 20-25 DC volts and produced a localized neck in the specimen. This specimen was then placed into a new solution for the second stage of polishing. This solution was made up of 2% perchloric acid in 2-butoxyethanol. Polishing took place at 15-20 DC volts, and the wire thinned until two separated needles were obtained. Finally, specimens were further micropolished at 10 DC volts such that very sharp needles having a tip radius of approximately 0.01-0.1  $\mu\text{m}$  were produced. The solution for micropolishing was the same as that used for second stage electropolishing.

## 4.5 Tensile Tests

Tensile tests were performed in order to determine which set of hot rolling conditions gives the best strength and to determine which hot rolling parameter contributes most to mechanical properties variability. Tensile specimens were cut along rolling direction, transverse direction and 45° to rolling direction. Four specimens were obtained for each direction. Two of them were tested until breakage, and the other two were used for purposes of evaluation of R-values. Tests for R-values were stopped at 12 % strain. The tests were performed using an MTS 880 machine. All tests were evaluated using a strain rate of (1E-3 per sec) 1.5 mm/min. The dimensions of the tensile specimens are shown in Figure 42 and correspond to ASTM specifications<sup>(79)</sup>.



R	Gage length	1.0"
W	Width	0.25"
T	Thickness	Material (0.25")
R	Radius of fillet	0.25"
L	Overall length	4"
A	Length reduced section	1.25"
B	Length grip section	1.25"
C	Width of grip section	0.5"

Figure 42 Dimensions of the tensile specimens obtained for the mechanical testing

The data obtained from the tensile tests was comprised of: lower yield point, tensile strength, yield point elongation, n value, and total elongation.

#### **4.6 Microhardness Measurements**

Microhardness tests were made on all samples for purposes of comparison with the results obtained from the tensile tests. Microhardness measurements were performed on a Leco M-400-G microhardness tester with a square pyramid diamond indentator. The load employed for testing the hot bands was 500 grams. The load employed for the cooling rate specimens was 200 grams. Grain boundary effect is present in all cases. The loading time used was 15 seconds.

## 5.0 RESULTS

A commercial grade 70 ksi (480 MPa) as-cast slab material was provided by Rouge Steel for simulation of conventional hot mill processing. In the laboratory rolling experiment, the processing temperatures were varied to obtain a target combination of 24 processing conditions. The samples were identified by the level (temperature) of the four processing variables and, these processing conditions are presented in Table A of Appendix A.

The mechanical properties of the laboratory rolled hot band were measured in the rolling, transverse and diagonal direction, and the LYP and TS results are presented in Tables B, C, and D of Appendix A. The overall variability of the LYP and TS, measured independent of the processing variation is shown in Table 7.

Table 7 Overall variability of LYP and TS

	<u>L.Y.P.</u>				<u>U.T.S.</u>			
	<u>Mean</u> (MPa)	<u>Std.</u> <u>Dev.</u>	<u>Coeff</u> <u>Var</u>	<u>Sample</u> <u>Size</u>	<u>Mean</u> (MPa)	<u>Std.</u> <u>Dev.</u>	<u>Coeff</u> <u>Var</u>	<u>Sample</u> <u>Size</u>
<u>RD</u>	524	21.0	4.0	89	606	22.81	3.7	89
<u>TD</u>	521	30.2	5.8	85	602	26.5	4.4	85
<u>DD</u>	517	18.3	3.5	69	593	17.0	2.8	69

## 5.1 Variability of Tensile Properties with Processing Condition

### 5.1.1 LYP

The variability of the processing conditions resulted in a significant variation of the LYP. In Table 8, all the 96 measurements, in the rolling direction (RD), were separated according to the level of the processing step. The variation in coiling temperature shows the largest variation in the LYP values. The average LYP for all the high coiling temperature conditions is 536 MPa, whereas the average value for the low coiling temperature condition is 512 MPa.

Table 8 Variability of the LYP with various processing conditions

	<u>Processing Parameter</u>	<u>Mean MPa</u>	<u>Std. Dev. MPa</u>	<u>Coeff. Variation</u>	<u>Sample Size</u>
L.Y.P.	High RHT	532	20.4	3.83	44
	Low RHT	516	19.5	3.77	45
	High RT	526	20.3	3.85	44
	Low RT	522	22.4	4.29	45
	High FT	523	18.6	3.55	28
	Medium FT	517	22.2	4.3	31
	Low FT	532	22.0	4.13	30
	High Coil	536	18.2	3.4	44
Low Coil	512	17.1	3.3	45	

Coiling at 650 C results in a larger LYP than the 550 C coiling condition for any given processing path. This is illustrated in Figure 43. In this Figure, the LYP is plotted vs the processing parameters, identified according to the given number codes. An 'X' replaces the varying processing parameter, coiling temperature, while the other 3 processing parameters remain constant. The 123x and 221x sets of processing parameters show the largest variation, 44 MPa, and 41 MPa respectively, whereas the 113X set has the smallest variation, only 10 MPa.

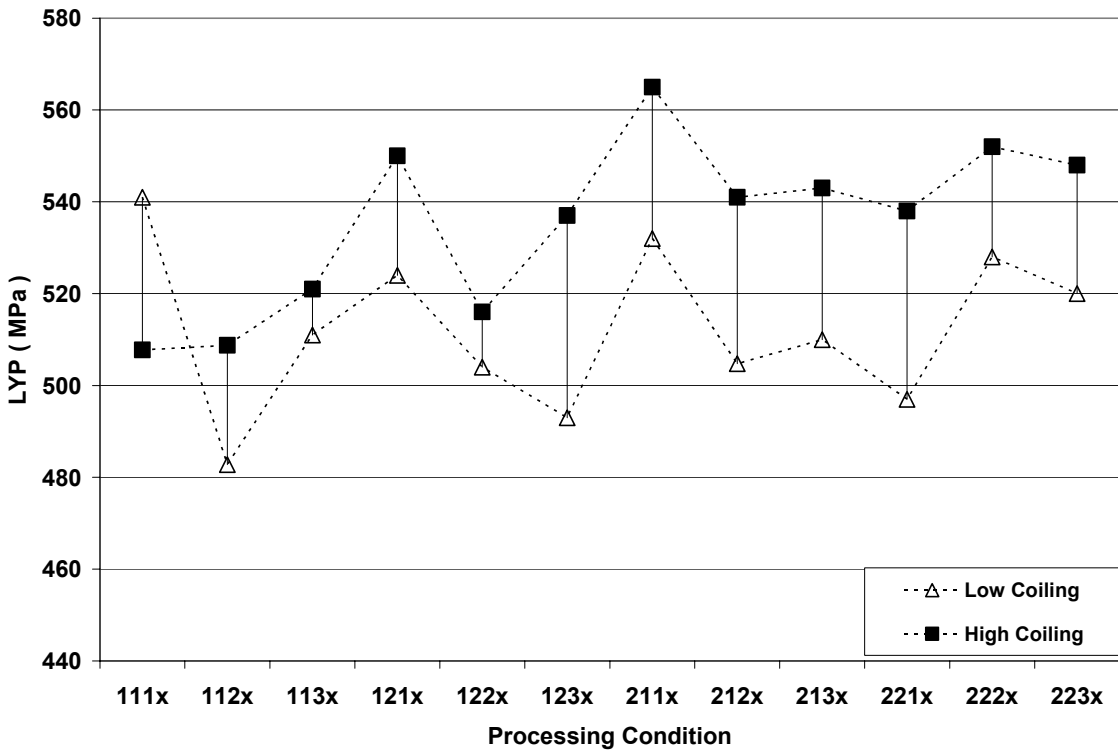


Figure 43 Effect of coiling temperature on LYP, for various processing conditions

The variation of the finishing temperature and its effect on the LYP can be observed in Figure 44. With the exception of the 22x1 set, and, to a much less extent, 11x2 and 22x2 sets, a low finishing temperature (900 C) gives a larger LYP than the medium and high finishing temperature, for all processing conditions. The 11x1 set gives the largest variation, 60 MPa, followed by the 12x2 set, with 34 MPa and 12x1 set, with 31 MPa. The smallest variation was given by the 22x2 and 11x2 set, with 14 MPa and 13 MPa respectively. In general, the LYP increases as the finishing temperature decreases. The mean LYP value for the FT at 900 C is 532 MPa, at 950 C is 517 MPa and at 1000 C is 523 MPa.

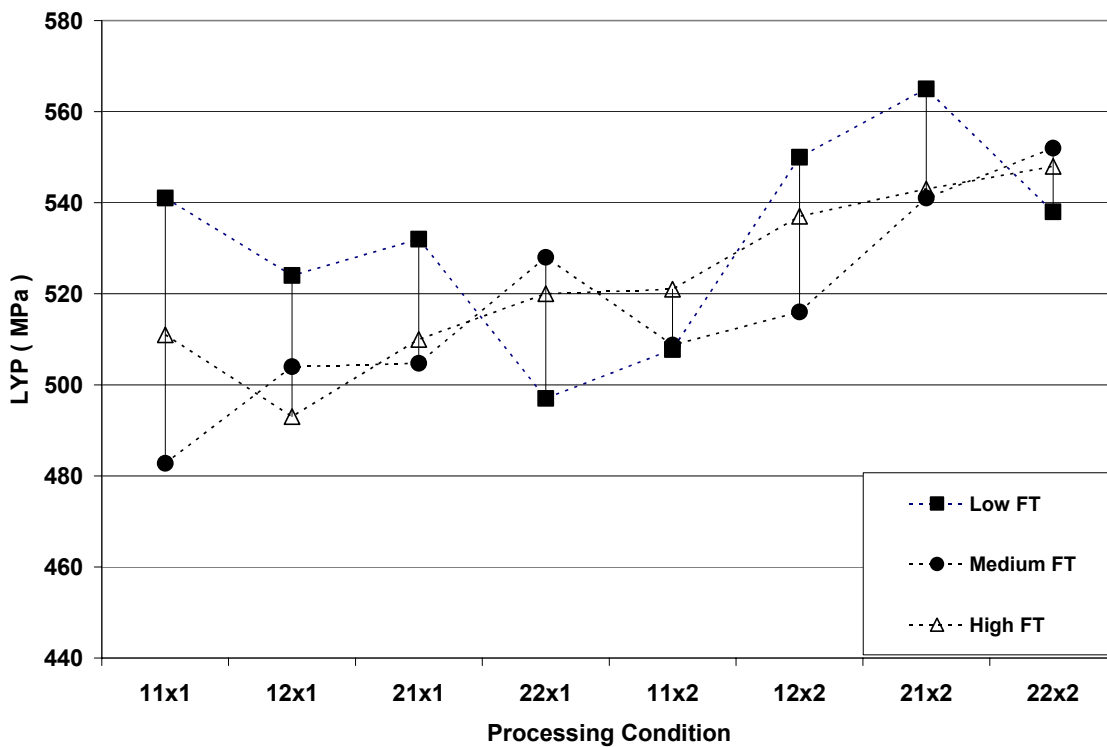


Figure 44 Effect of finishing temperature on LYP, for various processing conditions

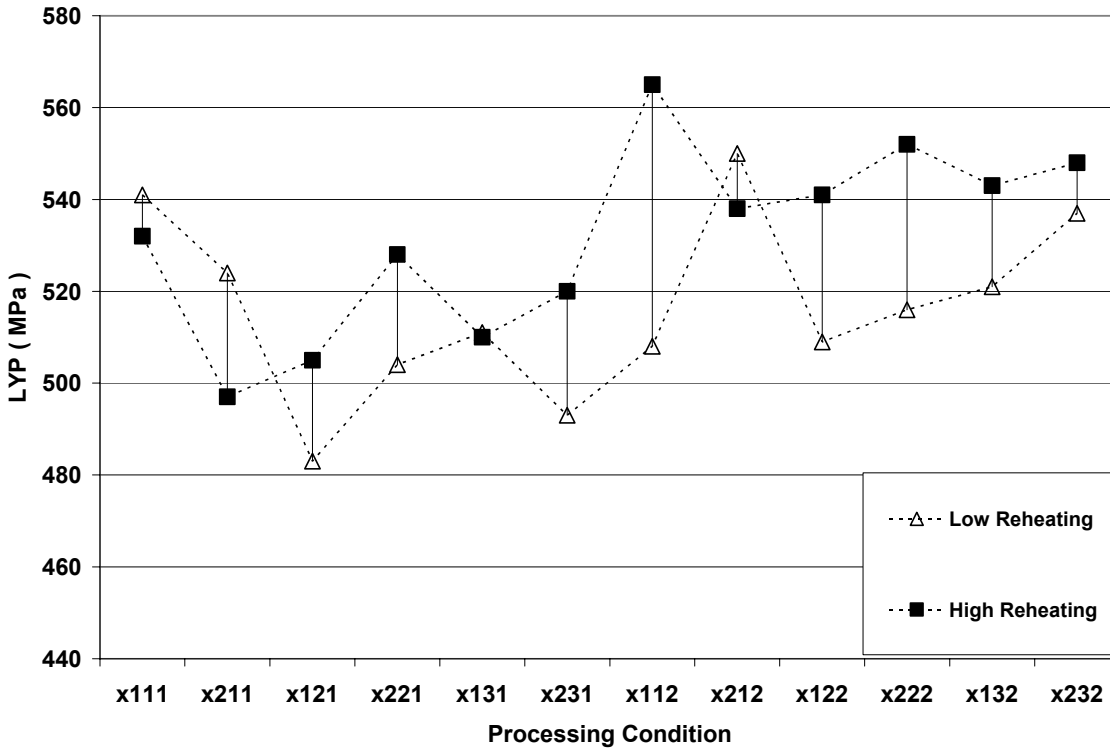


Figure 45 Effect of reheating temperature on LYP, for various processing conditions

Figure 45 shows the dependence of LYP with variation of reheating temperature conditions. The high reheating temperature (1280 C) conditions have a larger LYS than those reheated at 1200 C. The x112 set shows the largest variation, 60 MPa, while the x232 set shows only a 11 MPa variation, and the x131 set shows no variation at all. Also, in three cases, the low reheating temperature results in a larger LYP, i.e. x211 with a variation of 27 MPa, and less than 10 MPa for the x111 and x212 sets. The mean LYP values indicate that, in general, reheating at 1280 C results in a larger LYP than when reheating at 1200 C.

It is apparent, from Table 8, that the variation in roughing temperature has little effect on the LYP. However, examination of Figure 46 indicates that for some processing conditions, the variation of roughing temperature can result in a LYP variation as large as 42 MPa, as in the case of the 1x12 set. While it seems that a high roughing temperature increases slightly the LYP, in most of the cases the mean variability does not exceed more than 15 MPa, so it is reasonable to state that there is no significant effect of the roughing temperature on LYP variability.

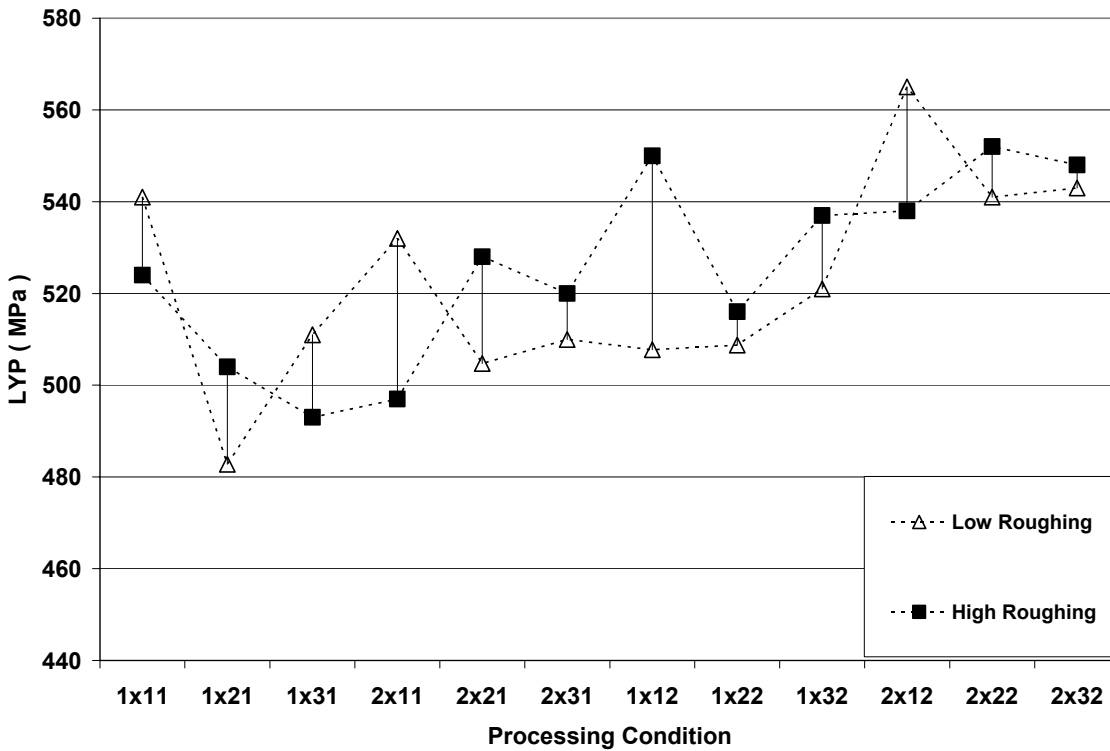


Figure 46 Effect of roughing temperature on LYP, for various processing conditions

### 5.1.2 UTS

The variability of the UTS for different processing conditions, in the rolling direction, is shown in Table 9. The variation in coiling temperature results in the largest variability in the UTS value, followed by the variation in reheating temperature.. The average UTS when coiling at 550 C is 593 MPa, whereas the average UTS at 650 C is 620 MPa.

Table 9 Variability of the UTS with various processing conditions

	<u>Processing</u> <u>Parameter</u>	<u>Mean</u> <u>MPa</u>	<u>Std. Dev.</u> <u>MPa</u>	<u>Coeff.</u> <u>Variation</u>	<u>Sample Size</u>
UTS	High RHT	616	22.24	3.6	44
	Low RHT	596	18.83	3.15	45
	High RT	610	21.9	3.6	44
	Low RT	602	22.9	3.8	45
	High FT	613	21.9	3.5	28
	Medium FT	600	23.2	3.8	31
	Low FT	605	22.6	3.7	30
	High Coil	619	21.3	3.44	44
Low Coil	593	14.4	2.42	45	

Figure 47 illustrates the UTS variation for all the processing conditions with varying coiling temperature. It can be observed that, coiling at 650 C, results in a larger UTS than coiling at 550 C, for all processing conditions, except for the 111X set. The 122X set of processing conditions shows a minimal variation of 10 MPa, while the 123X set has the largest variation, 48 MPa. The 211X, 213X and 221X also result in a UTS variation of about 40 MPa.

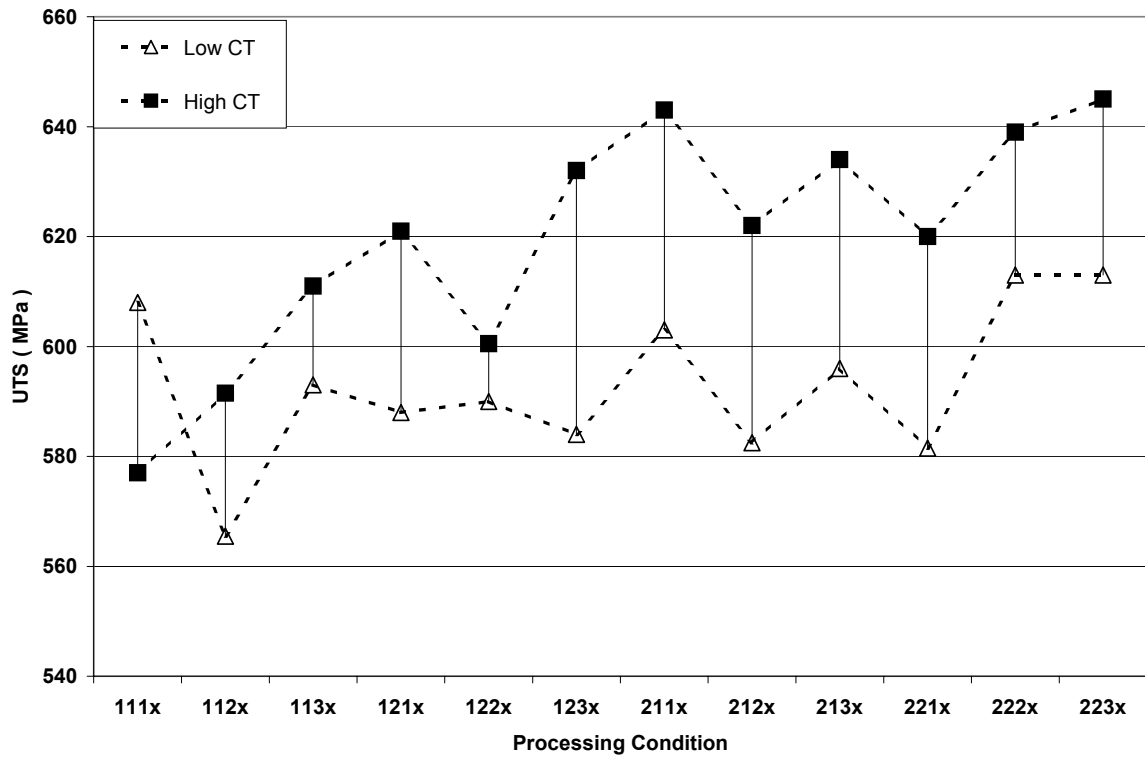


Figure 47 Effect of coiling temperature on UTS, for various processing conditions

The variation of UTS with different reheating conditions is shown in Figure 48. In general, reheating at 1280 C results in a larger UTS compared to those samples that were reheated at 1200 C. The largest variation in UTS, 60 MPa, is observed in the X112 set, and a minimal variation, about 5-10 MPa, is observed in the X111, X131, X211, X212, and X232 conditions.

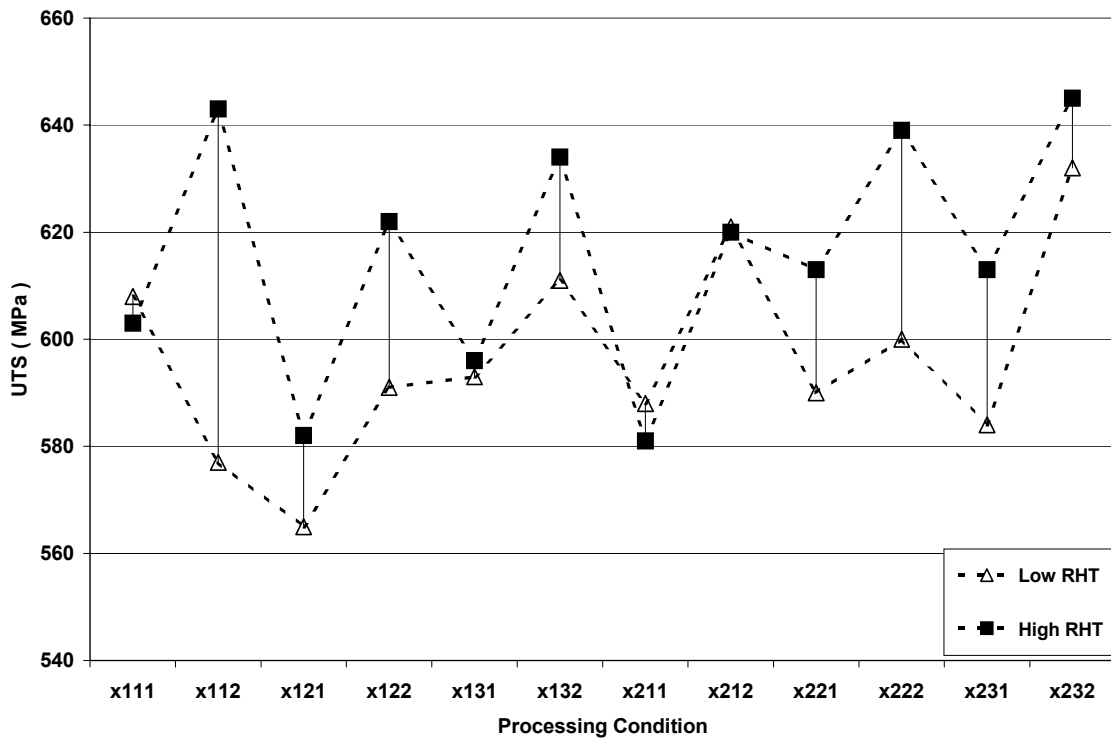


Figure 48 Effect of reheating temperature on UTS, for various processing conditions

Figure 49 shows the effect of the variation of finishing temperature on UTS. In general, a high finishing temperature results in a larger UTS value. The 11X1, 21X1 and 21X2 sets are the exception to these results, since a low finishing temperature results in a larger UTS value. The 11X1 set has the largest UTS variation, 42 MPa, and the 12X1 set shows only a variation of less than 6 MPa.

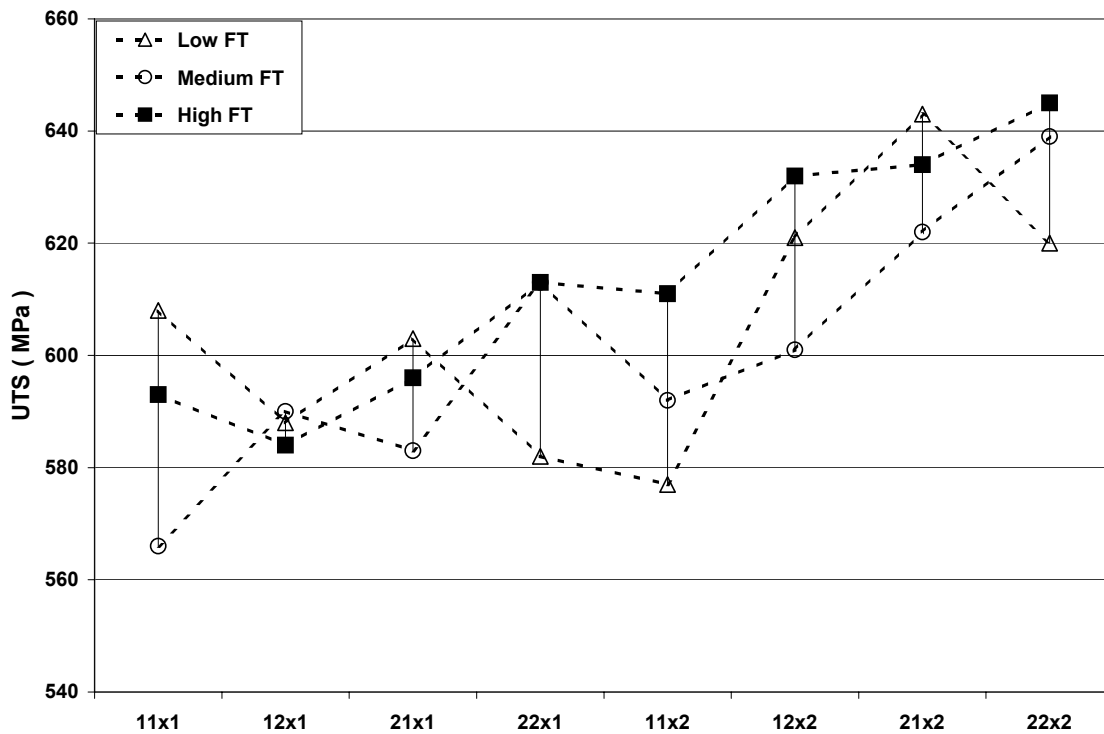


Figure 49 Effect of finishing temperature on UTS, for various processing conditions

A high roughing temperature, 1150 C, results in a larger UTS value than when roughing at 1050 C, Figure 50. The 1X31, 2X11 and 2X12 show, however, the opposite behavior, although the maximum variation is only 20 MPa. The largest variation, 49 MPa, is observed for the 1X12 conditions, while the 1X31, 1X22, and 2X32 conditions result only in about a 10 MPa variation in the UTS value.

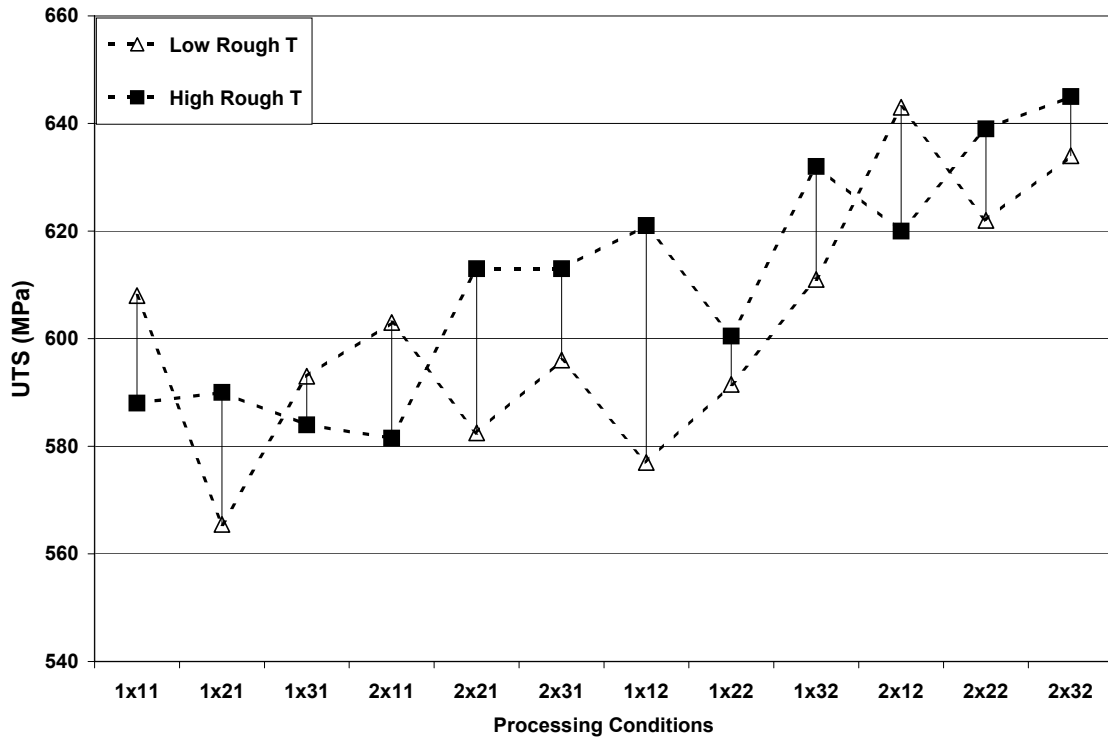


Figure 50 Effect of roughing temperature on UTS, for various processing conditions

### 5.1.3 YPE

The mean variation of the YPE with different processing conditions, ( RD ), is shown in Table 10. The largest variation in YPE is given by the variation in finishing temperature, while the reheating temperature gives the smallest variation. Figure 51 shows the variation of YPE with different levels of finishing temperature. It is observed that the highest finishing temperature, 1000 C, gives the smallest yield point elongation. Most of the processing condition sets, where FT is the variable, have a large variation, between 1.0 and 1.5% strain. The smallest variation in YPE was given by the 22x1 set, with a variation of only 0.3%. From Table 10, is clear that the average YPE increases as finishing temperature decreases.

Table 10 Variability of the YPE with various processing conditions

	<u>Processing Parameter</u>	<u>Mean %</u>	<u>Std. Dev. %</u>	<u>Coeff. Variation</u>	<u>Sample Size</u>
Y.P.E.	High RHT	2.03	0.63	31.03	44
	Low RHT	2.23	0.59	26.45	45
	High RT	1.91	0.54	28.27	44
	Low RT	2.35	0.61	25.9	45
	High FT	1.52	0.19	12.5	28
	Medium FT	2.42	0.47	19.4	31
	Low FT	2.45	0.55	22.4	30
	High Coil	2.30	0.59	25.6	44
	Low Coil	1.96	0.60	30.6	45

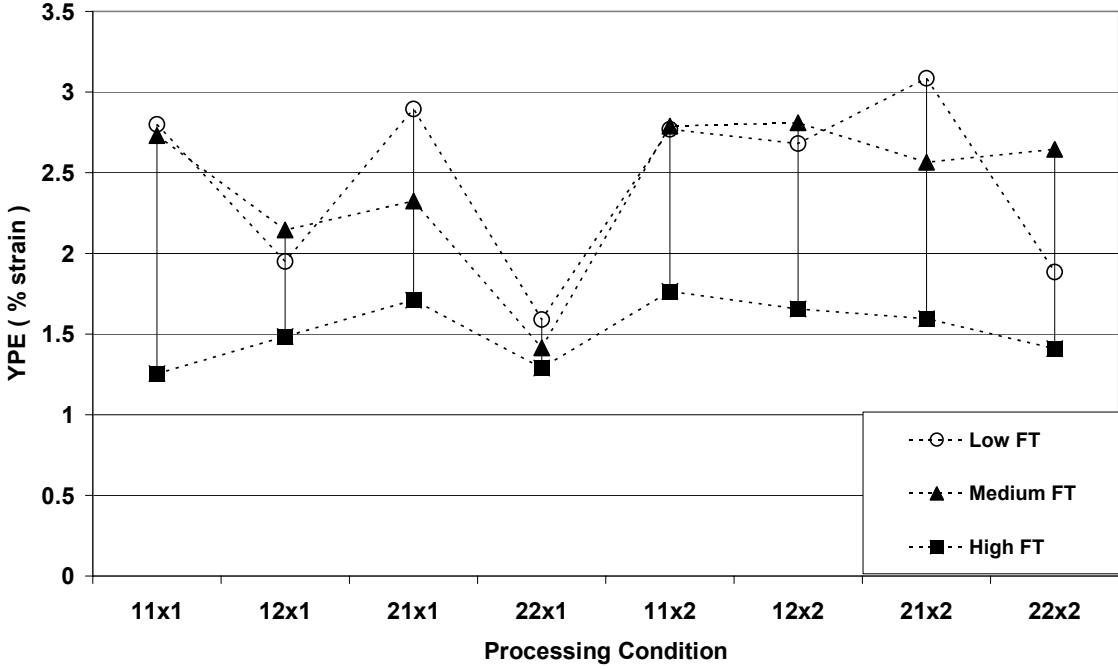


Figure 51 Effect of finishing temperature on YPE, for various processing conditions.

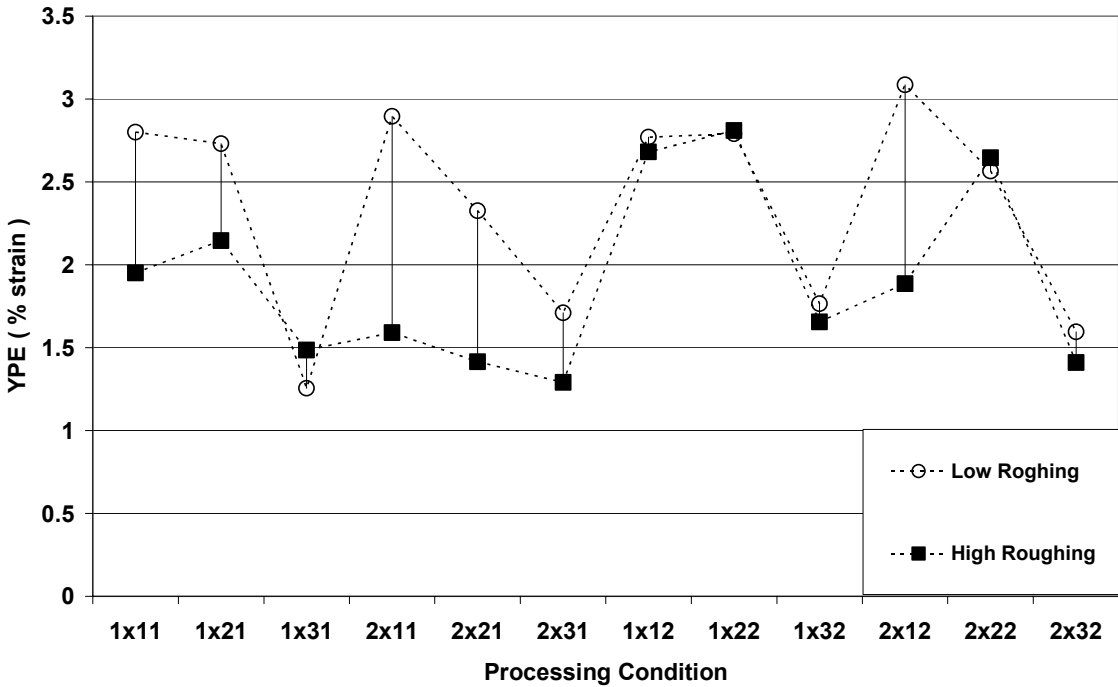


Figure 52 Effect of roughing temperature on YPE, for various processing conditions

The variation of roughing temperature also resulted in a marked variability in yield point elongation, as shown in Figure 52. It can be seen that the 2x11 and 2x12 processing sets have a variation in YPE as large as 1.3% and 1.2% strain respectively. Also, it is seen that, the low roughing temperature, 1050 C, results in a larger YPE. This is also reflected in Table 10, where the mean YPE value for the 1050 C roughing temperature is 2.35, whereas the value for the 1150 C roughing temperature is 1.91. However, there are five sets of processing parameters that practically show no variation in YPE with different levels of roughing temperatures.

The effect of coiling temperature on YPE is less marked. In Figure 53, it is shown that almost all of the processing condition sets have no variation in YPE with different coiling temperatures. The only significant variation, only of 1.2% strain, comes from the 222X processing set. Finally, no significant variation in YPE was found with varying reheating temperature, Figure 54, where the largest variation was only of 0.8% strain.

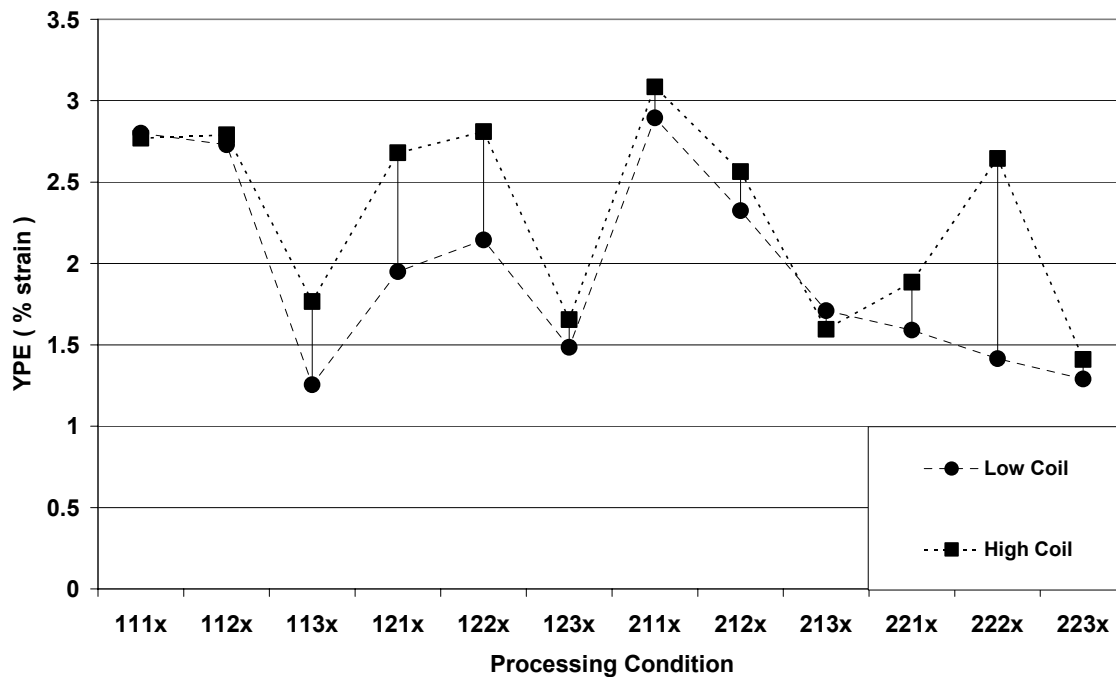


Figure 53 Effect of coiling temperature on YPE, for various processing conditions

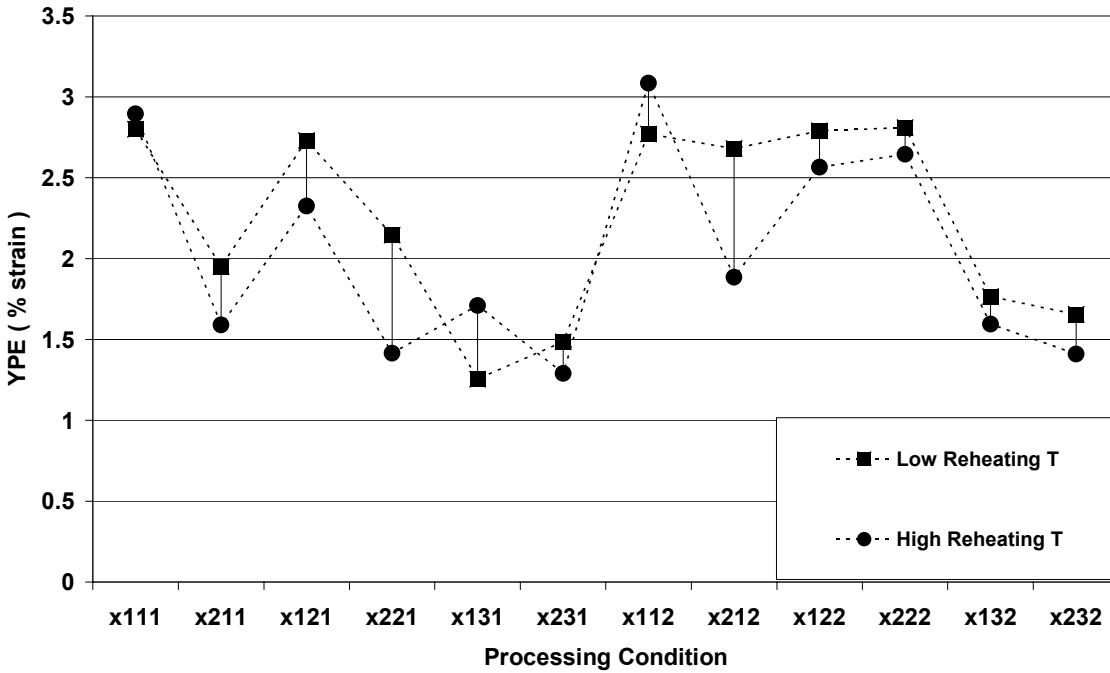


Figure 54 Effect of reheating temperature on YPE, for various processing conditions

#### 5.1.4 Work Hardening

The uniform true strain or 'n' value is commonly used to represent the work hardening exponent. The average variation of the uniform true strain value with different processing conditions is shown in Table 11. The variation of reheating and roughing temperatures gives the smallest variation in the work hardening exponent. On the other hand, variation in finishing temperature and coiling temperature results in a large variation of this property.

Table 11 Variability of the work hardening with various processing conditions

	<u>Processing Parameter</u>	<u>Mean</u>	<u>Std. Dev.</u>	<u>Coeff. Variation</u>	<u>Sample Size</u>
n Value	High RHT	0.1174	0.013	11.07	24
	Low RHT	0.1255	0.014	11.15	24
	High RT	0.1187	0.013	10.95	24
	Low RT	0.1242	0.015	12.07	24
	High FT	0.1103	0.013	11.78	16
	Medium FT	0.1253	0.013	10.37	16
	Low FT	0.1288	0.008	6.21	16
	High Coil	0.1304	0.008	6.13	24
Low Coil	0.1126	0.013	11.54	24	

Figures 55 and 56 show, respectively, the variation of work hardening at different levels of reheating and roughing temperatures. From Figure 55, it can be seen that there is a slight increase in work hardening for all the low reheating temperature conditions. The maximum variation is seen for the x111 and x221 conditions. Variation in roughing temperature does not have an effect on the work hardening exponent (Figure 56).

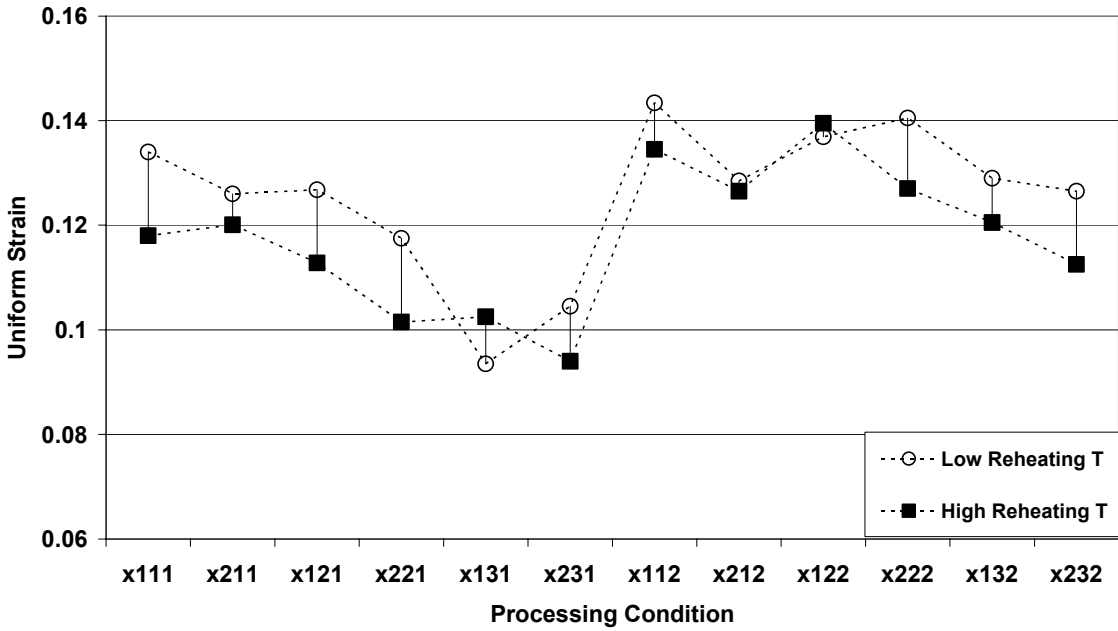


Figure 55 Effect of reheating temperature on the 'n' value, for various processing conditions

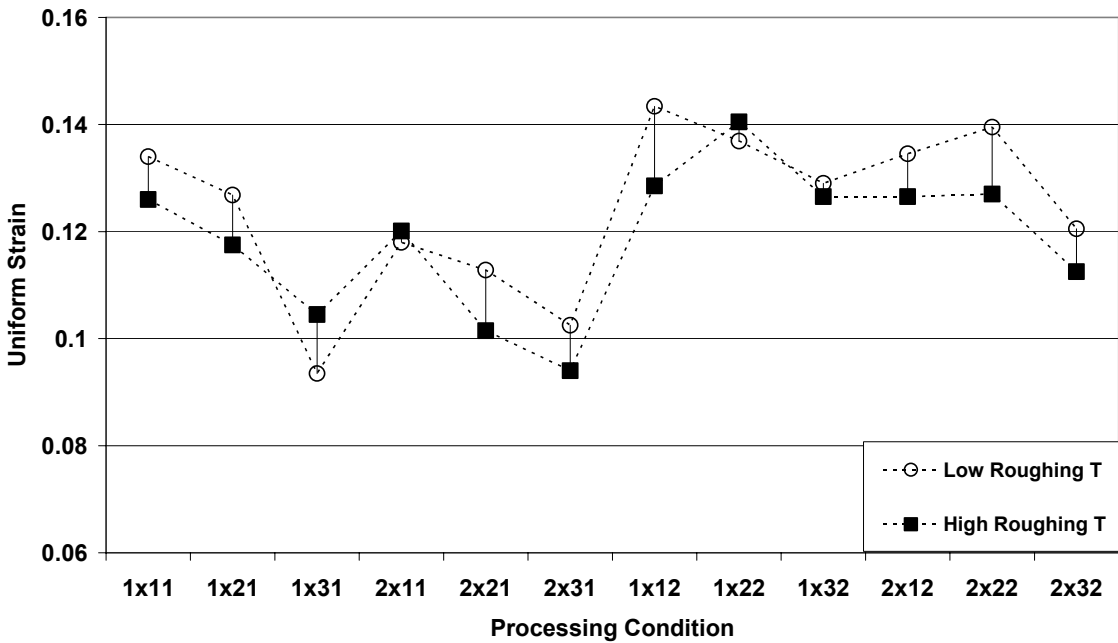


Figure 56 Effect of roughing temperature on the 'n' value, for various processing conditions

Variation in finishing and coiling temperatures results in a significant variation in work hardening. In Figure 57, the effect of finishing temperature on this property is shown. For all cases, the 1000 C finishing temperature results in the smallest work hardening value, while the low finishing temperature conditions give, especially with the combination of the low coiling temperature, the largest values. The 11x1 conditions show the largest variation in work hardening.

In general, for all processing conditions, coiling at 650 C gives a higher work hardening value than coiling at 550 C, Figure 58. The largest variation is seen for the 113x condition, while the 221x, 121x, 111x and 112x set of conditions only show a minimal variation.

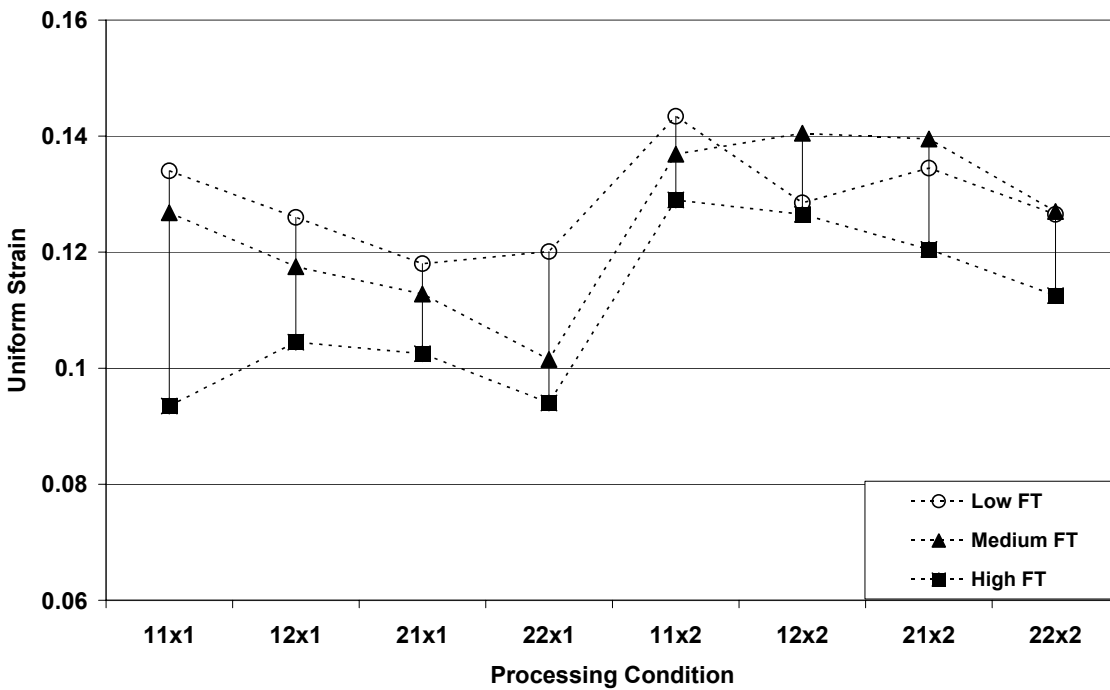


Figure 57 Effect of finishing temperature on the ‘n’ value, for various processing conditions

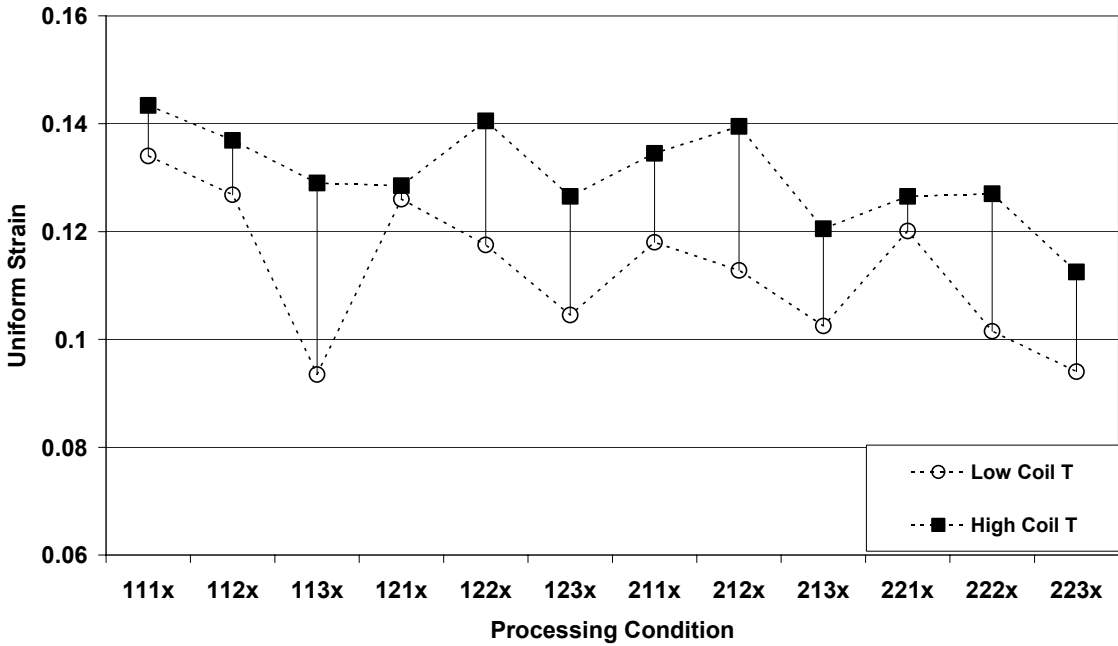


Figure 58 Effect of coiling temperature on the ‘n’ value, for various processing conditions

### 5.1.5 Total Elongation

Table 12 shows the average variation of the total elongation (rolling direction), from engineering stress-strain curves, for all the different processing conditions. The largest variation comes from the reheating temperature, followed by coiling temperature. The average total elongation for all the low reheating conditions is 35.9%, whereas the average for the high reheating temperatures is 33.1%. The roughing temperature gives the smallest variation. In this case, the mean total elongation, for all the low and high roughing temperatures are, 35.1% and 33.9%, respectively.

Table 12 Variability of the total elongation with various processing conditions

	<u>Processing Parameter</u>	<u>Mean %</u>	<u>Std. Dev. %</u>	<u>Coeff. Variation</u>	<u>Sample Size</u>
Total Elongation(%)	High RHT	33.18	2.58	7.77	24
	Low RHT	35.91	1.13	3.14	24
	High RT	33.93	2.50	7.36	24
	Low RT	35.15	2.21	6.28	24
	High FT	33.30	2.58	7.74	16
	Medium FT	35.20	2.21	6.27	16
	Low FT	35.13	2.15	6.12	16
	High Coil	35.69	1.21	3.38	24
Low Coil	33.39	2.77	8.29	24	

Figure 59 shows the variation in total elongation with different reheating temperatures. It is observed that the variation in total elongation is minimal when the high coiling temperature, 650 C, is used. However, variation in reheating temperatures, in combination with low coiling temperatures, 550 C, results in a large variation in total elongation. The largest variation is given by the X111 and X231 processing sets.

Similarly, Figure 60 shows that the variation in coiling temperature does not affect the total elongation in those cases where a low reheating temperature is used. If a high reheating temperature is used, a large variation in total elongation can be observed with variation in coiling temperature. In general, for all the processing conditions, coiling at 650 C, results in a larger elongation than when a coiling temperature of 550 C is used.

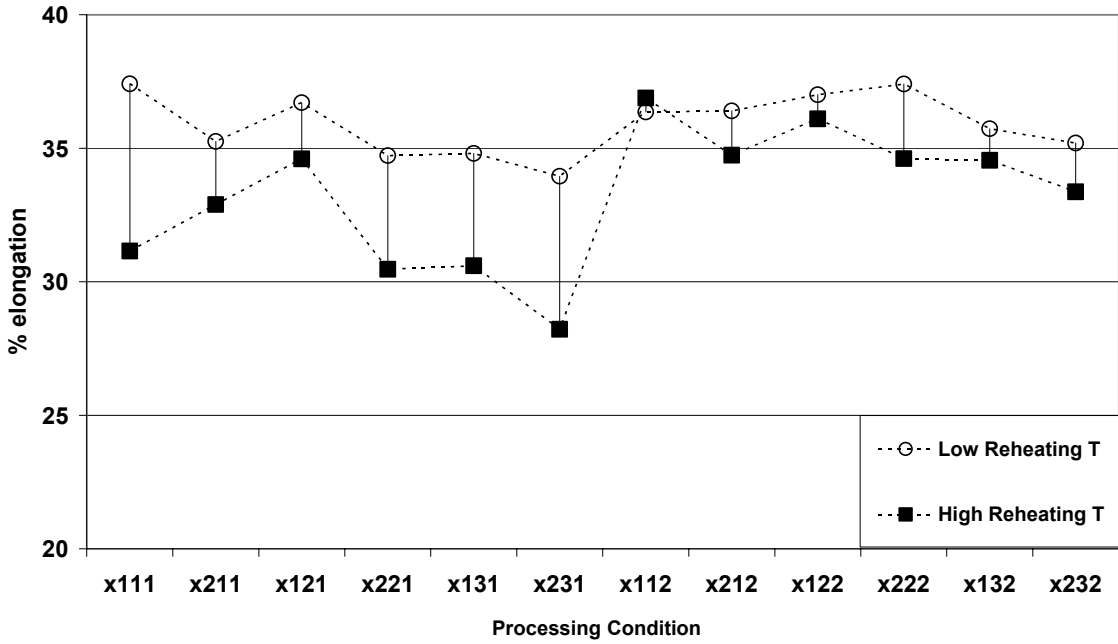


Figure 59 Effect of reheating temperature on %elongation, for various processing conditions

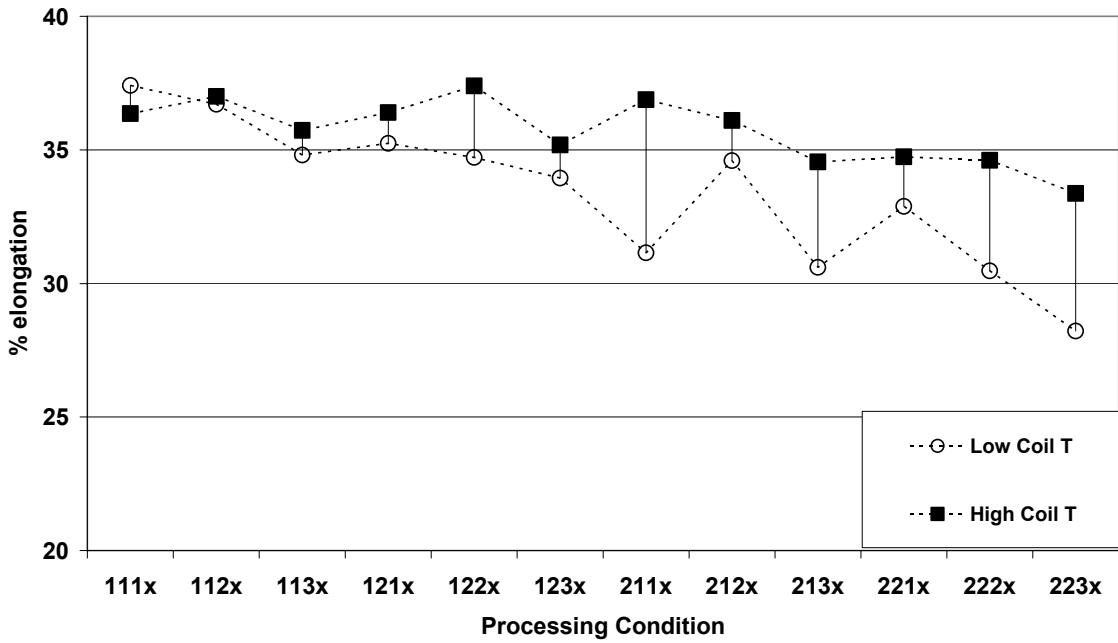


Figure 60 Effect of coiling temperature on %elongation, for various processing conditions

As in the case of the effect of reheating temperature, the variation in total elongation with different finishing temperatures is small if the 650 C coiling temperature is used. If the coiling temperature is 550 C, then the variation in finishing temperatures results in a large variation in total elongation, Figure 61. The largest variation is given by the 22X1 set, while the smallest variation is given by the 12X1 and 11X2 set.

In general, variation in roughing temperature does not have a significant effect on the variability of total elongation, as illustrated in Figure 62.

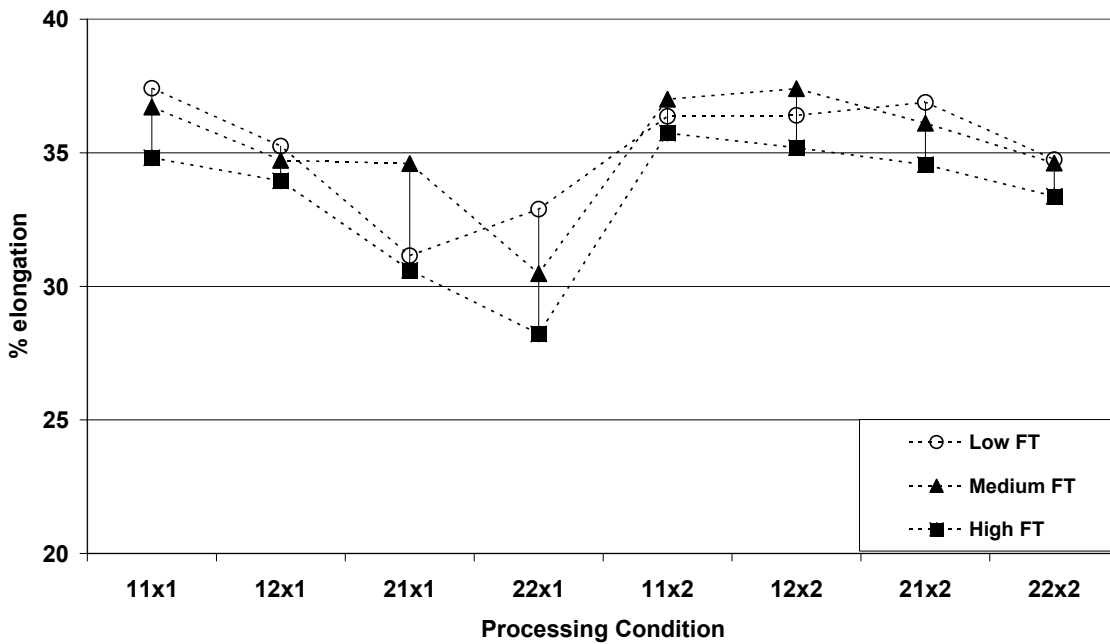


Figure 61 Effect of finishing temperature on %elongation, for various processing conditions

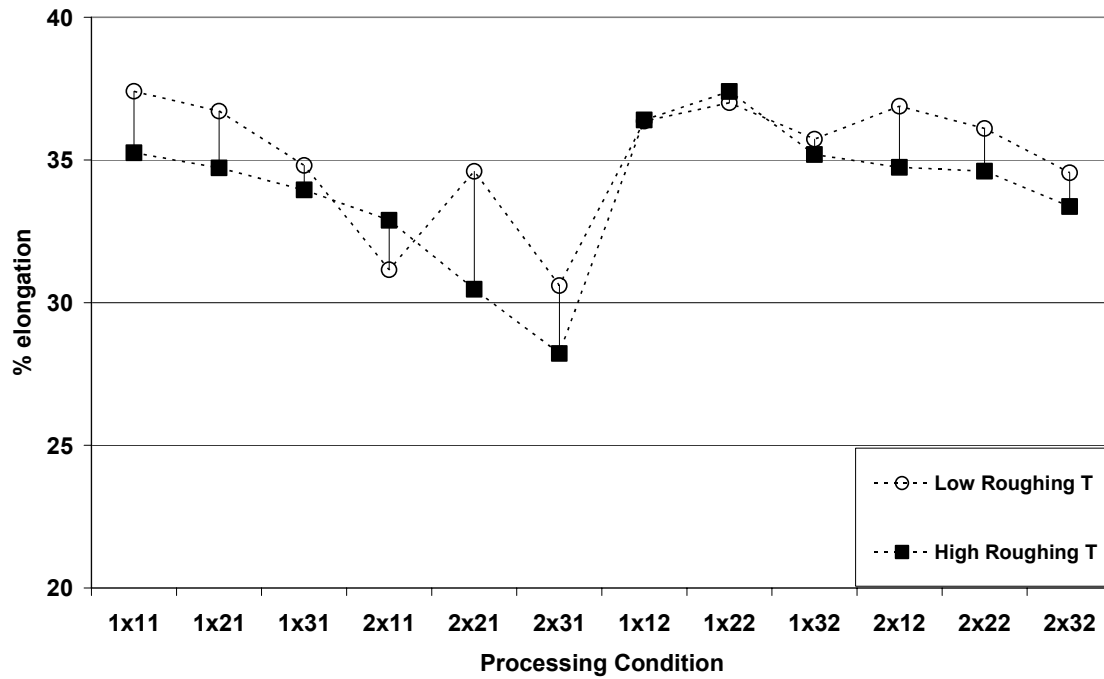


Figure 62 Effect of roughing temperature on %elongation, for various processing conditions

### 5.1.6 R-values

The variation of the processing conditions and its effect on the R-bar values and  $\Delta R$  values, is shown in Table 13, where the average values are shown for the different processing parameters.

Table 13 Variability of the R-bar and  $\Delta R$  values with various processing conditions

	<u>Processing Parameter</u>	<u>Mean R-bar</u>	<u>Std. Dev</u>	<u>Mean <math>\Delta R</math></u>	<u>Std. Dev</u>
R-bar and $\Delta R$ values	High RHT	0.966	0.043	-0.238	0.090
	Low RHT	0.967	0.058	-0.226	0.089
	High RT	0.943	0.039	-0.241	0.082
	Low RT	0.989	0.042	-0.229	0.097
	High FT	0.987	0.042	-0.254	0.091
	Medium FT	0.943	0.050	-0.246	0.100
	Low FT	0.957	0.043	-0.195	0.076
	High Coil	0.982	0.040	-0.25	0.078
Low Coil	0.951	0.049	-0.22	0.098	

In Table 14, the R-bar values and  $\Delta R$  values for the individual processing set of conditions are shown. It can be observed that the R-bar values range from 0.89 and 0.91 for the 2221 and 1211 sets, to 1.03 and 1.02 for the 1132 and 2132 set of conditions. In general, low roughing temperatures combined with high finishing temperatures contribute to R-bar values close to 1.

Also, in all the processing conditions, negative  $\Delta R$  values were obtained. The 1132 set has the closest value to zero, whereas the 2231 has the most negative value. The 1132 and 2111 processing conditions give the best combination for R-bar values and  $\Delta R$  values.

Table 14 R-bar and  $\Delta R$  values for different processing conditions

<u>Processing Condition</u>	<u>R-bar Value</u>	<u><math>\Delta R</math> value</u>
1131	1.006	-0.284
1132	1.029	-0.138
1211	0.91	-0.162
1221	0.925	-0.321
2111	1.001	-0.103
2112	0.933	-0.244
2122	1.012	-0.345
2131	0.924	-0.157
2132	1.02	-0.336
2212	0.9875	-0.271
2221	0.891	-0.158
2222	0.947	-0.163
2231	1.002	-0.359
2232	0.945	-0.253

### 5.1.7 Hardness Values

Table 15 shows the surface-to-surface hardness values obtained for the different hot bands. Figure 63 shows that high coiling temperatures result in higher hardness values, similar to those results observed in the tensile tests.

Table 15 Through-thickness hardness profile for hot-band samples

Condition	Hardness, VHN (500g)						Mean of	Mean of	Std.	Std.	Max-	Max-Min
							Mid-Four	Mid-Two	Dev	Dev	Min	of
									of	of	(6)	Mid-
									Six	Mid-		Four
										Four		
1111	201.0	191.0	195.0	203.0	200.0	196.0	197.3	199.0	4.5	5.3	12.0	12.0
1112	187	197	202	198	197	187	198.5	200.0	6.2	2.4	15.0	5.0
1121	186	204	200	205	203	193	203.0	202.5	7.5	2.2	19.0	5.0
1122	196	206	209	206	207	204	207.0	207.5	4.5	1.4	13.0	3.0
1131	190	193	200	199	191	197	195.8	199.5	4.2	4.4	10.0	9.0
1132	196	200	202	200	215	195	204.3	201.0	7.2	7.2	20.0	15.0
1211	216	198.5	201	199.5	206.5	217	201.4	200.3	8.3	3.6	18.5	8.0
1212	196.5	213	209	218	204.5	204	211.1	213.5	7.5	5.8	21.5	13.5
1221	173	184	184	198	189	187	188.8	191.0	8.1	6.6	25.0	14.0
1231	193	189	196.5	195	197	189	194.4	195.8	3.6	3.7	8.0	8.0
1232	208	202	203	204	210	207	204.8	203.5	3.1	3.6	8.0	8.0
2111	204.5	204	218	199	189	205	202.5	208.5	9.4	12.1	29.0	29.0
2112	195	209.5	210.5	211	201.5	205	208.1	210.8	6.3	4.5	16.0	9.5
2122	193.5	208	216.5	222	212	196	214.6	219.3	11.3	6.0	28.5	14.0
2131	195	203	209	207.5	201	201	205.1	208.3	5.1	3.8	14.0	8.0
2132	208.5	204.5	207.5	218	200	210	207.5	212.8	6.0	7.6	18.0	18.0
2212	199.0	206.0	214.5	203.5	209.5	204.5	208.4	209.0	5.3	4.8	15.5	11.0
2221	189	201	211	207	204.5	192	205.9	209.0	8.6	4.2	22.0	10.0
2222	193.5	199.5	205.5	214.5	211.5	191	207.8	210.0	9.6	6.7	23.5	15.0
2231	171.5	179	194.5	188	190	163.5	187.9	191.3	11.9	6.5	31.0	15.5
2232	200	210	205	203.5	219	203	209.4	204.3	6.8	7.0	19.0	15.5

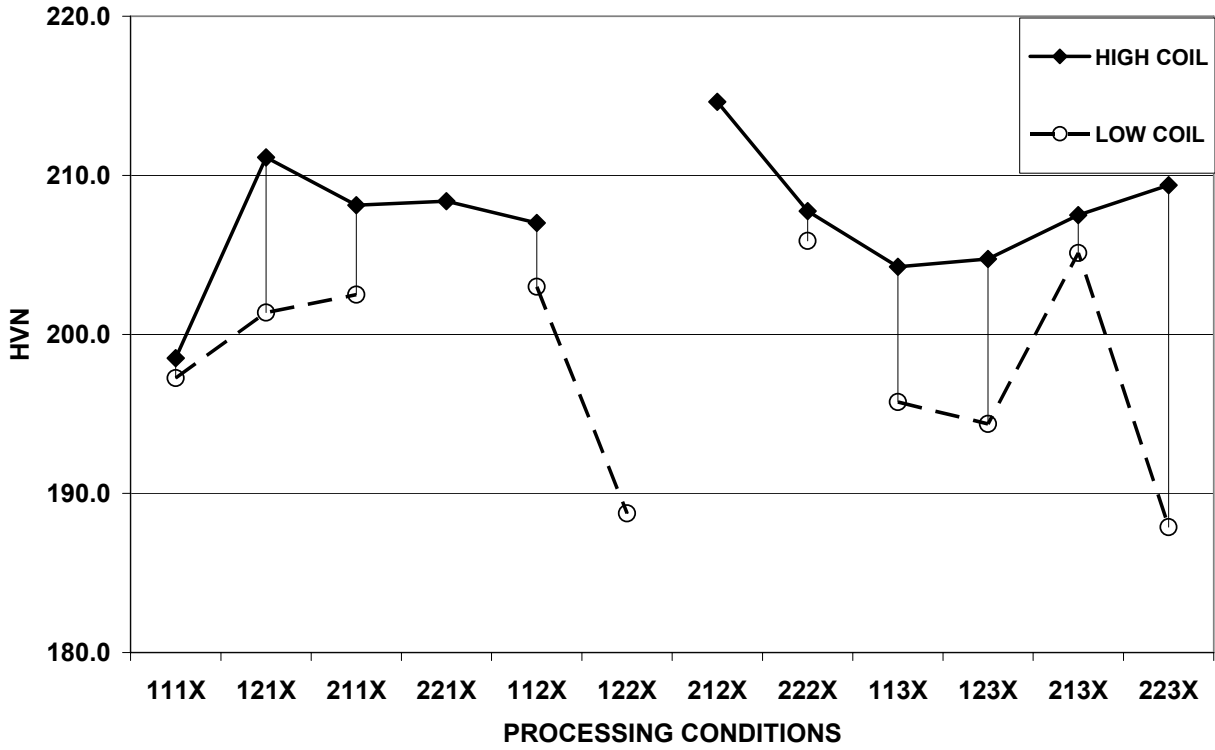


Figure 63 Variation of hardness (through thickness) with processing conditions, indicating the higher hardness values for the high coiling temperature conditions

## 5.2 Effect of Hot Rolling Parameters on the Microstructure

### 5.2.1 Effect of the Variation of the Processing Parameters on the Type of Phases

A range of forms of ferrite and other transformation products is produced in the Rouge 70 ksi steel, as listed below:

**F<sub>P</sub>** - Polygonal ferrite

**F<sub>N</sub>** - Non-Polygonal ferrite

**F<sub>B</sub>** - Bainitic ferrite

**P** - Pearlite

**C** - Grain boundary cementite

In Appendix B, the micrographs of the ferrite microstructures found for the different processing conditions are shown. The occurrence and amount of these phases varies significantly with different combinations of processing conditions. A qualitative and quantitative analysis of the resulting ferrite microstructures was undertaken by Wu<sup>(80)</sup>, and the main results will be described here.

A map of the occurrence of the phases in a Coiling-Finishing Temperature space is shown in Figure 64, and shows that with the combination of increasing finishing temperatures plus decreasing coiling temperatures the type of ferrite shifts from:

Polygonal → Non-polygonal → Bainitic

and, at the same time, the pearlite constituent is replaced with cementite at the condition of high finishing temperature and low coiling temperature.

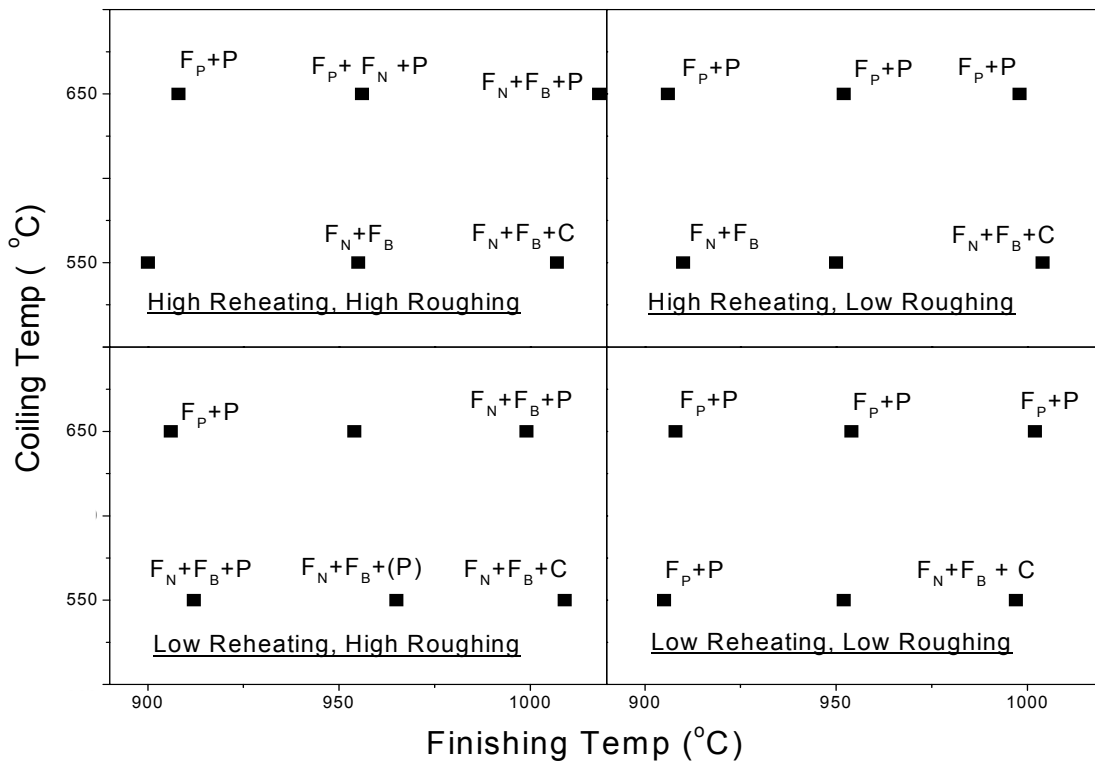


Figure 64 Effect of finishing and coiling temperature on the occurrence of different constituents, for the four combinations of reheating and roughing temperatures.

Table 16 shows an estimated amount of the volume fraction of the different microstructural features such as pearlite, polygonal, non polygonal and bainitic ferrite, and also indicates whether or not grain boundary cementite is formed. The average amount of polygonal ferrite ( Pf ) that results from the different levels of processing parameters is shown in Table 17.

Table 16 Occurrence and volume fractions of constituent phases

Condition	Polygonal Ferrite pct	Non-Poly. Ferrite pct	Bainitic Ferrite Pct **	Pearlite pct	Grain Boundary Cementite
1111	10	88		2	Yes
1112	40	56		4	
1122	50	48		2	
1131	10	80	9	<1.0	
1132	40	57		3	
1211	5	90	4	Yes	Yes
1212	85	5	5	Yes	
1221	3	95	1	1	
1231	9	85	6		
1232	8	90	1	Yes	
2111	10	89	1		Yes
2112	75	20		5	
2122	45	51		4	
2131	12	60	28		
2132	45	52		3	
2212	90	6		4	Yes
2221	18	30	52		
2222	50	47		3	
2231	14	41	45		
2232	12	80	5	3	

\*\* Given as the residual volume fraction after removal of polygonal and non-polygonal ferrite.

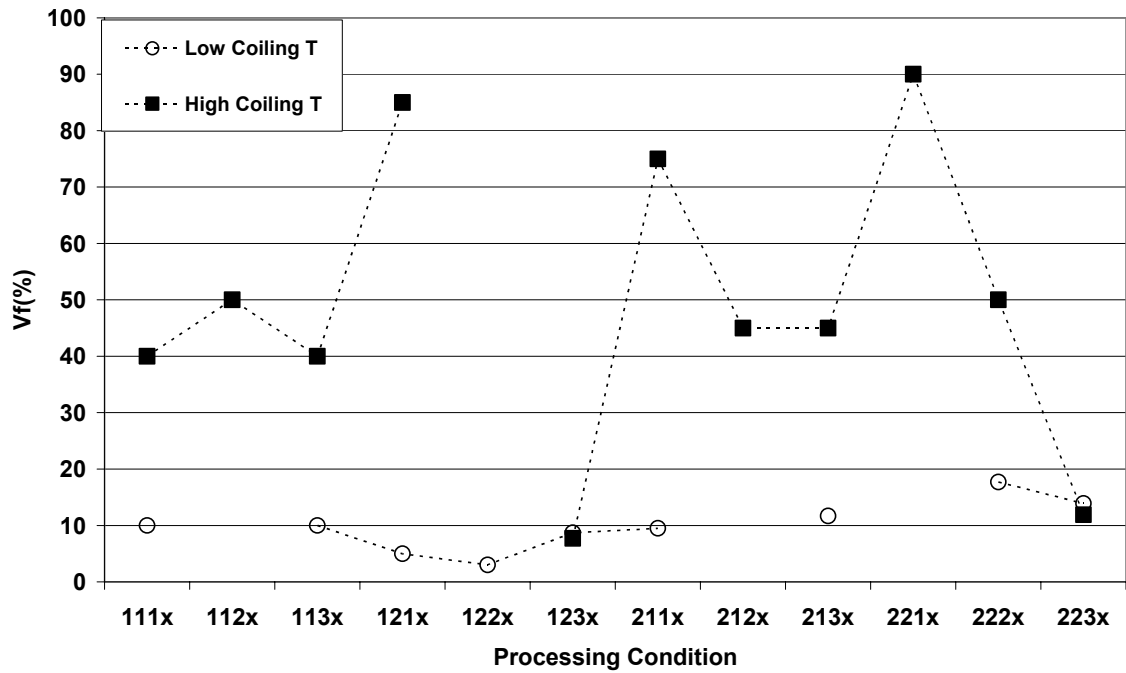


Figure 65 Variation of the volume fraction of polygonal ferrite, for different coiling conditions

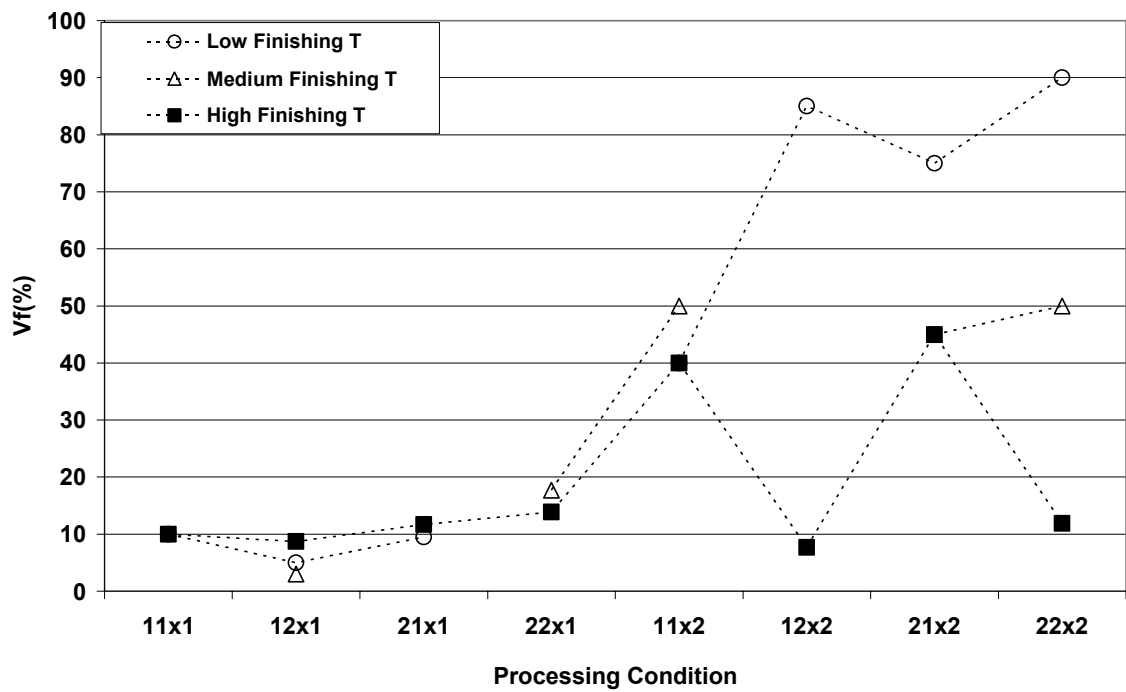


Figure 66 Variation of the volume fraction of polygonal ferrite, for different finishing conditions

Figure 65 shows that variation in coiling temperature results in a large variation in the volume fraction of polygonal ferrite. High coiling temperatures have the largest amount of polygonal ferrite, and the largest variation is seen in those conditions where a low finishing temperature is used. On the other hand, no variation is seen in the 123X and 223X conditions, where both were processed at the high roughing and high finishing temperature.

The effect of finishing temperature on the amount of polygonal ferrite is presented in Figure 66. It is obvious that at low coiling temperatures, the variation in finishing temperature does not give any variation in the amount of polygonal ferrite. However, when a coiling temperature of 650 C is used, the variation in the finishing temperature results in a rather large variation of the polygonal ferrite volume fraction. Low finishing temperatures contribute to a larger volume fraction, while high finishing temperatures result in almost no amount of polygonal ferrite. The 12X2 and 22X2 conditions have the largest variation; from 10% Pf at the high FT (1000 C), to about 90% when FT is 900 C.

As in the case of the effect of finishing temperature, the variation in roughing temperature is not important when a coiling temperature of 550 C is used, as shown in Figure 67. However, coiling at 650 C results in a somewhat large variation of polygonal ferrite volume fraction, at different levels of roughing temperatures.

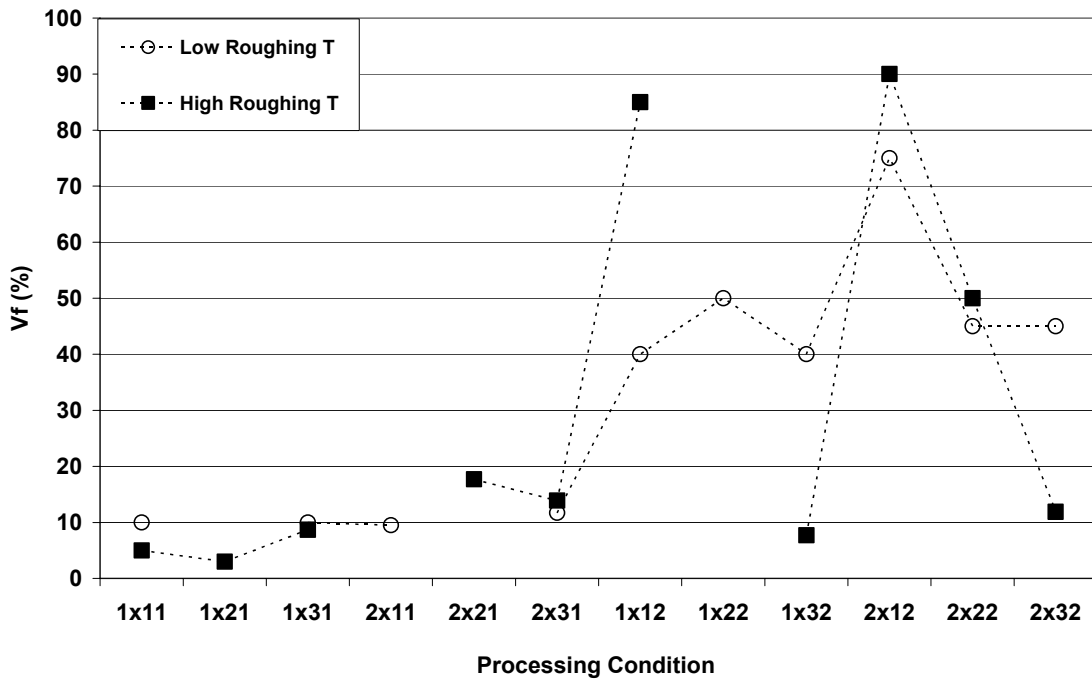


Figure 67 Variation of the volume fraction of polygonal ferrite, for different roughing conditions

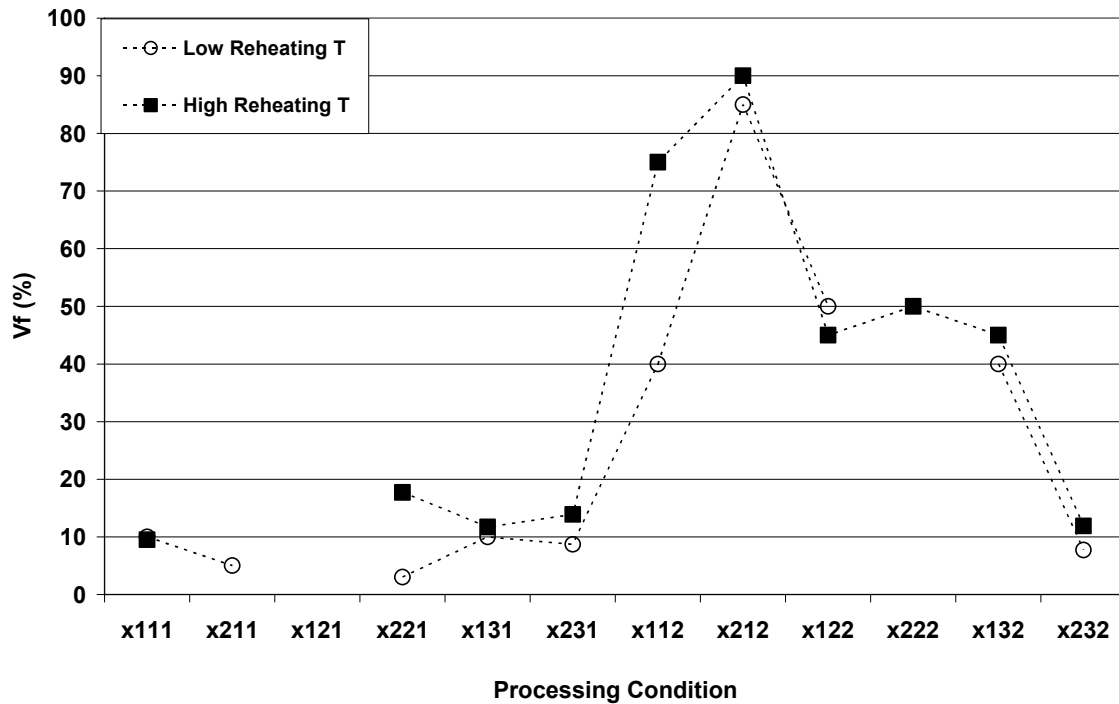


Figure 68 Variation of the volume fraction of polygonal ferrite, for different reheating conditions

Finally, in Figure 68, it is evident that the variation in reheating temperature does not result in any variability. Only the X112 condition shows a significant difference, where the high reheating condition results in 75 % Vf, while the low reheating condition only has a 40% Vf.

Table 17 Variability of the polygonal ferrite with various processing conditions

	<u>Processing Parameter</u>	<u>Vol. Fraction, Pct.</u>	<u>Std. Dev.</u>
Polygonal Ferrite (%)	High RHT	36.97	28.8
	Low RHT	25.94	27.0
	High RT	29.29	33.4
	Low RT	33.62	22.3
	High FT	18.61	14.9
	Medium FT	33.14	21.5
	Low FT	44.92	37.9
	High Coil	49.05	26.3
Low Coil	9.94	4.37	

### 5.2.2 Effect of Processing Parameters on the Grain Size

For those cases where the grain structure was sufficiently distinct, i.e., polygonal and non-polygonal ferrite, the grain size was measured and the results are given in Table 18. The grain size distributions were examined in terms of both normal and log normal distributions. As found in other studies, the distribution of the grain size in a given grain structure is better described as log normal<sup>(81)</sup>.

Table 18 Grain size variation with processing conditions

Condition	<D>, $\mu\text{m}$	Std. Dev of (D), $\mu\text{m}$	C.V (D), pct	Equiv. D of <lnD> $\mu\text{m}$	C.V (lnD), pct
1111	6.07	2.189	36.1	6.36	32.9
1112	7.23	2.437	33.7	6.82	33.8
1122	7.95	3.240	40.8	7.39	38.9
1132	8.60	2.732	31.8	8.17	31.5
1211	4.24				
1212	9.59	3.127	22.2	9.12	31.2
1221	9.37				
1232	7.30	2.303	31.5	6.96	32.2
2112	7.30	2.840	38.9	6.82	37.4
2122	7.11	2.912	40.9	7.24	37.2
2132	8.87	2.943	33.2	8.41	33.2
2212	9.25	4.270	46.2	8.41	44.8
2222	6.89	2.706	39.3	6.42	37.9
2232	4.50				

\* [C.V. = Coefficient of Variation, and < .... > denotes “mean”.]

The variability of the mean grain sizes for the different processing conditions is presented in Table 19 for the assumptions of normal grain size distributions. From the average values, it is observed that only the coiling temperature has a small effect on the variability of grain size. In order to gain a better understanding of how the processing conditions affect the final grain size, each processing parameter needs to be revised separately.

Table 19 Variability of the grain size

	<u>Processing Parameter</u>	<u>Grain Size (um)</u>	<u>Std. Dev. (um)</u>
Grain Size (um)	High RHT	7.32	1.69
	Low RHT	7.53	1.66
	High RT	7.30	2.26
	Low RT	7.57	0.89
	High FT	7.34	1.73
	Medium FT	7.83	1.12
	Low FT	7.28	1.99
	High Coil	7.69	1.41
Low Coil	6.78	2.17	

Figure 69 shows that the variation in reheating temperature has essentially no effect on the variability of the ferrite grain size. Neither the variation in roughing temperature, Figure 70, nor the variation in finishing temperature, Figure 71, appears to have a discernible effect on the grain size, since no significant pattern of dependence on processing conditions can be gleaned from those figures.

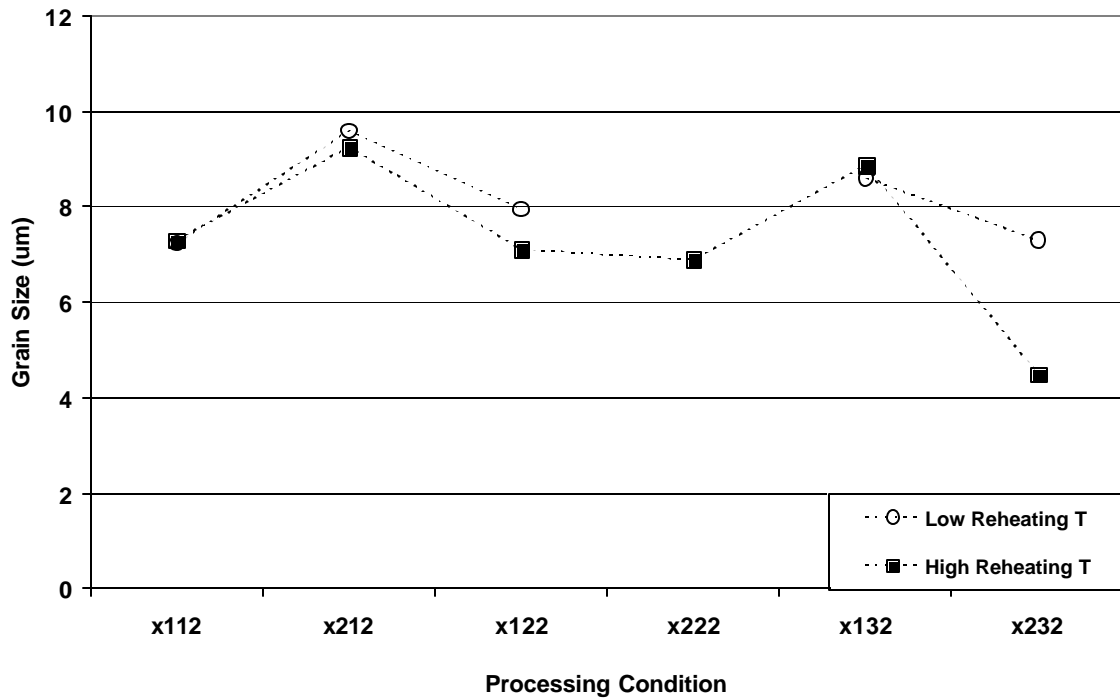


Figure 69 Variation of the grain size for different reheating temperatures

Only the variation in coiling temperature seems to have a significant impact on the variability of grain size. Figure 72 shows, for the conditions where the grain structure was sufficiently distinct to measure, that coiling at 650 C results in a larger grain size. However, for the 111X and 113X conditions, there is a difference of only 1 um in grain size. For the 121X condition, the difference in grain size between the low and high coiling temperature is considerably larger, 5.3 um.

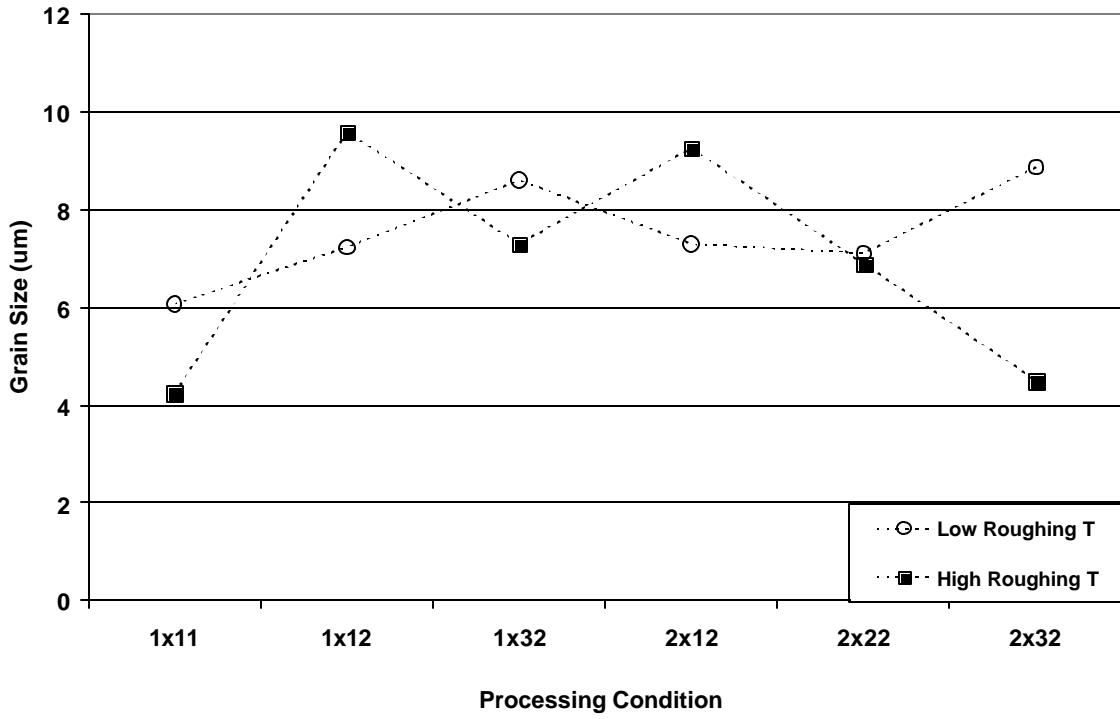


Figure 70 Variation of the grain size for different roughing temperatures

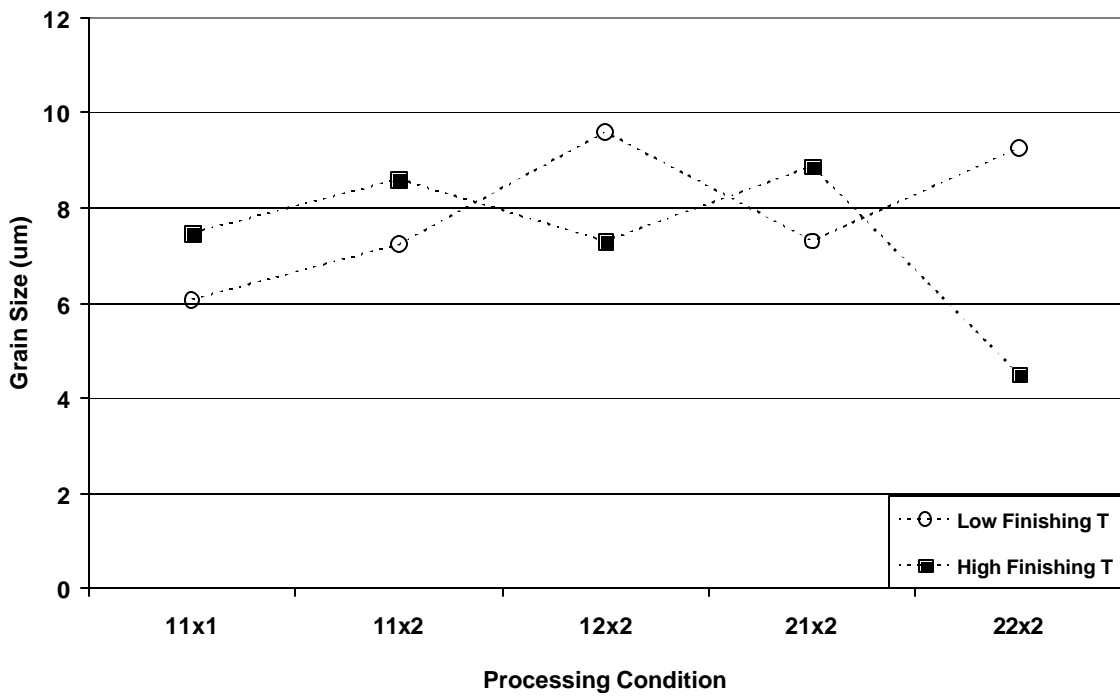


Figure 71 Variation of the grain size for different finishing temperatures

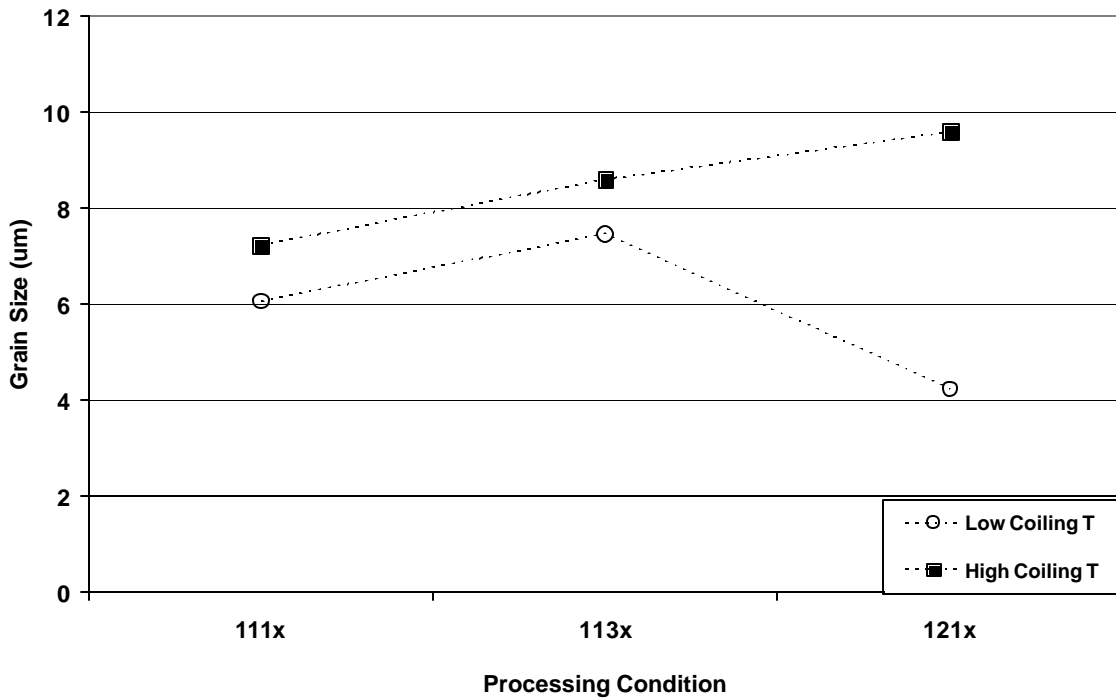


Figure 72 Variation of the grain size for different coiling temperatures

### 5.2.3 Grain Boundary Misorientation

Other features of the grain structure that may contribute to the flow stress are the grain boundary misorientation and the degree of texture or preferred orientation. To measure the grain boundary misorientation, the Electron Back Scattering Diffraction technique was used. Of interest is the fraction of the boundaries present as a “low-angle” component. This fraction was estimated by finding the area under the “low-angle” peak, and the resulting estimates are given in Table 20.

Table 20 Grain boundary misorientation

Condition	Mean Angle, Deg.	Fraction of Low Angle Boundaries Pct
Random	41.17	0.0
1111	40.57	15.1
1112	40.58	11.4
1132	41.35	11.1
1211	32.71	33
1212	41.94	7.4
1221	37.33	23.5
1232	39.56	16.3
2111	38.05	20.5
2112	36.07	24.5
2122	40.50	11.9
2131	41.03	11.8
2212	40.76	10.5
2221	37.04	25.5
2222	39.93	13.2
2231	40.71	16.2
2232	37.66	21.9
As-Cast	25.89	

Four samples reheated at the low temperature (1200 C) and roughed at the high temperature (1150 C), but with extreme levels of finishing and coiling temperatures, that is: 1211,1231,1212,and 1232 processing conditions, were analyzed, and the results are given in Figure 73. Three peaks are present in the frequency distribution curves, associated with low angle boundaries at about 10 degrees, medium angles at about 35

degrees, and high angle boundaries at about 55 degrees. Indicative of a structure with a highly dislocated substructure is a high 10 deg. peak, and also a high 35 deg. peak.

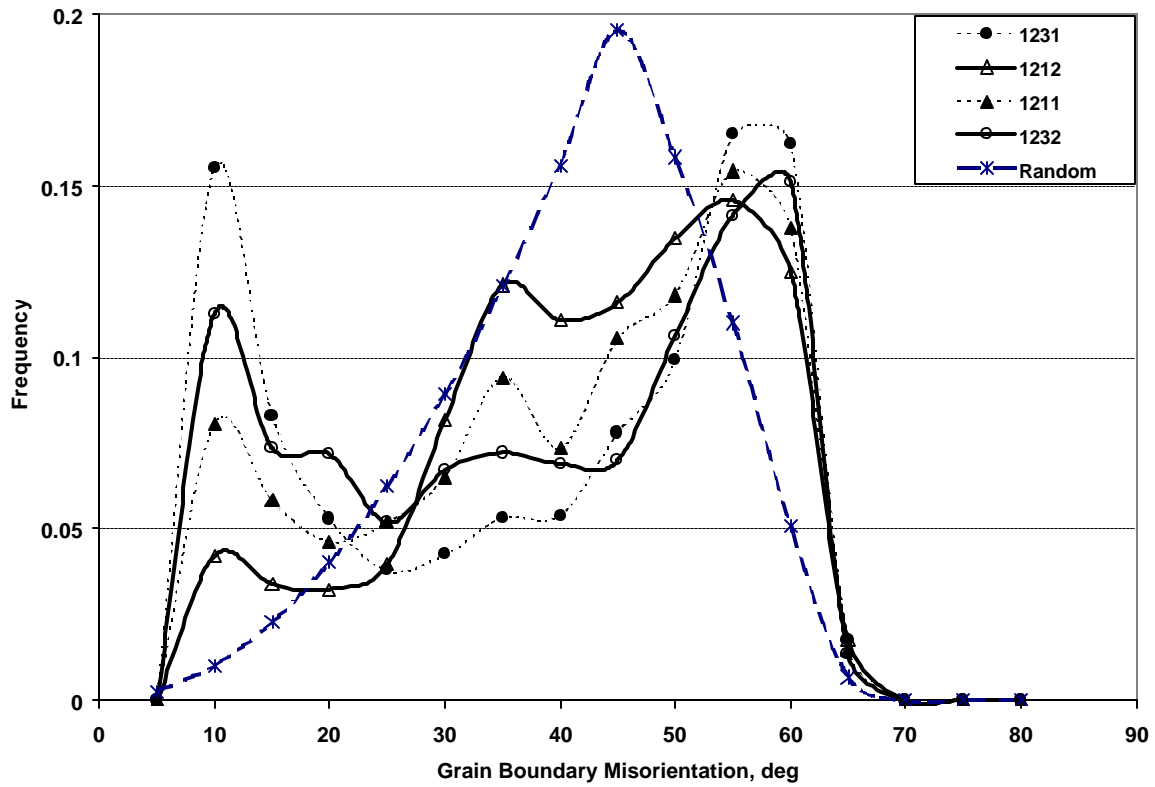


Figure 73 Frequency distribution of the grain boundary misorientation for four extreme conditions of finishing and coiling temperatures

Therefore, it becomes clear that high finishing temperatures and low coiling temperatures contribute to form a larger amount of substructure, as observed in Figure 74, where the average LAGB area fraction below 15 degrees misorientation, is shown for the different processing conditions.

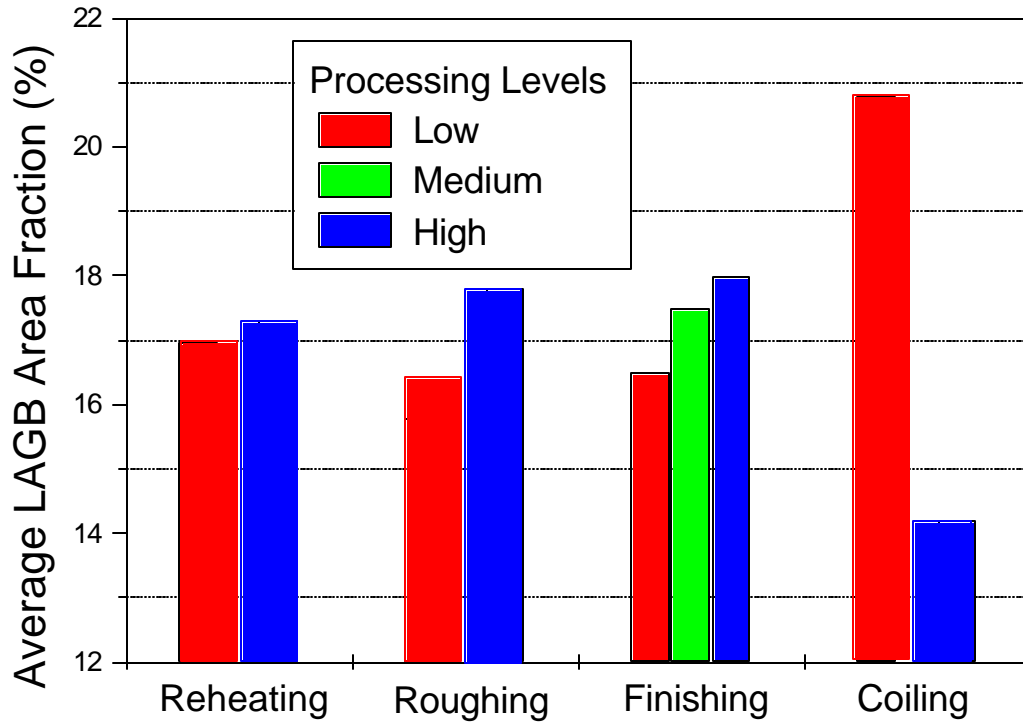


Figure 74 Average LAGB area fractions below 15 degrees misorientation, for the different processing conditions

#### 5.2.4 Dislocation Density

There is a very clear relation between processing and the resulting ferrite dislocation density. The variation of both finishing and coiling temperatures results in a large variability in dislocation density. On the other hand, different levels of reheating and roughing temperatures do not result in any significant variability. Table 21 lists the dislocation densities of various processing conditions; in Table 22, the mean dislocation density is shown for the different processing parameters. It becomes evident that the largest variability in dislocation density is due to variation in coiling temperature, where a low coiling temperature results in a large dislocation density value. Similarly, high finishing temperature conditions result in large contributions to dislocation density.

Table 21 Dislocation densities for various individual processing conditions

Processing Condition	Dislocation Density (E10 cm <sup>-2</sup> )
1211	3.55
1212	0.844
1231	5.6
1232	1.845
2111	3.72
2112	0.634
2131	4.72
2132	2.74
2212	0.76
2231	3.86
2232	0.92

Table 22 Average dislocation densities for the different processing parameters

	<u>Processing Parameter</u>	Dislocation Density (E10cm <sup>-2</sup> )	Std. Deviation (E10cm <sup>-2</sup> )
Dislocation Density (E10cm <sup>-2</sup> )	High RHT	1.84	1.74
	Low RHT	2.95	2.08
	High RT	1.84	1.74
	Low RT	2.95	1.74
	High FT	3.28	1.77
	Low FT	1.90	1.58
	High Coil	1.29	0.83
	Low Coil	4.29	0.86

Figures 75 and 76 show the effect of coiling and finishing temperature, respectively. In Figure 75, the largest variation comes from the 211X processing condition, where coiling at 650 C results in a dislocation density of 6.3E9 cm<sup>-2</sup>, whereas coiling at 550 C increases the dislocation density to a value as high as 3.72E10 cm<sup>-2</sup>. In a similar fashion, in Figure 76, the 21x2 condition gives the largest variability; i.e., finishing at 900 C only results in 6.3E9, whereas finishing at 1000 C raises the value to 2.7E10cm<sup>-2</sup>.

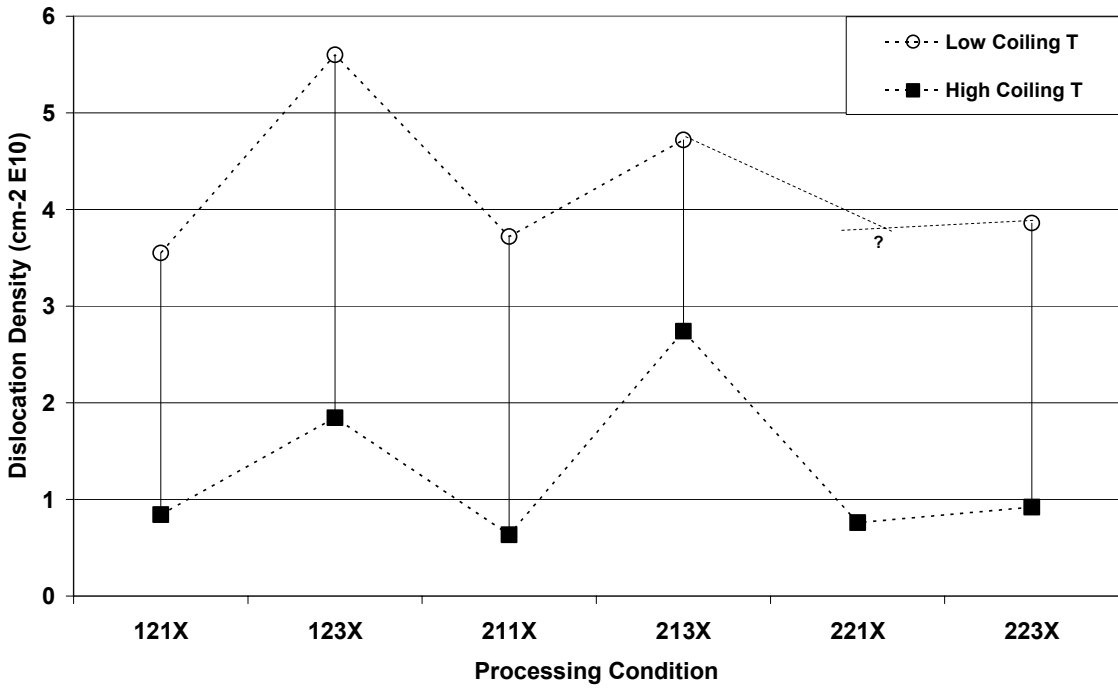


Figure 75 Effect of coiling temperature on dislocation density, for various processing conditions

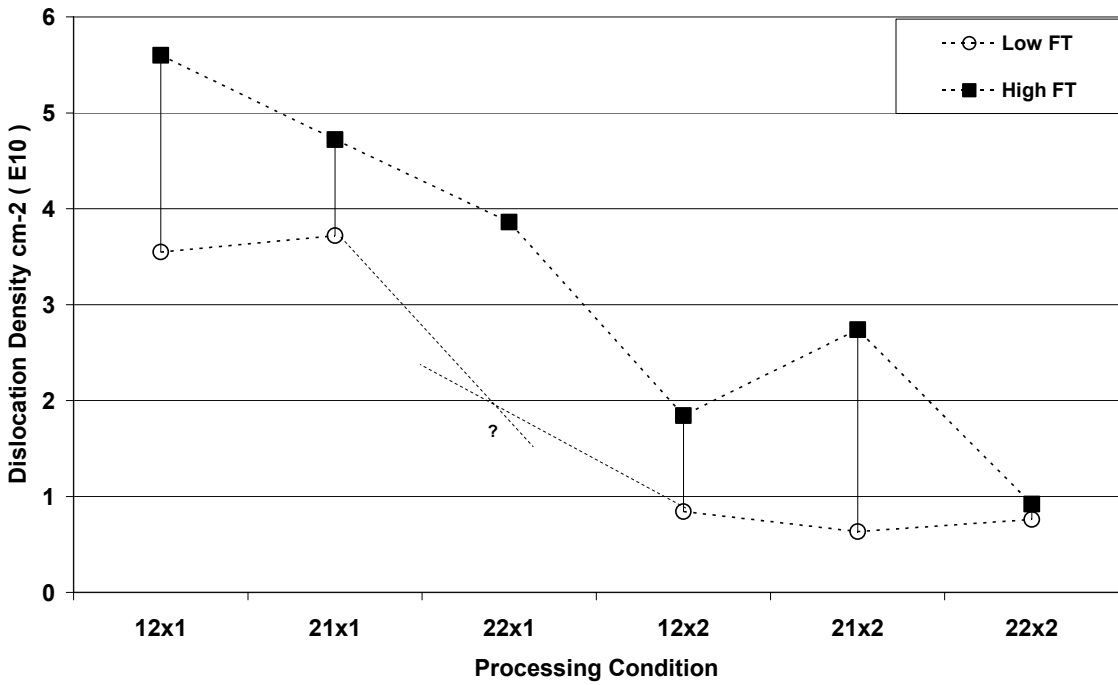


Figure 76 Effect of finishing temperature on dislocation density, for various processing conditions

### 5.2.5 Precipitation

The results of TEM examination indicated the absence of precipitates in most of the hot band samples. However, Atom Probe Ion Field Microscopy (APFIM) revealed a high density of clusters in samples coiled at the high temperature condition, 650 C. These clusters measure about 1-2 nm in diameter, and their nature is Nb,V(C, N).

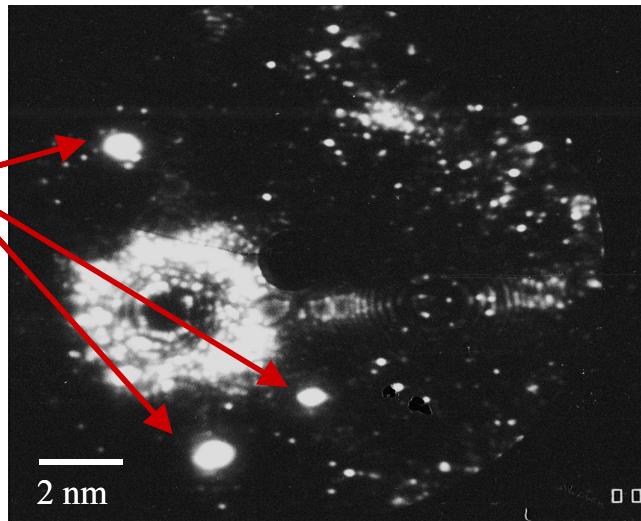
In general, samples coiled at 550 C resulted in no precipitate or cluster formation, while those samples coiled at 650 C revealed a high density of solute clusters when observed in the APFIM. Figure 77 shows APFIM images depicting the presence of clusters at the high coiling temperature conditions. At the low coiling temperature conditions, no clusters were observed.

A character plot is usually used to represent the nature of the precipitates that are found in the APFIM. By means of an ion-by-ion evaporation, the nature of these small particles was obtained, and the collected ions are represented as a character plot, which is shown in Figure 78. In Figure 79 the amount of each element found in two different clusters is shown.

**1132**

Pre-precipitation  
Stage

Nb,V(C,N)  
Clusters are  
shown here

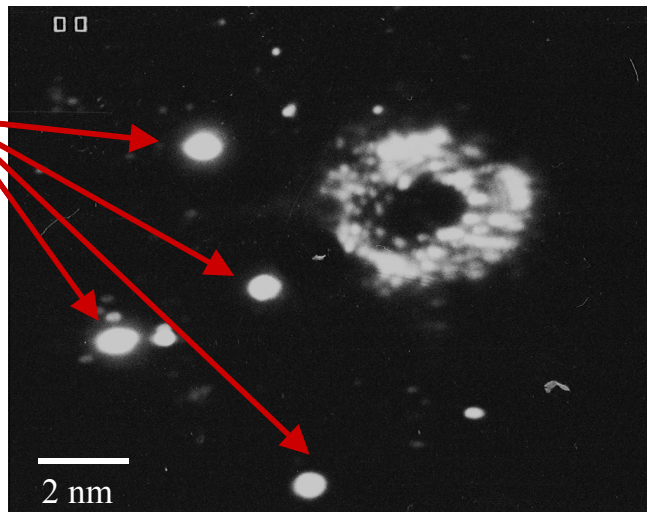


(a)

**2132**

Pre-precipitation  
stage

Nb,V(C,N)  
Clusters are  
shown here.



(b)

Figure 77 Presence of Nb,V(C,N) clusters in the samples coiled at 650 C (a) 1132 processing condition and (b) 2132 processing condition

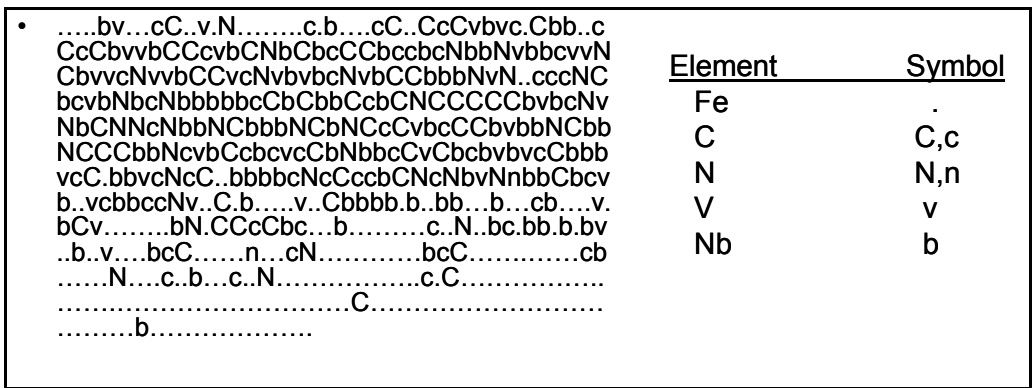


Figure 78 Character Plot from a small cluster, APFIM analysis

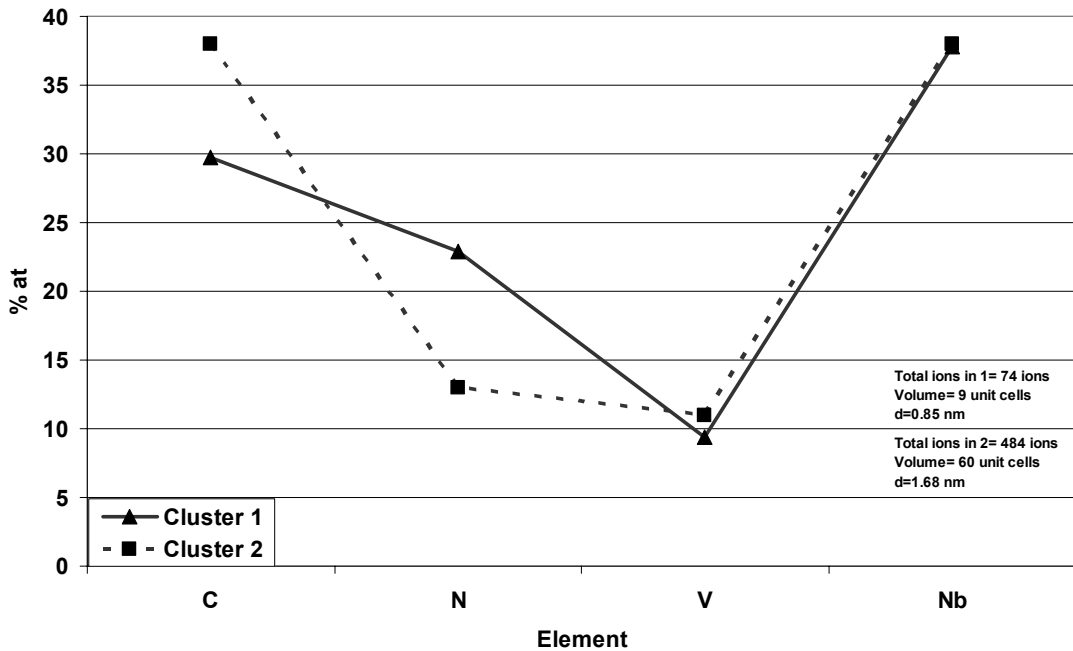


Figure 79 Composition and atomic percent of elements found in two clusters

### 5.3 Cooling Rate Experiment

#### 5.3.1 Effect of Variation of Cooling Rate on Hardness

The variation of cooling rates from the finishing temperature to the coiling temperature (FT to CT), and from the coiling temperature to the room temperature (CT to RT), and its effect on hardness, was evaluated, and the results are shown in Table 23.

Table 23 Hardness values for the different cooling rates from the finishing to coiling temperature, and coiling to room temperature at different coiling temperatures

Cooling Rate CT to RT	1 C/sec		0.1 C/sec		0.01 C/sec	
Cooling Rate FT to CT	5 C/sec	10 C/sec	5 C/sec	10 C/sec	5 C/sec	10 C/sec
CT ( C )						
550	203	191	197	195	202	216
600	205	210	218	208	279	225
700	210	213	207	193	188	204

The effect of coiling temperature and cooling rates, from the coiling temperature to room temperature (CT to RT), for a fixed cooling rate from the finishing pass to coiling temperature (FT to CT) of 5 C/sec, is shown in Figure 80 for Rouge steel. The variation of coiling temperature, at the fastest cooling rate, 1 C/sec, results in a very small variation of hardness. At 700 C, a maximum value of 210 is obtained, while at 550 C, it is 203. At the medium cooling

rate, 0.1 C/sec, the effect of coiling temperature results in a larger variability, where a peak in hardness can be appreciated, where the highest value, 218, is obtained at a coiling temperature of 600 C.

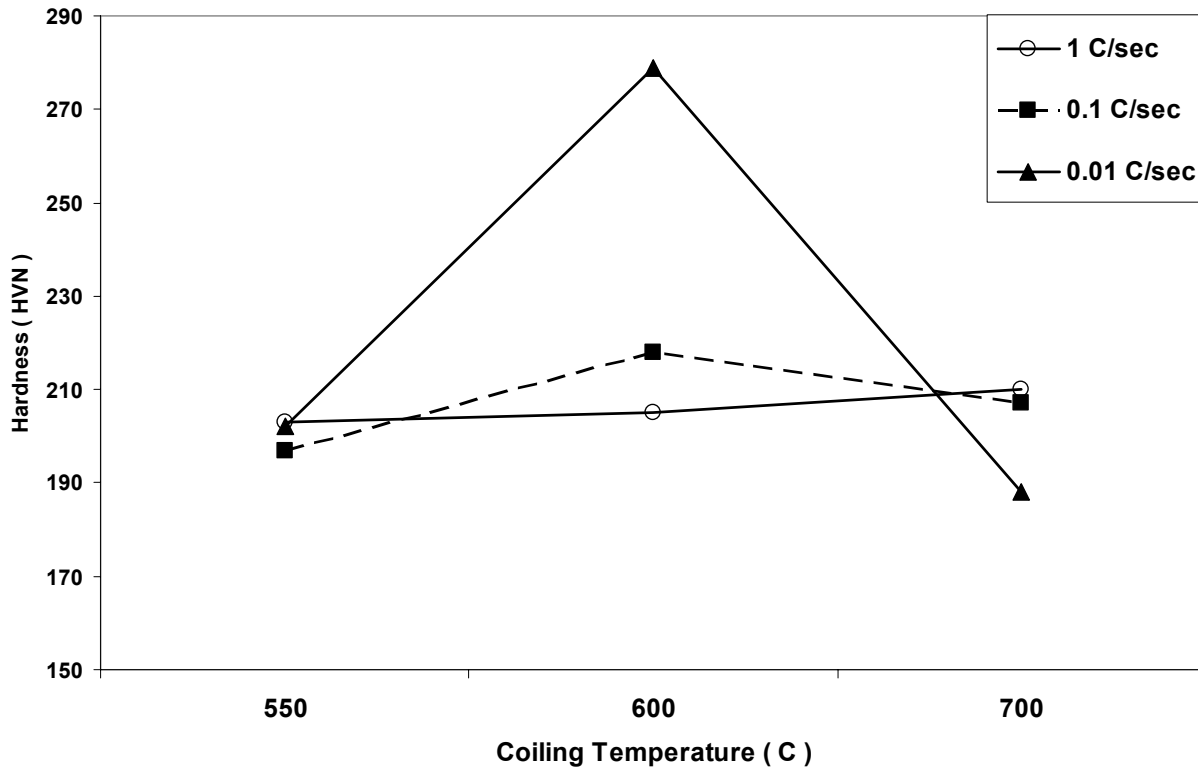


Figure 80 The effect of coiling temperature and cooling rate from the coiling temperature to room temperature (CT to RT), for a fixed cooling rate from the finishing pass to coiling temperature (FT to CT) of 5 C/sec

At the slowest cooling rate, 0.01 C/sec, the effect of coiling temperature proved to be very significant, and a peak in hardness at 600 C is observed. At 700 C, hardness decreased 22 VHN from the value obtained at the fastest cooling rate. However, at 600 C, hardness increased by 74 VHN from the value obtained at the fastest cooling rate. No effect in hardness is seen for the 550 C coiling temperature. Thus, it is evident that variation in cooling rates is not significant

when a 550 C coiling temperature is used. On the other hand, coiling at 600 C is very sensitive to variation in cooling rates.

The effect of increasing the cooling rate through the transformation temperature (FT to CT), from 5 C/sec to 10 C/sec, is observed in Figure 81. Figure 82 shows the comparison of the hardness values at the two cooling rates from the finishing to coiling temperatures.

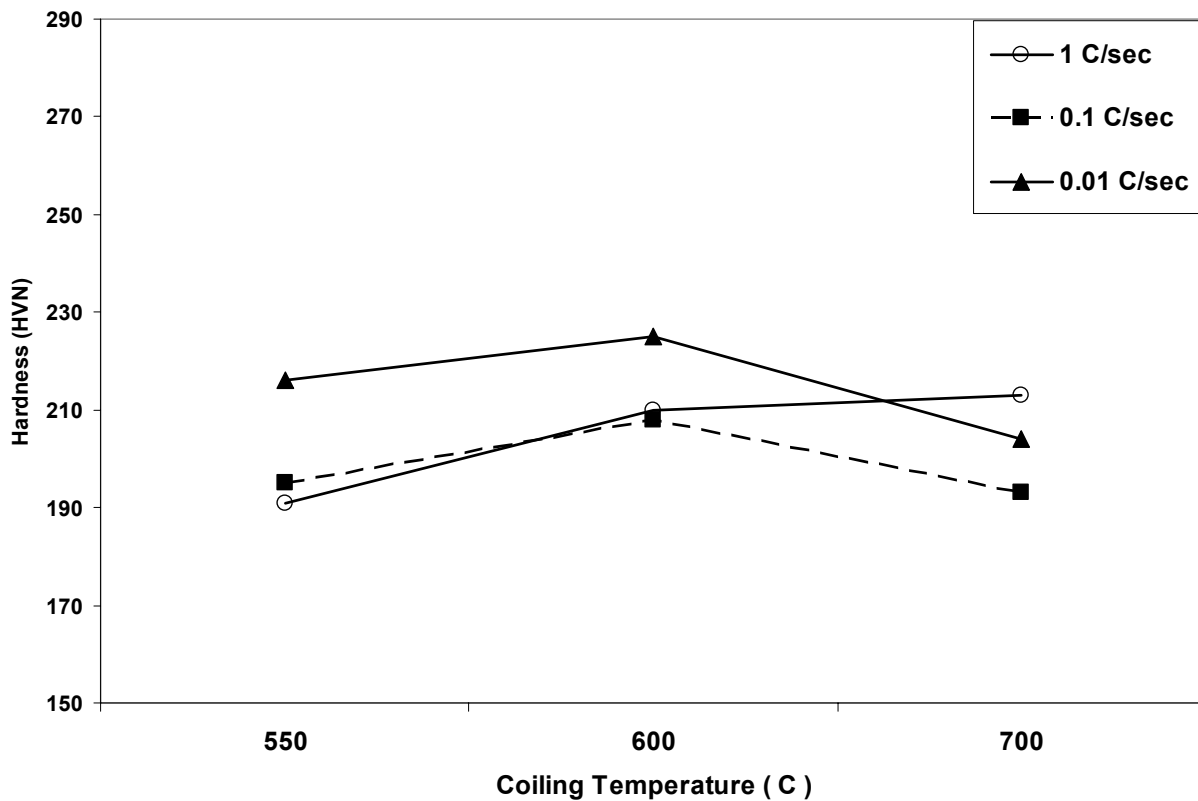


Figure 81 The effect of coiling temperature and cooling rate from the coiling temperature to room temperature (CT to RT), for a fixed cooling rate from the finishing pass to coiling temperature (FT to CT) of 10 C/sec

At the fastest cooling rate from coiling to room temperature, 1 C/sec, no significant variation in hardness was observed at the different coiling temperatures when the cooling rate through the transformation was increased from 5 to 10 C/sec.

At the medium cooling rate, 0.1 C/sec, the effect of increasing the cooling rate through the transformation temperature becomes more significant for the different levels of coiling temperature, and a small peak in hardness at 600 C is again observed. At 700 C and 600 C, there is a decrease of 10 and 15 VHN, respectively, from those values obtained at the cooling rate of 5 C/sec FT to CT. No significant variation is present in the 550 C coiling.

At the slowest cooling rate from CT to RT, 0.01 C/sec, the effect of increasing the cooling rate from FT to CT to 10 C/sec, at the different levels of coiling temperature results in a very different behavior than those cooled at the slow 5 C/sec cooling rate from FT to CT. At 700 C and 550 C, an increase of 15 VHN is observed. Coiling at 600 C, on the other hand, produces a significant loss of 55 VHN. Hence, the control of the cooling rate from the finishing to coiling temperature is very important.

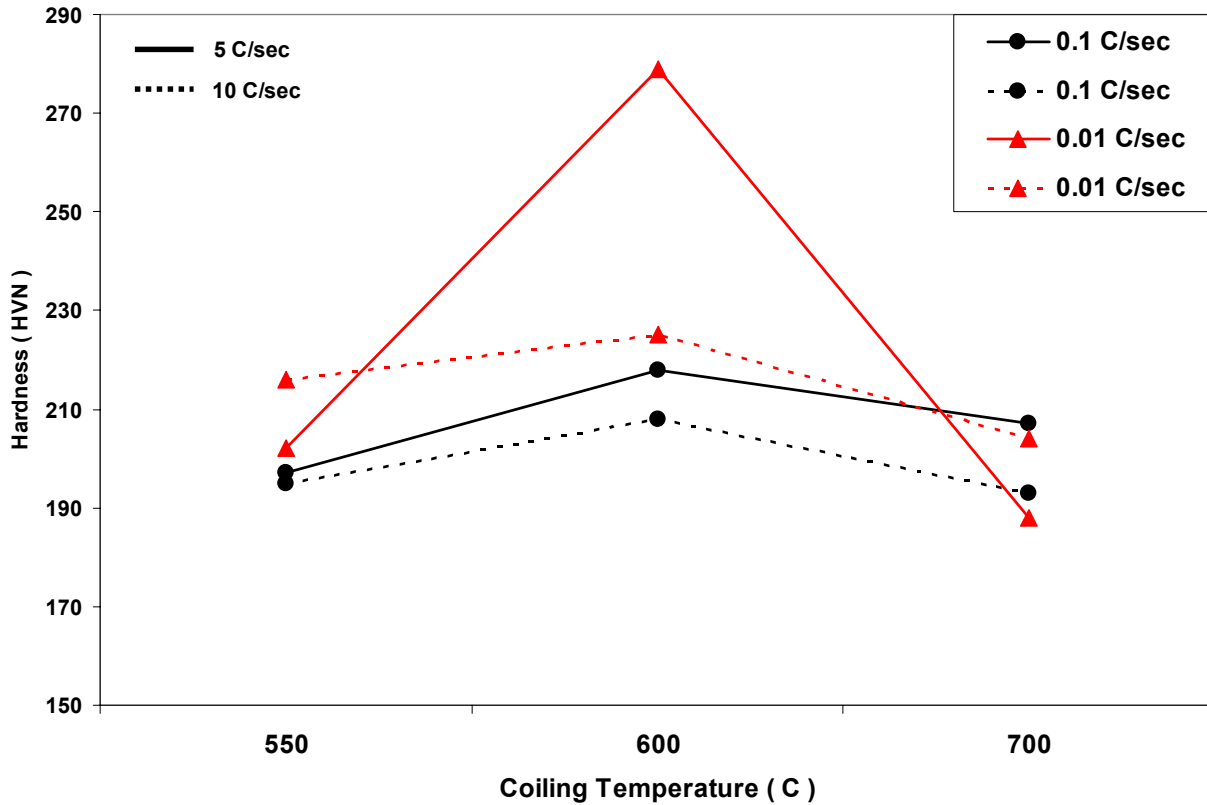


Figure 82 The effect of increasing the cooling rate through the transformation temperature is shown as a comparison of the hardness values obtained at both 5 C/sec and 10 C/sec, for different coiling temperatures and varying cooling rates from the coiling to room temperature

### 5.3.2 Effect of Cooling Rate on Microstructure

The effect of variation of cooling rate from the FT to CT at the 3 different coiling temperatures, and the cooling rate from CT to RT, is shown in Table 24. The estimated percentage of each microstructural feature is qualitatively described in consecutive order, from left to right, whereas the components in parenthesis mean a percent in the order of 5-10 %. Based on the different microstructures obtained, a CCT curve was developed for Rouge Steel, Figure 83. The microstructures observed for the different cooling rates and coiling temperature conditions are presented in Appendix C.

Table 24 Microstructural components in Rouge steel

	5 C/sec (FT to CT)	10 C/sec (FT to CT)
700 C, 1 C/sec*	P, UB, (NP, A)**	P, UB (NP, A)
700 C, 0.1 C/sec	P, (NP)	P, (NP)
700 C, 0.01 C/sec	P	P, (NP)
600 C, 1 C/sec	UB, NP, LB, (A)	LB+UB, A, (NP)
600 C, 0.1 C/sec	NP, A, (UB)	A, NP, (LB, UB)
600 C, 0.01 C/sec	NP, A, (P)	A, NP
550 C, 1 C/sec	LB, A, (NP)	UB+LB, (A)
550 C, 0.1 C/sec		UB, (LB, A, NP)
550 C, 0.01 C/sec	A, LB, (NP, UB)	A, NP, (LB)

\* Coiling temperature and cooling rate from CT to RT, respectively.

\*\* P=Polygonal ferrite, NP=Non-polygonal ferrite, A=Acicular ferrite, UB=Upper bainite, LB=Lower bainite

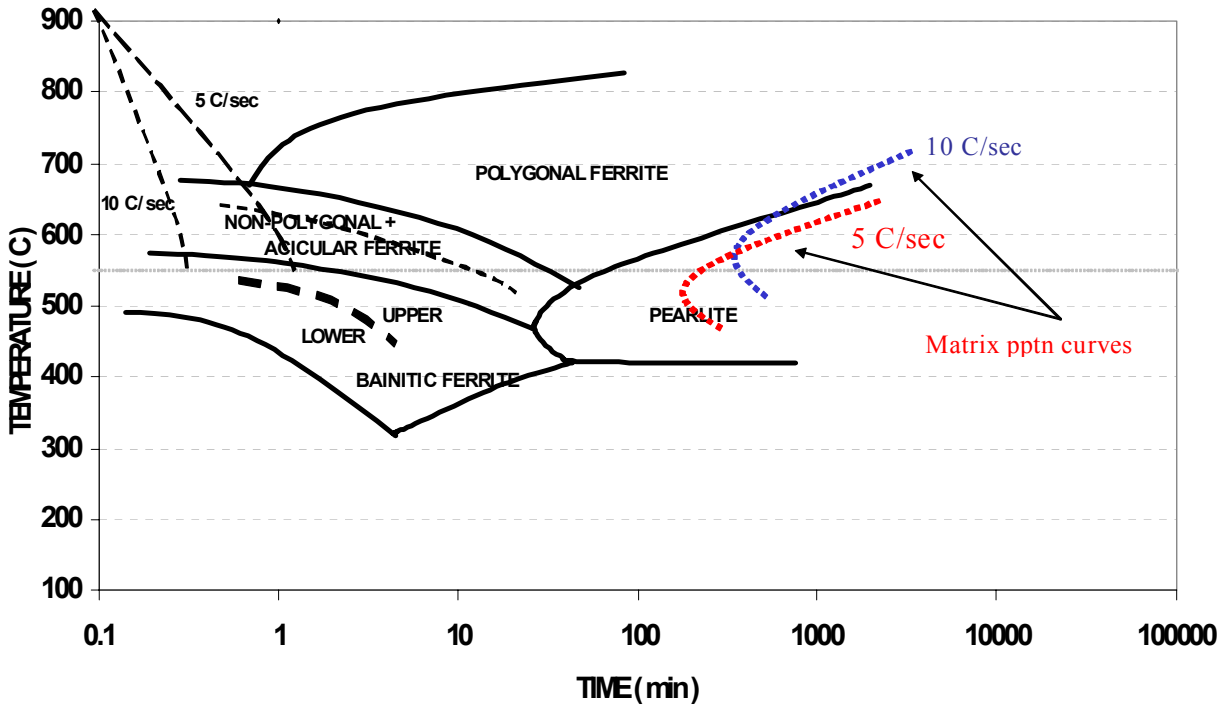


Figure 83 CCT diagram constructed from the different microstructures observed at the various cooling conditions

**5.3.2.1 Grain Size.** Depending on the coiling temperature and cooling rates, different grain sizes are developed. From Figure 84, it can be seen that grain size increases with increasing coiling temperature and also, some grain growth occurs from the 1 C/sec to the 0.01 C/sec cooling rate.

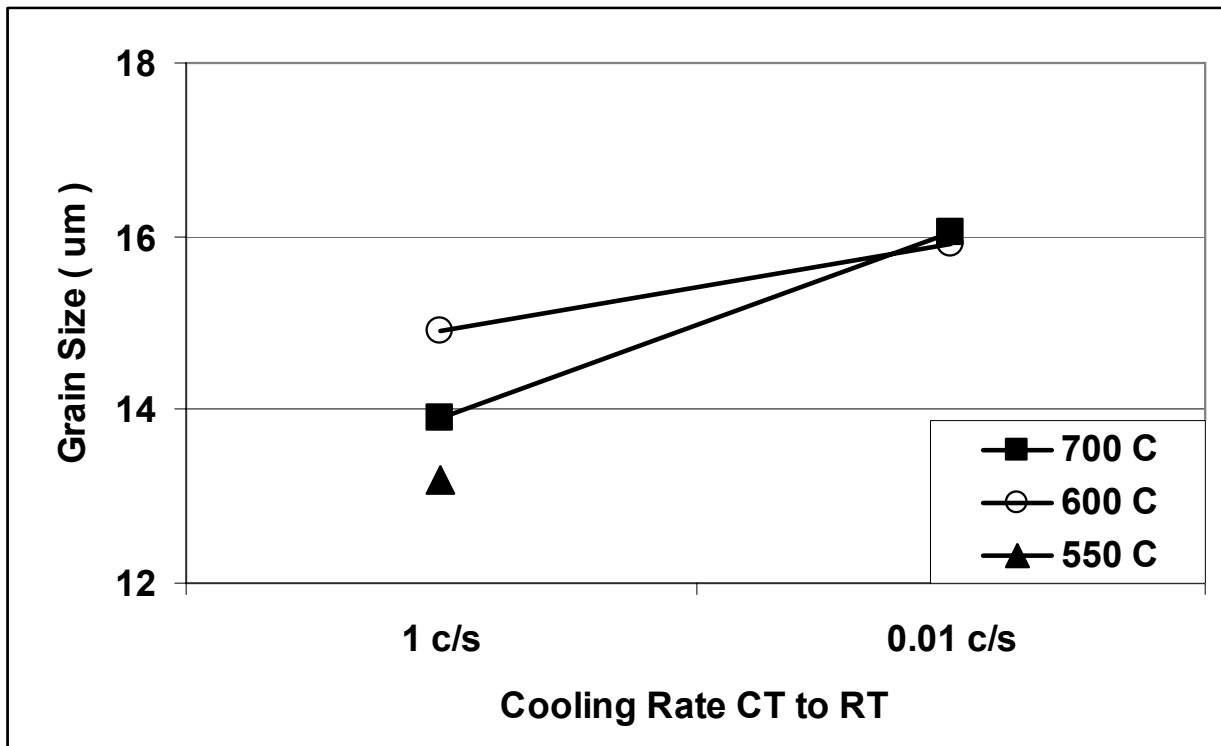


Figure 84 Variation in grain size for different coiling temperature and cooling conditions

**5.3.2.2 Precipitation.** TEM analysis shows that small precipitates are present in the samples that were cooled at 0.01 C/sec from the coiling temperatures of 600 C and 700 C. The particle size distributions are shown in Figure 85 for both coiling temperatures. For a 5 C/sec cooling rate from FT to CT, and coiling at 700 C, the average particle size is 10 nm, whereas when coiling at 600 C, the average particle size is 3 nm. Table 25 contains the particle analysis for samples coiled at 600 and 700 C, at a 0.01 C/sec cooling rate from CT to RT, and 5 C/sec from FT to CT.

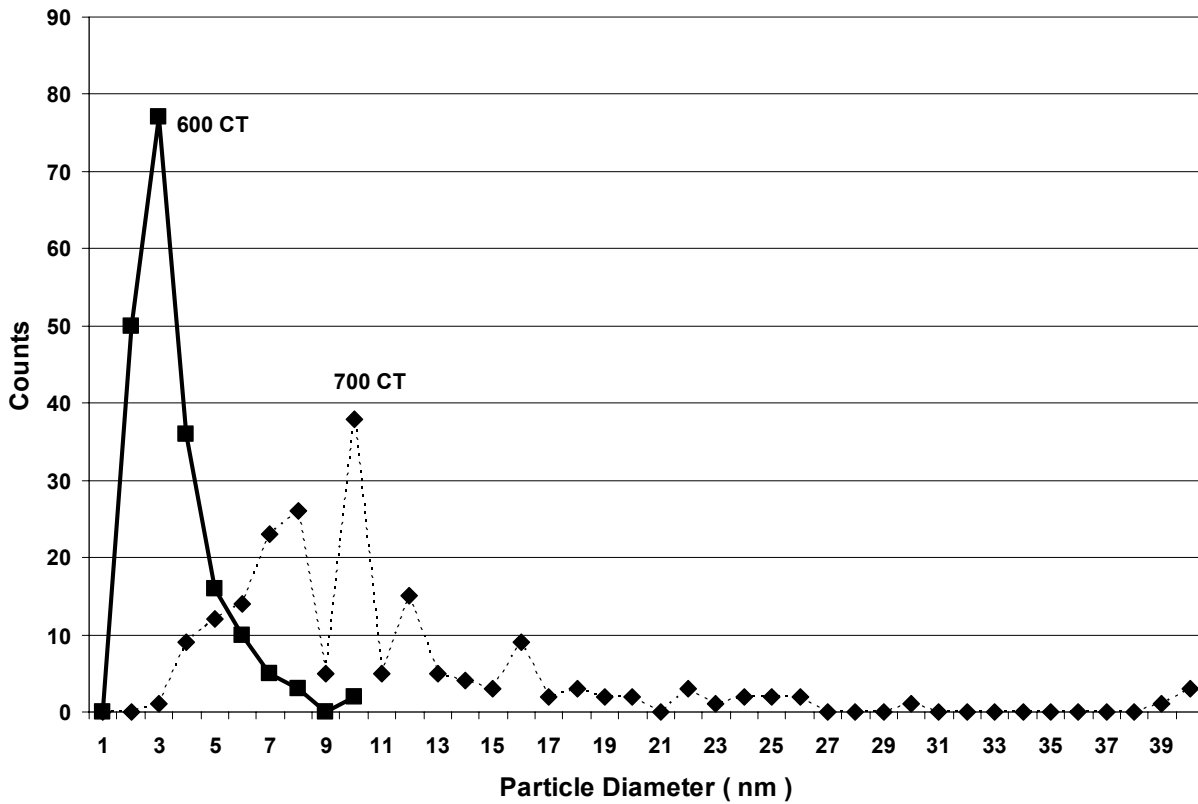


Figure 85 Particle size distribution for the 600 C and 700 C coiling temperatures, at a 0.01 C/sec cooling rate from CT to RT, and 5 C/sec from FT to CT

Using the modified Orowan-Ashby relation, the mean particle size and volume fraction at both coiling temperatures result in the same contribution to strengthening, that is, 40 MPa. However, the difference in hardness can be explained from the fact that at 600 C, the grain size is smaller, the dislocation density is greater, and also, most important, the formation of fine clusters in the sample coiled at 600 C. This cluster formation was verified using APFIM analysis, and a high density of small clusters, with a mean size of 1 nm was observed.

Table 25 TEM particle analysis for different coiling temperatures, with a 5 C/s cooling rate from FT to CT, and 0.01 C/s from CT to RT

Coiling Temp ( C )	Avg. Particle Size ( nm )	Total number of particles	Volume Fraction	Precipitation Strengthening (MPa)
700	10	196	3.69E-4	39.8 MPa
600	3	199	9.63E-5	40.6 MPa
550	none	none	none	none

Faster cooling rates, from the FT to CT, and from CT to RT, result in a suppression of precipitation. However, coiling at 600 C, cooling at 10 C/sec from FT to CT, and cooling only at 0.01 C/sec from CT to RT, a small peak in hardness is observed. APFIM shows a low density of clusters. This results in a low cluster volume fraction and, hence, in a smaller contribution to strengthening.

## 6.0 DISCUSSION

### 6.1 Microstructure Analysis

#### 2.1.1 Types of Ferrite

The different processing stages can have a strong effect on the microstructure development, which has a direct relationship to the final mechanical properties. Since the hot band microstructure is the vital link between hot mill processing and mechanical properties, a careful analysis of this microstructure was considered essential. Five types of phases/microconstituents were found in the simulated hot band processed in these experiments. They are polygonal ferrite ( $F_P$ ), non-polygonal ferrite ( $F_N$ ), bainitic ferrite ( $F_B$ ), pearlite (P) and carbon-rich microconstituents, i.e., grain boundary cementite (C), as shown in Figure 86<sup>(80)</sup>.

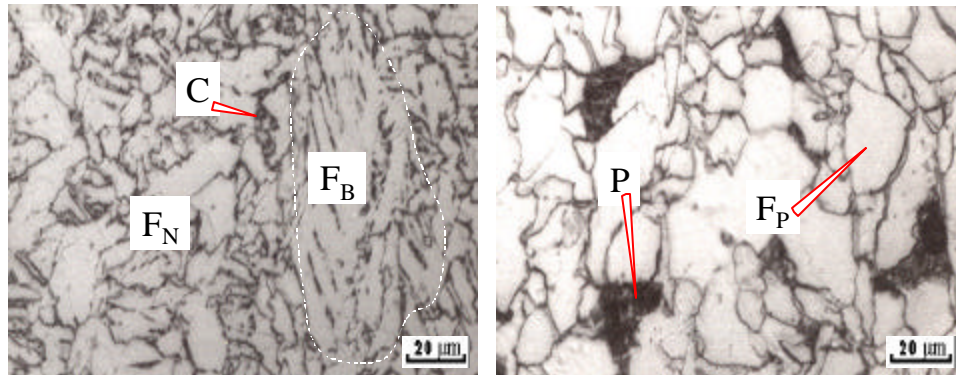


Figure 86 Typical phases in the hot band of the 70 ksi Rouge steel.

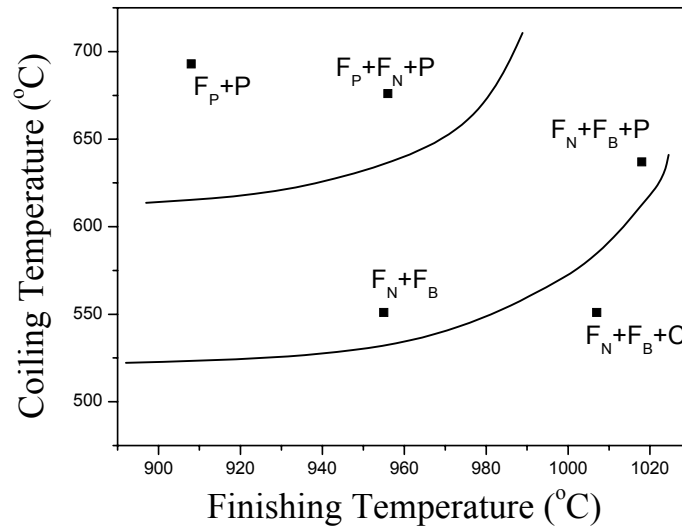


Figure 87 Microstructure evolution based on finishing and coiling temperatures

The final microstructure of each hot band is a combination of these five phases/microconstituents and the way they are combined is dependent on the processing path employed. Even though there is no significant variation in the final grain size, the evolution of the microstructure is more sensitive to variations in finishing ( $T_F$ ) and coiling ( $T_C$ ) temperatures than to reheating ( $T_{RH}$ ) and roughing ( $T_R$ ) temperatures. Figure 87 illustrates a microstructure evolution map that has been constructed<sup>(82)</sup>. Polygonal ferrite and pearlite are the dominant phases at the upper left corner, which has a low  $T_F$ , around 900°C and a high  $T_C$ , around 700°C. When  $T_F$  is increased and/or  $T_C$  is decreased,  $F_N$  will be formed and its volume fraction keeps increasing with less  $F_P$  being detected. Further changing  $T_F$  and  $T_C$  in this way will lead to the formation of  $F_B$  along with a decrease in the volume fraction of pearlite. At the lower right corner of Figure 87, which has a high  $T_F$  around 1000°C and a low  $T_C$  around 550°C, no significant amount of pearlite is detected and the carbon-rich microconstituents are found.

### 6.1.2 LAGB's

Another feature of the grain structure that may contribute to unexpected changes in the flow stress is the grain boundary misorientation. The Electron Back Scattering Diffraction (EBSD) technique was used to measure the grain boundary misorientation. The effect of the coiling temperature on the observed low angle grain boundary (LAGB) distribution is shown in Figure 88 as well as the theoretical distribution of grain boundary misorientation in a randomly oriented polycrystal.

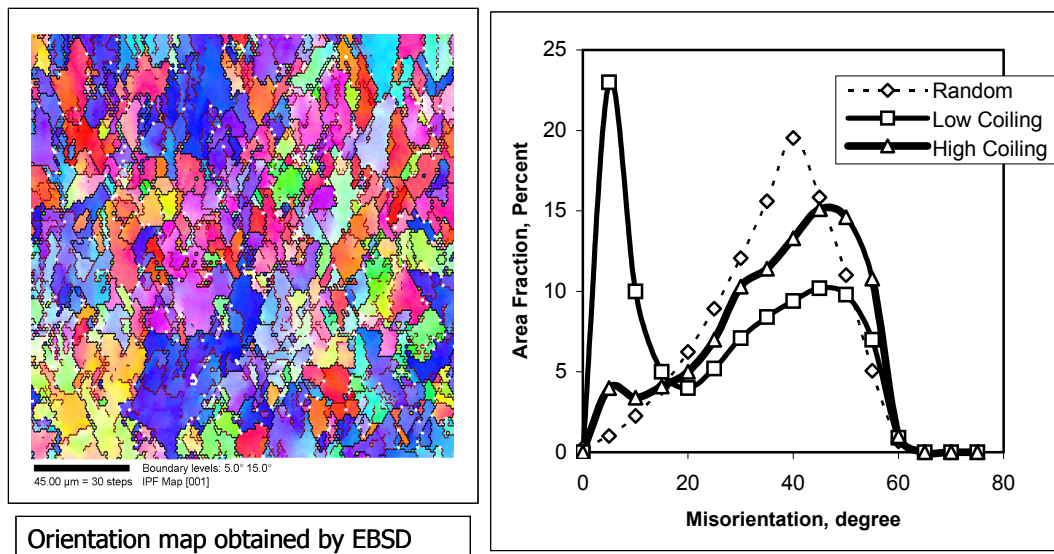


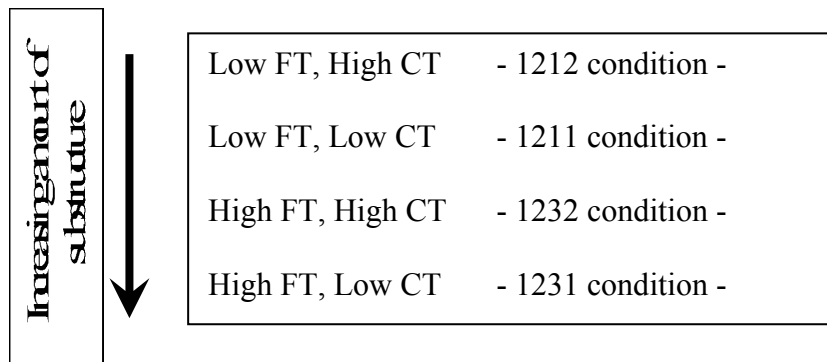
Figure 88 Orientation map obtained by EBSD and the effect of coiling temperature on low angle grain boundary distribution.

From comparison of the two distribution curves in Figure 88, it can be observed that for some processing conditions the measured distribution of the boundary misorientation may shift away from that of the random distribution. One point of interest then is the fraction of the boundaries represented by "low-angle" character. This fraction was estimated by measuring the

area under the “low-angle” peak. It is found that lower coiling temperatures lead to a much higher area fraction of the low angle grain boundary than did higher coiling temperatures. A larger effect is observed when varying the finishing temperature. Considering the microstructure evolution map in Figure 64 and 87, more LAGBs are found with increasing amounts of non-polygonal and bainitic ferrite. Both this variation in LAGB and the differences in the ferrite microstructure could cause variations in the final mechanical properties.

The amount of LAGB’s increases at high finishing temperatures and low coiling temperatures and it is minimum at the high coiling and low finishing temperatures.

The shift in the amount of LAGB’s can be interpreted as:



Although the shift in the grain boundary misorientation does correspond in a general fashion to the trend in the measured dislocation densities reported in Table 21 and 22, it should be noted that TEM analysis failed to reveal actual sub-grain structures for conditions 1212 and 1232 (Table 26).

Table 26 Relation between dislocation density and observed subgrain structure

Processing Condition	<u>Dislocation Density, E+10/cm<sup>2</sup></u>	<u>Sub-grain Structure</u>
Low FT, High CT (1212)	0.84	No
Low FT, Low CT (1211)	3.55	Yes
High FT, High CT (1232)	1.85	No
High FT, Low CT (1231)	5.60	Yes

### 6.1.3 Dislocation Density

The different processing conditions result in a large variation in the contributions from the different strengthening mechanisms. The effect of varying the processing conditions on the dislocation strengthening is shown in Figure 89. High finishing temperatures and low coiling temperatures result in a large strengthening from dislocation density, whereas the dislocation strengthening contribution at low finishing temperatures and high coiling temperatures is not very large.

Similar dislocation densities have been reported earlier by Honeycombe<sup>(83)</sup> and Thillou<sup>(84)</sup>, and closely agree with the values obtained in this work, as shown in Figure 90.

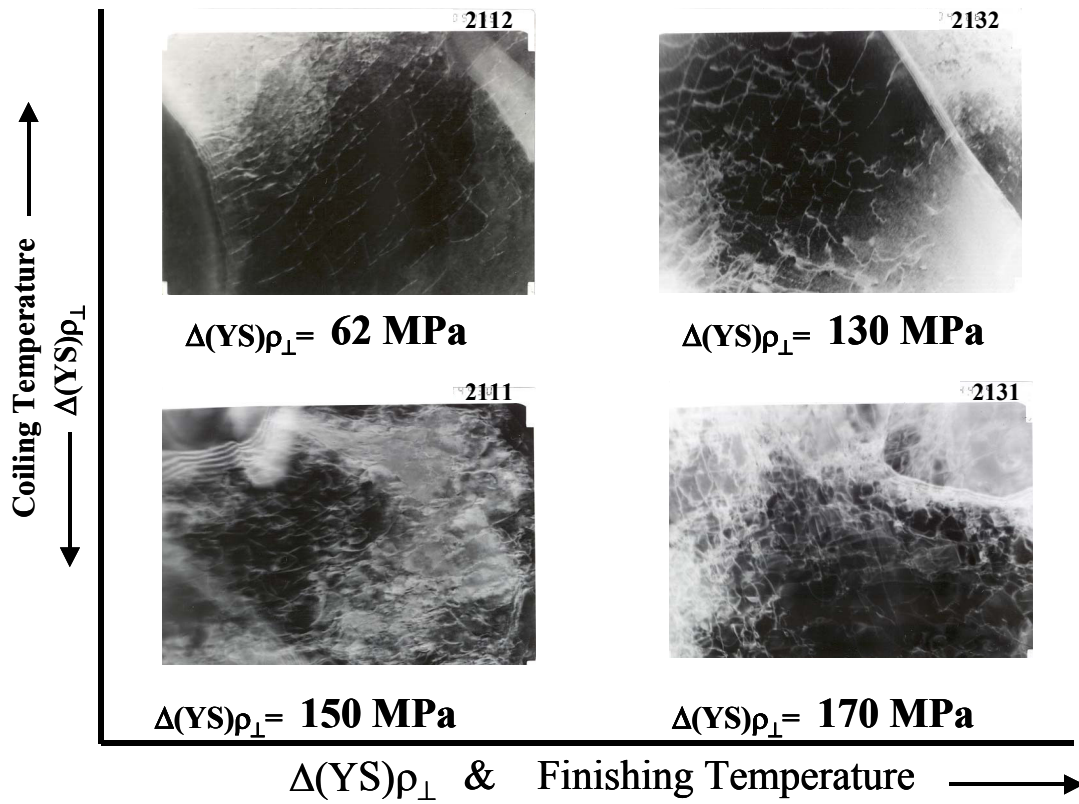


Figure 89 Effect of processing conditions on dislocation strengthening

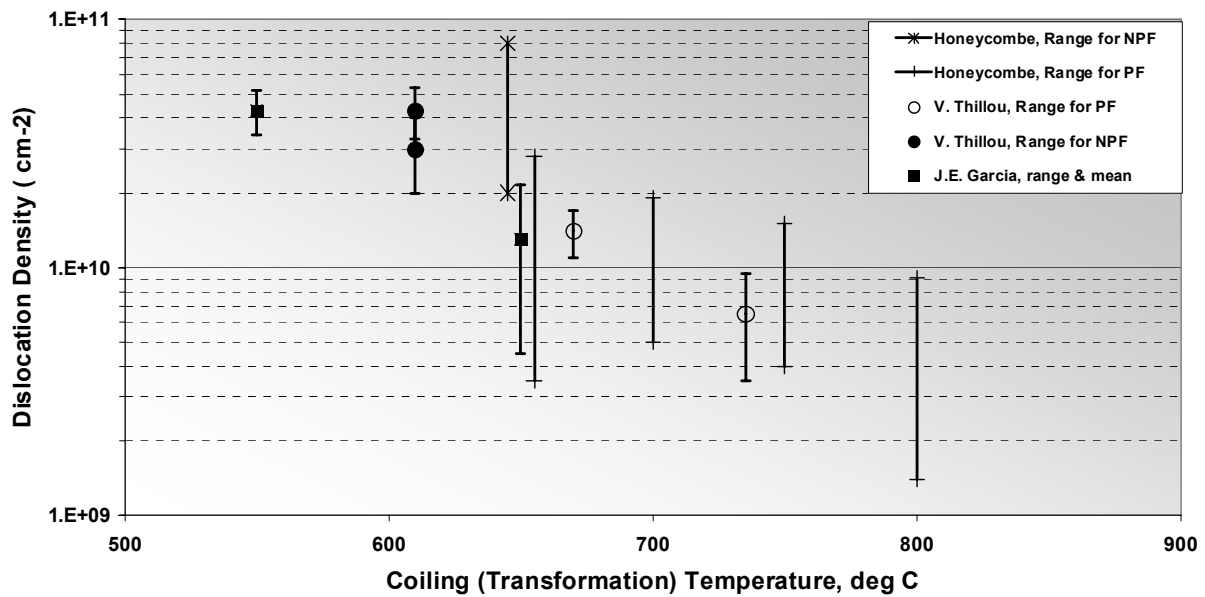


Figure 90 Range of dislocation densities as a function of coiling temperature

### 6.1.4 Precipitation

Similarly, different combinations in the processing conditions can affect precipitation hardening. While TEM analysis failed to reveal any significant precipitation, APFIM analysis showed that a high density of small particles, or “clusters”, with a size of 1-2 nm, are present in some processing conditions. These small clusters were observed in those conditions where a high coiling temperature, 650 C, was used, and no clusters were observed in the samples processed with the same rolling conditions, and coiled at 550 C, Figure 91. Therefore, precipitation strengthening can become an important strengthening mechanism for certain processing and coiling conditions, while for other processing conditions, precipitation hardening does not occur.

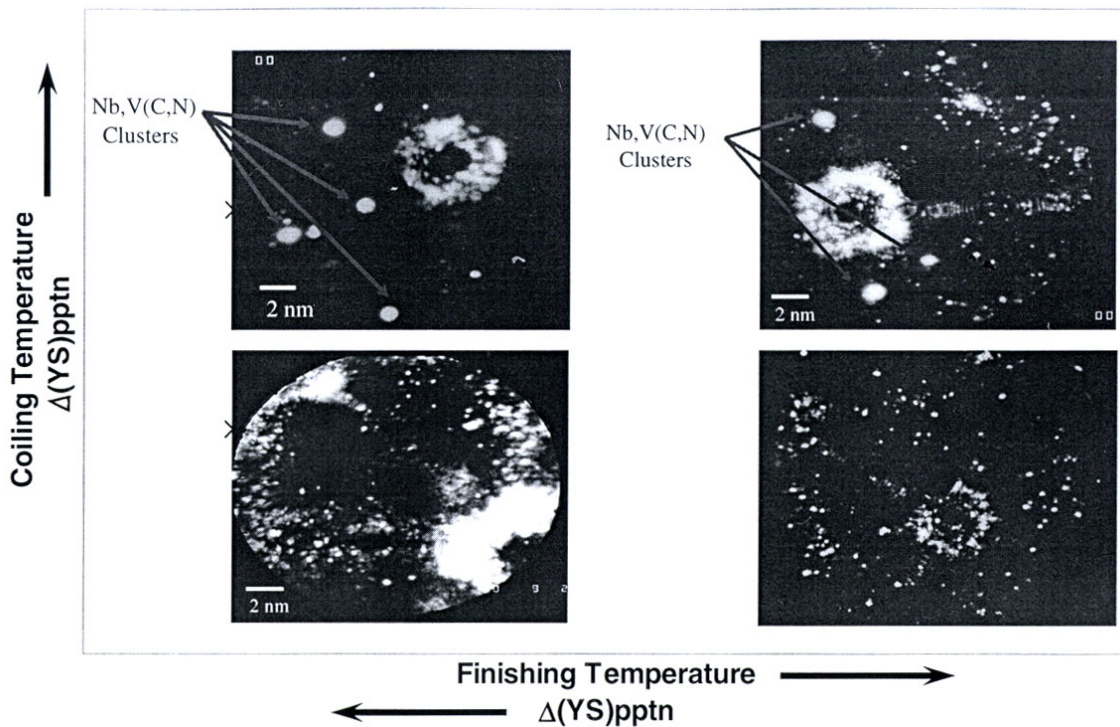


Figure 91 Effect of the processing conditions on the formation of small Nb,V(C,N) clusters

## 6.2 Tensile Properties

Mechanical testing indicates that the variation in the hot rolling parameters results in approximately a 10% variation in LYP. The variation in coiling temperature has the most important effect on the tensile properties variability, followed by finishing temperature, and reheating temperature. Variation in roughing temperature does not result in any notable variability in tensile properties. The effect of varying each hot mill processing parameter is observed in Figure 92.

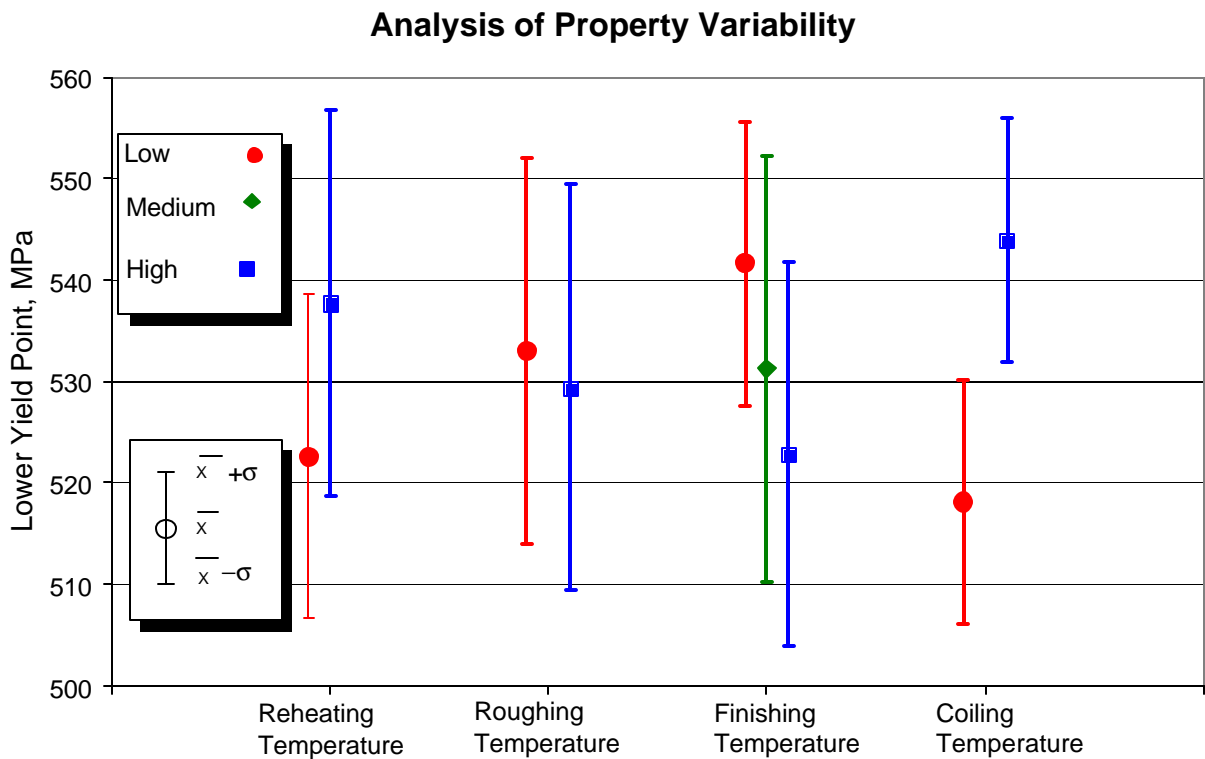


Figure 92 Analysis of the variability of the different hot mill processing parameters

Similarly, taking the mean LYP value obtained at the different processing conditions, we obtain the variation of the average LYP for individual hot mill processing parameters, which is shown in Figure 93.

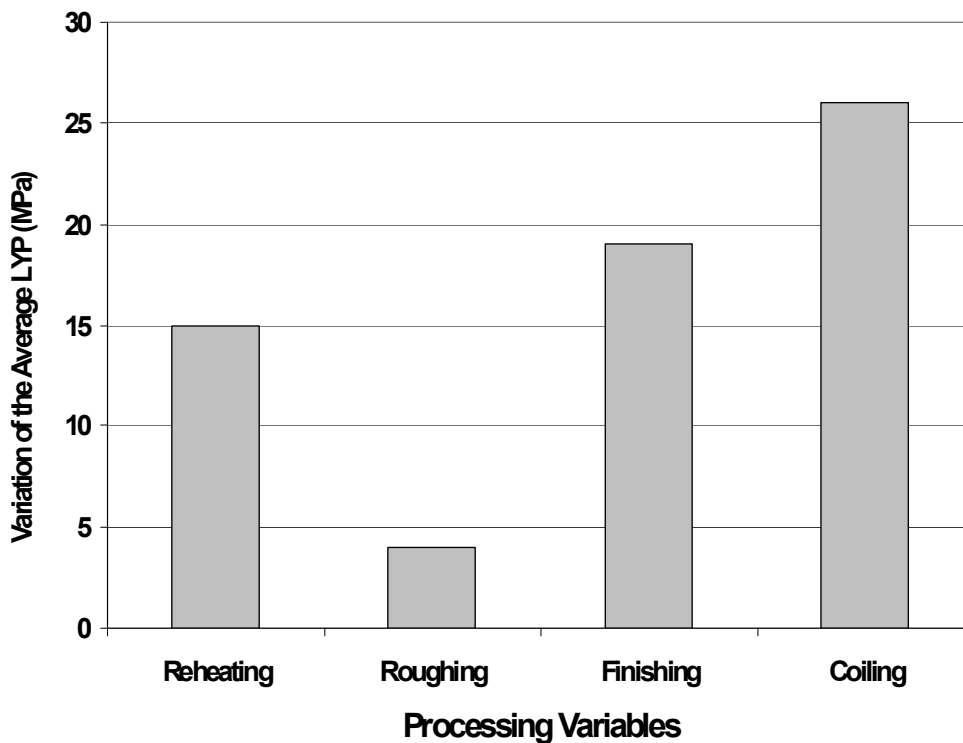


Figure 93 Effect of processing variation on the average LYP variability

Taking these average values, the variability in mechanical properties observed due to the variation in the hot mill processing parameters, does not exceed 7%. However, analyzing the variability obtained in certain individual sets of processing conditions, variations as large as 13% are observed. Therefore, an analysis of the contribution of each hot mill processing parameter must be made in order to gain a better understanding of the reasons controlling the variability.

Also, an analysis of the mechanical properties observed indicates that higher tensile values are obtained when testing in the transverse direction is done. Similarly, Meyer et al<sup>(85)</sup> have pointed out that a thermomechanically treated plate or hot strip presents a preferential orientation, which necessarily results from the transformation of the austenite that has undergone recrystallization. The predominant texture is  $\{112\}\langle 110\rangle$  and it brings about a yield strength anisotropy with maximum values, an average of 30 N/mm<sup>2</sup> increase, in the transverse direction.

### **6.3 Individual and Combined Effect of the Processing Parameters on the Tensile Properties and Microstructural Variability**

#### **6.3.1 Effect of the Reheating Temperature**

It has been found that an increase by 80 C in the reheating temperature results, in general, in an increase in LYP, Figure 94. In this Figure, as well as in Figures 95,96 and 97, a linear trendline is drawn to indicate, in the average, the general variation of LYP with different processing temperatures. The increase in LYP with increasing reheating temperatures has been observed before. Williams and Killmore<sup>(86)</sup> found an increase of 33 MPa in the LYP, in a X60 strip, by increasing the slab reheating temperature from 1160 to 1260 C. However, Lessells<sup>(87)</sup> found that the slab reheating temperature effect is not of great magnitude in tensile properties. Moreover, Abram and Paules<sup>(88)</sup> observed a slight increase in LYP when decreasing the reheating temperature from 1270 to 1100°C.

Research carried out by Repas<sup>(89)</sup> in a Nb-Ti steel shows that the highest yield strengths were obtained with a slab reheating temperature of 1260 C and a coiling temperature of 595 C. A slab reheating temperature of 1175 C, however, produced strengths about 21 MPa lower than

for the same coiling temperature. Also, the addition of 0.06%V increased the yield strength by about 48 MPa for a 595 C coiling temperature, and slightly more when coiled at 650 C.

The increase in tensile properties has been attributed to more Nb going into solution as reheating temperature increases, which eventually will be available for precipitation. While this may be true at coiling temperatures where fine precipitation can occur, coiling at low temperatures, 550°C, results in no precipitation. In this case, higher tensile properties can also be attributed to more solute Nb strengthening the ferrite lattice and increased hardenability, which in turn can lead to higher dislocation densities. Also, careful analysis shows that there is a tendency to increase the amount of LAGB at those samples processed at the higher reheating temperatures.

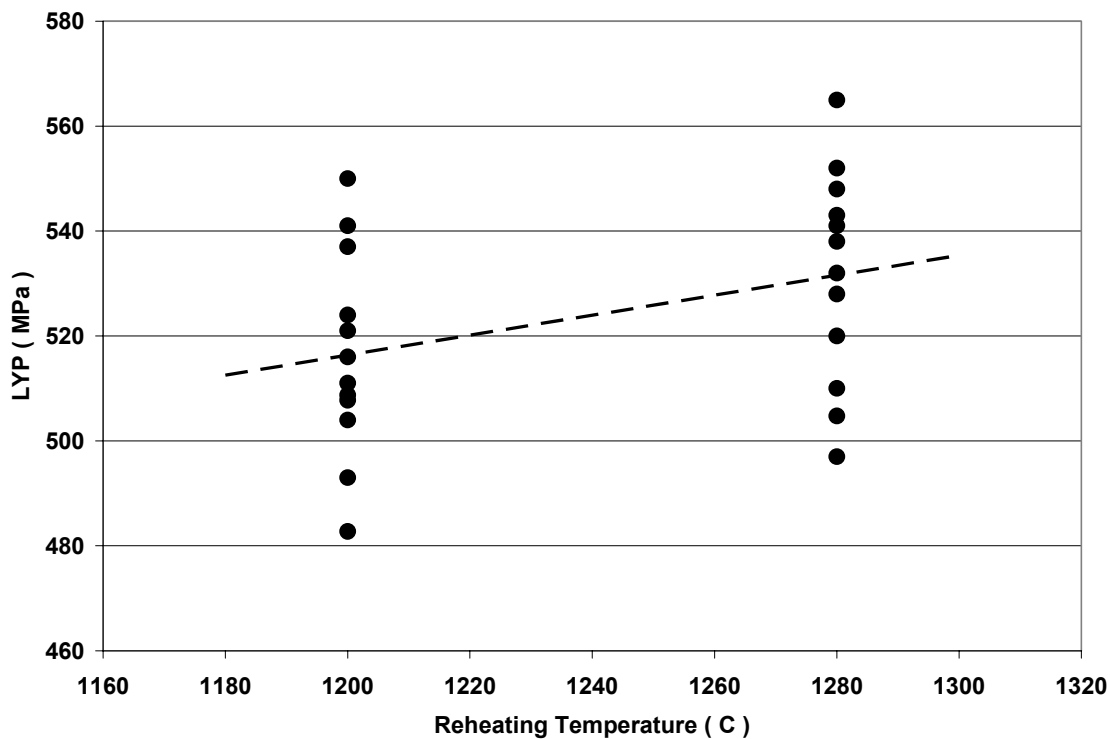


Figure 94 Variation of LYP with two different levels of reheating temperatures

### 6.3.2 Effect of Roughing Temperature

The effect of roughing temperature on the variation of mechanical properties is found to be minimal, as shown in Figure 95.

Deboer<sup>(90)</sup> found in a Nb-V steel that the variation in roughing temperature for different reheating conditions does not result in any variation in yield strength, and that for a Ti steel, a decrease in roughing temperature results in a small decrease in yield strength. The main effect found is a decrease in the transition temperature as roughing temperature decreased, resulting in an improvement in toughness. However, Lederer and Andreas<sup>(91)</sup> have shown that a final higher roughing temperature results in a higher strength and no influence in toughness.

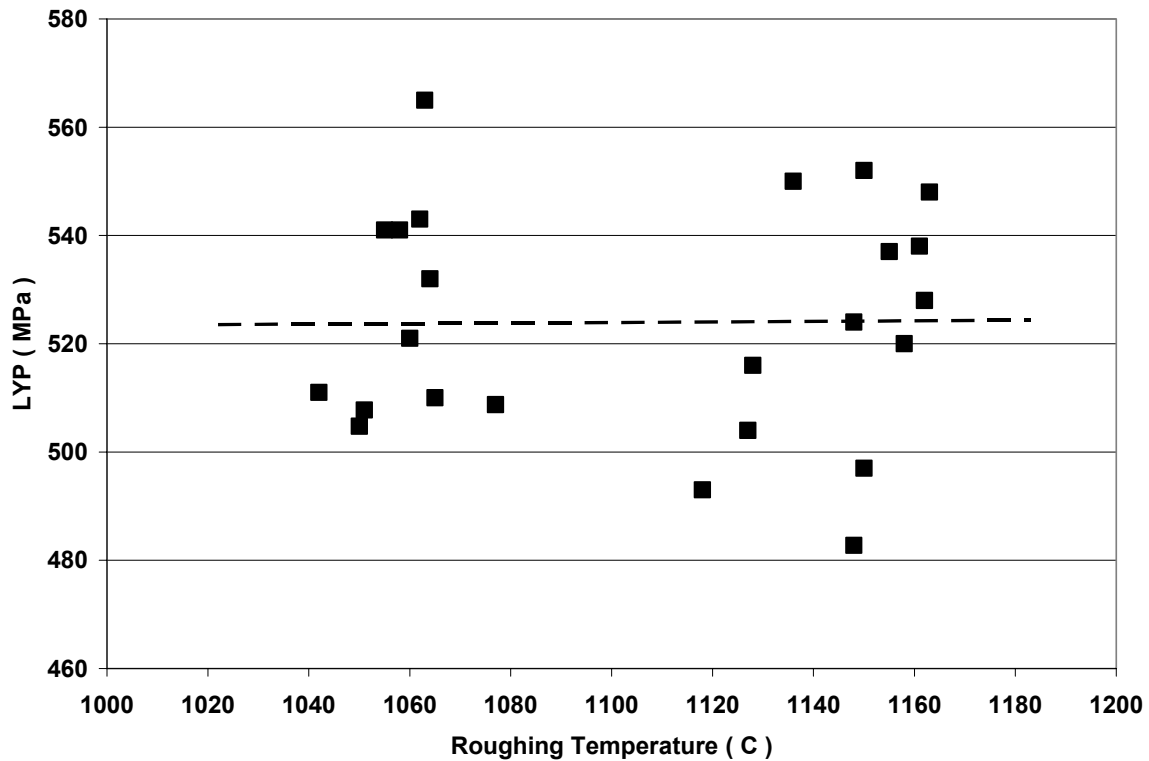


Figure 95 Variation of LYP for different roughing temperature conditions

There is no clear relation as to whether the variation in roughing temperature will result in an increase or decrease in mechanical properties. The variation observed in the 1X12 condition results in an increase in LYP as large as 42 MPa when roughing at the higher temperatures, whereas the 2X12 and 2X11 show the opposite behavior, resulting in higher LYP when low roughing temperature were used.

In general, there is a slight trend to obtain higher LYP values in the combination of high roughing temperatures and low reheating temperatures, and low roughing temperatures and high reheating conditions. Taking the largest spread in results, however, does not exceed a variability of 9%. To minimize variability in the tensile properties introduced in the roughing passes, the use of a subsequent high finishing temperature is better compared to using low finishing temperatures. Low roughing temperatures in combination with high finishing temperatures, result also in  $R\text{-bar}$  values close to 1.

The variation in roughing temperature does not have a discernible effect in the final grain size, LAGB's, dislocation density, nor types of phases and microconstituents.

### **6.3.3 Effect of Finishing Temperature**

The variation of the finishing temperature has a significant effect on the mechanical properties and microstructure of the hot rolled steel. Figure 96 represents the LYP data as a function of the finishing temperature and shows that rolling at a finishing temperature of 900 C results in a higher LYP than those plates rolled at 950 and 1000 C. Tensile strength, however, decreases with decreasing finishing temperature.

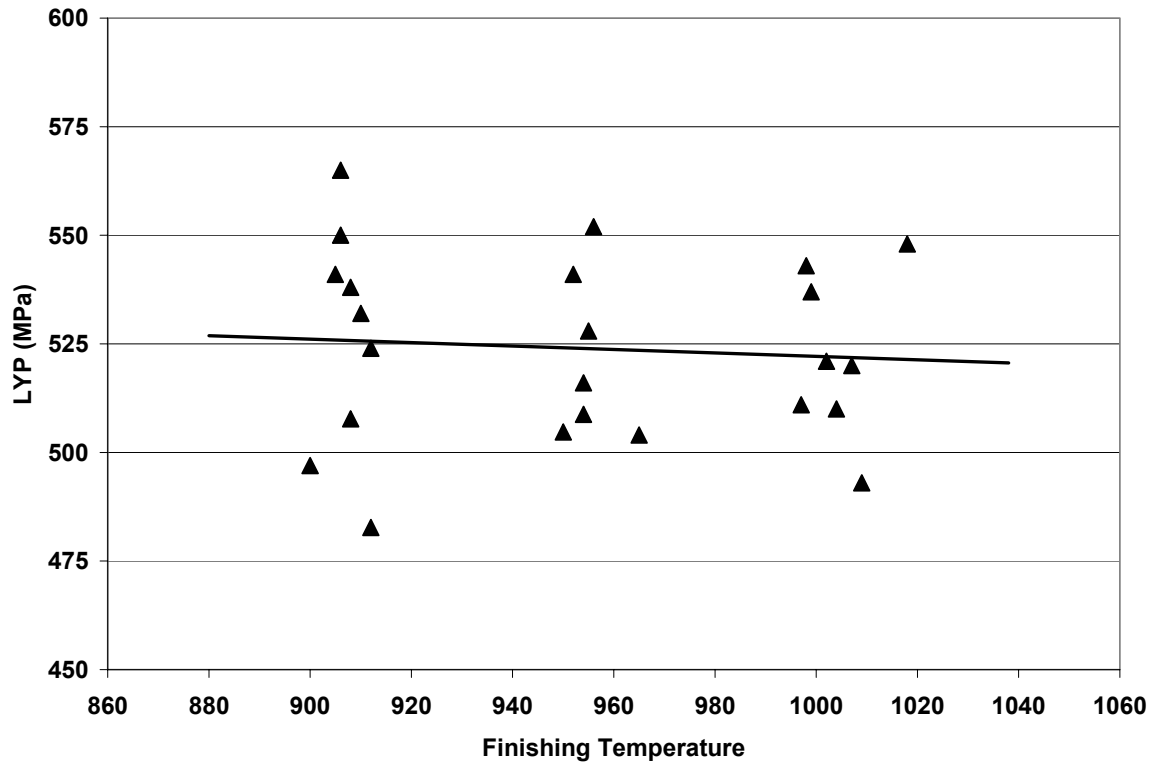


Figure 96 Variation of LYP for different finishing temperature conditions

Williams and Killmore<sup>(86)</sup> have reported similar results. They found that the yield strength increases as the finishing temperature decreases, and this becomes more important in Nb-Ti steels, followed by Ti-V steels. For Ti steels, there is essentially no effect without MAE additions. For a recrystallized controlled rolling steel, Simeck reports, on the other hand, that the variation in finishing temperature in the 900-1050 C range does not influence, strongly, the mechanical properties of a Ti-V-N steel, and that there is a tendency to obtain higher yield strengths, about 20 MPa, as finishing temperature increases in the 900-1000 C region.

Analysis of the phase map shown in Figure 64 indicates that rolling at 900 C gives rise to the formation of predominantly polygonal and non-polygonal ferrite microstructures, whereas

rolling at 950 and 1000 C results in the formation of a predominantly acicular ferrite and small islands of carbide constituents.

The different ferrite morphologies are the direct result of different austenite conditions, i.e.,  $S_v$  and solute content, after the final finishing pass. Fully recrystallized austenite prior to transformation will give rise to acicular ferrite. In contrast, if the austenite is pancaked, the resulting ferrite will display a polygonal ferrite. Finally, a partial recrystallization of austenite will result in the mixture of polygonal and acicular ferrite structures.

Militzer et al.,<sup>(92)</sup> have suggested that the amount of polygonal ferrite increases with increasing retained strain. A non-recrystallized, pancaked austenite structure will have a higher retained strain than a recrystallized structure, and increases with increasing deformation in the finishing passes and with low percent of recrystallization. Since the amount of retained strain increases with decreasing finishing temperature, this offers an explanation of the increasing content of polygonal ferrite at low finishing temperatures.

However, during a commercial thermomechanical rolling treatment, a temperature inhomogeneity exists over the length of the strip during the finishing stage, which can be observed in Figure 97. Reductions in the first or first two finishing stands can give rise to dynamic recrystallization during rolling. In the following passes, this is no longer the case. Only static recrystallization can occur, and depending on the steel quality, draft and temperature, there can be complete, incomplete or no static recrystallization<sup>(104)</sup>.

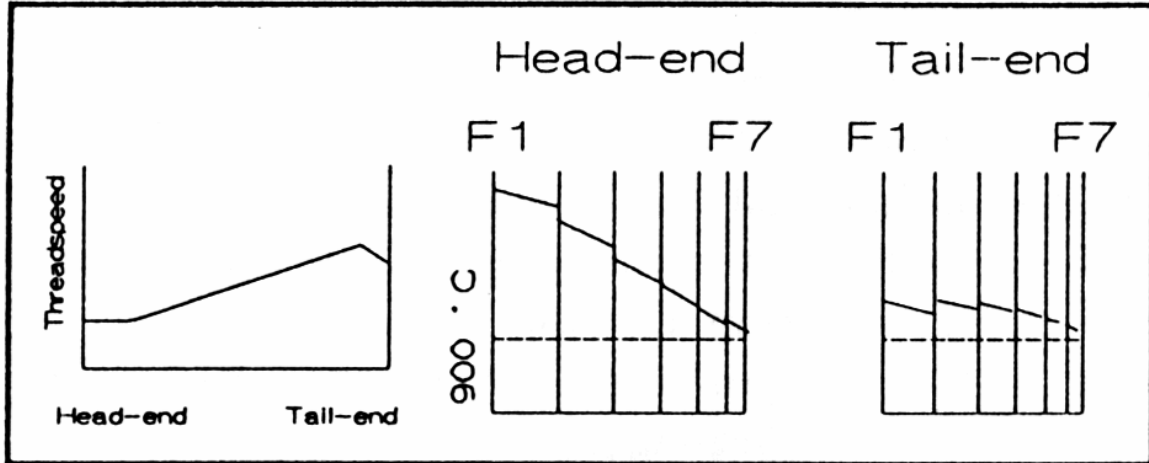


Figure 97 Temperature profile during the finishing stage

While it is expected that ferrite grain refinement will be obtained when finishing at low temperatures due to the increasing amount of  $S_v$  obtained, this seems to be unclear if we assume that position. In this study, there was no significant effect of the finishing temperature on the ferrite grain size. Similarly, Myllykoski<sup>(93)</sup> reported data supporting the position that for a Nb and a Nb-Ti steel, there is no effect of finish rolling temperature on ferrite grain size.

It has been pointed out that varying the finishing temperature results in a large variation in the observed type of ferrite. The finishing temperature has also a marked effect on other microstructural features, such as dislocation density and precipitation. These, however, do not explain the trend of the LYP results by themselves, especially if we consider the dislocation density. For example, looking at Figure 89, it is clear that the dislocation density increases with increasing finishing temperature. If we take the 2112 and 2132 conditions, we see that for the 2112 condition we have a dislocation density of  $0.6E10 \text{ cm}^{-2}$ , which corresponds to a dislocation strengthening contribution of 62 MPa, whereas the 2132 condition has a  $2.7E10 \text{ cm}^{-2}$  dislocation density, equal to a dislocation strengthening contribution of 130 MPa. The amount of LAGB's was also observed to increase at the higher finishing temperatures. While this seems to be

surprising due to the LYP values obtained, the dislocation densities measured are indeed accurate, and correspond to what is expected from the ferrite microstructures, since dislocation density increases with an increasing content of acicular ferrite and bainitic ferrite. It is worthwhile pointing out that, in fact, grain boundary cementite, and small islands of carbide phases, are present at 950 C finishing temperatures, and the largest amounts are seen at the finishing temperature of 1000 C. Therefore, it seems that there is a relation that indicates that the presence of these carbide phases, especially at grain boundaries, have the effect of decreasing the mechanical properties, perhaps either by modifying the  $K_y$  value, by causing grain boundary embrittlement, or by simply removing carbon from solution.

Precipitation took place in the samples coiled at 650 C. It can be expected that the precipitate volume fraction varies for different finishing temperatures, since more Nb in solution in the conditions rolled at high temperature can be obtained. This means that the volume fraction of Nb precipitation is higher in the low finishing temperature processing conditions, which corresponds to a higher contribution to precipitation strengthening. The increase in precipitate volume fraction at low finishing temperatures can be explained simply by considering the effect of retained strain. This would have a similar effect to that observed in the strain induced precipitation phenomena, where the kinetics of precipitate formation is greatly increased.

A schematic illustration for the estimation of strain retained prior to transformation is shown in Figure 98<sup>(94)</sup>. Also, it can be described as a function of temperature, time after pass rolling and prestrain.

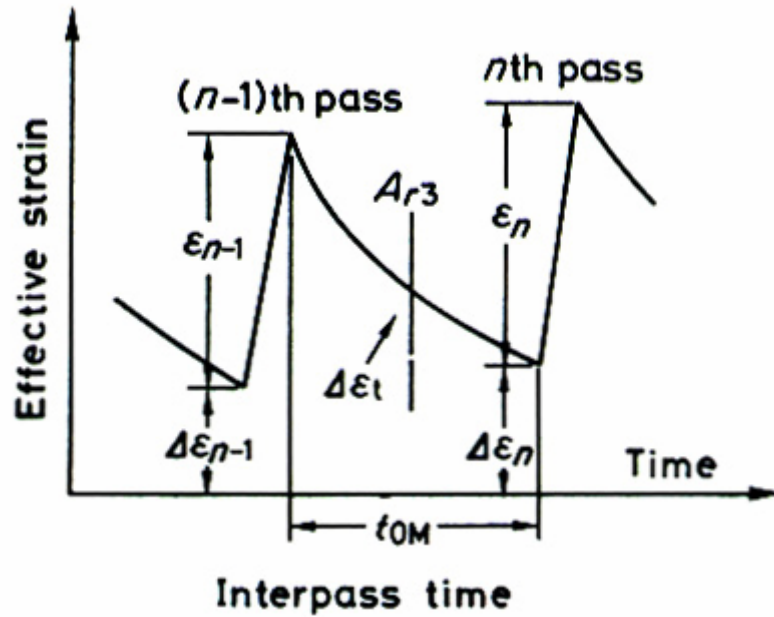


Figure 98 Schematic illustration for estimation of strain retained prior to transformation

Hence, while retained strain is often associated with contributing to ferrite grain size refinement, and to a larger extent to the formation of polygonal ferrite, it can also contribute in the precipitation phenomena. Therefore, as finishing temperature decreases, more retained strain is accumulated and consequently, larger amounts of polygonal ferrite are observed, and larger precipitate volume fraction can be expected. Then, again, while this offers an explanation for the high coiling temperature conditions, it doesn't provide one for the 550 C coiling temperature, where precipitation was absent. Therefore, attention must be given again to the fact that the only consistent microstructural feature present at high finishing temperatures is the carbide phases, which indeed can be responsible for the decrease in mechanical properties.

### 6.3.4 Effect of Coiling Temperature

The variation of the coiling temperature has the most significant effect on the variation of mechanical properties of the hot rolled steel plates. Figure 99 represents the LYP data as a function of the coiling temperature. It is clear that coiling at 650 C results in a higher LYP than coiling at 550 C.

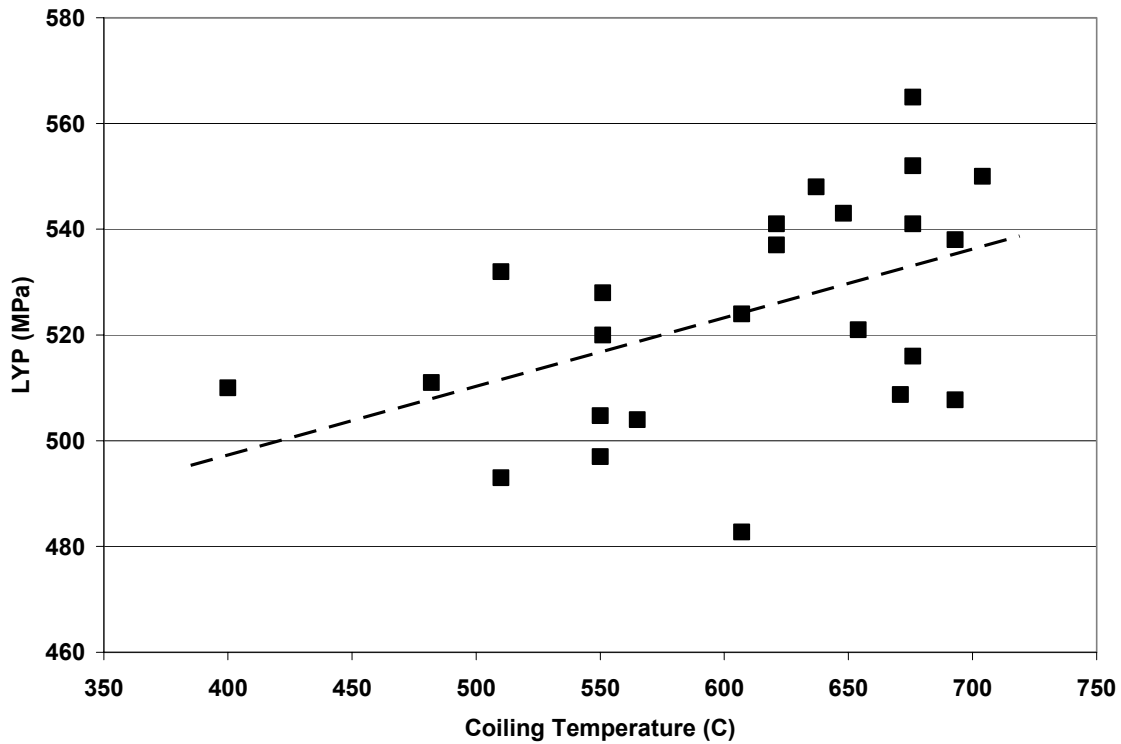


Figure 99 Variation of LYP for different coiling temperature conditions

The sensitivity of mechanical properties with varying coiling conditions has been investigated previously. Hulka<sup>(95)</sup> has found that there is an optimum cooling stop temperature which results in a yield strength increase of about 70 N/mm<sup>2</sup>. Similarly, Williams and Killmore<sup>(86)</sup> found that Nb, Nb-V, and Mo-Nb type X60 steels show different sensitivities of coiling temperatures with strip strength properties. In a model presented by Kwon<sup>(96)</sup>, the

precipitation strengthening effect was found to be dependent on the coiling temperature and Nb concentration. The peak strengths shift to higher coiling temperatures as %Nb is increased. Masi and Vito<sup>(97)</sup> have also found a maximum in yield strength with respect to coiling temperature, where the maximum strength is found at 600 C for different rolling schedules in a 0.04 Nb, 0.05 V steel. The peak position for maximum strengthening at varying coiling temperatures is very sensitive and can easily shift its position depending on the different amount and type of MAE used.

Coiling at 650 C gives rise to the formation of predominantly polygonal and non-polygonal ferrite microstructures, whereas coiling at 550 C results in the formation of a predominantly acicular ferrite, bainitic ferrite and small islands of carbide constituents. The formation of acicular and bainitic ferrite in the samples coiled at 550 C was expected to result in higher mechanical properties than those coiled at 650 C. Also, the amount of LAGB's and dislocation density is larger for those conditions coiled at 550 C. However, these samples resulted in lower tensile properties. The higher LYP found at the high coiling temperatures is entirely explained by the presence of clusters or very fine precipitates. APFIM analysis revealed a high density of these clusters in the samples coiled at 650 C. If we consider the maximum volume fraction that can precipitate as NbC, and/or VC, for a 2 nm particle size, the precipitation strengthening results in 100 MPa for NbC and 123 MPa for VC.

Thillou<sup>(98)</sup> has presented the Nb migration as a function of coiling temperature and time, for an average cooling rate of 28 C/sec. This is observed in Figure 100. It is clear that diffusivity of Nb in ferrite substantially decreases as coiling temperature decreases, and therefore, precipitation at low coiling temperatures becomes increasingly difficult to observe.

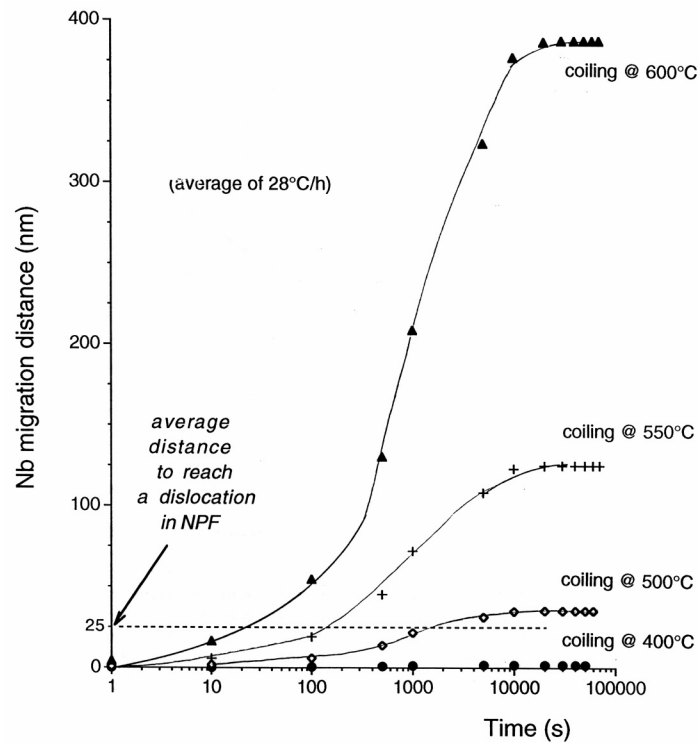


Figure 100 Nb migration as a function of coiling temperature and time

#### 6.4 Comparison of Laboratory Hot Rolling Experiment and Commercial Hot Band

A commercial 70 ksi HSLA hot band was used to compare the tensile values obtained in the laboratory hot rolling experiment. The commercial 70 ksi HSLA steel was finish-rolled at 900 C and coiled at 650 C. An extremely close agreement can be observed when a comparison of all the samples rolled at 900 C and coiled at 650 in the hot rolling experiment with the commercial hot band is done. Figure 101 shows that the 2212 processing condition has closer LYP and TS values when tested in both rolling and transverse directions. Following this close agreement, it can be expected that the reheating and roughing temperatures used in the processing of the commercial hot band were close to 1280 C and 1150 C, respectively.

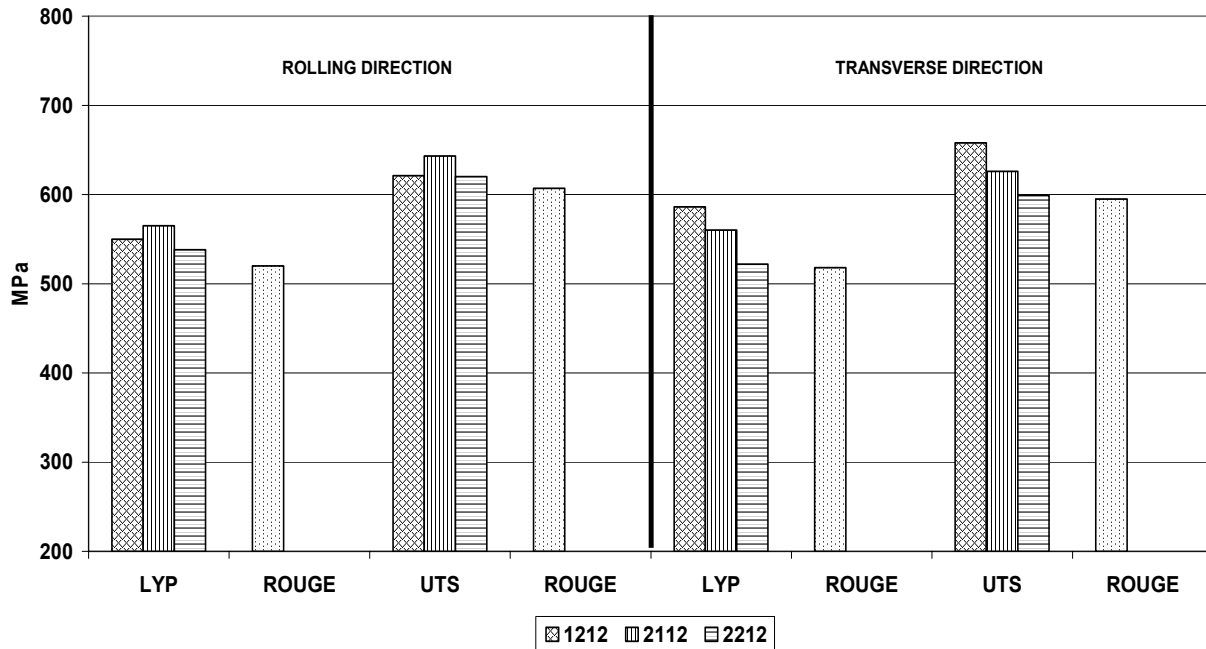


Figure 101 Comparison of LYP and TS values of laboratory and commercial thermomechanically rolled 70 ksi HSLA steel. Finishing temperature: 900 C, coiling temperature: 650 C.

### 6.5 Modeling the Effect of Microstructure Variability

To estimate the possible contribution of the various constituents, the following series of relationships was employed.

A. Contribution from Solute <sup>(99)</sup> For the solute strengtheners in the Rouge steel,

$$\Delta\sigma_{ss} = 32.5 \cdot (\text{wt.pct.Mn}) + 84.0 \cdot (\text{wt.pct.Si})(\text{MPa}) \dots\dots\dots(34)$$

B. Contribution from Dislocations <sup>(64)</sup>

$$\Delta\sigma_{\perp} = \alpha \cdot G \cdot b \cdot \rho^{0.5} = 7.82 \times 10^{-4} \cdot \rho^{0.5} (\text{MPa}) \dots (35)$$

where

$\alpha = 0.38$

b: Burger's Vector, =  $0.248 \times 10^{-7}$  cm

G: Shear Modulus, =  $8.3 \times 10^4$  MPa.

C. Contribution from Precipitates <sup>(100)</sup>

$$\Delta\sigma_{\text{ppt}} = \frac{M \cdot K \cdot G \cdot b}{\pi \cdot \sqrt{\pi}} \cdot \phi \cdot \frac{\sqrt{f}}{d} \cdot \ln\left(\frac{d}{2 \cdot b}\right) (\text{MPa}) \dots (36)$$

where

M = Taylor Factor = 2.0

K = 0.81

f = volume fraction of precipitates

d =  $2 \cdot R' = 2 \cdot \sqrt{2/3} \cdot R = \sqrt{8/3} \cdot R$  nm

R = particle radius = 1 nm

R' = apparent particle radius as seen by the dislocation in its slip plane also called the intercept diameter.

D. Contribution from Grain Boundaries <sup>(55,56)</sup>

$$\Delta\sigma_D = k_Y \cdot d^{-1/2} (\text{MPa}) \dots (37)$$

where

$k_Y = 16.20 \text{ MPa} \cdot (\text{mm})^{1/2}$  for the lower yield stress.

E. Contribution from Subgrains <sup>(101)</sup>

$$\Delta\sigma_{SG} = k_s \cdot \lambda^m / \sqrt{2} (MPa) \dots\dots\dots (38)$$

where

$$m = -1/2$$

$$k_s = 14 \text{ N(mm)}^{-3/2}$$

$\lambda$  = subgrain size with estimated value of 4.50  $\mu\text{m}$ .

F. Contribution from Phases. In a literature search, the only reference dealing with the contribution of the phases to the strength was that of the effect of pearlite on the ultimate tensile strength <sup>(102)</sup>.

$$\text{UTS} = 15.4 [ 19.1 + 1.8 (\% \text{Mn}) + 5.4 (\% \text{Si}) + 0.25 (\% \text{ pearlite } ) + 0.5 \langle D \rangle \exp^{-1/2} ] \text{ (MPa) } \dots (39)$$

where

$\langle D \rangle$  is grain diameter in mm.

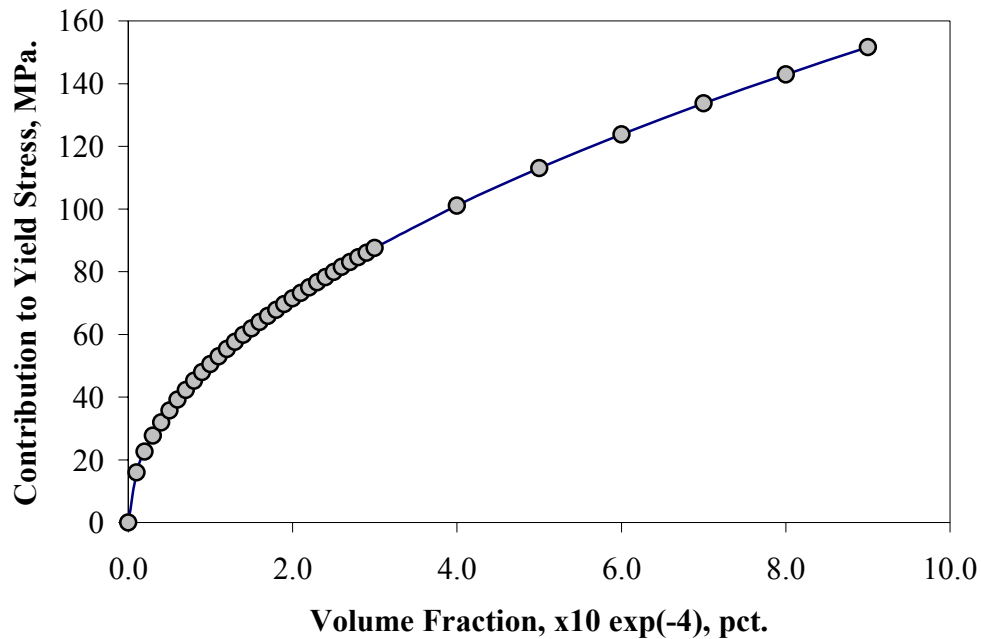


Figure 102 Dependence of the precipitate strengthening contribution to the yield strength, at different volume fractions, for a mean particle diameter of 2 nm.

### 6.5.1 Application of the Models

With the measured values obtained, the contributions to the yield strength can be calculated, and the linear addition method was adopted. Following Morcinek et al.,<sup>(103)</sup> the Peierls-Nabarro value was taken as 48 MPa in all cases, and the contribution from sub-grains was taken as an average value 148 MPa. For precipitation strengthening we know that the mean diameter of the clusters is close to 2 nm in the laboratory rolled Rouge steel. Application of Equation 36 produces the variation of the precipitate contribution with volume fraction shown in Figure 102. Because a reliable estimate of the particle volume fraction cannot be accurately taken from APFIM analysis, and taking into account the possible effect of finishing temperature on precipitate volume fraction, described earlier, a maximum NbC plus VC volume fraction of clusters is assumed for the low finishing-high coiling temperature conditions, and half of the

total volume fraction is assumed for the high finishing-high coiling conditions. Similarly, an analysis of the amount of LAGB's present at different combinations of finishing and coiling temperatures results in assigning 100% of the total possible contribution from LAGB's strengthening to the XX31 conditions, 75% to the XX32 conditions, 50% to the XX11 conditions, and finally, a 25% to the XX12 conditions. Because of the variability found in the type of ferrite, and adopting a rule of mixtures, a similar approach is given to the grain size strengthening component. The grain size strengthening in the XX12 conditions is calculated using 100% of the total possible contribution due to grain size. A combination of low finishing and low coiling temperatures, XX11, and high finishing-high coiling temperatures, XX32 results in an increasing amount of non-polygonal, acicular ferrite, and bainitic ferrite. At least 50% will be assumed not to contribute to the Hall-Petch equation. Finally, a very large amount of bainitic ferrite and grain boundary cementite is observed at the high finishing-low coiling temperature conditions, XX31. Therefore, only 25% of the possible grain size strengthening contribution will be assumed.

This attempt to estimate the contribution of the various constituents to the yield strength is summarized in Table 27 and represented graphically in Figure 103, along with a comparison of the calculated and measured yield stress. It is clear that the dislocation and precipitation strengthening contributions are very sensitive to different processing conditions and, for different processing conditions, only one of them apparently becomes the main strengthening mechanism.

Table 27 Calculated contributions of constituents to the lower yield stress

<u>Process.</u> <u>Cond'n</u>	<u>Peierls</u> <u>Nabarro</u> MPa.	<u>Solutes</u> MPa.	<u>Grain</u> <u>Bdy's</u> MPa.	<u>Disloc-</u> <u>ations</u> MPa.	<u>Sub-</u> <u>Grains</u> MPa.	<u>Precipi-</u> <u>tates</u> MPa.	<u>Calc.</u> <u>Total</u> MPa.	<u>Meas.</u> <u>YS</u> MPa.	<u>Calc. -</u> <u>Meas.</u> <u>Difference</u>
1211	48	50	125	147	74	0	444	524	-80
1212	48	50	165	72	30	223	588	550	38
1231	48	50	62	185	148	0	493	493	0
1232	48	50	95	106	111	157	567	537	30
2111	48	50	125	151	74	0	448	487	-39
2112	48	50	190	62	30	223	603	565	38
2131	48	50	62	170	148	0	478	510	-32
2132	48	50	86	129	111	157	581	569	12
2231	48	50	62	154	148	0	462	520	-58
2232	48	50	121	75	111	157	562	548	14
2212	48	50	168	68	30	223	588	559	29

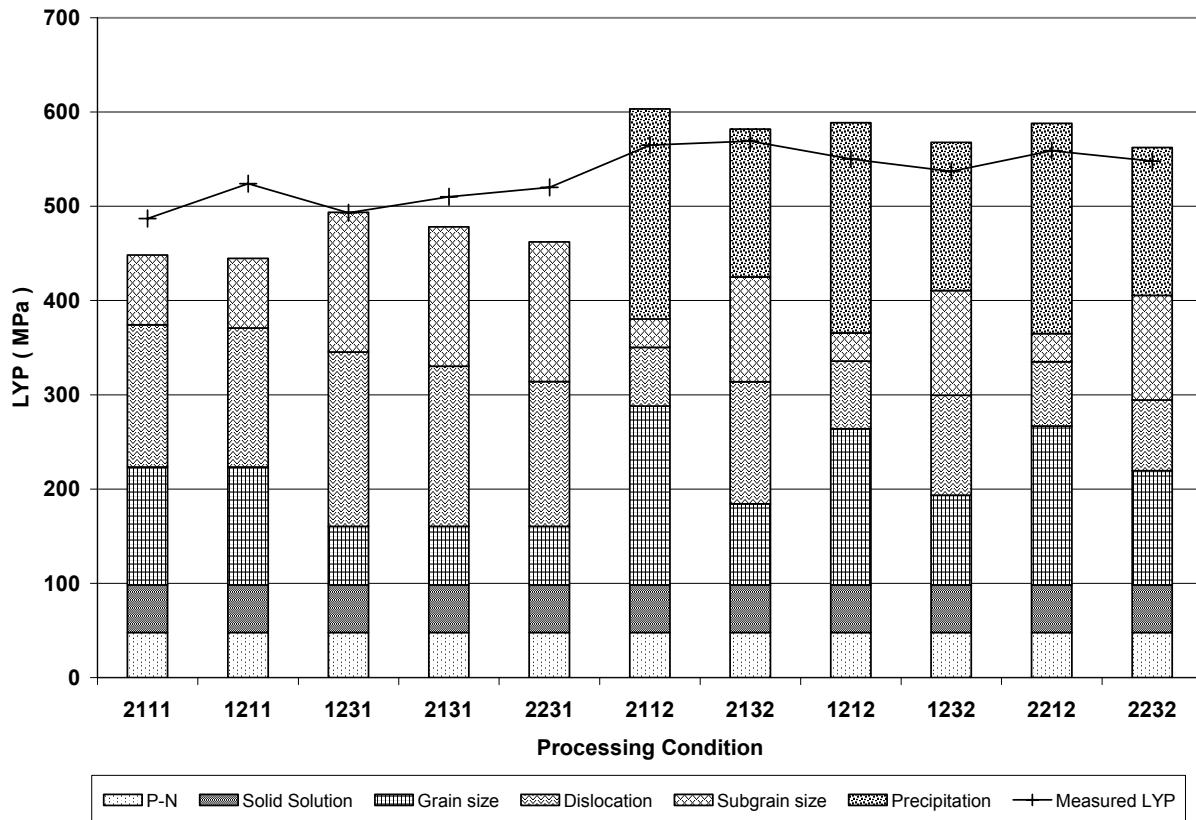


Figure 103 Calculated contributions to the lower yield stress, with processing conditions corresponding to the processing conditions 1211 through 2212.

Without the addition of the precipitate strengthening component, a comparison of the difference between the calculated versus the measured LYP values, as shown in Table 28 and in Figure 104, indicates that the lower finishing temperatures result in a larger precipitate strengthening contribution than when using high finishing temperatures.

Table 28 Comparison of the precipitation strengthening as a function of finishing temperature, obtained as the difference between the calculated LYP without the precipitation strengthening contribution and the measured LYP

Processing Condition	Calculated LYP without precipitate contribution (MPa)	Measured LYP (MPa)	Precipitate strengthening contribution (MPa), as the diff. between columns
1212 – Low FT	365	550	185
1232 – High FT	411	537	126
2112 – Low FT	380	565	185
2132 – High FT	425	569	144
2212 – Low FT	365	559	194
2232 – High FT	405	548	143

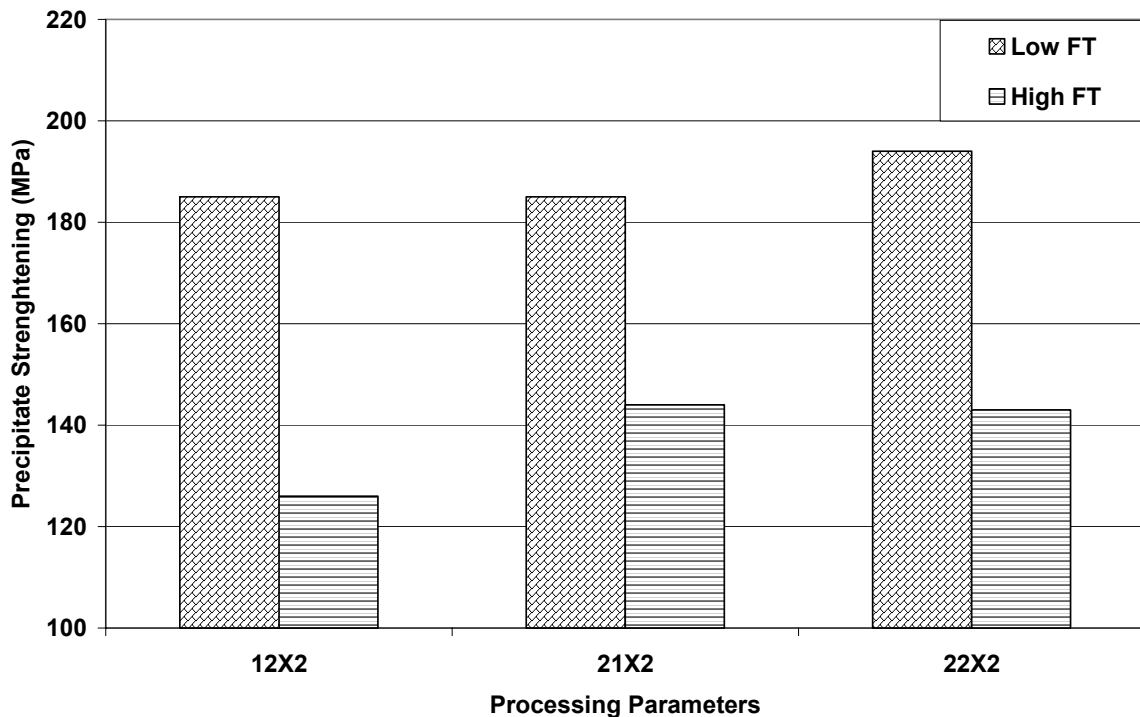


Figure 104 Effect of finishing temperature on precipitation strengthening, for samples coiled at 650 C

## 6.6 Combined Effect of Cooling Rate and Coiling Temperature on the Variability of Microstructure and Mechanical Properties

Because the variability found in the industry is much higher (>20%) than the maximum one found in this research (13%), it became obvious that the variation in the cooling rates from both the finishing to coiling temperature, and coiling to room temperature, could have an additional effect on the variability of the tensile properties. The results observed in the cooling rate experiment indicate that the variation in coiling temperature results in a maximum in tensile properties. The peak in hardness is observed at the slowest cooling rate, 0.01 C/sec, from the coiling temperature to room temperature. An increase in the cooling rate from the finishing to coiling temperature, from 5 to 10 C/sec, results in a decrease in the height of the hardness peak.

Since one of the main concerns is to obtain homogeneity of properties within a coil, it is important to realize that the cooling of a coil is a typical batch process with an inhomogeneous character. Huang<sup>(105)</sup> has developed a model where the cooling rates and temperature profiles at different positions within a coil can be observed. The envelope of the possible cooling paths in a 20 ton coil of strip 3 mm thick and 1400 mm wide, calculated at a coiling temperature of 700 C, is shown in Figure 106. Similarly, Hoogendoorn and Bodin<sup>(104)</sup> show in Figure 105, how the ends and sides of a coil cool in a different way than that of the bulk. Therefore, it can be expected that the transformation and precipitation behavior will be inhomogeneous, as well.

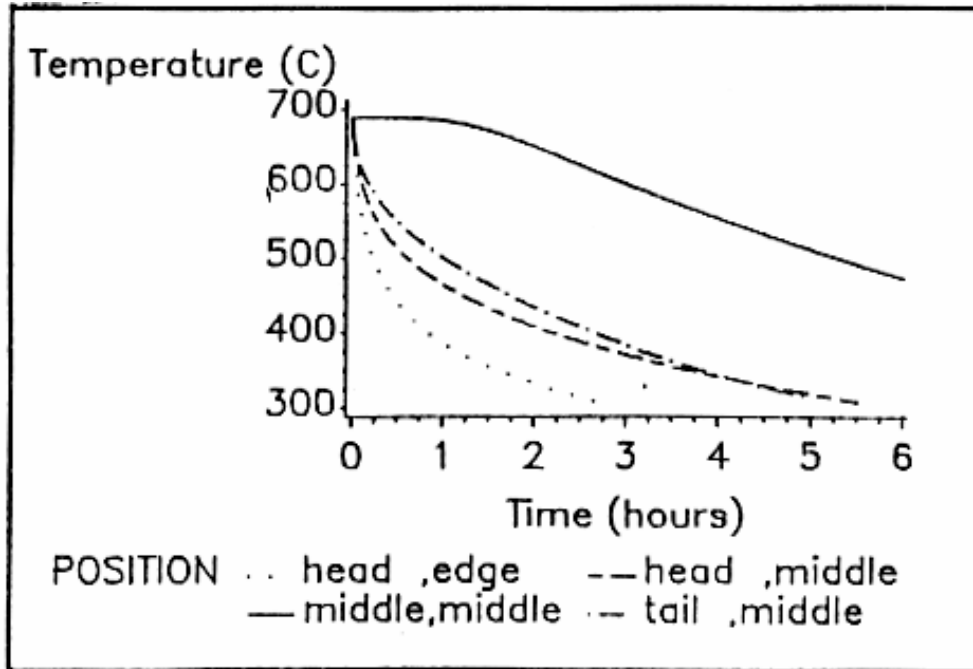


Figure 105 Cooling of the head and tail of a coil, at the edge and middle (centerline) positions

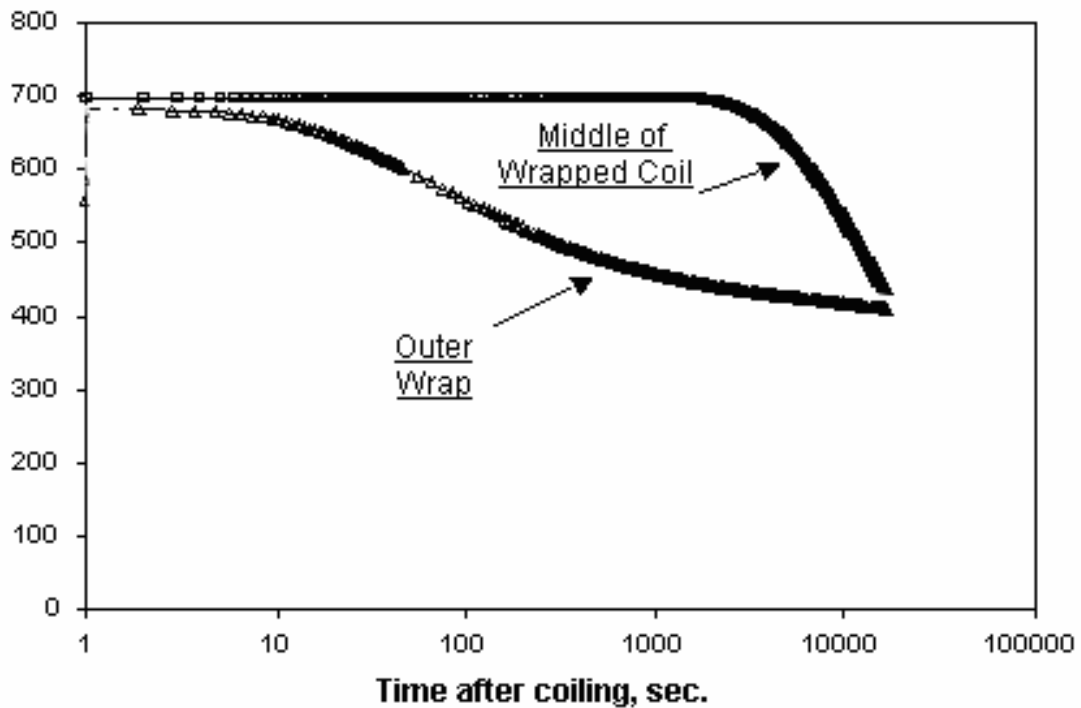


Figure 106 The two cooling curves that envelope the possible thermal paths in a coil for which the Coiling Temperature is 700 C. The locations of the thermal paths are on the centerlines of the outer wrap and the middle wrap of the coil.

Thillou<sup>(106)</sup> calculated the Nb migration distance at a coiling temperature of 450 C for the middle wrap and outer wrap of a coil. In Figure 107, it is observed that the Nb migration distance is much larger in the middle layers of a coil. On the other hand, Nb migration is less than 1 nm in the outer layers of a coil. This is the result of different cooling rates at different positions of the layers in a coil.

Hence, the observed hardness peak is the result of precipitation formation at the slow cooling rate, 0.01 C/sec, where Nb and V diffusivities are large enough for precipitation to take place. This variability in cooling rates and temperature profiles within a coil can result in a large variation in mechanical properties, due to the varying precipitate strengthening obtained at different positions within a coil, as has been shown in the results section of this work, in Figures 80 and 82.

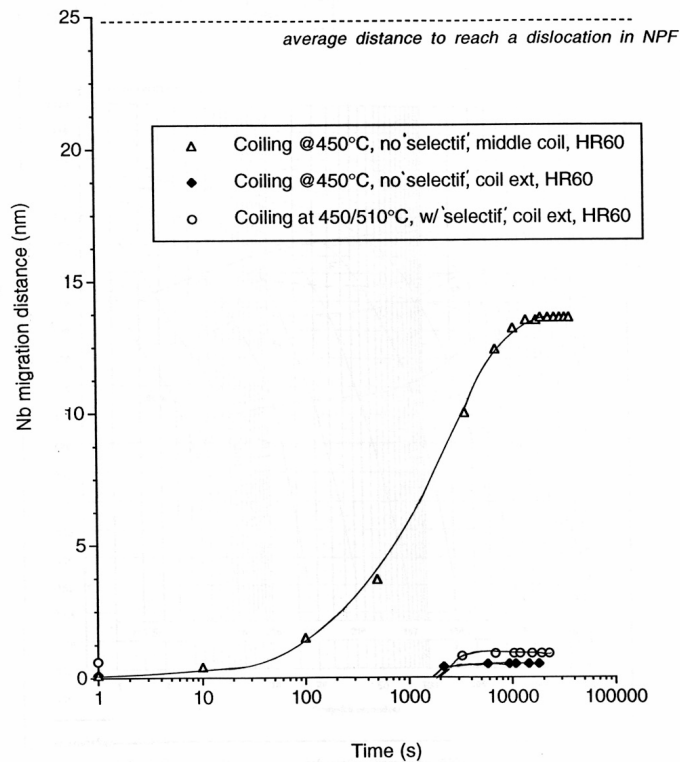


Figure 107 Nb migration distance for outer and middle wraps within a coil

A comparison of the ferrite microstructures of the two samples coiled at 600 C, and cooled at 0.01 C/sec to room temperature, are shown in Figure 108, where it can be observed that an increase in the cooling rate from the finishing to coiling temperature results in a large amount of acicular ferrite. This shift from diffusive to shear transformation appears to retard the kinetics of precipitate formation, as observed from the decrease in peak hardness in the sample cooled at 10 C/sec from the finishing to coiling temperature. Similar results are observed in experiments carried out with a 0.04 Ti – 0.06 Nb steel<sup>(107,108)</sup>, provided by Hylsa steel. The comparison of behavior observed in the Rouge and the Hylsa steel is shown in Figure 109.

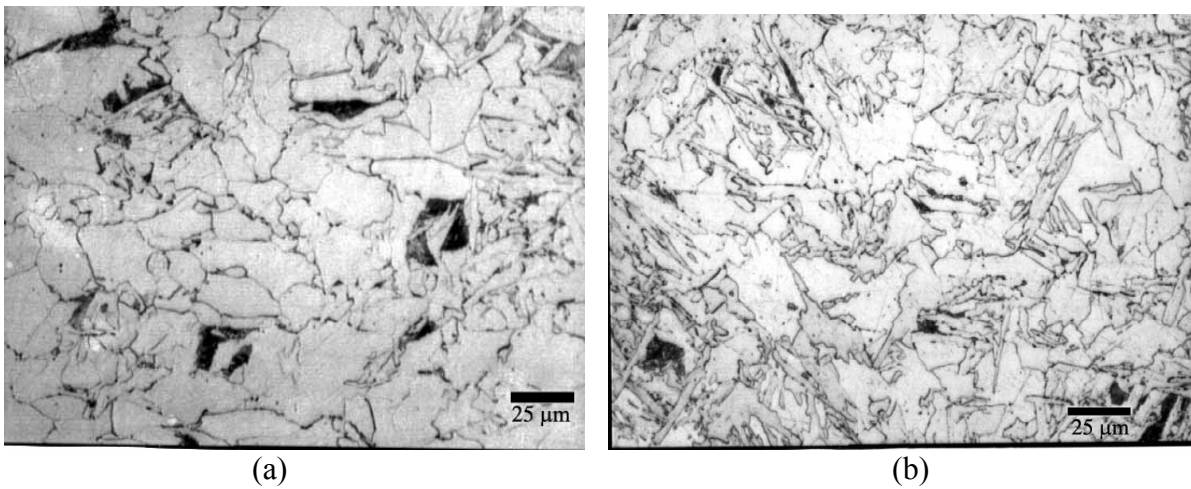


Figure 108 Shift in the type of ferrite from polygonal and non-polygonal to acicular ferrite cooling at (a) 5C/sec from finishing to coiling temperature and (b) 10 C/sec from finishing to coiling temperature. Coiling temperature: 600 C, cooling rate from coiling to room temperature: 0.01 C/sec

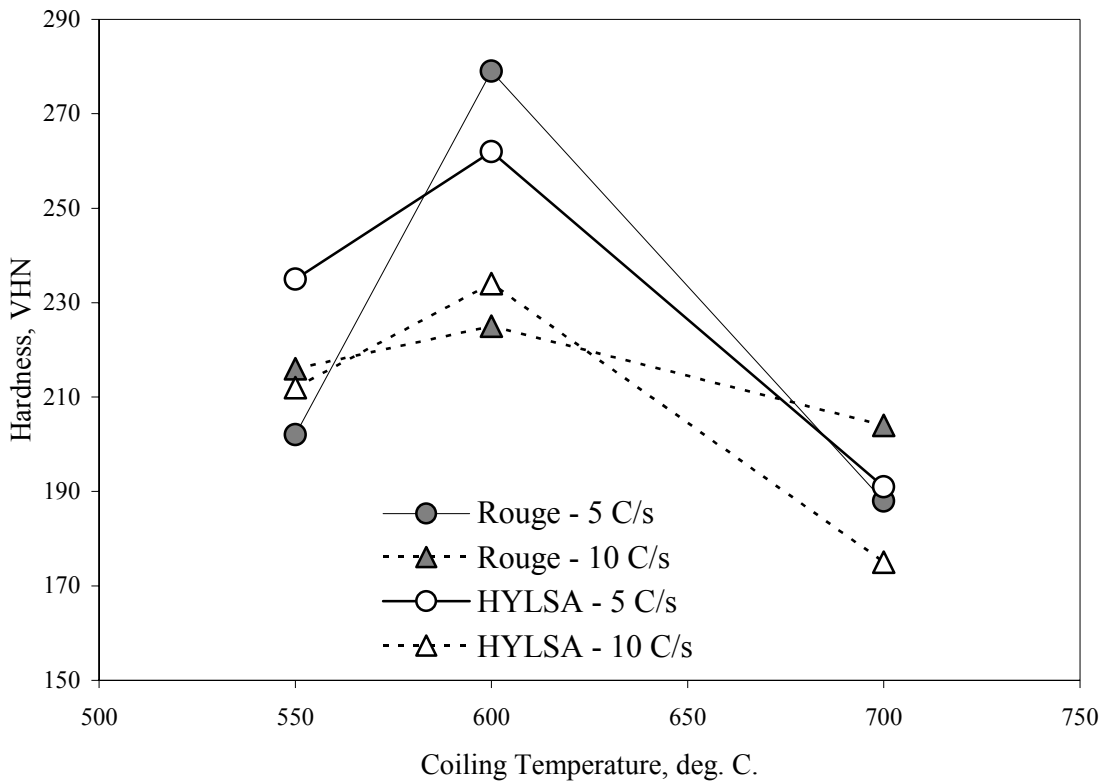


Figure 109 Hardness after cooling from the coiling temperature at 0.01 C/s. The two curves for each steel are for different cooling rates from the finishing to the coiling temperature

The difference between the hardness observed in the Rouge and the Nb-Ti steel indicates that an addition of Ti can interfere with the ability of Nb to form small NbC particles, as well as to decrease the amount of precipitate volume fraction. Kejian<sup>(109)</sup> found that a 0.01% Ti addition reduced, on the average, the yield strength of C-Mn-Nb steels by at least 12 MPa. He stated that:

$$\Delta\sigma_{pptn}(Nb) = 2500 (\%Nb \text{ at } Ar_3 - 0.5\% \text{ Ti})$$

This observed variation of strength with coiling temperature is consistent with the industrial and research experience in HSLA steels<sup>(111-120)</sup>. A review is summarized in Table 29. A majority of results concurred with our finding that there is indeed a maximum in strength at an intermediate coiling temperature. Examples from the literature are given in Figure 110.

Table 29 Summary of the literature review of the effect of coiling temperature on the yield strength of HSLA steels

Ref	Author	Composition	Processing	Observations
111	Vollrath	-	-	A coiling temperature of 490 C is found to be optimum for further processing. On annealing, precipitation strengthening is obtained above 550 C.
112	Honeycombe	0.033 Nb, 0.07 C, 1.07 Mn	Isothermal Transformation using high speed dilatometry	Coiling above 700 C: Interphase pptn occurs Between 700-600 C: Matrix pptn occurs Below 600 C: No pptn
113	Korchynsky	V-Ti-N	FT: 925-1045 C	Controlled cooling, 6.7 C/sec vs 1.0 C/sec resulted in an increase in pptn strengthening.
114	Olsson	0.12 C 1.50 Mn 0.03 Nb	Rh.T: 1250 C FT: 830-900 C	A coiling temperature of 600 C was found optimum for precipitation strengthening
115	Leber	0.084 C 1.41 Mn 0.07 Nb 0.056 V	Rh.T: 1250 C FT: 800 C	Coiling at 550 C + 120 min. resulted in an optimal coiling temperature for pptn strengthening. Precipitates were not observed in the TEM. AP-FIM was used and ppts were observed with a size of 1 nm, composition: V(CN) Pptn strengthening was 150 MPa
116	Bodin	0.08 C 1.6 Mn 0.05 Nb 0.02 & 0.15 Ti	Rh.T: 1250 C 9 finishing passes	Coiling at 400 C resulted in a higher YS than coiling at 600 C. However, for a 0.2 Ti, coiling at 600 C resulted in a higher YS. (strip steel)

Table 29 (continued)

Ref	Author	Composition	Processing	Observations
117	Wang	0.12 C 1.3 Mn	FT: 800 C Cooling rates: 2-10 C/sec	A 550 C coiling temperature results in an optimum YS. Also, YS increases with cooling rate.
118	Kwon	0.09 C 1.46 Mn 0.028 Nb	TTT & CCT at 0.01 C/sec followed by 1 hr at CT	For TTT: Coiling below 700 C: matrix pptn and at 650 C is found a minimum in ppte size: 3 nm For CCT: Coiling at 650 C the ppte size is 2nm; and coiling at 700 C and above resulted in a reduced precipitate volume fraction
119	Grozier	0.13 C 0.12 V 1.40 Mn	FT: 900 C	A peak in YS was observed when coiling at 590 C. An optimum range for coiling is found to be 580-635 C. Cooling simulated the inside wraps of a coil ( 28 C/hr ).
120	Bai	C-Nb	Various	Different literature data was plotted and shows a peak in YS vs coiling temperature. Peaking phenomena is reported for a Bethlehem Steel, Niobium Products, Nippon Steel, and IPSCO (low and high Nb). The shapes and positions of these curves are different from each other, due to different chemistries and different thermal histories.

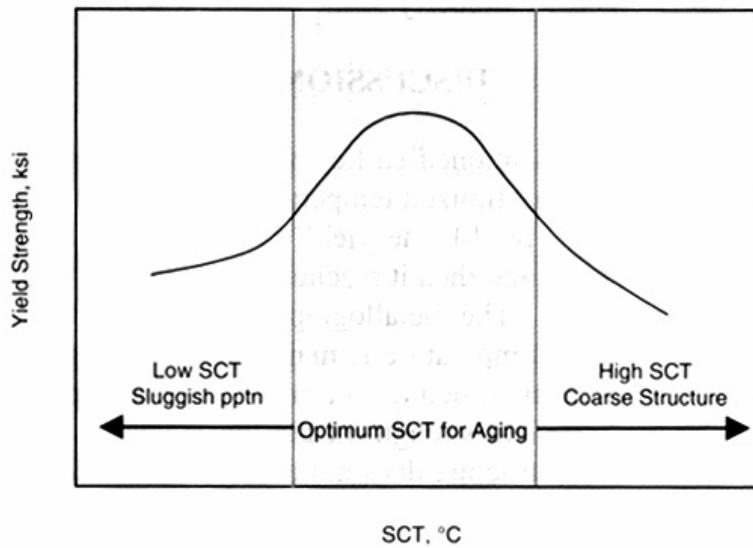
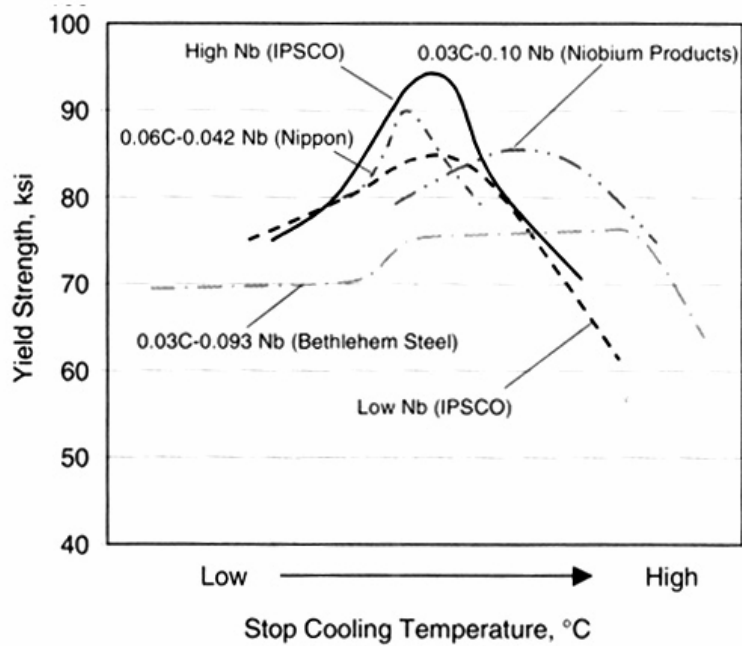


Figure 110 Effect of stop cooling temperatures on the yield strength and precipitation strengthening for various HSLA steels

Several models have been developed to calculate and predict the transformation and precipitation behavior of HSLA steels. Kwon and Lee<sup>(121)</sup> developed a model that predicts the behavior of a C-Mn, and Nb added steels. Figure 111 shows a retardation of the polygonal ferrite start time in the high temperature region of the TTT diagram of Nb steels, manifested through the stronger retardation effect of Nb on the diffusional transformation of polygonal ferrite than Widmanstatten ferrite and bainite transformation containing shear components. The calculated precipitation behavior of interface and matrix NbC revealed that both of the two precipitation-start curves was of the typical C-shape and exhibited similar nose temperatures. In the high temperature region, the progress of interphase precipitation is relatively faster than that of matrix precipitation, while in the low temperature region, the progress of interphase precipitation is relatively sluggish, resulting in predominantly matrix precipitation.

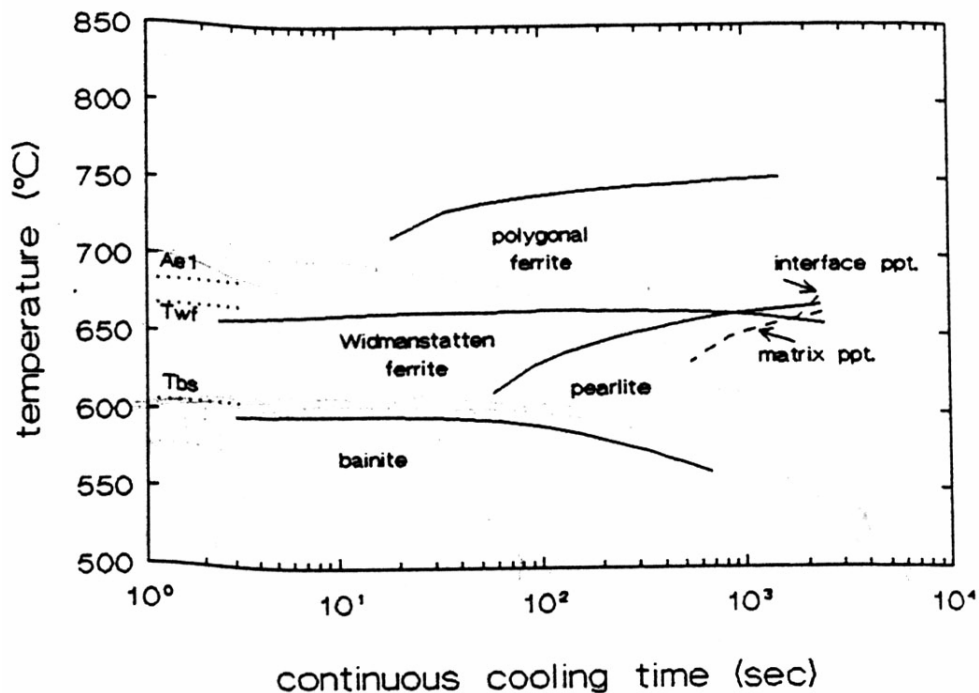


Figure 111 Calculated CCPT diagram of a 0.09% C - 1.46% Mn - 0.028 Nb steel

Zajac and Lagneborg<sup>(122)</sup> observed in a V steel that interphase precipitation forms at temperatures between 800-700 C, and randomly distributed VN particles are most common in samples transformed at 600-650 C. Kwon<sup>(96)</sup> has also found that the precipitation strengthening effect is dependent on the coiling temperature and Nb concentration. The peak strengths shift to higher coiling temperatures as Nb is increased.

Ouchi<sup>(123)</sup> has investigated the effect of cooling rate on ferrite grain size, as well as pearlite and bainite content. One of the observations is that the variation in the cooling rate from 5 to 10 C/sec results in no significant change in grain size, but there is a large increase in bainite content, while the pearlite amount goes to zero at cooling rates faster than 5 C/sec.

Myllykoski<sup>(124)</sup> found that an increase in cooling rate from 5 to 20 C/sec for a 0.03 Nb, and a 0.03 Nb-0.018 Ti, results only in a 1 um grain size refinement. On the other hand, Simecki<sup>(125)</sup> reports a ferrite grain size refinement of 5 um, from 11 to 6 um, with an increasing cooling rate from 1C/sec to 15 C/sec in a Ti-V and a Ti-V-Nb steel.

### **6.6.1 Types of Transformation Product**

The substantial variation of hardness with rate of cooling through the transformation from austenite, illustrated in Figure 82, prompted an examination of the mixture of ferrite and bainite types in the processed samples. The results, presented in Table 24, clearly show that the microstructural mixture is influenced in a systematic fashion not only by variation of the rate of cooling from the finishing temperature to the coiling temperature, but also by variation of the coiling temperature and rate of cooling from the coiling temperature to room temperature.

An examination of how the hardness may depend on the microstructural mix is given in Figure 112. It may be expected that the hardness would increase as the mix shifts from polygonal ferrite to lower bainite, but clearly this is not so. This indicates and supports the position that precipitation is enhanced in the presence of polygonal ferrite. Acicular and bainitic ferrite, on the other hand, retards the kinetics of precipitate formation. There is also considerable variability within a given mixture type.

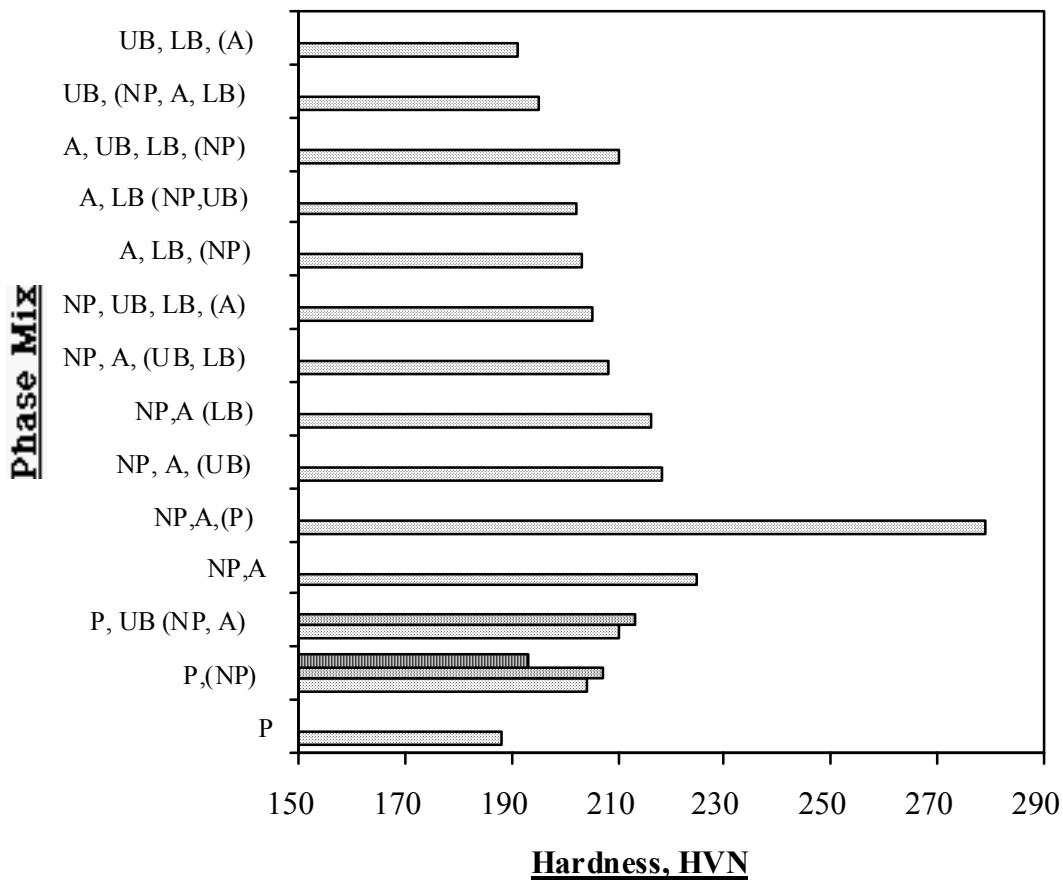


Figure 112 The variation of hardness of samples of Rouge Steel with different microstructural mixtures. The mixtures progress from polygonal ferrite to fully bainitic mixtures. P= Polygonal ferrite, NP=non polygonal ferrite, A=acicular ferrite, LB=lower bainite, UB=upper bainite

## 6.6.2 Precipitation and Cluster Formation

Extensive TEM analysis of the Rouge Steel samples revealed that precipitation occurred in samples coiled at 700 C and 600 C, but not at 550 C. When coiling at 700 C, the average precipitate size was found to be 9.2 nm, whereas at 600 C, the average precipitate size is 4.2 nm. Figures 113 and 114 show dark field micrographs where matrix precipitation can be observed. In Figure 108, where a coiling of 700 C was used, interphase precipitation is also observed. While the smaller particles present after the 600 C coiling treatment are expected to produce a higher yield stress, the observed volume fractions at 600 and 700 C are different. The precipitate contribution obtained from TEM observations at these two coiling temperatures is only 40 MPa.

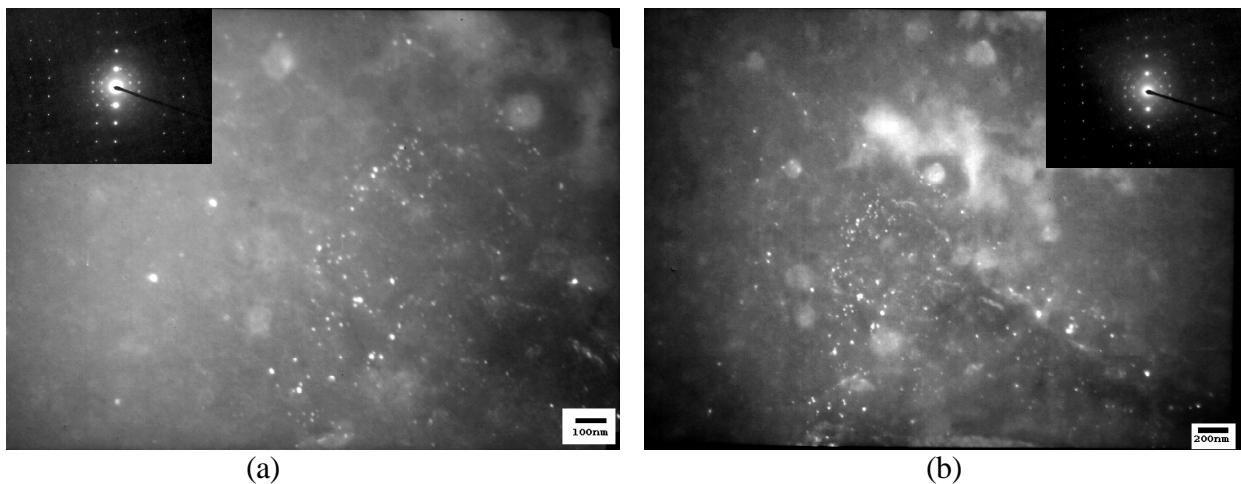


Figure 113 TEM dark field micrographs, (a) and (b). Precipitates formed during coiling, in the ferrite matrix, as observed in the diffraction patterns that show the Baker-Nutting relationship between precipitates and ferrite matrix. Processing conditions: Cooling rate FT to CT 5C/sec, Cooling rate CT to RT 0.01 C/sec, Coiling temperature 600 C.

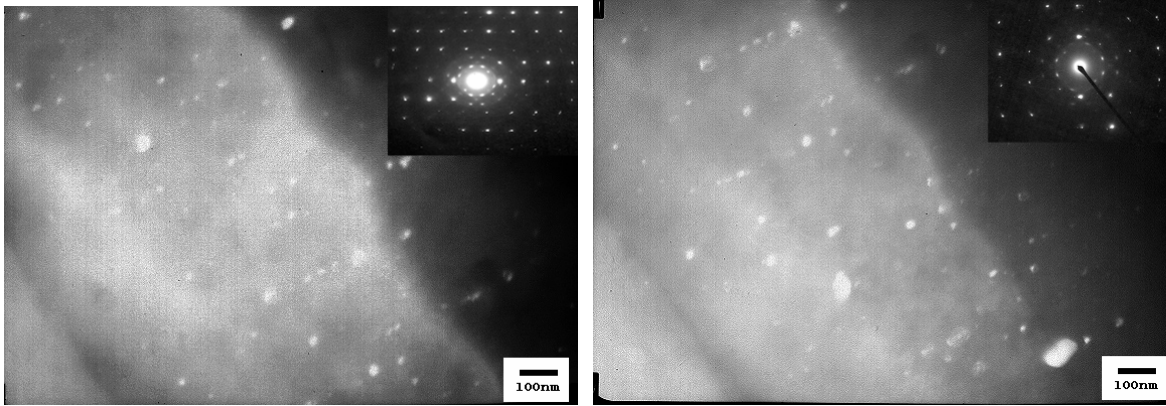


Figure 114 TEM dark field micrographs of precipitates formed during austenite to ferrite transformation as illustrated by the interphase precipitation, and during coiling in the ferrite matrix, as observed in the diffraction patterns showing the Baker-Nutting relationship between precipitates and ferrite matrix. Processing conditions: Cooling rate FT to CT 5C/sec, Cooling rate CT to RT 0.01 C/sec, Coiling temperature 700 C.

The large peak in hardness observed at 600 C is due to the formation of very fine Nb and V containing clusters, like those observed in the hot rolling experiment at the high coiling temperature condition.

Figure 115 shows a sequence of APFIM photographs taken at every five evaporated atomic layers. Here, a series of clusters appears in a ferrite matrix volume of  $3770 \text{ nm}^3$ . Only those bright spots that appear in two consecutive pictures were considered to be clusters. By taking an average cluster size of 1 nm, the cluster volume fraction is  $1.11\text{E-}3$ . This value is very close to the maximum volume fraction amount obtained by adding the calculated maximum NbC and VC precipitates :

$$0.00043 \text{ NbC} + 0.00066 \text{ VC} = 1.09 \text{ E-}3 (\text{NbC} + \text{VC})$$

The strength contribution at this volume fraction and particle size is calculated to be 160 MPa, or as large as 223 MPa if the two particle populations are considered separately. Coiling at 550 C results in no precipitate strengthening, but small Mn containing clusters were observed.

Faster cooling rates, from the FT to CT, and from CT to RT, result in a suppression of precipitation. However, coiling at 600 C, at a 10 C/sec from FT to CT, and only at the 0.01 C/sec from CT to RT, a small peak in hardness is observed. A very low density of clusters was observed.

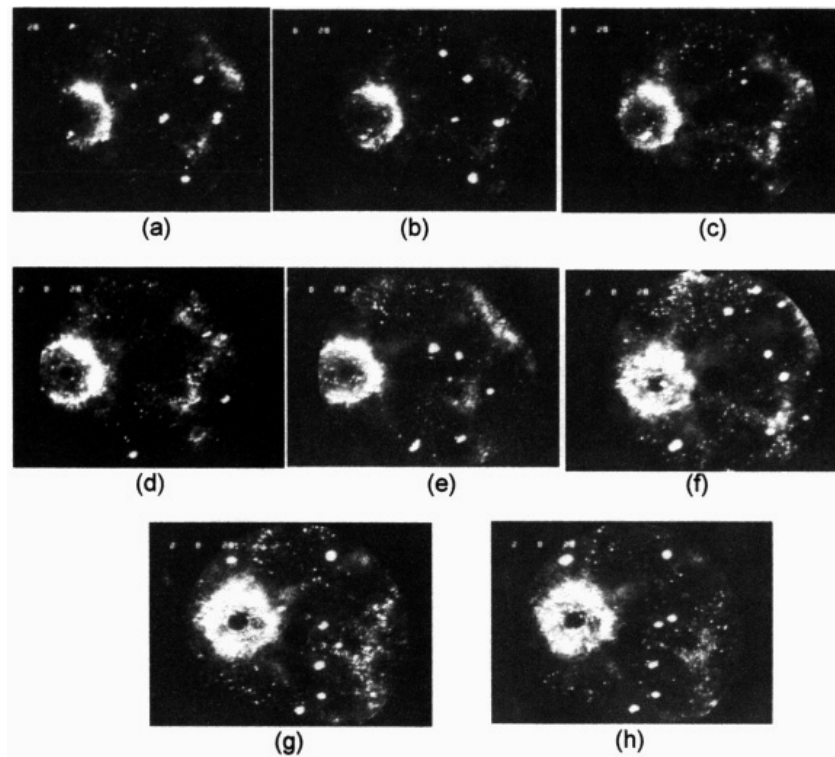


Figure 115 Sequence of APFIM pictures of ultra-fine Nb,V(C,N) particles, taken at every five atomic layer evaporation, with CT = 600 °C. The fine particles are seen to form and disappear around the large probe hole at left-of-center.

## 7.0 CONCLUSIONS

The variation of the hot rolling processing parameters has a significant impact on the variability of the microstructure and tensile properties of HSLA steels.

Different types of ferrite microstructures and phases are observed for different processing conditions: at low coiling temperatures and high finishing temperatures, the volume fraction of polygonal ferrite decreases, and, acicular and bainitic ferrite, as well as carbide phases, i.e. grain boundary cementite, increases. At high coiling temperature and low finishing temperature, polygonal ferrite is observed.

The contributions from the various strengthening mechanisms vary for different processing conditions. At low coiling and high finishing temperature, LAGB's and dislocations become important strengthening mechanisms. At high coiling temperature and low finishing temperature, grain size and fine precipitation are the most important strengthening mechanisms.

The source of variability found in the hot rolling experiment is largest with the variation of coiling temperature, followed by finishing temperature. The variation of roughing temperature results in no significant variability. The maximum measured level of variability in LYP is 12%.

Additional variations in tensile properties are observed for different levels of cooling rates, from the finishing to coiling temperature, and from the coiling temperature to room temperature.

The variability in hardness increases at slow cooling rates from the coiling to room temperature.

A peak in hardness is observed at intermediate coiling temperatures, at slow cooling rates.

An increase in cooling rate from the finishing to coiling temperature decreases the height of the hardness peak.

The large variability found in industry is the result of different cooling rates that are observed within a coil, being also affected by the coiling temperature.

Coiling at 600 C results in the largest variation in properties for different cooling rates.

Coiling at 550 C results in the smallest variation in properties for different cooling rates.

Cooling rates faster than 0.1 C/sec decrease the hardness variability for any given coiling temperature.

## **APPENDICES**

## APPENDIX A

### Processing Conditions and Mechanical Properties of the Individual Hot Bands

Table A Processing conditions of the laboratory hot rolled HSLA steel

<u>Combination of Conditions</u>	Temperature, °C				
	<u>Reheat</u>	<u>Rough</u>	<u>Finish</u>	<u>End Cool</u>	<u>Coil (Nominal)</u>
1111	1200	1059	905	621	550
1112	1200	1051	908	693	650
1121	1200	1059	952	552	550
1122	1200	1116	958	677	650
1131	1200	1042	997	482	550
1132	1200	1061	1003	654	650
1211	1200	1148	913	607	550
1212	1200	1102	1048	-	650
1221	1200	1128	965	566	550
1222	1200	1106	954	677	650
1231	1200	1118	1009	510	550
1232	1200	1116	1006	654	650
2111	1280	1064	910	510	550
2112	1280	1064	906	677	650
2121	1280	-	-	-	550
2122	1280	1055	952	677	650
2131	1280	1066	1004	399	550
2132	1280	1063	999	649	650
2211	1280	-	-	-	550
2212	1280	1162	908	693	650
2221	1280	1162	956	552	550
2222	1280	1151	957	677	650
2231	1280	1159	1007	552	550
2232	1280	1164	1019	638	650

\* Note that for the combinations in Table A, '1' represents the lowest temperature condition level.

Table B LYP and TS values for the different processing conditions, in the rolling direction

Proc. Cond.	Test 1		Test 2		Test 3		Test 4		Avg LYP	Avg UTS
	LYP	UTS	LYP	UTS	LYP	UTS	LYP	UTS		
1111	556	633	528	589	541	604	506	568	541	608
1112	488	559	519	595	514	589	510	579	508	580
1121	496	575	477	556	479	563	479	560	483	563
1122	513	595	506	588	500	586	516	594	509	591
1131	548	638	483	559	502	583	480	560	511	593
1132	550	644	502	590	512	600	491	577	521	611
1211	541		522	589	509	588	519	591	524	588
1212	574	653	540	610	537	600			550	621
1221	516	597	495	579	503	596	474	558	504	590
1222	518	600	525	601	510	597	511	595	516	598
1231	529	619	441	529	510	605			493	584
1232	546	645	525	619	541	632			537	632
2111	484	558	546	616	568	637			532	603
2112	570	656	563	639	564	636	492	570	565	643
2121	511	583	512	582	495	577	501	580	505	580
2122	542	627	550	628	533	613			541	622
2131	536	624	496	581	498	585	500	586	510	596
2132	569	664	521	612	540	626	518	608	543	634
2211	502	577	513	586	491	573	482	569	497	576
2212	560	652	524	600	531	609	533	611	538	620
2221	535	625	526	612	524	604	497	577	528	613
2222	557	638	550	640	551		520	603	552	639
2231	502	600	543	635	517	606			520	613
2232	561	662	542	636	541	637			548	645

Table C LYP and TS values for the different processing conditions, in the transverse direction

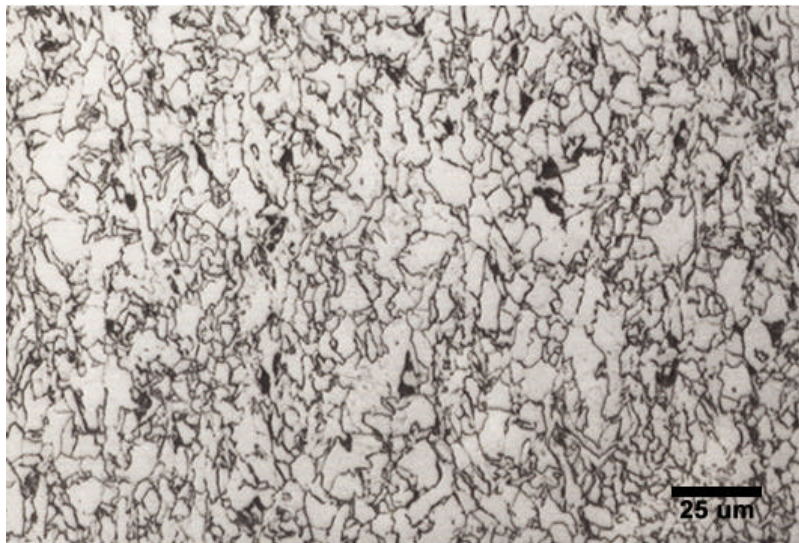
Proc. Cond	Test 1		Test 2		Test 3		Test 4		Avg LYP	Avg UTS
	LYP	UTS	LYP	UTS	LYP	UTS	LYP	UTS		
1111	546	613	546	617	560	622	595	655	562	627
1112	518	592	516	591	524	590	531	593	522	591
1121	497	578	481	570	521	596	478	560	494	576
1122	519	601	521	606	522	598	511	585	518	598
1131	495	588	489	581	474	556	518	605	494	582
1132	534	629	526	616	515	607	517	611	523	616
1211	536	612	528	605					532	608
1212			552	622	599	673	608	678	586	658
1221	529	615	543	627	498	586	522	602	523	607
1222	505	591	504	588	513	596	507	586	507	590
1231	391	488	450	539	406	503	517	607	441	534
1232	513	611	496	600	515	617			508	609
2111	664	733	369	440	528	597			520	590
2112	554	625	565	628	560				560	626
2121	521	595	506	583	514	583	512	582	513	586
2122	536	608	524	599			570	647	543	618
2131	545	631	522	611	318	414	520	610	529	617
2132	549	643	550	634	500	600	565	654	541	633
2211	513	590	511	590	511	588	513	587	512	589
2212	470	545	237	320	528	601	570	651	522	599
2221	432	507	507	585	531	609	517	595	497	574
2222	564	648	551	637	560	653	570	650	561	647
2231	485	594	473	576	487	551			481	574
2232	487	587	532	635	491	592			503	604

Table D LYP and TS values for the different processing conditions, in the diagonal direction

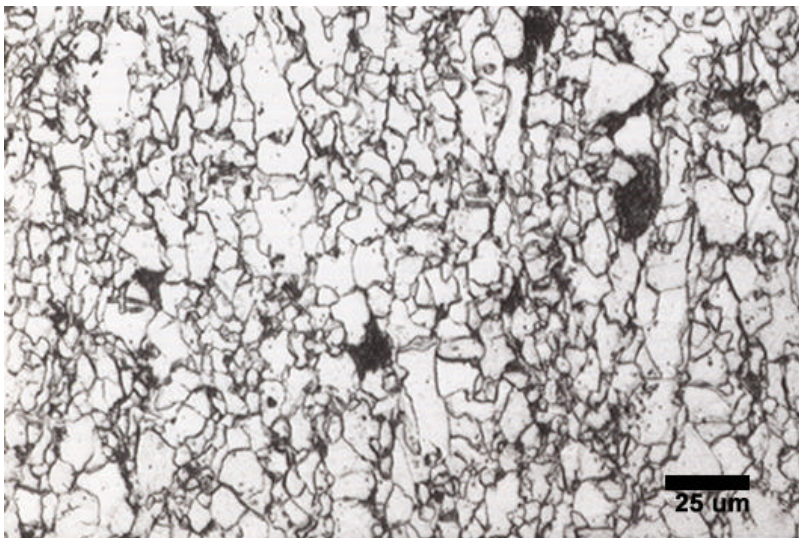
Proc. Cond	Test 1		Test 2		Test 3		Test 4		Avg LYP	Avg UTS
	LYP	UTS	LYP	UTS	LYP	UTS	LYP	UTS		
<b>1111</b>					518	574	540	597	529	585
<b>1131</b>	491	567	493	571	498	579	491	572	493	572
<b>1132</b>	510	600	521	607	479	565	546	630	514	600
<b>1211</b>	514	581	520	591	521	588	542	607	524	592
<b>1212</b>					521	590			521	590
<b>1221</b>	482	562	489	566	502	583	504	586	494	574
<b>1231</b>	456	541	467	546	465	547	470	561	464	549
<b>1232</b>					527	614	511	602	519	608
<b>2111</b>	526	597	537	605	542	609	533	603	534	603
<b>2112</b>	520	585	515	578	542	600	545	606	530	592
<b>2122</b>	532	610	520	601	538	617	532	608	530	609
<b>2131</b>	508	595	504	591	505	593	498	582	504	590
<b>2132</b>	516	594	516	596	528	611	532	617	523	604
<b>2212</b>	530	601	533	610	528	601	536	607	532	605
<b>2221</b>	526	606	513	591	533	610	523	600	524	602
<b>2222</b>	529	610	523	608	533	609	530	603	529	607
<b>2231</b>	520	606	495	587	508	594	488	580	503	592
<b>2232</b>	526	622	528	624	524	618	541	632	530	624

## APPENDIX B

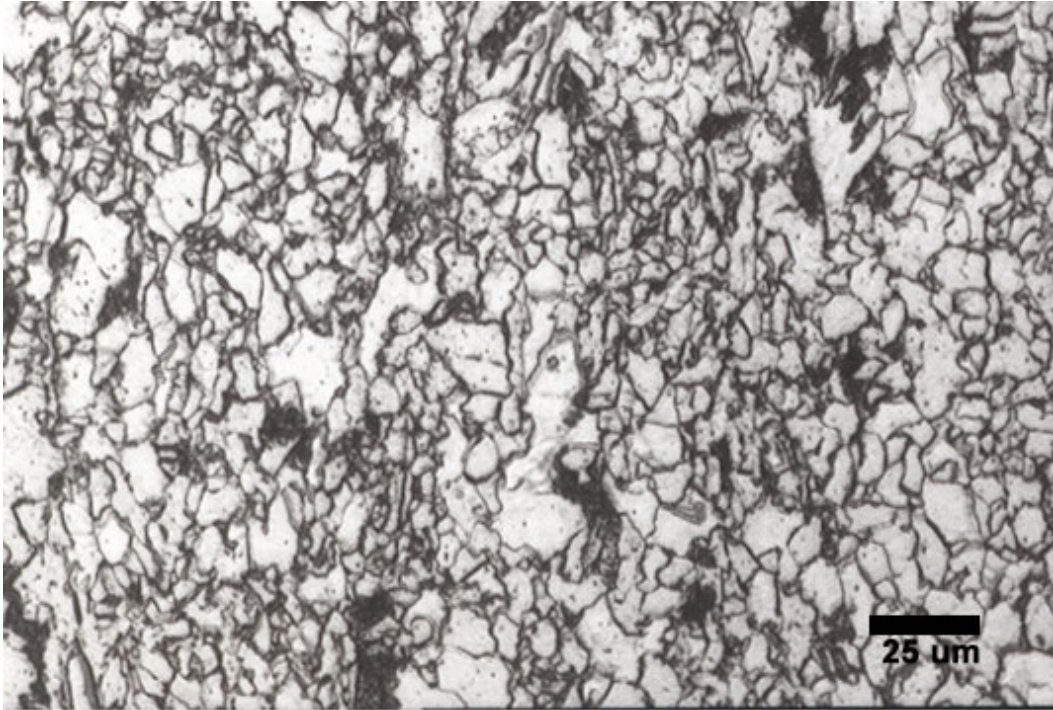
### Micrographs of the Various Hot Bands Obtained After the Laboratory Hot Rolling Trials



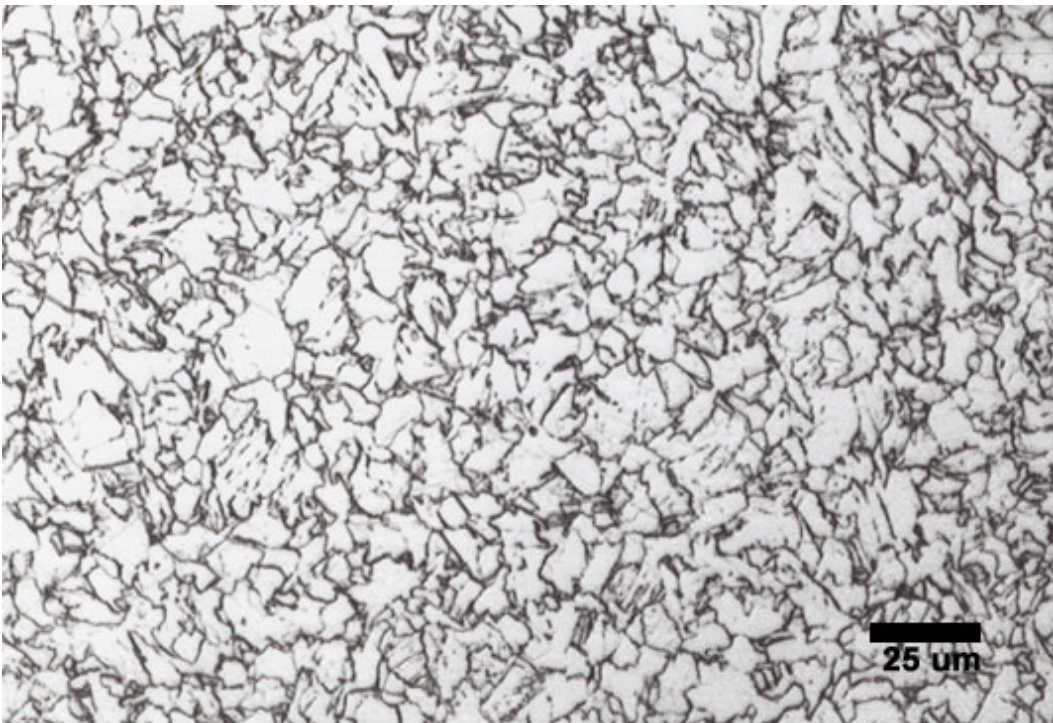
B-1 Processing Condition 1111



B-2 Processing Condition 1112



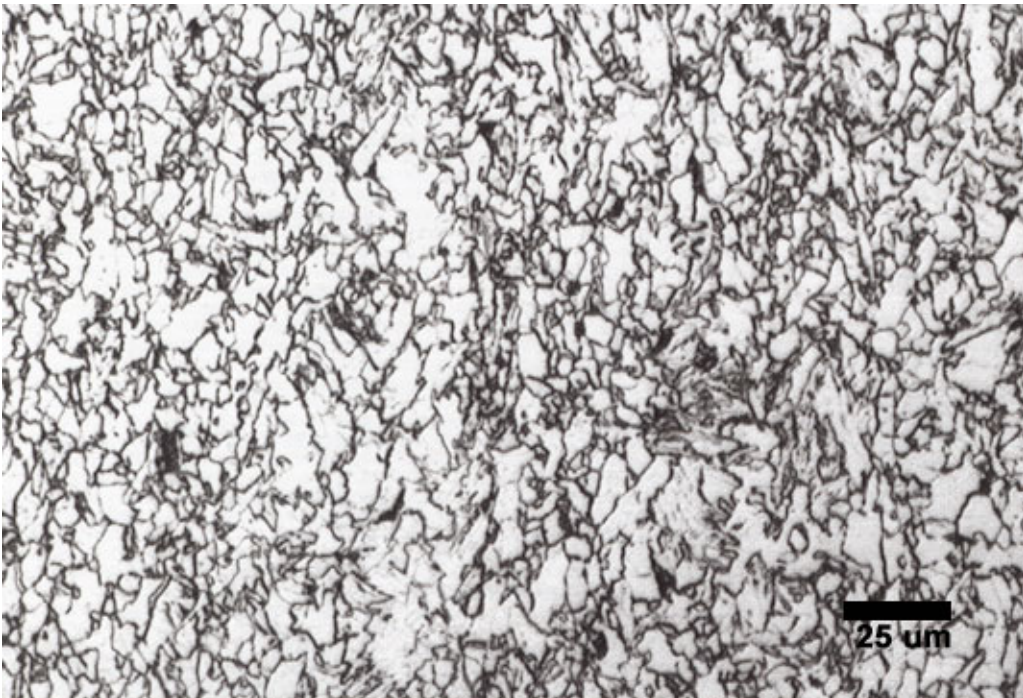
B-3 Processing Condition 1122



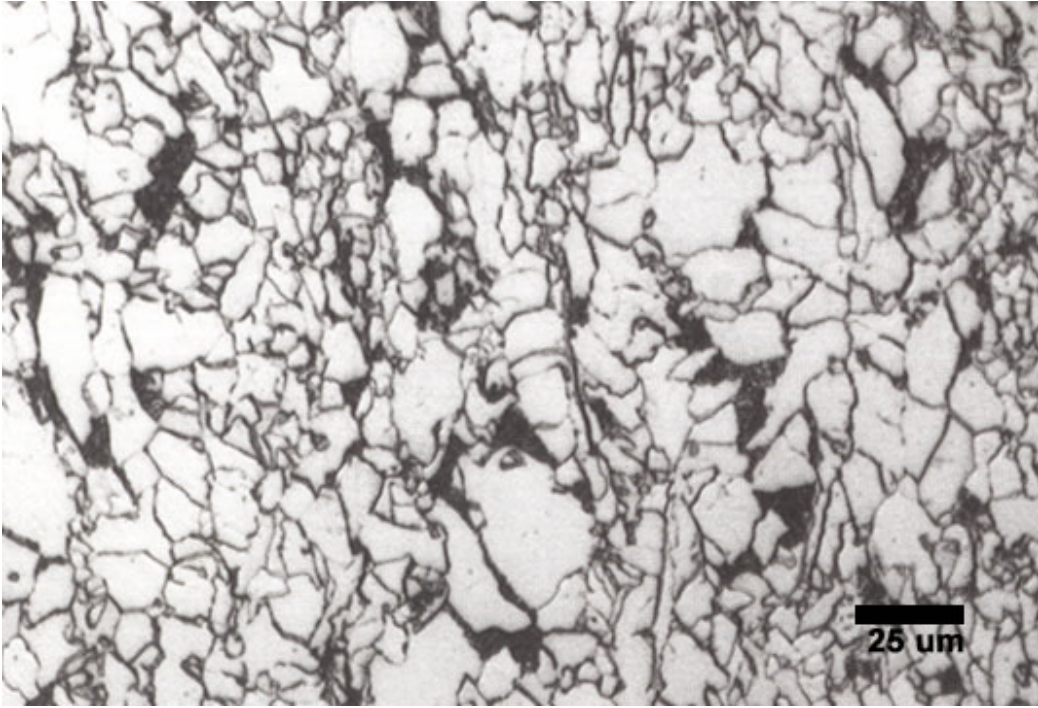
B-4 Processing Condition 1131



B-5 Processing Condition 1132



B-6 Processing Condition 1211



B-7 Processing Condition 1212



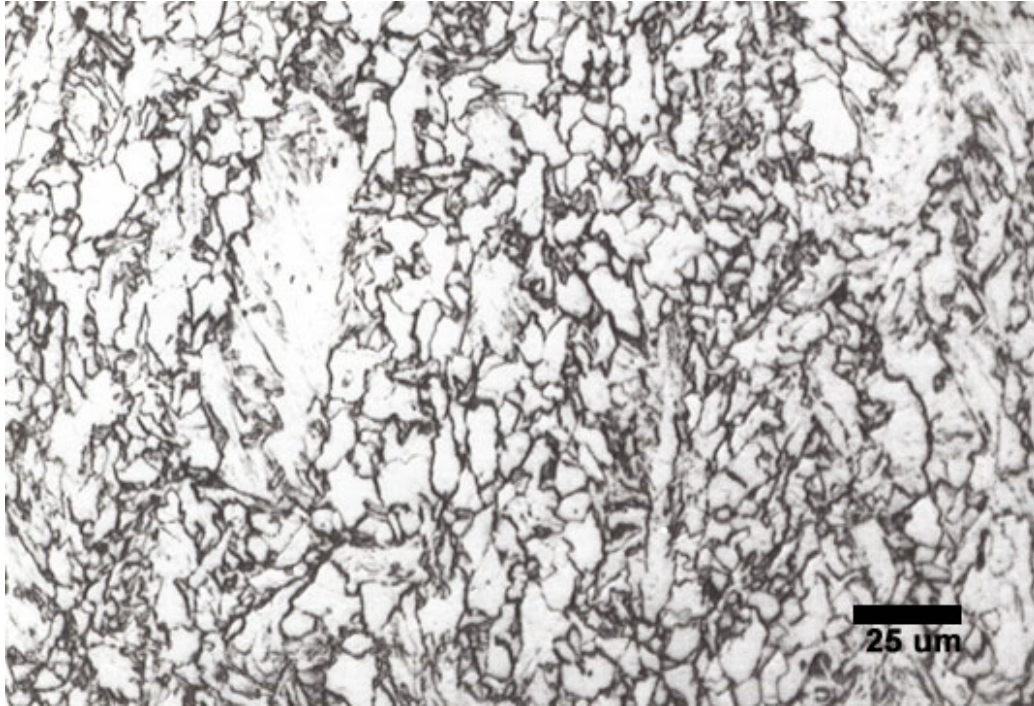
B-8 Processing Condition 1221



B-9 Processing Condition 1231



B-10 Processing Condition 1232



B-11 Processing Condition 2111



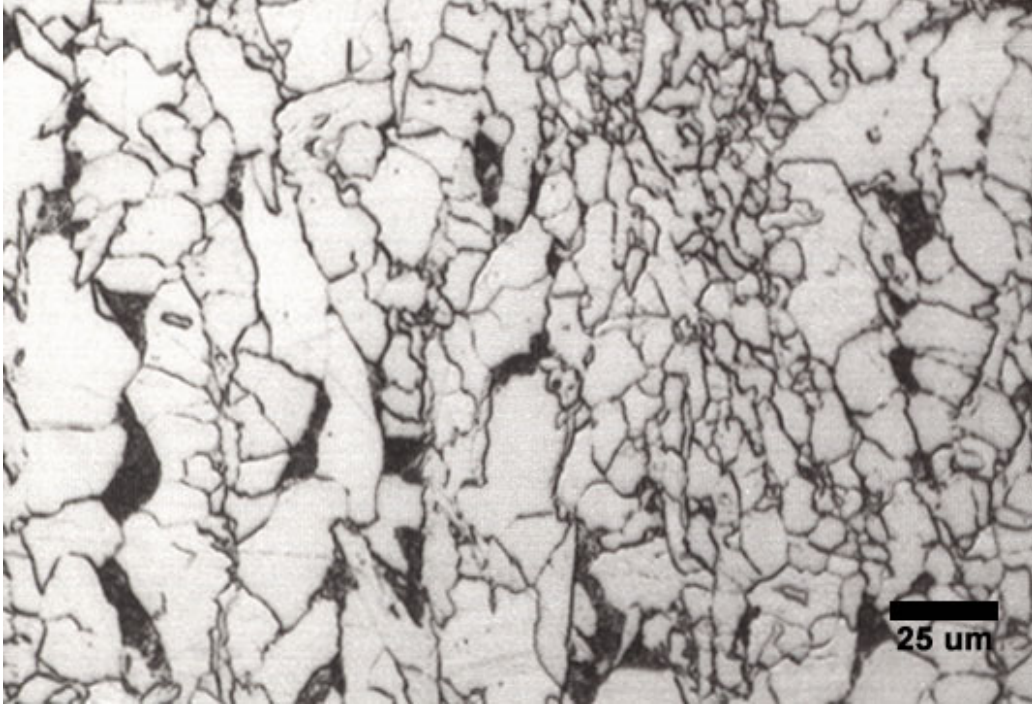
B-12 Processing Condition 2112



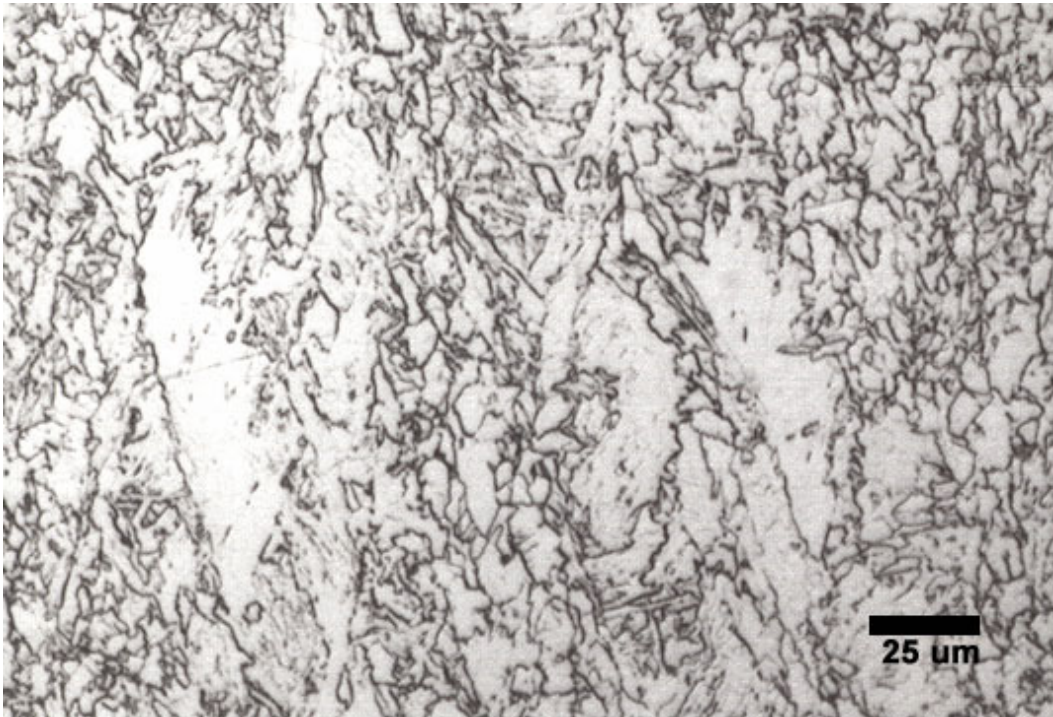
B-13 Processing Condition 2122



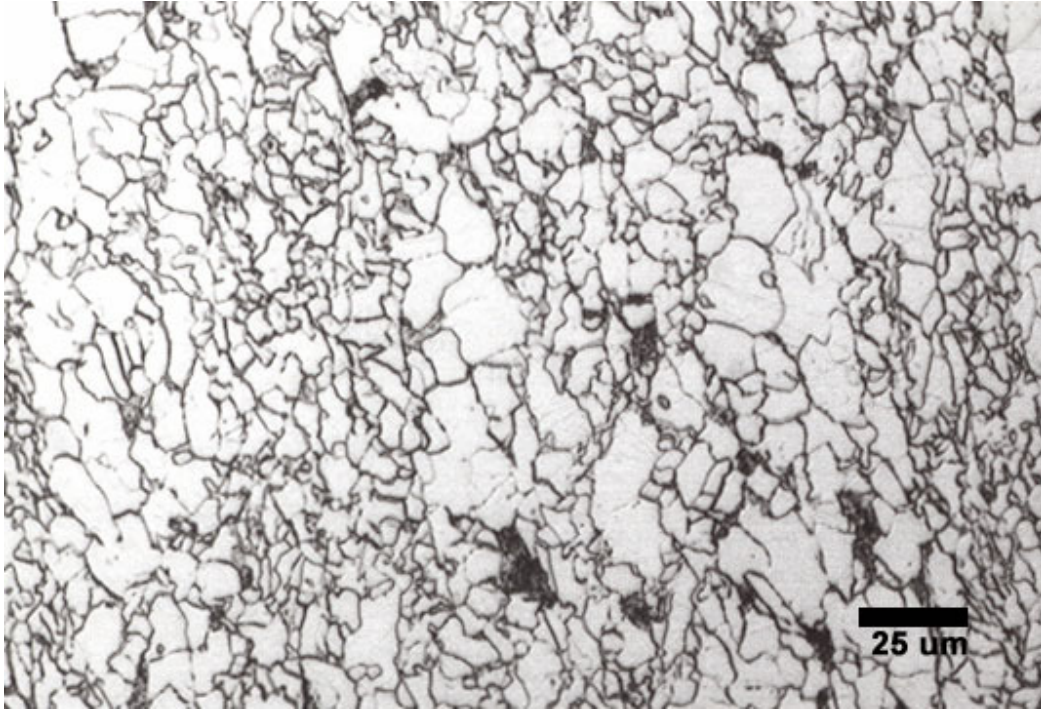
B-14 Processing Condition 2131



B-15 Processing Condition 2212



B-16 Processing Condition 2221



B-17 Processing Condition 2222



B-18 Processing Condition 2231



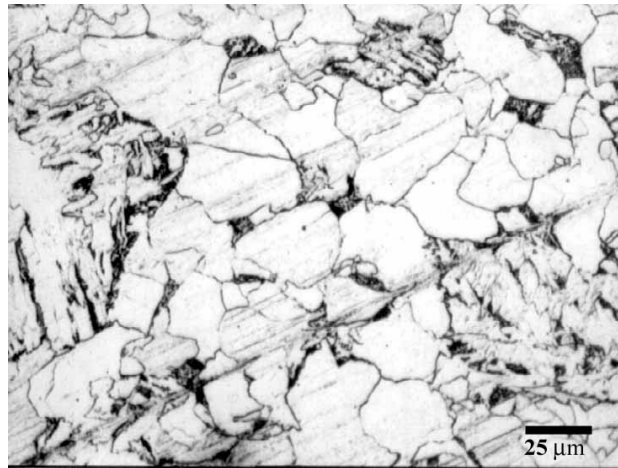
B-19 Processing Condition 2232

## APPENDIX C

### Micrographs from Cooling Rate Experiment with Rouge Steel

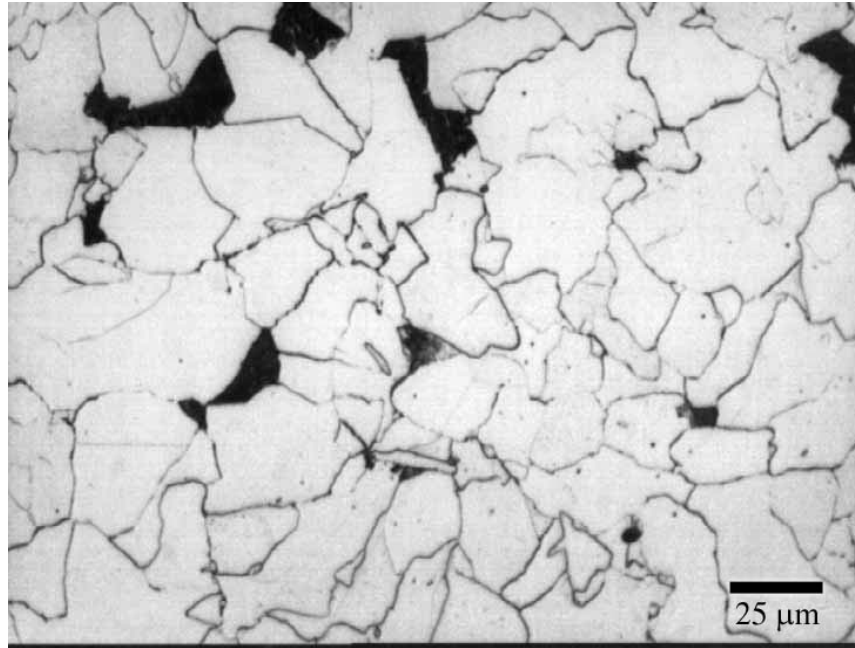


C-1 700 C, 5 C/sec, 1 C/sec

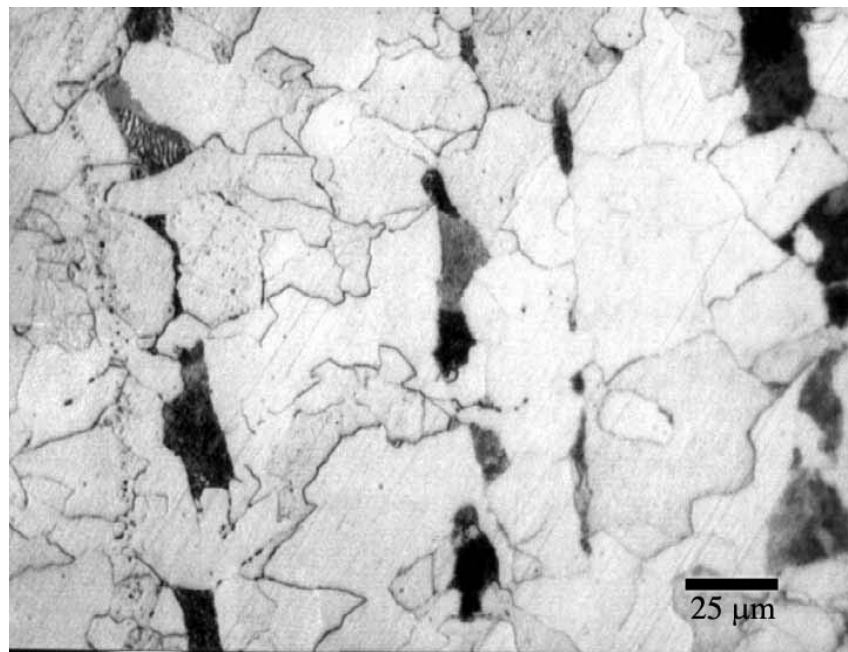


C-2 700 C, 10 C/sec, 1 C/sec

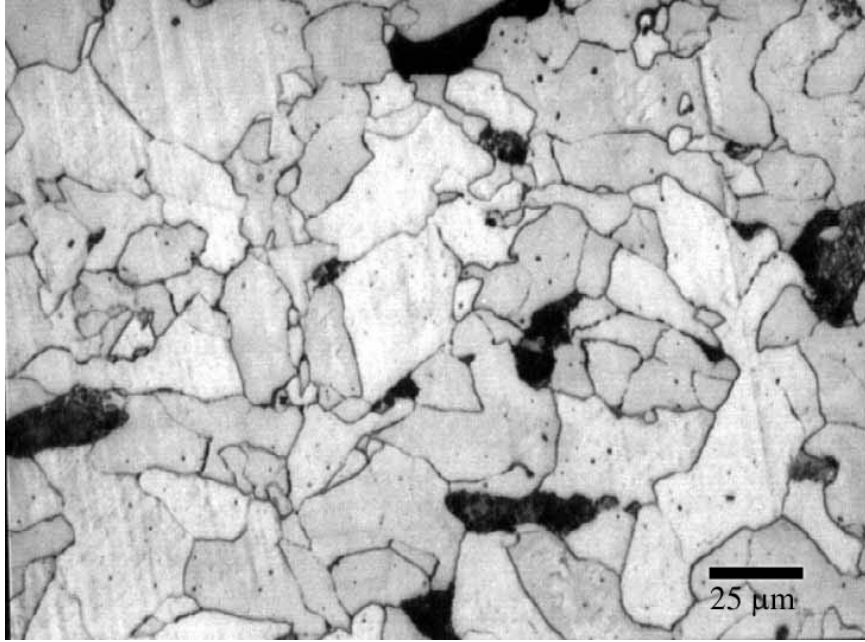
\* Text in figures refers to coiling temperature, cooling rate from the finishing to coiling temperature, and cooling rate from the coiling to room temperature, respectively.



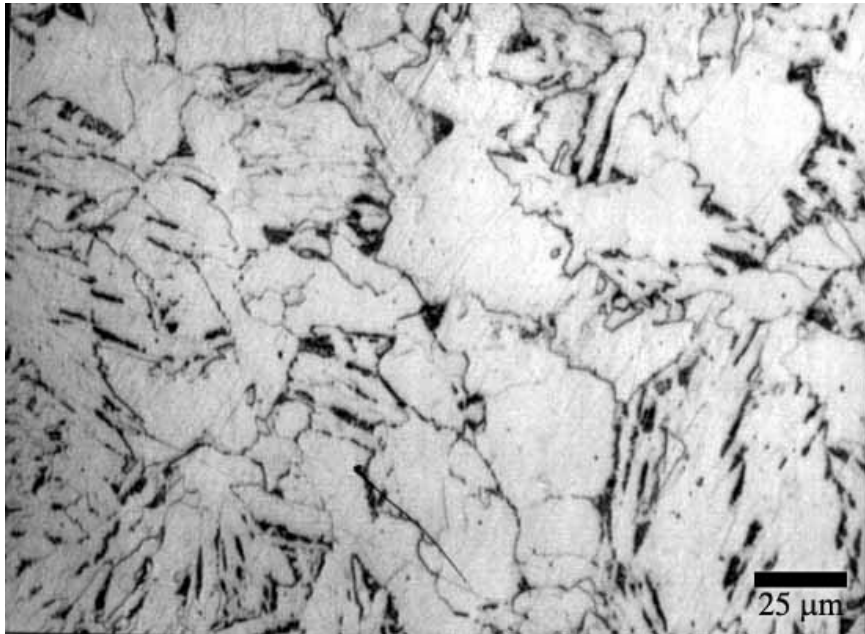
C-3 700 C, 10 C/sec, 0.1 C/sec



C-4 700 C, 5 C/sec, 0.01 C/sec



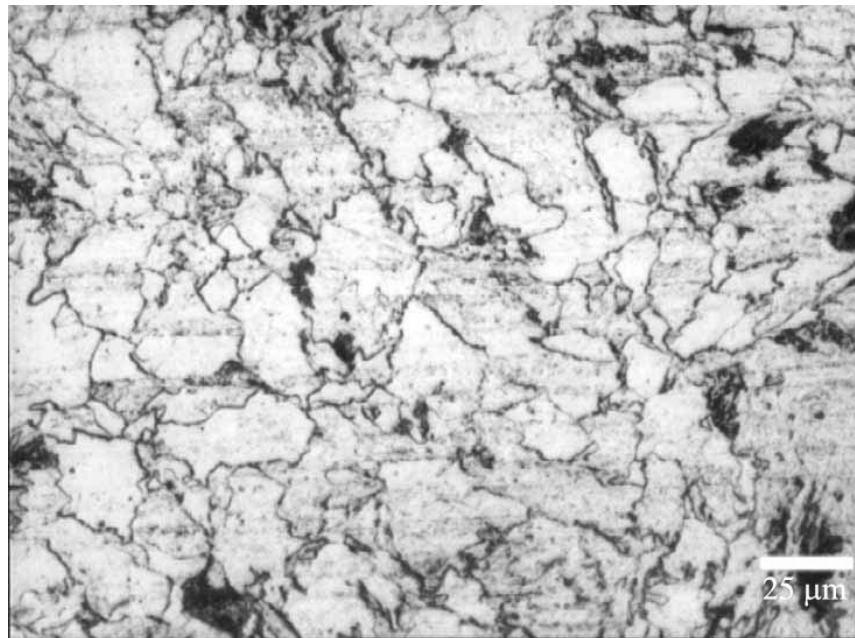
C-5 700 C, 10 C/sec, 0.01 C/sec



C-6 600 C, 5 C/sec, 1 C/sec



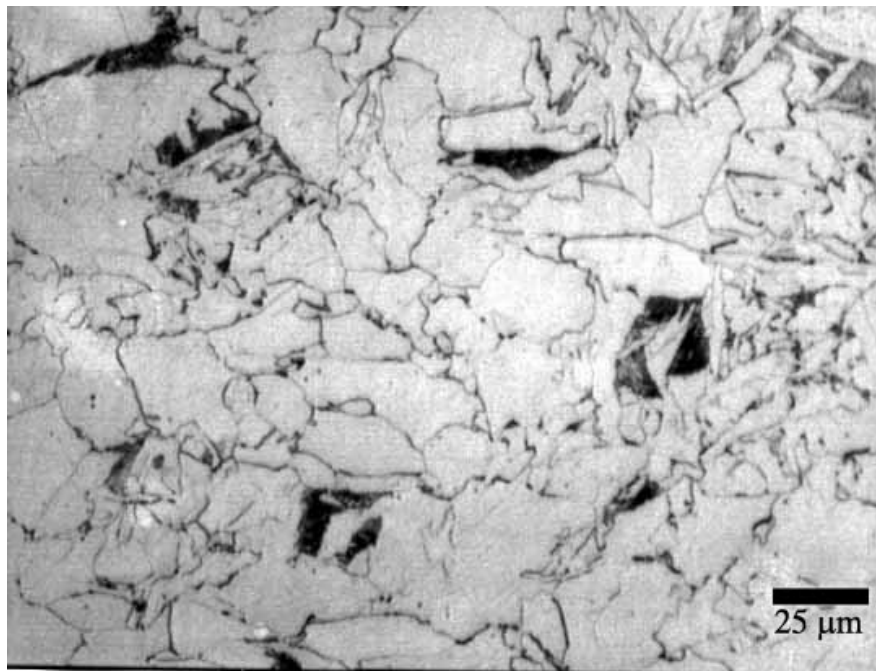
C-7 600 C, 10 C/sec, 1 C/sec



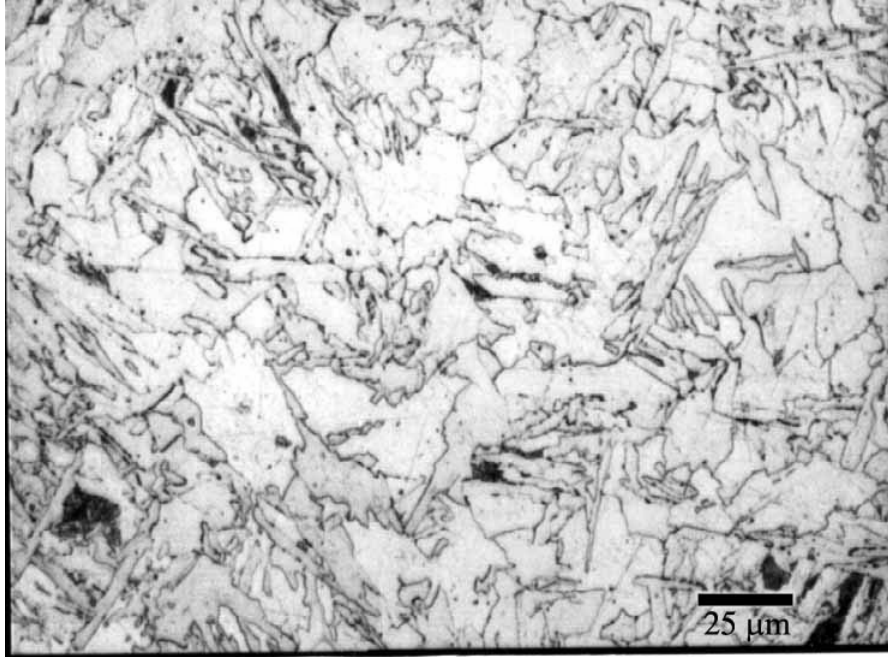
C-8 600 C, 5 C/sec, 0.1 C/sec



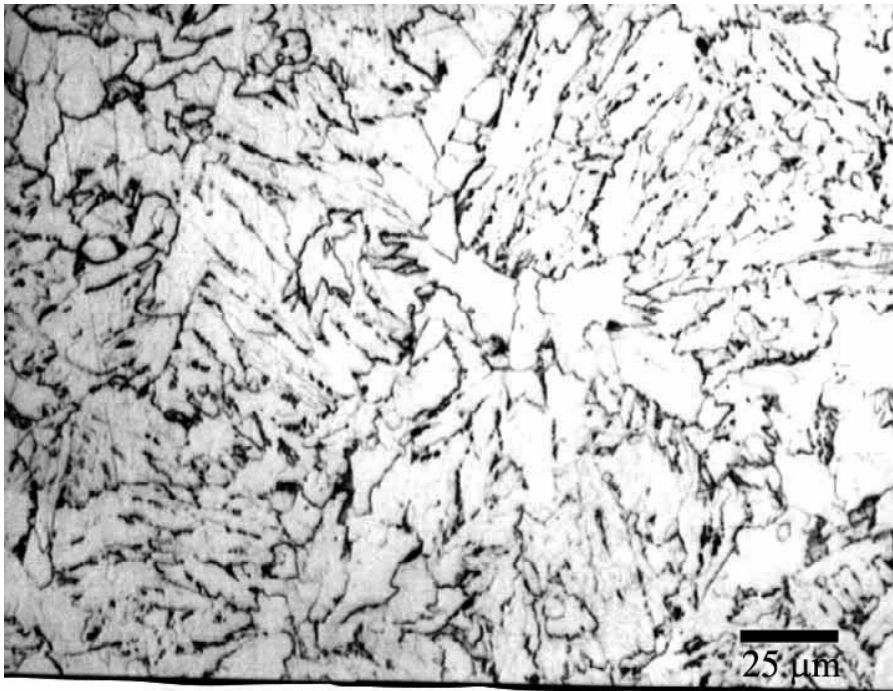
C-9 600 C, 10 C/sec, 0.1 C/sec



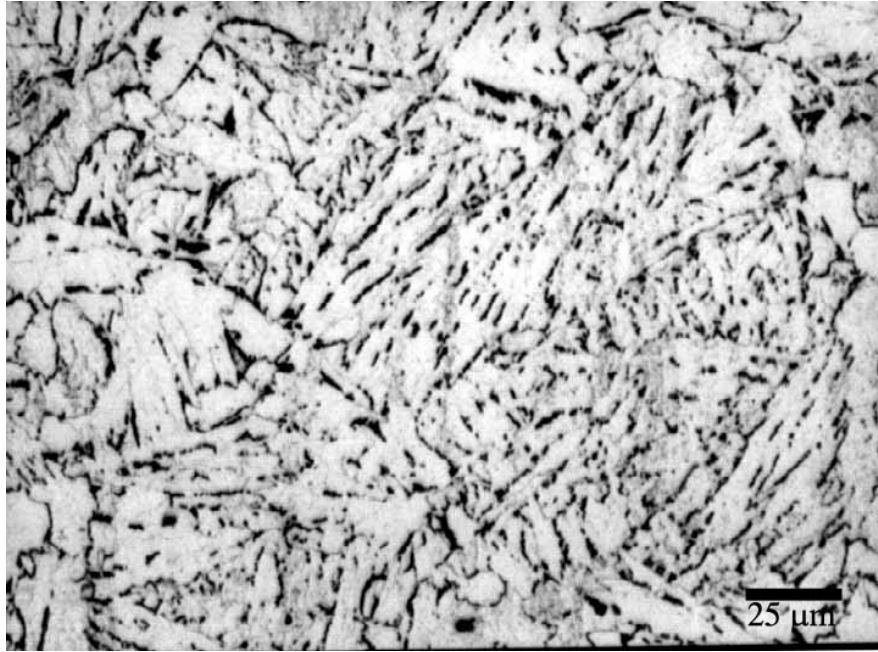
C-10 600 C, 5 C/sec, 0.01 C/sec



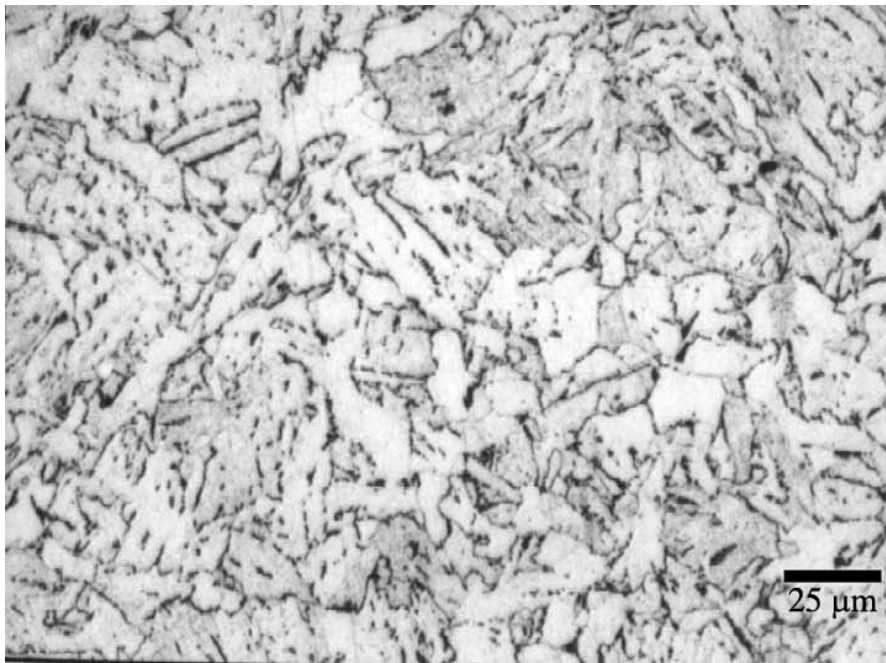
C-11 600 C, 10 C/sec, 0.01 C/sec



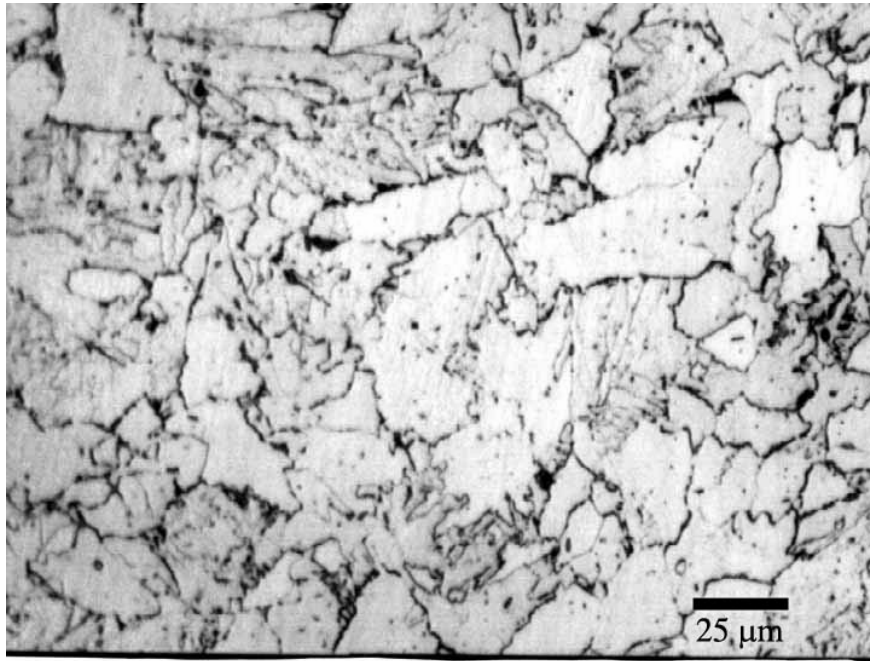
C-12 550 C, 5 C/sec, 1 C/sec



C-13 550 C, 10 C/sec, 1 C/sec



C-14 550 C, 10 C/sec, 0.1 C/sec



C-15 550 C, 5 C/sec, 0.01 C/sec



C-16 550 C, 10 C/sec, 0.01 C/sec

## **BIBLIOGRAPHY**

## BIBLIOGRAPHY

1. E. Oren, "Automotive Materials and Technologies for the 21<sup>st</sup> century", Ironmaking and Steelmaking 25, 1998, pp 67-71
2. Jared Stein, "The Effect of Process Variables on Sheet Metal Springback", SAE Paper No. 982299, 1998, pp. 65-73.
3. E. Oren and W. Ptashnik, "Improvements in the Uniformity of High Strength Automotive Sheet Steels", Proceedings of the 40<sup>th</sup> Mechanical Working and Steel Processing Conference, Pittsburgh 1998, pp 11
4. J. K Patel, P.J Evans, "The Effect of Processing Conditions on the Consistency or Mechanical Properties for Nb-HSLA strip steels", Proceedings of the 41<sup>st</sup> Mech. Work and Steel Proc. Conf., Baltimore MD, 1999, pp445-458
5. A. J. DeArdo, "The Physical Metallurgy of Thermomechanical Processing of MA steel", Proceedings of Thermec '97, edited by T. Chandra and T. Sakai, TMS, vol 1, 1997, pp13-30
6. M. Cohen, S. Hansen, "On the Fundamentals of HSLA Steels", Proceedings of an International Conference on HSLA Steels '85, Metallurgy and Applications, Beijing, China, edited by J.M Gray, ASM International, 1986, pp 61-71
7. H. DeBoer, et al., "Thermomechanical Treatment of HSLA Steels Fundamentals and Recrystallization", Proceedings of an International Conference on HSLA Steels '85, Metallurgy and Applications, Beijing, China, edited by J.M Gray, ASM International, 1986, pp 548
8. E.J. Palmiere, University of Pittsburgh, Unpublished Research, 1990.
9. L.J. Cuddy and J.C. Raley, "Austenite Grain Coarsening in Microalloyed Steels", Metall. Trans. A, 1983, vol 14A, pp 1989-1995
10. Llewellyn, "Steels, Metallurgy and Applications", Reed International, 1992, pp 75
11. I. Weiss et al., "The Influence of Nb, V and N, on the response of Austenite to Reheating and Hot Deformation in MA Steels", Proceedings of Therm. Proc. of MA 95, pp 51

12. A.J. DeArdo, "Fundamental Metallurgy of Nb in Steels", The International Symposium Niobium 2001, AIME-TMS, 2001
13. R.M. Poths, R.L. Higginson, and E.J. Palmiere, "Complex Precipitation Behavior in a Microalloyed Plate Steel", Scripta Materiala, vol 44, 2001, pp 147-151
14. I. Weiss, G.L. Fitzsimons, et al, "The influence of Nb, V and N on the response of Austenite to Reheating and Hot Deformation in Microalloyed Steels", Proceedings of the International Conference on the Thermomechanical Processing of Microalloyed Austenite, edited by A.J. DeArdo, AIME,1981, pp 33-58
15. R.K. Amin and F.B. Pickering, "Austenite grain coarsening and the effect of TMP on Austenite Recrystallization", Proc. Therm. Proc of MA 95, pp 1-30
16. R.K. Amin and F.B. Pickering, Proc. Therm. Proc of MA 95, pp 14
17. C. Zener, quoted by C.S Smith, Trans AIME, 175 (1948), pp 47
18. T. Gladman, "Grain Refinement in Multiple Microalloyed Steels", HSLA Steels, Processing, Properties and Applications, ed. by G. Tither, TMS, 1992, pp4-6
19. T. Glandman, "On the Theory of Precipitate Particles on Grain Growth in Metals", Proc. Roy. Soc., Series A, 294(1966), pp 298
20. T. Gladman, Encyclopedia of Materials Science and Engineering, ed, M.M. Bever, 1986, pp 2045
21. M. Hillert, Acta Metallurgica, Vol.13, 1965. pp 227
22. O. Kwon and A.J DeArdo, "Interactions between Recrystallization and Precipitation in Hot-Deformed MA Steels", Acta Metall. Mater., v 39, N4, 1991, pp 537
23. M. Militzer, E. Hawbolt, T. Meadowcroft, "Microstructural Model for the Hot Strip Rolling of High Strength Low Alloy Steels", Metallurgical and Materials Transactions A, Vol 31A, April 2000, pp 1244
24. L.J. Cuddy, "The Effect of Microalloy Concentration on the Recrystallization of Austenite during Hot Deformation", Proceedings of Thermomechanical Processing of MA Austenite, ed A. J. DeArdo, G. Ratz, TMS-AIME, 1982, pp129
25. I. Tamura and C. Ouchi, Thermomechanical Processing of High Strength Low alloy Steels, 1988, pp 82
26. A.J. DeArdo, C.I. Garcia, E.J Palmiere, "Thermomechanical Processing of Steels", ASM Metals Handbook, vol 4, Heat Treating, 1991, pp237-255

27. O.Kwon, "Static Recovery and Recrystallization of Hot Deformed FCC Materials", PhD Dissertation, University of Pittsburgh, 1985
28. Llewellyn, "Steels, Metallurgy and Applications", Reed International, 1992, pp76
29. D.Q. Bai, S. Yue, "Effect of Deformation Parameters on the no-rxn temperature, in Nb bearing Steels", Met. Trans. A, vol 24A, N10, 1993, pp 2151
30. F.J. Humphreys, M. Hatherly, "Recrystallization and Related Annealing Phenomena" Pergamon, Elsevier Science, 1996
31. M. Korchynsky, "Twenty Years since Microalloying '75", Proceedings of Therm. Proc. of MA '95, pp 6
32. Yamamoto, Ouchi, "The Effect of Microalloying Elements on the Recovery and Recrystallization in deformed Austenite", Proceedings of the International Conference on the Thermomechanical Processing of Microalloyed Austenite, edited by A.J. DeArdo, AIME,1981, pp 613
33. S.S Hansen et al., "Niobium Carbonitride Precipitation and Austenite Recrystallization in Hot Rolled MA Steels", Metall. Trans A, 19BO, Vol 11A, 387
34. F.B. Pickering, Physical Metallurgy and the Designs of Steels, Materials Science Series, Applied science publishers LTD, 1978, pp33
35. H. Nordberg, B. Aronsson, J. Iron and Steel Institute, vol 206, 1968, pp1263
36. F.B. Pickering, Physical Metallurgy and the Designs of Steels, Materials Science Series, Applied science publishers LTD, 1978, pp 68
37. J.D. Grozier, "Production of MA strip and plate by controlled cooling", Proceedings of MA 75, 1975, edited by M. Korchynsky, 1977, pp 245
38. M. Militzer, E. Hawbolt, T. Meadowcroft, "Microstructural Model for the Hot Strip Rolling of High Strength Low Alloy Steels", Metallurgical and Materials Transactions A, Vol 31A, April 2000, pp 1245
39. K. Narita, Transactions from the Iron and Steel Institute, Japan, vol 15, 1975, pp147
40. T. Gladman, "Grain Refinement in Multiple Microalloyed Steels", HSLA Steels, Processing, Properties and Applications, ed. by G. Tither, TMS, 1992, pp 3
41. K. Hulka, et al., "High Temperature Thermomechanical Processing Background and Application", Proceedings of MA 95, ISS 1995, pp 239

42. T. Araki, M. Enomoto, "Microstructural Problems of Controlled Rolled and Cooled Very Low Carbon Hsla Steels" Proceedings of the 2<sup>nd</sup> International Conference on HSLA Steels: Processing, Properties and Applications, edited by G. Tither, TMS, Beijing, China, 1990, pp95
43. I. Madariaga, I. Gutierrez "Role of the Particle-Matrix Interface on the Nucleation of Acicular Ferrite in a Medium Carbon Microalloyed Steel", Acta Materiala, Vol 47, No. 3, 1999
44. A.M Sage, "An Overview of the Use of Microalloys in HSLA Steels with particular reference to Vanadium and Titanium", Proceedings of the 2<sup>nd</sup> International Conference on HSLA Steels: Processing, Properties and Applications, edited by G. Tither, TMS, Beijing, China, 1990, pp 52
45. T. Gladman, "The Physical Metallurgy of HSLA Steels", Chapter 3, The Institute of Materials, 1997, pp 102
46. T. Gladman, "The Physical Metallurgy of HSLA Steels", Chapter 5, The Institute of Materials, 1997, pp 207
47. T. Gladman, "The Physical Metallurgy of HSLA Steels", Chapter 5, The Institute of Materials, 1997, pp 188
48. O. Kwon and A.J DeArdo, "Interactions between Recrystallization and Precipitation in Hot-Deformed MA Steels", Acta Metall. Mater., v 39, N4, 1991, pp 534-535
49. J.J. Jonas and I. Weiss, "Effect of precipitation on recrystallization in MA Steels", Metal Science, 1979, pp 238-245
50. W.C Leslie, Physical Metallurgy, Vol 2, chapter 17, Edited by Cahn and Haasen, Elsevier Science, 1996, pp 1569
51. J.M. Gray, A.J DeArdo, "Austenite Conditioning Alternatives for Microalloyed Steel Products", Proceedings of an International Conference on HSLA Steels '85, Metallurgy and Applications, Beijing, China, edited by J.M Gray, ASM International, 1986 , pp 83
52. T. Gladman, "The Physical Metallurgy of HSLA Steels", Chapter 5, The Institute of Materials, 1997, pp 199
53. H. Takechi, H. Kato, "Rolling and Annealing Textures of Low Carbon Steel Sheets", Transactions of the Metallurgical Society of AIME, vol 242, 1968, pp56-65
54. G.E. Dieter, "Mechanical Metallurgy", Chapter 6, McGraw-Hill, 3<sup>rd</sup> Edition, 1986, pp190
55. E.O. Hall, Proceedings from the Physical Society, 1951, vol 64B, pp 747

56. N.J. Petch, "The Cleavage Strength of Polycrystals ", Journal of the Iron and Steels Institute, vol 174, 1953, pp25-28
57. T. Gladman and F.B. Pickering, "Yield, Flow and Fracture of Polycrystals", ed T.N. Baker, London, Applied Science Publishers, pp141, 1983
58. J. Irvine et al., " Grain Refined C-Mn Steels", Journal of the Iron and Steel Institute, vol 205, 1967, pp161-182
59. N.J Petch, "Theory of the Yield Point and of Strain-Aging in Steel", Advances in Physical Metallurgy, ed J. A Charles and G.C. Smith, The Institute of Metals, 1990, pp 11-12
60. B. Mintz, "Importance of  $K_y$  (Hall-Petch Slope) in determining strength of steels", Metals Technology, vol 11, 1984, pp 265-272
61. B. Mintz, H. Ke, G.D. Smith, " Grain size Strengthening and its Relationship to Grain Boundary Segregation of Carbon", Materials Science and Technology, vol 8, 1992, pp537-540
62. T. Gladman, "The Physical Metallurgy of HSLA Steels", Chapter 7, The Institute of Materials, 1997, pp 286
63. F.B. Pickering, Physical Metallurgy and the designs of steels, Materials Science Series, Applied science publishers LTD, 1978, pp65
64. M.F. Ashby, "Strengthening Methods in Crystals" edited by A. Kelly and R.B. Nicholson, Elsevier Science, London. 1971, pp137
65. R.W. Honeycombe, F.B. Pickering, "Ferrite and Bainite in Alloy Steels", Metallurgical Transactions, vol 3, 1972, pp 1099-1112
66. R.W.K. Honeycombe, G.M. Smith," Yield Point in Microalloyed Ti Steels", 6<sup>th</sup> International Conference on the Strength of Metals and Alloys, edited by R.C. Gifkins, vol 1, 1982, pp 407-412
67. M. Takahashi and H. Bhadeshia, "Model for transformation from upper to lower bainite", Materials Science and Technology, 1990, vol 6, pp 592
68. E. Orowan, "The Theory of Yield without particle shear", Symposium on Internal Stresses in metals and alloys, 1948, London Institute for metals. Pp 451
69. R.B. Nicholson, "Effect of Second Phase Particles on the Mechanical Properties of Steel", Iron and Steel Institute, London, 1971, pp1

70. M.F. Ashby, "The Theory of the Critical Shear Stress and work hardening of dispersion hardened crystals", Proc. of Oxide Dispersion Strengthening, 1966, Ed by Ansell, 1968 pp 143
71. T. Gladman, "Structure-Property Relationships in High- Strength MA Steels", Proceedings of MA'75, Washington, 1975. pp 37
72. J.C. Li, "Petch Relation and Grain Boundary Sources, Transactions of the Metallurgical Society of AIME, vol, 227, 1963, pp 239
73. I. Kozasu, "Hot Rolling as a High Temperature Thermo-Mechanical Process", Proceedings of MA'75, Washington, 1975 pp 130.
74. I. Kozasu, "Hot Rolling as a High Temperature Thermo-Mechanical Process", Proceedings of MA'75, Washington, 1975 pp 129
75. R. Herberz, H. Wiegels, Stahl Eisen, vol 101, 1981, pp29
76. Electroless Nickel Plating, Metals Handbook, vol 5; Surface cleaning finishing and coating , 9<sup>th</sup> Edition, ASM, 1982, pp219-243
77. S.S. Brener and M.K. Miller, "Atomic Scale Analysis with the Atom Probe", Journal of Metals, vol 35(3), 1983, pp 54-58
78. Jack Washburn, "Strain Hardening", Strengthening Mechanisms in Solids, Papers presented at a Seminar of the American Society for Metals, Oct., 1960, pp51-57
79. Standard Methods of Tension Testing of Materials, ASTM Designation E8-69, "Annual Book of ASTM Standards", ASTM
80. J.E. Garcia, J. Wu, A.J. DeArdo, P. Wray, "Reducing the Variability of HSLA Sheet Steels", AISI and DOE Technical Roadmap Program, Project No. 9807, 5<sup>th</sup> Quarterly Report, 2000
81. P. J. Wray, "The Quantitative Description of Grain Structures", BAMPRI Memorandum, June 30, 1999.
82. J.E. Garcia, J. Wu, A.J. DeArdo, P. Wray, "Reducing the Variability of HSLA Sheet Steels", AISI and DOE Technical Roadmap Program, Project No. 9807, 7<sup>th</sup> Quarterly Report, 2001
83. C.M. Sellars, "Options and Constraints for Thermomechanical Processing of Microalloyed Steel", Proceedings of an International Conference on HSLA Steels '85, Metallurgy and Applications, Beijing, China, edited by J.M Gray, ASM International, 1986, pp 73-82

84. V. Thillou, M Hua, et al., “ Precipitation of NbC and Effect of Mn on the Strength Properties of Hot Strip HSLA Low Carbon Steel”, Materials Science Forum, vols 284-286 (1998), pp 314
85. Meyer and Strazsburger, “Effect and Present Application of the Microalloying Elements Nb, V, Ti, Zr and B in HSLA Steels”, Proceedings of an International Conference on HSLA Steels ‘85, Metallurgy and Applications, Beijing, China, edited by J.M Gray, ASM International, 1986, pp 29
86. J G Williams, C R Killmore, “Modern Technology for Linepipe Steel Production (x60 to x80 and beyond) Proceedings of MA’95 Pittsburgh, 1995, pp 121
87. J. Lessells “Use of Microalloying Elements to Improve Mechanical Properties in Plates”, Proceedings of an International Conference on HSLA Steels ‘85, Metallurgy and Applications, Beijing, China, edited by J.M Gray, ASM International, 1986, pp 618
88. H. Abrams, J.R. Paules, “Production Technology of Bethlehem’s HSLA Plate Steels, -Past, Present and Future”, Proceedings of an International Conference on HSLA Steels ‘85, Metallurgy and Applications, Beijing, China, edited by J.M Gray, ASM International, 1986, pp 586
89. Paul E. Repas, “Hot-Rolled Cb-Ti and Cb-Ti-V Sheet Steels with 415 to 620 MPa Yield Strengths”, Proceedings of an International Conference on HSLA Steels ‘85, Metallurgy and Applications, Beijing, China, edited by J.M Gray, ASM International, 1986, pp 935
90. H. De Boer, H. Beenker “Thermomechanical Treatment of HSLA Steels Fundamentals and Realization”, Proceedings of an International Conference on HSLA Steels ‘85, Metallurgy and Applications, Beijing, China, edited by J.M Gray, ASM International, 1986, pp 548
91. A. Lederer “ Influence of Thermomechanical Rolling of HSLA Steel Plates on Mill Production and Design”, Proceedings of an International Conference on HSLA Steels ‘85, Metallurgy and Applications, Beijing, China, edited by J.M Gray, ASM International, 1986, pp508
92. M. Militzer, E. Hawbolt, T. Meadowcroft, “Microstructural Model for the Hot Strip Rolling of High Strength Low Alloy Steels’, Metallurgical and Materials Transactions A, Vol 31A, April 2000, pp 1248
93. L. Myllykoski, P.Mantyla, ”Advances in the Accelerated Cooling of Plates”, Proceedings of MA’95 Pittsburgh, 1995, pp 183
94. T. Tanaka, “ Science and Technology of Hot Rolling Process of Steel”, Proceedings of MA’95, Pittsburgh, 1995, pp 177

95. K.Hulka H.G. Hillengrand, "High Temperature Thermomechanical Processing Background and Application", Proceedings of MA'95, Pittsburgh, 1995, pp 242
96. O.Kwon, K. Lee, "Modeling of Austenite Evolution and Transformation for MA Strips", Proceedings of MA'95, Pittsburgh, 1995, pp 258
97. De Vito, L Masi, "Hot Rolled Coil for Special Applications", Proceedings of an International Conference on HSLA Steels '85, Metallurgy and Applications, Beijing, China, edited by J.M Gray, ASM International, 1986, pp 954
98. V. Thillou, "Precipitation of Nb in Ferrite in HSLA Steels" Unpublished Research, 1997
99. J. Li , F. Sun , W. Xu, "On the evaluation of yield strength for microalloyed steels", Scripta Metallurgica et Materiala, vol 24, 1990, pp1393-1398
100. R. W. Guard, "Mechanism of Fine-particle Strengthening", Strengthening Mechanisms in Solids, Papers presented at a Seminar of the American Society for Metals, Oct. 13 and 14, 1960, pp253-278
101. J. D. Embury, A. S. Keh and R. M. Fisher, "Substructure Strengthening in Materials Subject to Large Plastic Strain", Trans. Met. Soc. AIME, vol 236, September 1966, pp1252-1260
102. F. Pickering, "Towards Improved Toughness and Ductility ", Climax Molybdenum Co., 1971, p. 9.
103. P. Morcinek. V. Smid, T. Heczko, T. Prnka., "Effects of controlled rolling and microalloying on properties of strips and plates", Proceedings of Microalloying 75, October 1-3 1975, Washington DC, edited by M. Korchynsky et al, Union Carbide Corporation, (1977), pp 272-278.
104. M. Hoogendoorn, A. Bodin, "Accelerated Cooling of Strips: From Coiling Temperature Control to Heat Treatment", Proceedings of MA'95, Pittsburgh, 1995, pp 263
105. Huang, Unpublished Research, University of Pittsburgh, 2002
106. V. Thillou, "Precipitation of Nb in Ferrite in HSLA Steels" Unpublished Research, 1997
107. J.E. Garcia, J. Wu, A.J. DeArdo, P. Wray, "Reducing the Variability of HSLA Sheet Steels", AISI and DOE Technical Roadmap Program, Project No. 9807, 8<sup>th</sup> Quarterly Report, 2001

108. J.E. Garcia, J. Wu, A.J. DeArdo, P. Wray, "Reducing the Variability of HSLA Sheet Steels", AISI and DOE Technical Roadmap Program, Project No. 9807, 9<sup>th</sup> Quarterly Report, 2002
109. H. Kejian, T.N Baker, "The Effect of Small Ti additions on the Mechanical Properties and the Microstructure of controlled Rolled Nb-bearing HSLA plate steel" Materials Science and Engineering A, vol 169A, No.1-2, 1993, pp53-65
110. A.C. Kneissl, C.I Garcia, A.J. DeArdo, "Characterization of Precipitates in HSLA Steels", Proceedings of an International Conference on HSLA Steels '85, Metallurgy and Applications, Beijing, China, edited by J.M Gray, ASM International, 1986, pp99-105
111. Vollrath et al., "Influence of TM-rolling parameters on properties of microalloyed cold rolled steels", MA '88 Conf. Proc., ISS-AIME, 1988, pp. 355-357
112. R.W. Honeycombe et al., "Carbide precipitation in HSLA steels" Processing, Microstructure and Properties of HSLA Steels, TMS, ed by A. J . DeArdo, Pittsburgh, PA, 1988, p 11.
113. Korchynsky et al., "Microalloying and TM treatment " Processing, Microstructure and Properties of HSLA Steels, TMS, ed by A. J. DeArdo, Pittsburgh, PA, 1988. p 182.
114. Olsson et al., " Microstructure and mechanical properties of continuously annealed high strength cold rolled steel sheets microalloyed with Nb" Processing, Microstructure and Properties of HSLA Steels, TMS, ed by A. J . DeArdo, Pittsburgh, PA, 1988.
115. Leber et al., "On the strength properties of Nb-bearing low carbon bainitic forging steels". Processing, Microstructure and Properties of HSLA Steels, TMS, ed by A. J DeArdo, Pittsburgh, PA, 1988.
116. Bodin et al., "Development of hot rolled formable steel having a YS of 700 MPa". Materials Solutions '97 on Accelerated Cooling/Direct Quenching Steels. Indianapolis, Indiana, 1997.
117. Wang et al., "Establishment of TMCP process in the plate mill of CSC". Materials Solutions '97 on Accelerated Cooling/Direct Quenching Steels. Indianapolis, Indiana, 1997.
118. Kwon et al, "Modeling of precipitation during coiling in Nb-bearing HSLA steels". Materials Solutions '97 on Accelerated Cooling/Direct Quenching Steels. Indianapolis, Indiana, 1997.
119. Grozier, "Production of microalloyed strip and plate by controlled cooling". Proceedings of MA '75 Conf. Proc., ISS-AIME, Washington, DC., 1975.

120. Dengqi Bai, et al., "Processing, microstructure and mechanical properties of a Nb-bearing high strength linepipe steel" 43<sup>rd</sup> MWSP Conf. Proc., ISS, Volume XXXIX. Charlotte, NC, 2001, p. 552
121. O. Kwon, K. Lee, "Modeling of Austenite Evolution and Transformation for MA Strips", Proceedings of MA'95 Pittsburgh, 1995, pp 251
122. S. Zajac, R. Lagneborg, "The Role of Nitrogen in Microalloyed Steels", Proceedings of MA'95, Pittsburgh, 1995, pp 321
123. I. Kozasu,"State of the Art in Microalloyed Plate Production", Proceedings of MA'95, Pittsburgh, 1995, pp 95
124. L.Myllykoski, P. Mantyla, "Advances in the Accelerated Cooling of Plates", Proceedings of MA'95, Pittsburgh, 1995, pp 183
125. T.Siwecki, B. Hutchinson, "Recrystallization Controlled Rolling of HSLA Steels". Proceedings of MA'95 Pittsburgh, 1995, pp 197